Enzyme and device driven solutions for sustainable wastewater bioremediation and monitoring

A thesis submitted in partial fulfilment of the

requirements for the degree of

Doctor of Philosophy

by

SATYAM

(196106020)

Under the supervision of

Professor Sanjukta Patra

Department of Biosciences and Bioengineering

Indian Institute of Technology Guwahati

Guwahati-781039, Assam, India

July 2025

Dedicated to

The pursuit of pure water(s) and the unwavering support of my family

INDIAN INSTITUTE OF TECHNOLOGY GUWAHATI

Department of Biosciences and Bioengineering

Assam, Guwahati-781039

Declaration

I hereby declare that the research findings presented in this thesis, entitled **"Enzyme and Device Driven Solutions for Sustainable Wastewater Bioremediation and Monitoring,"** are the result of research work carried out by me in the Department of Biosciences and Bioengineering, Indian Institute of Technology Guwahati, India, under the supervision of **Professor Sanjukta Patra**.

I also declare that the contents of this thesis have not been submitted, in whole or in part, for any other degree, diploma, fellowship, associateship, or any similar title of any other University or Institution to the best of my knowledge and belief.

In keeping with academic norms for reporting research, due acknowledgments have been made wherever the findings of other researchers have been cited in this thesis.

Date: 23-04-2025

Satyam

Place: IIT Guwahati

Satyam

INDIAN INSTITUTE OF TECHNOLOGY GUWAHATI

Department of Biosciences and Bioengineering

Assam, Guwahati-781039

Sanjukta Patra
Professor
Department of Biosciences and Bioengineering

Tel. No.: +91-361-2583210
Fax No.: +91-361-2582249
E-mail: sanjukta@iitg.ac.in

Certificate

This is to certify that the thesis entitled "**Enzyme and Device Driven Solutions for Sustainable Wastewater Bioremediation and Monitoring**" being submitted to the Indian Institute of Technology Guwahati by **Satyam** for the award of the degree of Doctor of Philosophy in Biosciences and Bioengineering is a bonafide record of research work carried out by him. The contents of this thesis have not been submitted, either in part or in full, to any other University or Institute for the award of any degree or diploma.

Date: 17-7-2025

Place: IIT Guwahati

Professor Sanjukta Patra

(Supervisor)

Acknowledgments

Embarking on a PhD journey is akin to navigating a labyrinth of challenges, discoveries, and growth, a voyage made possible only through the collective support of mentors, colleagues, friends, and family. As I conclude this transformative chapter at IIT Guwahati, I extend my deepest gratitude to those who illuminated my path, fuelled my perseverance, and shared in both my struggles and triumphs.

Foremost, I express my profound gratitude to my supervisor, ***Prof. Sanjukta Patra****, whose unwavering guidance, intellectual rigor, and relentless encouragement shaped every facet of this journey. Her expertise in microbial technology, coupled with her patience in nurturing my scientific curiosity, transformed challenges into opportunities for growth. I am equally thankful for her trust in my abilities, which empowered me to evolve as an independent researcher. I am also deeply grateful to my administrative supervisor,* ***Dr. Priyadarshi Satpati****, for his advice, constructive feedback, and encouragement during my research endeavours. His guidance has been instrumental in refining my understanding and approach to scientific problems.*

I wish to express my heartfelt thanks to my doctoral committee members- ***Professor Rakhi Chaturvedi, Dr. Soumen Kumar Maiti, and Dr. Rajkumar P. Thummer,*** *for their valuable insights, constructive feedback, and support throughout this journey. Their expertise and suggestions have significantly contributed to shaping my research.*

I am fortunate to have been a part of the Enzyme and Microbial Technology Laboratory, where I had the pleasure of working alongside an incredible team, each with unique expertise. I sincerely thank my current lab members- ***Mukesh Akula, Mayur Mahindra Kedare, Ghadir Nofal, Tarun Gangar, Risha Hazarika, Shrinidhi Bhat, and Senthamiz Ravichandran****, for their camaraderie, stimulating discussions, and support. Additionally, I am grateful to* ***Dr. Satakshi Hazra and Dr. Prithwi Chayan Chatterjee****, our former lab members, for their guidance and collaboration in the initial phases of my research.*

I would also like to extend my gratitude to ***Prof. Utpal Bora****, our current Head of the Department, and former Heads of the Department,* ***Prof. V. Venkata Dasu****,* ***Prof. Kannan Pakshirajan, Prof. Latha Rangan****, and* ***Prof. Rakhi Chaturvedi****, for their continuous support and for ensuring a conducive research environment. My sincere appreciation also goes to the Department of Biosciences and Bioengineering (BSBE), IIT Guwahati, and all the* ***faculty and staff members*** *for their assistance and cooperation during my doctoral journey.*

*I acknowledge the financial support from the **Ministry of Human Resource Development** (MHRD), India; **Indian Institute of Technology Guwahati**; **North-East Centre for Biological Sciences and Healthcare Engineering** (NECBH); and the **Indo-EU Horizon 2020 project** (BT/IN/EU-WR/60/SP/2018) funded by DBT, New Delhi.*

*Beyond academics, my journey was made more fulfilling by the presence of my wonderful friends, **Hari, Vishnu, Anshuman, Surabhi, Shilpi, and Robin**, who have been my pillars of strength, always keeping me motivated and offering their expertise and input whenever needed. A special note of gratitude goes to **Payal**, without whom I cannot imagine my PhD journey. Her unwavering support, whether through technical discussions or simply being there during moments of uncertainty, has been invaluable.*

*Lastly, I extend my deepest gratitude to my family, **Maa, Papa, Didi, and Shivam**, for their unconditional love, sacrifices, and encouragement. This accomplishment is as much yours as it is mine.*

As I close this chapter, I carry forward the lessons, relationships, and resilience forged during these years, a testament to the power of collective effort and unwavering determination.

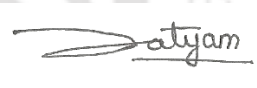

Date: 05-04-2025

Place: IIT Guwahati

Satyam

Table of Contents

Abstract

The escalating global water pollution crisis, driven by industrial, agricultural, and urban activities, endangers ecosystems, biodiversity, and human health. A diverse array of contaminants including organic compounds, heavy metals, microbial pathogens, microplastics, and synthetic dyes further exacerbates these risks. Conventional water treatment methods, while effective to a degree, face limitations in cost, efficiency, and environmental sustainability, necessitating innovative solutions to address persistent and emerging pollutants. Additionally, plastic waste mismanagement and inefficient real-time monitoring hinder timely interventions. This thesis addresses these challenges through sustainable, innovative solutions that enhance environmental resilience. A key focus was developing enzyme-assisted systems to improve wastewater treatment. By optimizing the Hu-XO enzyme from *P. pastoris* to generate hydrogen peroxide in situ, a synergistic Fenton system was engineered, achieving >99% decolorization of dyes like Congo red and significant reductions in BOD (91.8%) and COD (86%). The process eliminated dependence on external H_2O_2 and acidic conditions and showed 99% antimicrobial efficiency, validated via bioluminescence inhibition and phytotoxicity assays. To tackle plastic pollution, protein engineering was employed to enhance PET hydrolases. The Mors1 PETase from Antarctic *Moraxella* TA144 was modified (K93I, E221I, R235F), producing $Mors1^{MUT}$ with superior thermal stability and activity at pH 9, retaining 98% activity and achieving a 4.16-fold increase in PET hydrolysis efficiency. This reduces energy demands and enables scalable biological recycling. For safe drinking water, an energy-efficient, modular distillation system was developed using piezoelectric ultrasonic misting, thermoelectric Peltier modules, and UV-C sterilization. Built from biodegradable PLA, it achieved 83% water recovery, removing 490 mg/L NaCl, 1.5×10^8 CFU/mL *E. coli*, 50 mg/L Congo red, and 60 µL/L toluene/o-xylene. Integrated VOC valves and precise temperature control minimized energy use, outperforming reverse osmosis systems. To support real-time water monitoring, a solar-powered, IoT-enabled device was designed with multiparametric sensors (temperature, DO, turbidity, TDS) and GPS. Built on open-source platforms (Firebase, Plotly.js), it eliminates recurring server costs and enables AI/ML-based analytics, empowering end-user with timely, actionable insights. Collectively, this work highlights how biotechnology, materials science, and digital tools can holistically address wastewater challenges, promoting sustainable pollutant degradation, plastic recycling, water purification, and monitoring.

List of Abbreviations

4,4′-DTPY	4,4′-dithiodipyridine
A-His-Ab	anti-His-tag antibody
A. fischeri	*Aliivibrio fischeri*
AFM	Atomic Force Microscope
AI	Artificial Intelligence
AMP	Adenosine Monophosphate
ANOVA	Analysis of Variance
AOPs	Advanced Oxidation Processes
API	Application Programming Interface
APS	Ammonium Persulfate
ATR	Attenuated Total Reflectance
B. subtilis	*Bacillus subtilis*
BHET	bis-hydroxyethyl terephthalate
BMGY	Minimal Glycerol Yeast Extract
BMMY	Buffered Minimal Methanol Yeast Extract
BOD	Biological Oxygen Demand
BPA	Bisphenol A
C. arietinum	*Cicer arietinum*
CCD	Central Composite Design
CD	Circular Dichroism
CLC	Calcutta Leather Complex
CLI	Command Line Interface
CSIR-CLRI	Council of Scientific and Industrial Research–Central Leather Research Institute
COD	Chemical Oxygen Demand
CR	Congo Red
DALYs	Disability-Adjusted Life Years
DC	Direct Current
DO	Dissolved Oxygen
E. coli	*Escherichia coli*
ECL	Enhanced Chemiluminescence
ESI	Electrospray Ionization
EtBr	Ethidium Bromide
Fig	Figure
FTIR	Fourier Transform Infrared
GAC	Granular Activated Carbon
GAR-IgG-HRP	goat anti-rabbit IgG-HRP antibody
GB	Giga byte
GIS	Geographic Information Systems
GMP	Guanine Monophosphate
GPS	Global Positioning System
GRAPE	Greedy Accumulated Strategy for Protein Engineering
HPC	Heterotrophic Plate Counts
HRP	Horseradish Peroxidase
HTML	Hypertext Markup Language
Hu-XDH	Human Xanthine Dehydrogenase
Hu-XO	Human Xanthine Oxidase
IoT	Internet of Things
LCSNs	Low-Cost, Open-Source Wireless Sensor Networks
LSLB	Low Salt Luria Bertani
MHET	Mono-hydroxyethyl terephthalate
ML	Machine Learning
MOF	Metal-Organic Framework
MS	Mass Spectrometry

MWCO Molecular Weight Cutoff

Ni–NTA Nickel–Nitrilotriacetic Acid

OPH Organophosphorus Hydrolase

P. pastoris *Pichia pastoris*

PAHs Polycyclic Aromatic Hydrocarbons

PBST Phosphate-Buffered Saline with Tween 20

PCBs Polychlorinated Biphenyls

PCL Polycaprolactone

PE Polyethylene

PET Polyethylene Terephthalate

PI Propidium Iodide

PLA Polylactic Acid

POPs Persistent Organic Pollutants

PP Polypropylene

PPCPs Pharmaceuticals and Personal Care Products

PS Polystyrene

PBS Phosphate Buffered Saline

Q/TOF-MS Quadrupole Time-of-flight Mass Spectrometry

RAG Retrieval-Augmented Generation

RFU Relative Fluorescence Unit

RMS Root Mean Square

RO Reverse Osmosis

ROS Reactive Oxygen Species

RPM Revolutions Per Minute

RSM Response Surface Methodology

RX Receive Across

SBCs Single-Board Computers

SCK Serial Clock

SDG 6 Sustainable Development Goals

SDI Serial Digital Interface

SDS–PAGE Sodium Dodecyl Sulfate-Polyacrylamide Gel Electrophoresis

SEC Size Exclusion Chromatography

SEM Scanning Electron Microscopy

SMS Short Message Service

SUP Supernatant

TAE Tris-acetate-EDTA

TDS Total Dissolved Solids

TEM Transmission Electron Microscopy

TEMED N,N,N',N'-Tetramethylethylenediamine

TPA Terephthalic Acid

TX Transmit Across

UF Ultra Filtration

URL Uniform Resource Locator

UTLIWW Untreated Leather Industry Wastewater

UV Ultraviolet

V Volt

V. radiata *Vigna radiata*

VCC Voltage Common Collector

VOCs Volatile Organic Compounds

WHO World Health Organization

WSNs Wireless Sensor Networks

YPD Yeast Extract Peptone Dextrose

mA Milliampere

mAh Milliampere-hour

mU Milliunit

List of Figures

List of Tables

Chapter 1 Introduction & Review of Literature

Abstract

The growing global water pollution crisis poses significant threats to human health, ecosystems, and biodiversity. This chapter delves into the complex issue of water contamination caused by various pollutants, including organic, inorganic, microbial, and emerging substances like microplastics and synthetic dyes. Organic pollutants, such as pesticides and pharmaceuticals, are particularly concerning due to their bioaccumulation and persistence in aquatic systems. Inorganic contaminants, including heavy metals, present grave risks to both human health and ecological balance, while microbial pathogens are major contributors to waterborne diseases, especially in areas with inadequate sanitation. Emerging pollutants, such as endocrine disruptors and microplastics, further exacerbate the problem by introducing unprecedented risks to environmental and public health. Conventional water treatment methods, including physical, chemical, and biological approaches, are effective but face limitations in cost, efficiency, and environmental sustainability. Advanced technologies, such as nanotechnology, enzyme-based treatments, and MOFs, provide innovative solutions, yet require further optimization for widespread application. Integrating IoT-enabled real-time water monitoring systems offers sustainable water resource management, supported by open-source technologies like single-board computers for cost-effective and customizable solutions. This thesis addresses existing gaps by proposing advanced bio-oxidative processes, energy-efficient distillation units, and IoT-based monitoring systems.

1.1 Introduction

The global water pollution crisis has emerged as a critical issue, impacting the health of humans, ecosystems, and the planet's biodiversity. Water pollution, defined by the presence of contaminants that degrade water quality, is a multifaceted problem driven by various types of pollutants [1]. Organic pollutants like putrescible organic waste can increase the microbial load and deplete DO in water bodies, endangering aquatic life forms. Inorganic contaminants, particularly heavy metals like lead, arsenic, cadmium, mercury, and others, can bioaccumulate at higher food chain trophic levels and cause severe illness and even death. Microbial contaminants, including pathogens, are a significant concern as they can cause waterborne diseases such as cholera, typhoid, and diarrhoea. These pathogens are often introduced through domestic sewage and can have devastating effects on public health (Ahmad et al., 2024).

In addition to these traditional pollutants, emerging contaminants such as plastics and microplastics have become a significant concern. Microplastics, which are plastic particles less than 5 mm in size, can be ingested by aquatic organisms and have been found in many drinking water sources globally, highlighting the need for new strategies to address these pollutants [3]. The impacts of water pollution are far-reaching and severe. Waterborne diseases caused by microbial contaminants affect millions worldwide, particularly in regions with inadequate sanitation infrastructure [4]. The disruption of ecosystems due to pollution can lead to biodiversity loss, as seen in the formation of "dead zones" in coastal areas where dissolved oxygen levels are too low to support most aquatic life. Aquatic organisms are particularly vulnerable to water pollution. For instance, thermal pollution from industrial activities and global warming can alter fish's metabolic rates and reduce water's dissolved oxygen levels, making it inhospitable for many species [5,6].

Conventional treatment methods, such as physical, chemical, and biological treatments, have been employed to mitigate water pollution. However, these methods often have limitations in terms of effectiveness and sustainability. There is a continuous effort to innovate and enhance these methods to make them more efficient and environmentally friendly. Modern advanced techniques, including adsorption, AOPs, MOF, nanotechnology, and engineered enzyme-based bioremediation, are being developed to address the complexities of water pollution [7]. Parallel to these developments, the increase in global water pollution spurred research and development in creating standalone water purification devices for domestic use. These systems utilized a variety of technologies, including RO, UF, distillation, activated carbon filtration, and UV

purification, each tailored to address specific contaminants. RO systems, for example, effectively removed dissolved salts, heavy metals, and bacteria by pushing water through a semipermeable membrane. UF technology, using larger membrane pores than RO, eliminated larger particles, bacteria, and some viruses, all without requiring electricity. UV purification, a chemical-free option, used light to neutralize bacteria and viruses, while activated carbon filters removed chlorine, VOCs, and unpleasant odours to improve water taste. Many systems combined these methods for comprehensive purification and even incorporated remineralization to restore essential minerals after filtration. Although these technologies offered various advantages, each came with certain limitations, sparking ongoing research to develop more sustainable, efficient, and user-friendly solutions for safe drinking water in homes worldwide [8].

Effective water pollution management relies heavily on accurately sensing water parameters. As the adage goes, *"We can only act on those which we can sense"*. Conventional sensing devices, such as spectrophotometers and electrochemical sensors, have been used to monitor water quality. However, these devices often have limitations in terms of real-time monitoring and remote sensing capabilities. Integrating IoT technology in water-sensing devices has revolutionized data collection and remediation efforts. IoT-based sensors can provide real-time data on various water parameters, enabling prompt action to be taken in response to changes in water quality. These sensors also facilitate remote monitoring, reducing the need for physical sampling and enhancing the efficiency of water management systems [9,10].

1.2 Types of water pollutants

Water, an essential resource for all life, is vulnerable to contamination from a myriad of sources. Fig 1.1 illustrates the various types of pollutants that contaminate water sources. Understanding the diverse nature of these pollutants is crucial for developing effective strategies to protect and remediate water resources. This section explores the main types of water pollutants, drawing on scientific research to offer a thorough overview.

1.2.1 Organic and biochemical pollutants

Organic pollutants are primarily composed of carbon and hydrogen and originate from natural and anthropogenic sources. A significant contributor is sewage, which carries domestic wastewater containing various organic compounds, including human waste, food scraps, dye stuffs, and detergents. Animal waste from agricultural operations and food processing waste from industries further contribute to organic pollution, introducing proteins, fats, and

carbohydrates into water bodies. Decaying plant matter also releases organic substances, such as tannins and lignins, which can impact water quality [11].

1.2.2 Inorganic and chemical pollutants

Inorganic pollutants encompass a wide range of non-carbon-based substances, including heavy metals, acids, alkalis, and salts. Heavy metals like mercury, lead, and arsenic are often released from industrial processes and mining activities, posing severe health risks. Acids and alkalis can alter the pH of water, disrupting aquatic life and corroding infrastructure. Inorganic salts, including chlorides and sulphates, can increase water salinity, affecting its suitability for drinking and irrigation. Pesticides, herbicides, and industrial chemicals are also major contributors to inorganic pollution. These chemicals are used extensively in agriculture and manufacturing, and their runoff can contaminate water bodies, harming aquatic organisms and potentially entering the food chain. Pharmaceuticals, fertilizers, and petrochemicals are additional sources of inorganic pollutants, with potential impacts on human and environmental health [12].

1.2.3 Nutrient and agricultural pollutants/runoffs

Nutrient pollution, primarily caused by excessive nitrogen and phosphorus, is a major concern for water quality. Phosphates and nitrates are essential nutrients for plant growth but can cause eutrophication in water bodies, leading to algal blooms, oxygen depletion, and fish kills. Agricultural runoff is a significant source of these nutrients, carrying fertilizers, animal waste, and soil erosion into waterways. Ammonia, animal hormones, and antibiotics are also present in agricultural runoff, posing additional risks to aquatic ecosystems and human health [13].

1.2.4 Microbiological contaminants

Microbiological contaminants include various disease-causing microorganisms, such as bacteria, viruses, protozoa, and parasitic worms. These contaminants primarily originate from untreated sewage, animal waste, and agricultural runoff. They can cause a range of waterborne diseases, posing significant health risks to humans and animals [14].

1.2.5 Particulate and sediment pollutants

Particulate and sediment pollutants consist of suspended solid particles, including soil particles, silt, clay, and microplastics. These pollutants can reduce water clarity, affecting light penetration and photosynthesis in aquatic plants. They can also clog fish gills, smother benthic organisms, and transport adsorbed pollutants, such as heavy metals and pesticides.

Microplastics, tiny plastic particles, are emerging as a significant concern due to their persistence in the environment and potential impacts on aquatic organisms and human health [15].

1.2.6 Thermal and radioactive pollutants

Thermal pollution occurs when heated water from industrial processes, such as power plants, is discharged into water bodies. This can increase water temperature, affecting dissolved oxygen levels and disrupting aquatic life. Radioactive pollutants, originating from nuclear power plants, medical facilities, and research institutions, can pose long-term health risks due to their radioactive decay [16].

1.2.7 Atmospheric and emerging pollutants

Atmospheric pollutants, such as acid rain and airborne particulates, can also contribute to water pollution. Acid rain, caused by sulphur dioxide and nitrogen oxide emissions, can lower the pH of water bodies, harming aquatic life. Airborne particulates can carry various pollutants, including heavy metals and organic compounds, which can deposit into water bodies through atmospheric deposition. Emerging pollutants are a growing concern, encompassing a wide range of chemicals and materials not traditionally monitored in water. These include personal care products, endocrine disruptors, and nanomaterials. Personal care products, such as shampoos, lotions, and fragrances, contain various chemicals that can enter water bodies through wastewater, potentially affecting aquatic organisms and human health. Endocrine disruptors are chemicals that can interfere with the endocrine system, causing developmental and reproductive problems in humans and wildlife. Nanomaterials, due to their small size and unique properties, are increasingly used in various applications, but their potential impacts on water quality and human health are still being investigated [17].

While all pollutants pose some degree of risk, those of greatest concern include heavy metals like mercury and arsenic, persistent organic pollutants such as pesticides and pharmaceuticals, microplastics, radioactive waste, organic waste, dye stuffs, pathogenic, and microbes due to their potential for long-term ecological damage and human health impacts. Effective water quality management requires a thorough understanding of these pollutants and their interactions within aquatic ecosystems [11]. Since this thesis focuses on the multifaceted challenge of water contamination stemming from diverse organic sources, including dye stuffs, microbes, and microplastics, these specific pollutants and their implication are explored in detail in subsequent sections.

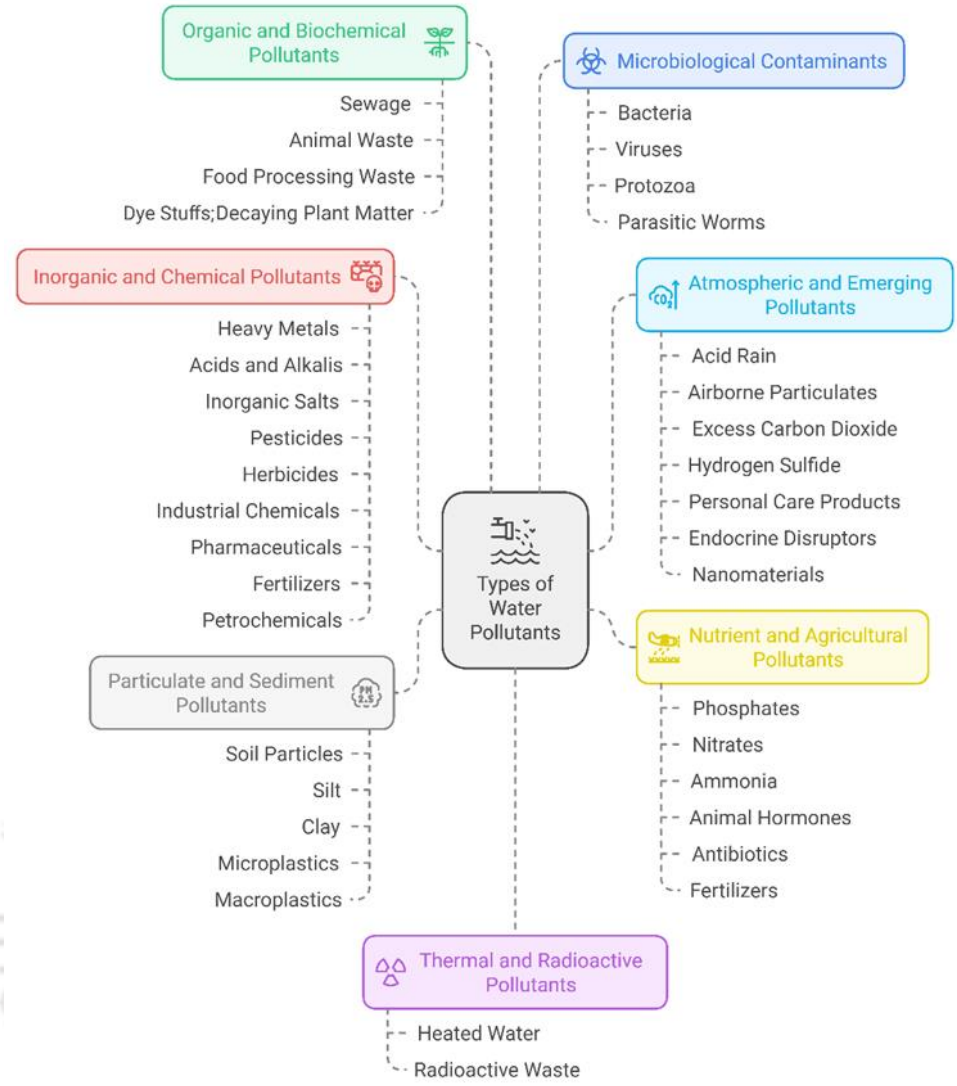

Fig 1. 1 Diverse range of pollutants that can contaminate water sources

1.3 Organic contaminants

Organic water contaminants consist primarily of carbon and hydrogen compounds, often accompanied by oxygen, nitrogen, sulphur, or halogens. The structural diversity of these contaminants ranges from simple hydrocarbons to complex organic acids, pesticides, and surfactants. Many of these compounds are characterized by low water solubility and high chemical stability, leading to persistence in the environment and potential bioaccumulation. A significant fraction of organic contaminants consists of POPs such as PCBs and PAHs. These compounds resist environmental degradation through chemical, biological, and photolytic processes, allowing them to persist in the environment for extended periods. When introduced into aquatic ecosystems, these pollutants bind to sediments or accumulate in organisms' lipid tissues, entering and magnifying through food webs. Organic pollutants such as phthalates and

certain synthetic dyes can exhibit estrogenic activity, interfering with endocrine systems in both aquatic and terrestrial organisms [11,18].

1.3.1 Sources of organic contaminants

1.3.1.1 Sewage and domestic wastewater

Domestic wastewater contains a myriad of organic substances, including proteins, fats, carbohydrates, surfactants, and synthetic compounds like personal care products and pharmaceuticals. High organic load in sewage, coupled with nutrients like nitrogen and phosphorus, enhances the BOD in water bodies, potentially leading to oxygen depletion. The PPCPs are often chemically stable, making them resistant to conventional wastewater treatment processes and contributing to their persistence in aquatic environments. Surfactants, a major component of domestic waste, lower surface tension, altering the properties of water and affecting organisms sensitive to these changes [19].

1.3.1.2 Agricultural runoff and animal waste

Intensive agricultural practices produce vast amounts of organic pollutants, including animal manure and fertilizer residues. Animal waste, rich in nitrogenous compounds like ammonia and organic phosphates, enters water bodies through runoff, contributing to nutrient overload and eutrophication. Additionally, organic residues from pesticides and herbicides, often containing complex aromatic structures and halogen substitutions, have limited biodegradability and high persistence in soils and sediments. Certain pesticides like organochlorines and organophosphates, widely used in agriculture, are persistent and toxic to aquatic life even at low concentrations [20].

1.3.1.3 Industrial effluents

Industrial wastewaters are often highly variable in composition, containing dyes, oils, solvents, and by-products from chemical processes. Organic compounds from industries, especially in the textile, food processing, and paper sectors, introduce a complex mix of hydrocarbons, aldehydes, and ketones into water bodies. The textile industry, for instance, uses dyes and solvents that are resistant to biodegradation, such as azo dyes, which are composed of nitrogen-nitrogen double bonds (N=N) and aromatic rings. Upon degradation, azo dyes can release aromatic amines, some of which are carcinogenic and pose significant risks to human and ecological health. In the paper industry, chlorinated organic compounds generated during

bleaching processes are another persistent class of pollutants with known toxic and mutagenic effects [21,22].

1.3.1.4 Natural sources

Organic compounds also enter water systems naturally, particularly from decaying plant materials. When leaves, wood, and other plant parts break down, they release tannins and lignins, phenolic compounds that can alter the water's pH, colour, and oxygen levels. Lignins, for example, are complex polymers that are resistant to biodegradation and can form by-products when subjected to photolytic degradation. In heavily forested or marshy regions, this natural leaching process may impart a brownish colour to the water, reducing its aesthetic value and affecting light penetration, which is essential for photosynthetic aquatic plants [23].

1.3.2 Impact of organic pollutants on aquatic systems and human health

Organic contaminants in aquatic systems disrupt both chemical and biological balance. High organic loadings from sewage, agricultural runoff, and industrial effluents increase the BOD, creating hypoxic or even anoxic conditions. When oxygen levels fall, aerobic organisms, including fish and invertebrates, struggle to survive, leading to reduced biodiversity. This oxygen depletion also affects the breakdown of organic matter, promoting anaerobic conditions that can result in the formation of harmful gases like methane and hydrogen sulphide. Organic pollutants such as POPs and PAHs exhibit bio-accumulative and biomagnifying properties, allowing them to concentrate as they move up the food chain [18,24].

Synthetic dyes and pesticides are another concern due to their toxic, mutagenic, and sometimes endocrine-disrupting properties. Azo dyes, commonly used in textiles, can release aromatic amines, which are harmful even in low concentrations. Similarly, pesticide residues from organophosphates can inhibit acetylcholinesterase, an enzyme crucial for nerve function, affecting both aquatic organisms and humans who may ingest contaminated water or food. Additionally, the accumulation of PPCPs and estrogen-mimicking compounds disrupts endocrine functions, affecting reproductive health in aquatic organisms. Fish, for instance, exhibit altered sex ratios and reproductive behaviours when exposed to these contaminants, which may have long-term implications for species survival [25,26]. The diversity of organic pollutants and their impacts on water quality and aquatic health are summarized in Table 1.1, providing a detailed view of how various contaminants from different sources contribute to environmental degradation and pose risks to human and ecosystem health.

Table 1. 1 Table 1. 1 Types, sources, and impacts of major organic pollutants in aquatic environments

Type of organic pollutant	Primary sources	Impact on water quality	Impact on aquatic and human health
Sewage and Domestic Waste	Domestic wastewater, pharmaceuticals, surfactants	High BOD, nutrient overload, turbidity	Oxygen depletion, growth of pathogenic organisms, accumulation of PPCPs affecting human health
Agricultural Runoff and Animal Waste	Animal manure, fertilizers, pesticide residues	Nutrient overload, hypoxia, increased COD	Eutrophication, bioaccumulation of pesticides, endocrine disruption from hormone residues
Industrial Effluents (Dyes, Solvents)	Textile dyes (e.g., azo dyes), oils, and paper by-products	Persistent organic matter, colour changes, chemical stability	Carcinogenic effects from aromatic amines, toxicity, endocrine disruption, neurological disorders
Natural Decay (Plant Matter)	Decaying leaves, wood, lignins, tannins	Brownish colour, altered pH, reduced transparency	Formation of toxic by-products, reduced photosynthetic activity, impact on fish and benthic organisms

1.4 Microbial contaminants

Microbial water pollutants are harmful microorganisms, including bacteria, viruses, and protozoa, found in water sources that can pose severe risks to human health. These pathogens are primarily responsible for various waterborne diseases, with the potential to cause severe illness or even death. The WHO estimates that contaminated water contributes to approximately 2.2 million deaths annually, with the most vulnerable populations often located in developing countries where access to clean water is limited. Furthermore, even non-pathogenic microbes can deplete dissolved oxygen in water bodies, impacting aquatic life and disrupting the ecosystem balance. Microbes, being omnipresent in the environment, could readily enter water bodies. However, the key sources of these pathogenic microbes include human and animal waste, agricultural runoff, stormwater runoff, and abandoned mines [14].

1.4.1 Types of microbial water pollutants

The major types of microbes that can contaminate water include bacteria, viruses, and protozoa, with numerous subtypes depending on the water type (marine or freshwater) and characteristics (Fig 1.2). This section discusses the primary types of pathogenic microbes that commonly affect humans. Bacteria, such as *E. coli*, *V. cholerae*, *Salmonella* spp., *Campylobacter* spp., and

Shigella spp., are single-celled organisms that can reproduce rapidly in contaminated water, causing serious gastrointestinal illnesses like cholera, typhoid fever, and diarrhoea. The presence of *E. coli* in water is especially noteworthy as it serves as a key indicator of recent faecal pollution, suggesting the possible existence of additional dangerous microorganisms. Coliform bacteria, a subgroup found in the environment and intestines of warm-blooded animals, serve as critical indicators of microbiological safety in water [14]. Waterborne viruses, including Hepatitis A and E, are transmitted through the faecal-oral route and are prevalent in areas with inadequate sanitation, causing acute epidemics characterized by fever, jaundice, and other systemic symptoms [27]. Protozoa, such as *Giardia* and *Cryptosporidium*, are microscopic parasites that can survive harsh environmental conditions, making them resilient to conventional water disinfection methods. *Giardia* causes giardiasis, while *Cryptosporidium* is associated with outbreaks of gastrointestinal illness, both being transmissible through recreational and drinking water contaminated with faeces. The presence of these diverse microbiological pollutants underscores the critical need for effective water treatment and sanitation practices to protect public health [28].

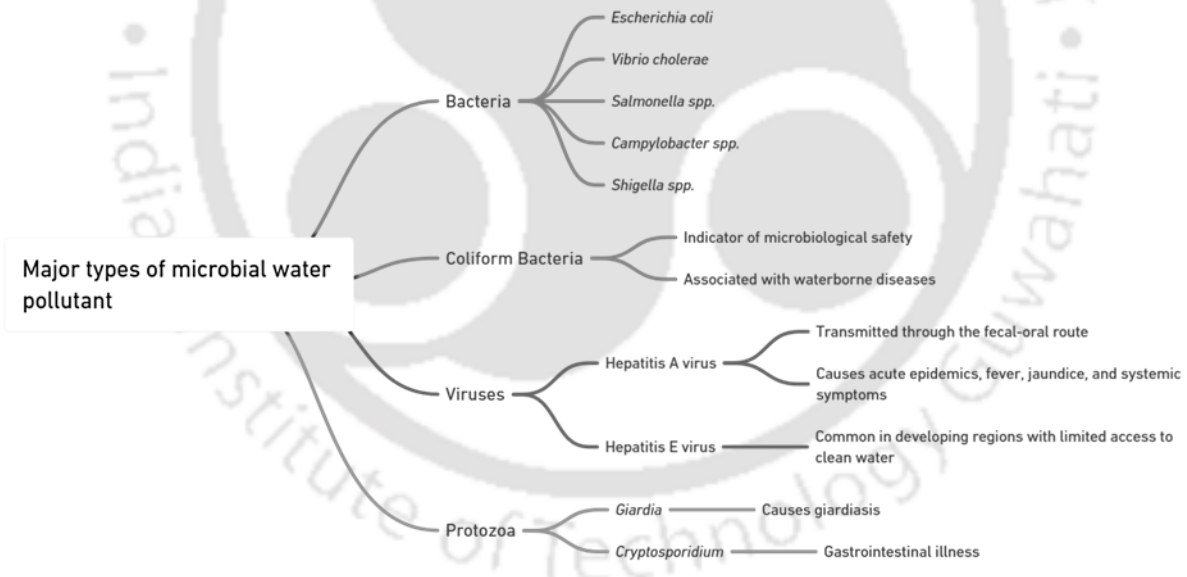

Fig 1. 2 Major types of microbial water pollutants

1.4.2 Impact of microbial water pollutants on human health

Microbiological water pollutants have a profound impact on human health, contributing significantly to the global disease burden. Waterborne diseases, caused by pathogenic microorganisms in contaminated water, lead to approximately 2.2 million deaths each year and result in an annual loss of 8.2 million DALYs. The severity of these diseases is especially high in developing countries, where limited access to clean water and sanitation increases

vulnerability to infections [14]. Unsafe water sources and inadequate sanitation contribute significantly to the disease burden, with studies showing a loss of 917.2 years of healthy life due to suboptimal sanitation and an additional 58.8 years lost to poor handwashing practices. These findings highlight the need for improved water quality standards and sanitation services, especially in rural and underserved areas [29]. Moreover, approximately 15% of the global population lives in water-stressed areas, increasing the risk of contracting these diseases from contaminated sources. Vaccination programs have shown effectiveness in reducing hospitalizations from waterborne diseases; for example, a rotavirus vaccine program significantly reduced hospital admissions for rotavirus-related illnesses among children under five. These public health interventions underscore the importance of comprehensive strategies, including vaccination, sanitation improvements, and access to clean water, to mitigate the health impacts of microbial water pollutants [30].

1.5 Dye based contaminants

Dye-based water pollutants encompass a wide variety of synthetic and natural dyes used across multiple industries, most notably in textiles, leather, and cosmetics. These dyes are primarily synthetic compounds designed for long-lasting colour, making them inherently resistant to natural degradation. Common categories of dyes released into water systems include azo, reactive, acid, and disperse dyes. Azo dyes, among the most widely used, have been highlighted for their potential mutagenic and carcinogenic effects, raising significant health and environmental concerns. Because of their chemical stability, these dyes persist in water environments, complicating their removal and leading to chronic contamination. These pollutants affect water quality in various ways; for example, they reduce transparency, alter the pH, and carry heavy metals and other toxic compounds, which further degrade water ecosystems [31].

1.5.1 Source of dye-based water pollutants

The primary sources of dye-based water pollutants are industrial wastewater discharges, especially from the textile, leather, and cosmetic industries. The textile industry alone accounts for a considerable portion of global dye pollution, as it uses extensive amounts of synthetic dyes that are often discharged without adequate treatment. Other significant contributors include the leather tanning industry, where dyes and additional chemicals used in treating hides leach into water systems, and the cosmetics industry, which introduces synthetic dyes through the disposal of personal care products. Beyond these industries, dye pollutants also come from

pharmaceutical, paper, and food processing sectors, where colorants are used in both production and packaging. Often, the disposal practices in these industries lack adequate wastewater treatment infrastructure, resulting in untreated or partially treated dye effluents entering rivers, lakes, and other water bodies, contributing to widespread environmental degradation [32].

1.5.2 Impact of dye-based water pollutants

The environmental and health impacts of dye-based water pollutants are profound and multifaceted. Environmentally, dye pollutants disrupt aquatic ecosystems by inhibiting light penetration, which is essential for photosynthesis in aquatic plants. This disruption can lead to reduced oxygen levels, harming fish and other aquatic organisms and reducing overall biodiversity. Additionally, some dyes are toxic and bioaccumulate in the tissues of aquatic organisms, creating toxic effects that extend up the food chain and impact both wildlife and human health. From a human health perspective, dye pollutants are associated with a range of adverse effects. Some dyes, particularly azo dyes, have been linked to carcinogenic, mutagenic, and allergenic reactions, posing risks to populations consuming contaminated water or exposed to contaminated environments. Table 1.2 provides a summary of major dye types, their primary industrial sources, effects on water quality, and associated risks to human health and aquatic ecosystems. The persistence of dye pollutants in water systems requires costly and complex treatment methods to mitigate their effects, underscoring the need for stricter regulations and improved wastewater treatment technologies to protect both ecological and public health [33].

1.6 Plastic pollutants

Plastic pollution in water bodies has emerged as one of the most pressing environmental issues of the 21st century. The ubiquity of microplastics, in particular, has raised significant concerns regarding their impact on human health, ecosystem integrity, and the overall quality of water resources. The problem is compounded by the lack of standardized methods for sampling, extracting, and identifying microplastics, which hampers the accuracy and reliability of occurrence studies. The presence of microplastics in drinking water, freshwater sources, and marine environments has been well-documented. These tiny plastic particles, often smaller than 5 mm, originate from various sources including the degradation of larger plastic debris, microbeads in personal care products, and synthetic fibers from clothing. The infiltration of microplastics into water systems is not only a visual and ecological issue but also poses potential health risks to humans and wildlife [3]. The SDG 6 emphasize the importance of

ensuring safe and affordable drinking water, which is now threatened by the pervasive presence of microplastics. As research continues to unravel the complexities of microplastic pollution, a multifaceted approach is necessary to address this global issue [34].

Table 1. 2 Overview of major dye types: sources, water quality impacts, and health risks

Dye type	Primary source	Impact on water quality	Impact on human or aquatic health
Azo Dyes	Textile, leather industries	High colour intensity, pH alteration, turbidity	Carcinogenic amines upon degradation; toxic to fish
Reactive Dyes	Textile industries	High COD, BOD; resistant to biodegradation	Skin and respiratory irritants; reduced growth in aquatic life
Acid Dyes	Leather, wool industries	Lowers dissolved oxygen levels	Can bioaccumulate, toxic to fish and aquatic plants
Basic Dyes	Paper, cosmetic industries	Increases turbidity, COD	Skin and eye irritation; toxic to aquatic organisms
Direct Dyes	Textile, paper industries	Causes turbidity and reduces light penetration	Can cause allergic reactions; potential toxic effects on fish
Sulphur Dyes	Textile and leather industries	Increases pH and COD levels	Long-term exposure toxic to aquatic life; respiratory irritants

1.6.1 Sources and types of plastic pollutants

Plastic pollutants enter water bodies through multiple sources, including industrial discharges, wastewater treatment facilities, agricultural runoff, and municipal waste. Each type of plastic exhibits distinct properties that contribute to its environmental impact. Table 1.3 provides a detailed overview of various plastic types, highlighting their properties, common applications, and the associated environmental and health hazards when they pollute aquatic systems. Understanding these types helps identify the specific hazards associated with various plastics and guides policy-making for more effective waste management [35].

Table 1. 3 Types, properties, uses, and harmful effects of common plastic pollutants found in water bodies

Type of plastic	Nature/properties	Common uses	Harmful effects
PE	Light, durable, water-resistant	Plastic bags, bottles, packaging films	Physical blockage in marine animals, entanglement; releases toxic chemicals when degraded.
PP	Tough, lightweight, heat-resistant	Food containers, bottle caps, straws	Ingestion leads to starvation and malnutrition in marine life; releases toxic additives.
PVC	Dense, chemical-resistant, often plasticized	Pipes, medical equipment, packaging	Releases carcinogenic dioxins upon degradation; toxic for aquatic life; endocrine disruptor in humans.
PS	Lightweight, brittle, poor barrier to oxygen	Foam containers, disposable cups, insulation	Leaches toxic styrene monomers; blocks digestive tracts of marine animals.
PET	Strong, lightweight, recyclable	Beverage bottles, food packaging	Accumulates in marine life; absorbs harmful chemicals that enter food chains.
Nylon (Polyamides)	Strong, elastic, abrasion-resistant	Fishing nets, ropes, textiles	Ghost fishing, entanglement, ingestion by marine species; releases microplastics.
Microplastics (e.g., fibers from clothing)	Very small particles (<5mm), can be synthetic or derived from larger plastics	Microbeads in fibers from synthetic clothes	Easily ingested by aquatic organisms; bioaccumulation in food webs; carries pollutants like heavy metals.

1.6.2 Effects of plastic pollutants in water bodies on humans and ecosystems

Plastic pollution has extensive impacts on aquatic ecosystems and human health. Marine life suffers physical harm from entanglement in larger items like plastic bags and fishing nets, which restrict movement and can lead to injury or death. Marine organisms, from fish to seabirds, also suffer digestive damage and malnutrition upon ingesting plastics, while smaller

particles, or microplastics, are widely mistaken for food and accumulate within organisms, transferring up the food chain and impacting predators. Beyond physical damage, plastics release or absorb toxic chemicals such as BPA and dioxins, which leach into water, contaminating habitats and disrupting reproductive, developmental, and immune functions in wildlife and humans due to endocrine-disrupting chemicals. Fig 1.3 delineates the impact of plastic pollution in water bodies. At an ecosystem level, plastic accumulation, especially on the ocean floor, disrupts benthic environments, impairing nutrient cycling and oxygenation [36]. Human health risks arise as these pollutants bioaccumulate in marine organisms, carrying toxins and pathogens that enter human bodies through seafood consumption, potentially leading to cancer, neurodevelopmental issues, and chronic diseases. Plastic pollution also burdens drinking water sources, where microplastics carry toxic substances, and imposes economic costs by impacting tourism, fishing, and cleanup efforts, representing a growing strain on public health and economic resources [37].

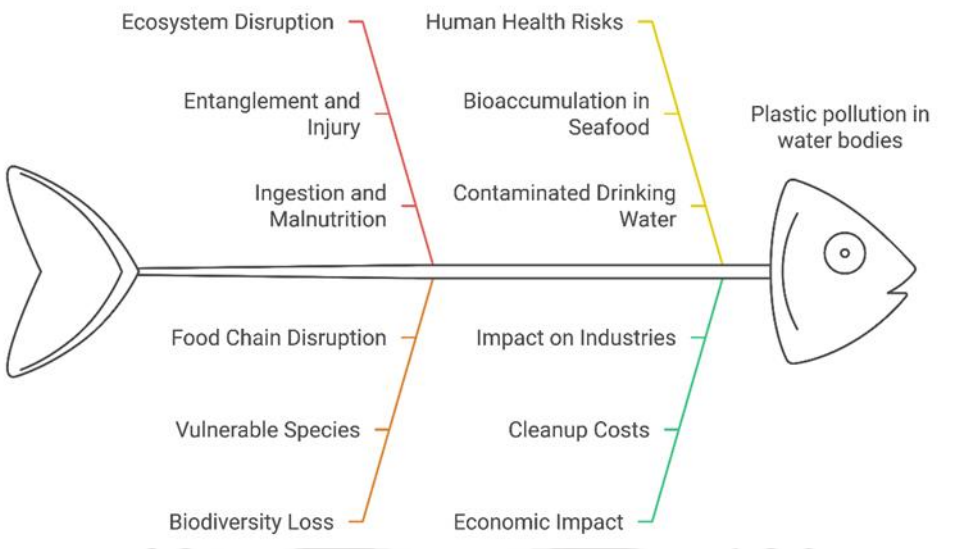

Fig 1. 3 Impact of plastic pollution in water bodies

1.7 Comparative assessment of different water remediation techniques

The global rise in water contamination due to industrial activities, agricultural runoff, and urbanization has necessitated the development of effective water remediation techniques. These methods are diverse, with each employing distinct mechanisms to remove contaminants. Broadly, remediation methods can be classified into physical, chemical, biological, and advanced material-based approaches.

1.7.1 Physical remediation techniques

Physical remediation techniques aim to separate contaminants based on physical properties without altering their chemical structure, using methods such as filtration, sedimentation, flotation, and electrochemical processes. Filtration separates suspended solids from water via porous materials, including membrane filtration (micro, ultra, nanofiltration, and reverse osmosis) and activated carbon filtration. Membrane filtration effectively removes particles, pathogens, and some dissolved organics, though it is costly and energy-intensive, while activated carbon is particularly effective for adsorbing organic pollutants but requires frequent replacement. Sedimentation and flotation rely on density differences to remove particles; sedimentation uses gravity to settle solids, and flotation employs air bubbles to lift particles. Both are cost-effective for large-scale uses, like municipal wastewater treatment, but do not remove dissolved contaminants and often need additional processing. Electrochemical methods such as electrocoagulation, electrooxidation, and electrodialysis use electric fields to aggregate and separate contaminants, with electrocoagulation being especially effective for industrial effluents, although it demands high energy input and regular maintenance [38].

1.7.2 Chemical remediation techniques

Chemical remediation methods use reactive substances to degrade, neutralize, or remove pollutants, making them particularly effective for organic contaminants, heavy metals, and pathogens. These techniques generally offer fast and effective treatment, although they often come with high energy or chemical demands. Notable chemical methods include AOPs, coagulation, and various Fenton processes.

1.7.2.1 Advanced oxidation processes

AOPs are highly effective for degrading a broad range of organic pollutants. They work by generating highly reactive radicals, particularly hydroxyl radicals (•OH), which rapidly break down contaminants into harmless end products like carbon dioxide and water. Methods under AOPs include ozonation, UV/H_2O_2 treatment, and photocatalysis. Although AOPs offer a powerful means of pollutant degradation, they can be costly, energy-intensive, and require specialized equipment and safety measures due to the use of reactive agents [39].

1.7.2.2 Fenton processes

The Fenton process is a specific AOP that uses hydrogen peroxide (H_2O_2) in the presence of iron ions (Fe^{2+}) to generate hydroxyl radicals. These radicals are potent oxidizing agents that

can effectively decompose a wide array of organic pollutants into benign byproducts. The Fenton process has gained significant attention due to its simplicity, effectiveness, and relatively low cost compared to other AOPs [40]. Fenton process can be of the following types:

- Classical Fenton process: This method involves the direct reaction of hydrogen peroxide with iron salts under acidic conditions (typically pH 2–4). It is widely used for treating industrial effluents rich in organic compounds [40].
- Photo-Fenton Process: This variation enhances the Fenton reaction by using UV or visible light to accelerate radical generation, making the process faster and more efficient. The photo-Fenton process is highly effective for the mineralization of persistent pollutants [41].
- Electro-Fenton Process: This process uses electrochemical methods to regenerate iron ions, allowing continuous radical generation without the need to add excess iron. This method can reduce sludge formation and is suitable for large-scale treatment [42].
- Heterogeneous Fenton Process: In this approach, solid iron catalysts (such as iron oxides or supported iron nanoparticles) replace soluble iron salts. This method improves stability and recyclability and minimizes sludge production [42].

The Fenton process is highly regarded in industrial wastewater treatment due to its efficiency and environmental benefits. It rapidly degrades a wide range of organic contaminants, including dyes, pharmaceuticals, and industrial chemicals, by generating powerful hydroxyl radicals. This process is relatively simple and relies on inexpensive iron salts, making it a practical option in many settings. Additionally, it produces minimal toxic byproducts, as hydrogen peroxide breaks down into water and oxygen, and iron is generally non-toxic. However, the process requires a significant amount of hydrogen peroxide, which is costly and adds to operational expenses. Optimal performance also demands an acidic environment (pH 2–4), necessitating pH adjustments that increase treatment complexity and costs. Moreover, it generates iron hydroxide sludge, which requires proper disposal. To address these limitations, variations like the electro-Fenton and heterogeneous Fenton processes have been developed, which help reduce sludge production and optimize hydrogen peroxide usage, making the Fenton process more sustainable and cost-effective [40,41].

1.7.2.3 Coagulation and flocculation

Chemical coagulation and flocculation are commonly used to remove suspended solids and reduce turbidity in water. Chemicals such as alum, ferric chloride, and organic polymers are

added to water, which causes fine particles to clump together into larger aggregates (flocs) that can be easily separated. This method is widely used in municipal and industrial wastewater treatment plants due to its effectiveness and simplicity. However, it produces significant amounts of sludge that require handling and disposal. Additionally, the added chemicals can sometimes introduce unwanted residuals into the treated water [43].

1.7.3 Biological remediation techniques

Water pollution, particularly by organic compounds, heavy metals, and other toxic pollutants, poses severe environmental and health risks. Biological remediation techniques harness the power of microbial consortia, enzymes, and engineered enzymes to purify water efficiently. These methods are often eco-friendly, cost-effective, and capable of addressing a wide range of pollutants. The subsection below focuses on microbial consortia-based remediation, enzyme-based techniques, and engineered enzymes for water treatment[44].

1.7.3.1 Microbial consortia-based remediation

Microbial consortia-based remediation uses diverse communities of bacteria, fungi, and other microorganisms to collectively break down pollutants in water, leveraging the metabolic diversity of these communities for more effective treatment than single-species systems. These consortia, which include bacteria, fungi, and algae, work together to degrade various contaminants, including hydrocarbons, heavy metals, and synthetic compounds. They can function in both aerobic and anaerobic environments, with aerobic consortia breaking down organic pollutants like phenols and pesticides, and anaerobic consortia reducing heavy metals and chlorinated compounds in low-oxygen conditions. Often forming biofilms on surfaces within treatment systems, these microbial communities establish stable environments that enhance pollutant adsorption, degradation, and inter-microbial cooperation. Nutrient availability and environmental factors like temperature, pH, and salinity are crucial for optimizing their performance. Microbial consortia have been effectively applied in wastewater treatment plants, industrial effluent management, and bioremediation of oil spills, as well as in advanced applications like bioreactors and wetlands designed for specific pollutants [45].

1.7.3.2 Enzyme-based water remediation techniques

Enzyme-based remediation techniques utilize isolated enzymes capable of catalyzing specific biochemical reactions that break down contaminants in water. Unlike whole-cell systems, enzyme-based methods can work in wide environmental conditions and do not require microbial growth phase lag, making them ideal for quick action on range of pollutants. The use

of free enzymes offers rapid degradation and precise targeting of pollutants, while immobilized enzymes on solid supports enhance stability and recyclability. Enzyme-based remediation is commonly applied in the degradation of trace organic contaminants in water, such as in the treatment of pharmaceutical residues, agricultural runoff, and industrial wastewater [46]. Table 1.4 delineates major types of enzyme used in water remediation.

Table 1. 4 Enzymes commonly used in water remediation and their target pollutants

Enzyme	Target Pollutant(s)	Mechanism of Action	Applications
Laccase	Phenols, dyes, pharmaceuticals	Oxidizes phenolic compounds, dyes, and certain drugs	Textile wastewater, industrial effluents
Peroxidase	Phenolic compounds, dyes	Oxidizes phenolic pollutants using hydrogen peroxide	Industrial wastewater, dye and phenol removal
Nitrilase	Nitriles (e.g., cyanides)	Hydrolyses nitriles into acids and ammonia	Cyanide-contaminated industrial wastewater
Urease	Urea, ammonia	Hydrolyses urea into carbon dioxide and ammonia	Ammonia reduction in wastewater
Lipase	Oils, fats, grease	Hydrolyses fats and oils into fatty acids and glycerol	Wastewater from food and oil processing industries
Chloroperoxidase	Chlorinated organics	Catalyzes the breakdown of chlorinated organic compounds	Removal of pesticides, chlorinated solvents
Tyrosinase	Phenols, polyphenols	Oxidizes phenols to quinones	Pesticide and phenolic waste removal
Nitrate Reductase	Nitrate compounds	Reduces nitrate to nitrite or nitrogen gas	Nitrate removal from agricultural runoff
Cytochrome P450	PAHs (Polycyclic aromatic hydrocarbons)	Oxidizes PAHs, increasing their water solubility	Remediation of hydrocarbons, industrial effluents
Dehalogenase	Halogenated compounds	Cleaves halogen atoms from organic molecules	Treatment of chlorinated

			pesticides and solvents
Cellulase	Organic matter (cellulose)	Breaks down cellulose into glucose	Organic pollutant removal in wastewater
OPH	Organophosphate pesticides	Hydrolyses organophosphate bonds in pesticides	Pesticide and agrochemical industry effluents
Aldehyde Dehydrogenase	Aldehydes	Oxidizes aldehydes to carboxylic acids	Industrial wastewater containing aldehydes
Arylesterase	Aromatic esters	Hydrolyses aromatic esters	Treatment of aromatic ester pollutants

[47–51]

1.7.3.3 Engineered enzymes for water remediation

Advances in genetic engineering and protein design have enabled the creation of enzymes specifically tailored for water remediation, enhancing their specificity, stability, and pollutant-degradation efficiency. Engineered enzymes overcome limitations of natural enzymes, such as vulnerability to harsh environmental conditions or restricted substrate ranges, by being optimized for targeted pollutants. Techniques like directed evolution and site-directed mutagenesis allow iterative improvements in enzyme performance under extreme conditions, such as high salinity, temperature, or pH, by inducing mutations or modifying specific amino acids to boost catalytic efficiency and stability. Additionally, hybrid enzymes or fusion proteins can integrate multiple catalytic activities in one enzyme such as combining esterase and laccase domains to address complex pollutant mixtures in wastewater. Furthermore, engineered enzymes are often designed to resist heavy metals, improving efficacy in metal-contaminated waters by enhancing pollutant-binding affinity and structural robustness in toxic environments [52].

1.7.4 Nanotechnology based techniques

Nanotechnology provides innovative approaches to water remediation by utilizing materials with high surface area, reactivity, and specificity. Key nanotechnology-based methods include nanosorbents and nanocatalysts. Nanosorbents, such as carbon nanotubes, graphene oxide, and nano-iron oxides, demonstrate excellent adsorption properties for contaminants like heavy metals, organic pollutants, and pathogens; they are highly effective even at low concentrations but can be costly and carry potential environmental risks from nanoparticle leaching. Nanocatalysts, including TiO_2 and ZnO nanoparticles, boost AOPs by increasing reaction surface area. These nanomaterials are especially useful for photocatalysis under UV or visible light, enabling the breakdown of various organic pollutants. However, environmental concerns regarding nanoparticle use limit their large-scale application [7].

Selecting a suitable water remediation technique depends on pollutant type, resources, and treatment needs. Table 1.5 compares water remediation techniques, outlining their mechanisms, target pollutants, advantages, limitations, costs, and applications for a clearer understanding of their practical strengths and constraints. Among chemical methods, the Fenton process is effective for rapidly degrading organic pollutants via hydroxyl radicals but requires acidic conditions and H_2O_2, making it ideal for industrial wastewater. Enzyme-based remediation, on the other hand, provides a precise, eco-friendly option, especially useful in

mixed contaminant scenarios. Both Fenton and enzyme-based methods offer targeted, adaptable solutions, with Fenton suited for quick industrial applications and enzyme-based approaches aligned with sustainable treatment goals.

Table 1. 5 Comparison of key water remediation techniques

Technique	Mechanism	Primary Pollutants	Advantages	Limitations	Cost	Applications
Filtration	Physical separation	Suspended solids, pathogens	Simple, effective for particles	Ineffective for dissolved contaminants	Moderate	Municipal and industrial water treatment
Sedimentation	Gravity separation	Suspended solids	Low cost, simple	Limited to larger particles	Low	Wastewater treatment
Electrocoagulation	Electric field-induced coagulation	Metals, suspended solids	Effective for complex matrices	High energy requirements	Moderate	Industrial effluent treatment
AOPs	Radical generation (hydroxyl radicals)	Organic pollutants	Broad-spectrum degradation	Energy-intensive, costly chemicals	High	Industrial and municipal wastewater
Fenton Process	Hydroxyl radical production via H_2O_2 + Fe	Organic pollutants	Cost-effective	Works best in acidic conditions, sludge production	Moderate	Industrial wastewater
Coagulation /Flocculation	Chemical aggregation	Suspended solids, turbidity	Effective, commonly used	Sludge generation	Low	Municipal and industrial wastewater
Microbes-Based Bioremediation	Microbial degradation	Organics, some heavy metals	Sustainable, eco-friendly	Slower for complex contaminants	Low	Wastewater, soil remediation
Enzyme-Based Remediation	Enzymatic catalysis	Organic pollutants	Highly specific, adaptable	Enzyme stability and reuse challenges	Moderate - High	Precision treatments, specific organics

Nanosorbents	Adsorption	Heavy metals, organics	High efficiency, low concentration removal	Expensive, potential toxicity risks	High	Advanced water purification
Nanocatalysts	Photocatalysis	Organics, pathogens	High reactivity, possible sunlight activation	Environmental concerns on nanoparticle release	High	High-end purification applications
MOFs (Adsorption)	Selective adsorption	Heavy metals, dyes	High selectivity, multifunctional	Costly synthesis, stability issues	High	High-end purification applications
MOFs (Catalysis)	Catalytic degradation	Organic pollutants	High efficiency, multifunctional	Stability issues in water	High	Research, advanced applications

1.7.5 Metal organic framework based techniques

Metal-organic frameworks are porous materials composed of metal ions linked with organic ligands, providing a high surface area and adjustable porosity that make them effective for selective adsorption and catalytic applications in water treatment. MOFs can selectively adsorb contaminants such as heavy metals and dyes, with some engineered to include functional groups that enhance adsorption efficiency, while others exhibit photocatalytic properties for multifunctional treatment. Additionally, certain MOFs can catalyze pollutant degradation through Fenton-like reactions or photocatalysis, effectively removing organic pollutants. However, MOF synthesis remains costly, and their stability in water can be limited, with their durability under real-world conditions still being evaluated [7].

1.8 The evolution of domestic water purification systems

The quest for clean and safe drinking water has been a cornerstone of human civilization, spanning thousands of years. From ancient methods of boiling and straining to the sophisticated RO technologies of today, the evolution of domestic water purification systems has been marked by significant advancements. These developments in domestic water purification technologies have significantly influenced public health outcomes in recent decades. Access to clean water is a fundamental right, yet over 2 billion people worldwide still lack safe drinking water. Recent innovations in water purification technologies, including advanced filtration systems and sustainable practices, have been transformative in providing clean water access to underserved communities. These technologies ensure the availability of safe drinking water and protect health by preventing waterborne diseases [53]. The subsection below delineates key technologies used in modern domestic water purification.

1.8.1 Distillation

Distillation is a time-tested and effective method for purifying water by boiling it and collecting the condensed steam, which is free of many contaminants. This process effectively removes dissolved solids, bacteria, viruses, and other microorganisms, making it a reliable option for water purification. However, distillation requires a significant amount of energy, can be slow, and may not remove certain VOCs with lower boiling points than water. Distillation systems can also be bulky, making them impractical for some households. Due to these factors, distillation is commonly used in areas where access to clean water is limited, or water sources are severely contaminated [54].

1.8.2 Ceramic candle

Ceramic candle filters are a widely used method for household water purification, employing a porous ceramic element, which is often combined with materials like silver or carbon to enhance its filtering capability. The ceramic element contains small pores that trap and remove impurities, effectively filtering out bacteria, viruses, and parasites from the water. These filters are known for their effectiveness against a broad spectrum of contaminants, offering a reliable solution for households. They are also relatively affordable, easy to maintain, and accessible for domestic use. However, ceramic candle filters have slower flow rates compared to other filtration methods, which can be a limitation for some users. Maintenance involves periodically cleaning the ceramic element, typically by scrubbing it, or replacing it entirely once its filtering performance starts to diminish. This ensures that the filter continues to work effectively over time [55].

1.8.3 Activated charcoal filtration

Activated charcoal, or activated carbon, is a highly effective and widely used water purification method created from organic materials like coconut shells, wood, or coal. These raw materials undergo an activation process at high temperatures in an oxygen-free environment, significantly increasing the carbon's surface area. This activation can be achieved through physical methods, involving heating in an inert gas or chemical methods using acids, bases, or salts. Activated charcoal filters are particularly effective at removing organic chemicals, improving taste, and eliminating odors from water [56]. They can remove chlorine, chloramine, VOCs, pesticides, and hydrogen sulfide. However, these filters are ineffective against specific contaminants, such as iron, nitrates, and some heavy metals. There are two main types of activated charcoal filters: GAC filters, which contain loose carbon granules, and carbon block filters, which are made by compressing these granules into a solid block. Carbon block filters are generally more effective at filtration, though they may reduce water pressure more than GAC filters. Activated charcoal filters have a limited lifespan and require regular replacement, with the frequency depending on the contaminant levels and water usage. Proper installation and ongoing maintenance are essential to keep these filters effective [57].

1.8.4 Ultraviolet light disinfection

Ultraviolet light disinfection is a chemical-free method for purifying water that uses UV radiation to kill microorganisms. As water flows through a UV light chamber, the UV rays penetrate and disrupt the DNA of bacteria, viruses, and other pathogens, rendering them unable

to reproduce and effectively neutralizing them. Although UV disinfection is highly effective against microbial contaminants, it does not remove particulate matter or dissolved solids. Its effectiveness can be limited by water turbidity, as suspended particles may block UV light. Additionally, UV systems require a steady power source and periodic replacement of the UV lamp to maintain efficacy. UV disinfection is often used alongside other filtration methods to provide comprehensive purification, making it particularly suitable for well water or other non-municipal sources that may carry microbial contamination [58].

1.8.5 Ultrafiltration

Ultrafiltration is a membrane-based process that effectively removes various contaminants from water. It operates by forcing water through membranes with pores that are smaller than those used in microfiltration but larger than those in reverse osmosis, enabling it to filter out particulate matter, bacteria, pathogens, and some dissolved solids. The filtration process relies on pressure to push water through the membrane, capturing contaminants on one side. UF is particularly effective when combined with other filtration methods to improve overall water quality. However, UF membranes can be prone to fouling, which decreases their efficiency over time, making regular cleaning or membrane replacement essential for sustained performance. This technology is versatile, used in both whole-house and point-of-use systems, and is often paired with activated carbon or UV light to provide comprehensive water purification [59].

1.8.6 Reverse osmosis

Reverse osmosis is a highly effective water purification method that removes a broad spectrum of contaminants. The process works by forcing water through a semi-permeable membrane under pressure, allowing only water molecules to pass through while blocking larger particles, including dissolved solids, heavy metals, bacteria, viruses, and other microorganisms. RO systems are capable of removing almost all kind of known water contaminants, making them especially effective for eliminating dissolved solids, heavy metals, and microbial pollutants. However, they also remove beneficial minerals, which can result in a flatter taste in the water. RO systems produce some wastewater and require regular replacement of the membrane to maintain performance. These systems are commonly used in both whole-house and point-of-use applications and are particularly beneficial for households with high levels of dissolved solids or heavy metals in their water supply [60].

Each of these modern technologies has unique strengths and limitations, making it essential to choose the right combination based on the specific water quality issues and needs of the household. Table 1.6 presents a comparative analysis of domestic water purification technologies, including contaminants removed, advantages, and limitations. Recent research and development efforts are focused on creating novel techniques that overcome current limitations, with an emphasis on high water recovery and sustainability.

Table 1. 6 Comparative analysis of key domestic water purification technologies

Technology	Primary contaminants removed	Key feature	Key drawbacks
Ceramic candle filter	Bacteria, protozoa	Inexpensive, effective for bacteria removal	Fragile, limited effectiveness against viruses, chemicals
Activated charcoal	Chlorine, organic compounds, and some heavy metals	Improves taste, removes chlorine and organics	Ineffective against microbial contaminants, needs frequent replacement
Ultrafiltration	Bacteria, protozoa, some viruses	Suitable for microbial contaminants, low-energy	Ineffective against dissolved salts, chemicals
UV disinfection	Bacteria, viruses, protozoa	Effective, chemical-free disinfection	Requires clear water, power-dependent, ineffective against chemicals
Reverse osmosis	Dissolved salts, heavy metals, organics, microbes	Comprehensive contaminant removal	Expensive, generates wastewater, removes minerals, low recovery
Distillation	All dissolved solids, heavy metals, microbes	High purity, effective for all contaminants	Energy-intensive, slow, costly to operate

1.9 Importance of critical water parameters in assessing water quality

Determining the precise concentration of individual impurities in water is inherently challenging due to the complex matrix of contaminants present, ranging from diverse organic and inorganic pollutants. The sheer diversity of pollutants, each requiring specialized detection methods such as gas chromatography for volatile organics or atomic absorption spectroscopy for trace metals renders comprehensive analysis resource-intensive and often impractical [61]. Furthermore, many contaminants exist at trace levels yet pose significant health risks,

necessitating ultrasensitive instrumentation. Regional variability in regulatory standards further complicates uniform assessment. Consequently, water quality evaluation prioritizes critical water parameters indicators that integrate the cumulative effects of multiple contaminants and provide actionable insights into ecological and human health risks. These parameters, including BOD, COD, DO, TDS, turbidity, temperature, and pressure, serve as pragmatic proxies for pollution levels, enabling efficient monitoring and regulatory compliance [62]. An integrated one-stop solution incorporating a real-time multiparametric device equipped with sensors for monitoring key water quality parameters can significantly streamline the assessment process. By enabling rapid and accurate data collection, such a system can conserve both time and resources while facilitating the design of targeted remediation protocols tailored to specific wastewater types.

1.9.1 Oxygen-related parameters: BOD, COD, and DO

BOD and COD are pivotal in assessing organic pollution. BOD measures oxygen consumed by aerobic microorganisms decomposing organic matter over five days at 20°C, reflecting biodegradable waste levels. The BOD of any water depends on the microorganisms present in the wastewater, which in turn are influenced by the nutritional value the wastewater provides. Different industrial wastewaters such as those from textile, dairy, petrochemical, and pharmaceutical industries have distinct compositions and may harbor different microbial consortia, affecting the rate and extent of organic matter degradation. Textile wastewater often contains starch-based sizing agents, natural dyes, cellulose fibers, and organic surfactants that can support microbial growth, although some dyes or metals may inhibit it. Dairy effluent is rich in lactose, proteins, and fats, providing readily biodegradable nutrients that promote rapid microbial activity. Petrochemical wastewater includes hydrocarbons, alcohols, and organic acids, which are less biodegradable but can be metabolized by specialized microbes, particularly when supplemented with nutrients like nitrogen or phosphorus. Pharmaceutical effluents may contain residual sugars, solvents, and fermentation byproducts that support microbial growth, though the presence of antimicrobial compounds can suppress general microbial activity and necessitate resistant strains. According to the WHO, BOD levels in clean surface waters should ideally remain below 3 mg/L, while values exceeding 6 mg/L indicate significant organic pollution. High BOD (>30 mg/L) is typical in untreated sewage or industrial effluents, risking oxygen depletion in aquatic ecosystems [63]. COD, determined via chemical oxidation, quantifies total organic content within hours, including non-biodegradable substances. While COD lacks biodegradability differentiation, its rapidity complements BOD

in pollution management. COD levels in uncontaminated waters are generally <10 mg/L, but industrial discharges can elevate this to >100 mg/L [64].

DO, the oxygen available for aquatic life, is inversely influenced by organic load and temperature. The WHO emphasizes that DO concentrations in healthy aquatic ecosystems should exceed 5 mg/L to sustain fish and microbial balance. Levels below 2 mg/L (hypoxic conditions) are lethal to most aquatic organisms, signaling eutrophication or thermal pollution. These parameters collectively gauge impact of organic pollution on water health [65]. Fluctuations and impairments in BOD, COD, and DO levels in wastewater can arise from various factors, with industrial, municipal, and agricultural discharges playing a crucial role in contributing to pollution that impacts these parameters.

1.9.2 Physico-chemical Indicators: TDS and turbidity

TDS, the sum of dissolved inorganic salts and organic matter, affects water salinity, taste, and conductivity. The WHO recommends a TDS limit of <600 mg/L for drinking water, with levels >1,000 mg/L deemed unpalatable and potentially harmful to aquatic habitats. Elevated TDS often stems from agricultural runoff, industrial discharge, or geological leaching [66].

Turbidity, caused by suspended particles, reduces light penetration, hindering photosynthesis and promoting pathogen attachment. The WHO stipulates turbidity levels in drinking water should be <1 NTU (nephelometric turbidity units) after treatment, though <5 NTU is provisionally acceptable in some contexts. High turbidity (>10 NTU) in surface waters correlates with sediment pollution and microbial risks [67].

1.9.3 Environmental regulators: temperature and pressure

Temperature profoundly influences aquatic ecosystems by modulating DO solubility (cooler water holds more oxygen) and metabolic rates of organisms. While the WHO does not specify strict temperature limits, natural surface waters typically range between 10–25°C. Thermal pollution from industrial discharges (>3°C above ambient) can disrupt breeding cycles and species distribution [68].

Pressure, though less frequently discussed in surface waters, governs groundwater dynamics and gas solubility. In drinking water distribution systems, the WHO recommends maintaining pressures of 5–10 bars to prevent contamination ingress. In deep aquifers, pressure changes affect geological stability and dissolved gas release, potentially mobilizing contaminants like methane or radon [69].

1.10 Growing need for integrated technologies for monitoring water quality

The rising demand for safe water, driven by industrialization, urbanization, and agricultural intensification, has underscored the need for advanced water quality monitoring systems to protect public and ecological health. Increasingly, untreated industrial, domestic, and agricultural discharge pollutes rivers, lakes, and other natural water bodies, introducing a range of contaminants that severely affects human and environmental safety. Traditional lab-based methods for water quality assessment, while accurate, are time-consuming and often fail to provide real-time data, which is crucial given the rapidly changing dynamics of natural water bodies affected by fluctuating wastewater discharge levels [70]. To address these challenges, the development of modern real-time sensors has enabled continuous water quality monitoring, yielding timely insights that inform preventive and corrective measures. Recent advances in the IoT have further transformed water monitoring by enabling seamless, automated data collection, transmission, and analysis. IoT-based systems, comprising WSNs, interconnected sensors, and cloud platforms, allow continuous monitoring of essential parameters such as pH, temperature, dissolved oxygen, conductivity, and turbidity. Additionally, IoT technologies support remote access and real-time alerts via emails, SMS, or dashboards, ensuring swift responses to contamination events. The advent of open-source SBCs such as the ESP32, Arduino, and Raspberry Pi has made IoT-based water monitoring systems more accessible, fostering innovation among researchers and developers. The integration of Geographic GIS and data analytics in these systems enables detailed visualization and analysis of water quality trends, contamination sources, and flow patterns, facilitating informed decision-making for sustainable water resource management [71].

1.10.1 Single board computers for IoT enabled water monitoring

Single-board computers are compact, cost-effective, and versatile devices that can be integrated with various sensors to create IoT-based water monitoring systems. They facilitate real-time data processing, wireless communication, and remote accessibility, making them ideal for distributed water quality monitoring. Each SBC platform offers distinct capabilities and limitations, and the following table provides a comparative assessment of some popular options, helping to choose the right board based on the requirements. Each board has unique advantages depending on the scope of the water monitoring application. Arduino boards, for instance, are ideal for beginner projects due to their simplicity and affordability but may not support complex data handling. ESP32 boards, with built-in Wi-Fi and Bluetooth, are popular for low-power IoT systems. Raspberry Pi and Beagle Bone, on the other hand, offer high

processing power, allowing for advanced data processing and analysis, and are best suited for comprehensive, multi-sensor monitoring projects [10,72]. Table 1.7 presents a comparative assessment of commonly used SBCs in IoT-enabled water monitoring systems.

Table 1. 7 Comparison of popular SBCs for IoT based water management/monitoring systems

Board	Processing Power	Connectivity	Energy Consumption	Cost	Suitability for Water Monitoring
Arduino	Low	Limited (Bluetooth, WiFi with modules)	Low	Low	Suitable for basic sensor integration and simple applications, limited for complex data handling
ESP32	Medium	Built-in WiFi and Bluetooth	Moderate	Very Low	Excellent for low-power, remote IoT applications due to connectivity and low cost
Raspberry Pi	High	Ethernet, WiFi, Bluetooth	Moderate to High	Moderate	High processing power, supports complex data processing and multiple sensors
Beagle Bone	High	Ethernet, WiFi with modules	High	High	Suitable for industrial-scale applications, supports extensive GPIO

1.10.2 Impact of open source boards and sensors on sustainable water management

Single board computers like Arduino, ESP32, and Raspberry Pi have proven to be effective and cost-efficient tools for IoT-enabled water monitoring, especially in developing regions where proprietary systems may be financially prohibitive. Proprietary water monitoring devices from large corporations often come with high costs due to research and development expenses, intellectual property rights, and recurring fees for servers and software, making them inaccessible to many communities. In contrast, open-source SBCs and sensors offer a more

affordable alternative that reduces these financial barriers. Open-source hardware platforms enable customization, allowing developers to tailor water quality monitoring systems to specific local needs without the constraints of proprietary designs. This flexibility is further enhanced by the compatibility of generic sensors across multiple platforms, providing a sustainable solution adaptable to diverse settings [73].

The open-source model also fosters collaboration and continuous improvement, as the large developer communities around platforms like Arduino and Raspberry Pi share resources and technical knowledge, reducing the dependency on costly support services. This collaborative approach effectively disperses the research and development workload, eliminates intellectual property constraints, and minimizes recurring costs associated with server and software maintenance. Fig 1.4 highlights the fundamental difference between proprietary vs open-source devices for water monitoring. By making real-time water monitoring systems accessible and customizable, open-source SBCs contribute to more sustainable and scalable water management practices, empowering individuals, organizations, and communities to safeguard their water resources and support sustainable water management at a local and global scale [74].

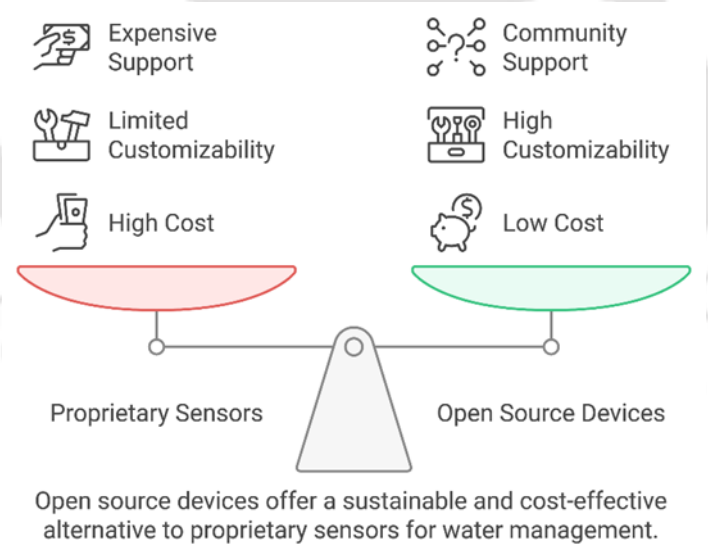

Fig 1. 4 Comparison of proprietary and open-source devices for water monitoring

1.11 Perspectives on lacuna

Water pollution poses a critical threat to environmental and human health, driven by various contaminants including heavy metals, organic and inorganic pollutants, microbial pathogens, and emerging contaminants like microplastics. Despite significant advancements in

understanding these pollutants and developing diverse remediation techniques, several gaps in the field remain. Specifically, the challenges in water pollution research include:

- Techniques like filtration and sedimentation remove suspended solids effectively but are less effective with dissolved contaminants. Membrane filtration, though useful, is costly and energy-intensive, particularly for removing salts and specific chemicals.
- Adsorption with materials like MOFs efficiently removes organic pollutants and heavy metals, but the potential environmental risk from improperly disposed adsorbed pollutants necessitates advanced, often costly, disposal solutions.
- Nanotechnology-based solutions (e.g., nanosorbents) provide high contaminant removal but risk nanoparticle leaching, raising concerns about toxicity and long-term environmental impacts that require careful regulation.
- Microbial consortia offer sustainable and eco-friendly remediation for various pollutants, but they are slow for complex contaminants and need specific conditions (nutrients, temperature) that are hard to maintain universally.
- Highly effective for organic pollutant degradation, the Fenton process requires acidic conditions and large amounts of hydrogen peroxide, leading to high costs and excess iron hydroxide sludge, posing disposal challenges.
- Enzyme-based methods are adaptable and specific but limited by the need for stable conditions; challenges with enzyme stability and reuse restrict their broader application.
- Reverse osmosis systems are efficient in water purification but generate significant wastewater and consume considerable power, highlighting a need for innovation to reduce waste and improve sustainability.
- Real-time water monitoring has advanced significantly but relies on expensive proprietary software.

1.12 Motivation of the research work

This research is driven by the pressing need for innovative and sustainable solutions in water remediation, purification, and monitoring. With growing environmental and public health concerns surrounding water quality, this work seeks to address current limitations in the field by developing advanced methodologies that are efficient, cost-effective, and adaptable to varied environmental contexts.

1.13 Objectives of the thesis

- Novel Human xanthine oxidase-coupled Fenton reaction for advanced bio-oxidation of pollutants in sustainable wastewater treatment.
- Engineered Mors1 enzyme from Antarctic bacteria *Moraxella* TA144 for enhanced thermal stability and activity for polyethylene terephthalate degradation.
- Development of energy efficient water distillation unit using Piezoelectric and Peltier technologies with sterile UV-C integrated water collector.
- Development of IoT enabled real-time water monitoring system with hybrid power management and remote data accessibility.

1.14 Organization of the Ph.D. thesis

Chapter 1 introduces water pollution as a critical global issue impacting human health, ecosystems, and biodiversity. It categorizes pollutants into organic, inorganic, microbial pathogens, and emerging contaminants like microplastics and endocrine disruptors. Organic and inorganic pollutants are noted for their persistence and health risks, while microbial pathogens cause waterborne diseases, especially in areas with poor sanitation. Emerging pollutants raise concerns for ecosystem and public health. The chapter critiques conventional water treatment methods and highlights advanced technologies like nanotechnology, enzyme-based treatments, and IoT-enabled monitoring for sustainable water management. It also identifies key research gaps, emphasizing the need for cost-effective, eco-friendly remediation techniques. The chapter underscores the urgency of developing innovative solutions, focusing on bio-oxidative processes, enzyme engineering, energy-efficient distillation and IoT integrated modern sensing technologies to enhance water purification and monitoring systems.

Chapter 2 begins with the cloning, expression, and purification of the Hu-XO enzyme in Pichia pastoris. It then explores the innovative use of the Hu-XO-coupled Fenton reaction for sustainable bio-oxidation of industrial wastewater pollutants, targeting complex contaminants such as azo dyes, microbes, and leather industry effluents. The chapter highlights the inefficiencies and high costs of conventional methods, emphasizing the need for advanced remediation strategies. The Hu-XO/Fenton system synergistically employs hydroxyl radicals from hydrogen peroxide for effective degradation and detoxification of pollutants, including antimicrobial effects. Statistical optimization via RSM identifies ideal enzyme dosage, reagent concentration, and reaction time for maximum decolorization, mineralization, and microbial reduction. Significant reductions in BOD and COD improved water quality, while toxicity assessments using *A. fischeri* bioluminescence and seed phytotoxicity assays confirmed

reduced ecological hazards. This study establishes the Hu-XO/Fenton reaction as an eco-friendly, cost-effective solution for industrial wastewater management.

Chapter 3 explores the cloning, expression, purification, and characterization of the wild-type (Mors1WT) and engineered mutant (Mors1MUT) enzymes from the Antarctic bacterium Moraxella TA144, designed to enhance PET degradation. Mors1MUT was developed by introducing strategic mutations into critical turn regions to improve thermal stability and catalytic efficiency, guided by computational tools like the DDMut server. Both genes were cloned into the pPICZαA vector, expressed in P. pastoris, and validated through colony PCR and Sanger sequencing. Purification involved Ni-NTA affinity and size exclusion chromatography, with identity confirmed via SDS-PAGE and Western blotting. Comparative analysis demonstrated that Mors1MUT exhibited superior pH and thermal stability and a 4.16-fold increase in PET degradation efficiency. Surface analysis of PET films treated with Mors1WT and Mors1MUT using SEM and AFM revealed significantly greater erosion by Mors1MUT. This study underscores the potential of enzyme engineering for sustainable plastic degradation.

Chapter 4 introduces an energy-efficient water distillation unit combining piezoelectric ultrasonic mist technology, thermoelectric Peltier modules, and UV-C sterilization to tackle water purification challenges caused by urbanization and industrialization. Constructed using biodegradable PLA materials, the system removes contaminants such as dissolved salts, microbial pathogens, dyes, and VOCs. Ultrasonic transducers produce a fine mist evaporated by a Peltier module for efficient phase change and precise temperature control. A UV-C light strip ensures microbial disinfection, while a VOC escape valve prevents volatile contaminants from condensing with purified water. Testing showed the system effectively removed salt, microbes, and VOCs, achieving 83% water recovery at 60 watts of power. Fluorescence microscopy confirmed its antimicrobial efficacy. This compact, sustainable unit surpasses traditional methods in efficiency and environmental impact, offering a practical domestic purification solution.

Chapter 5 describes development of an IoT-enabled real-time water monitoring system that integrates advanced sensors, hybrid power management, and remote data access to overcome limitations of traditional methods. At its core, an ESP32 microcontroller interfaces with sensors to measure temperature, humidity, DO, turbidity, and TDS. A GPS module enables geolocation for spatial water quality tracking. The device, housed in a durable, buoyant PLA casing, is

powered by a hybrid setup of solar panels and rechargeable lithium polymer batteries for autonomous operation in remote areas. Data is transmitted to a Firebase realtime database and visualized via a web interface using Plotly.js and Leaflet.js for interactive charts and maps. AI and ML readiness enhances predictive modeling and automated responses to water quality changes. Open-source tools and Firebase hosting ensure scalability and cost-effectiveness. This innovative system is ideal for resource-limited settings, offering affordable, reliable water quality monitoring for sustainable development.

Chapter 6 gives a brief conclusion and future perspective, summarizing the significant findings of this work, which addressed water pollution and monitoring challenges through innovative solutions. Key contributions include the development of the Hu-XO-coupled Fenton system for effective degradation of industrial pollutants, an engineered enzyme (Mors1MUT) for enhanced PET degradation, an energy-efficient water purification unit utilizing piezoelectric and Peltier technologies, and an IoT-enabled water monitoring system integrating advanced sensing and hybrid power. These advancements underscore the potential of bio-inspired and technological innovations to achieve sustainable water management. Future research should focus on scalability, cost-effectiveness, and integration with existing infrastructure for broader applications.

Chapter 2. Xanthine oxidase driven bio-Fenton system for advanced pollutant degradation in sustainable wastewater treatment

Abstract

Hu-XO plays a critical role in purine metabolism, catalyzing the oxidation of hypoxanthine to xanthine and further to uric acid while reducing molecular oxygen to reactive oxygen species. Herein, we report an innovative Fenton-assisted Hu-XO catalytic system for wastewater bioremediation, demonstrating its dual utility in degrading industrial organic pollutants and azo dyes such as CR while exhibiting exceptional antimicrobial effects. The Hu-XO gene was optimized and heterologously expressed in *P. pastoris* using the pPICZαA vector, enabling efficient in situ H_2O_2 production and eliminating the need for external H_2O_2. A synergistic Hu-XO–Fenton reaction was developed and optimized, achieving a 91.8% reduction in BOD and an 86% reduction in COD in industrial wastewater. Additionally, under optimized conditions, over 99% decolorization of CR was achieved, with advanced spectroscopic and mass spectrometric analyses confirming its structural breakdown into less toxic byproducts. The system demonstrated significant antimicrobial activity, as validated through stress assays, electron microscopy, and live/dead viability tests, effectively reducing microbial loads in treated wastewater. Toxicity assessments, including bioluminescence inhibition using *A. fischeri* and phytotoxicity tests on seeds, further confirmed the safety and reduced environmental toxicity of the treated samples. By overcoming challenges such as high reagent costs, acidic pH requirements, and incomplete degradation, this enzyme-assisted Fenton system provides a sustainable, efficient solution for wastewater treatment and pollutant remediation.

2.1 Background

Wastewater, a complex mixture of organic and inorganic contaminants, poses a global environmental challenge. Conventional treatment methods, such as ion exchange, flotation, and chemical precipitation, are widely employed and have proven effective in various contexts. However, these methods may face limitations, including lower removal efficiency for specific pollutants, high energy consumption, and the potential generation of hazardous sludge, which can complicate disposal and increase costs. Biological treatments, including activated sludge, remain indispensable and are the most commonly used methods in wastewater treatment because of their ability to break down a wide range of pollutants. Nonetheless, they can be less effective against complex pollutants with intricate chemical structures. Microalgae-based treatments, while promising, face challenges related to scalability and efficiency [7,75].

Microbial contamination in water and industrial wastewater from sectors such as the textile industry adds to the complexity of wastewater treatment [76]. Textile industry effluents are particularly concerning due to their high chemical load, which includes dyes, heavy metals, and other recalcitrant pollutants. Among these, azo dyes represent a major environmental challenge owing to their synthetic nature and resistance to degradation. One of the most problematic azo dyes is CR, also known as Direct Red 28, with a color index of 22120. Widely used in the textile, paper, and leather industries, CR is an anionic, metachromatic dye whose extensive presence in industrial effluents leads to significant environmental issues [77]. By impeding sunlight penetration in aquatic systems, it disrupts photosynthesis in aquatic plants and algae, causing an increase in BOD. Moreover, its toxic and carcinogenic properties pose severe risks to aquatic organisms and human health. These detrimental impacts underscore the need for advanced and efficient treatment strategies for CR-contaminated wastewater [78].

In this context, Fenton processes, which involve the generation of OH^- radicals through the reaction of H_2O_2, offer significant advantages over traditional remediation methods. These processes are highly effective at degrading diverse organic contaminants, including azo dyes like CR, and can achieve total mineralization, making them excellent tools for wastewater remediation. However, the high cost of H_2O_2 is a notable drawback, prompting a shift toward modern Fenton processes that utilize alternative or in situ sources of H_2O_2 [79]. Such advancements not only enhance the economic feasibility of treatment but also provide a robust solution for mitigating the environmental risks associated with industrial effluents, particularly those contaminated with CR and other persistent dyes.

In recent years, the role of oxidative enzymes in environmental biotechnology has garnered considerable attention. However, the potential of Hu-XO in bioremediation has not been explored, possibly due to challenges associated with its expression in bacterial systems due to its large size and post translational modification requirements. Hu-XO is a multifunctional enzyme that is involved primarily in the catabolism of purine nucleotides. It plays a critical role in converting purines, such as GMP and AMP, into hypoxanthine or xanthine, which are further oxidized to uric acid. During these reactions, molecular oxygen is reduced to H_2O_2 and O_2^- (Equations 1 & 2). XO plays a crucial role in the production of ROS, which are essential in both physiological and pathological processes. While ROS can serve as signaling molecules, their excessive production is associated with oxidative stress, leading to cellular damage and contributing to conditions such as cardiovascular diseases, diabetes, and neurodegenerative disorders [80]. Additionally, the role of XO in ROS production suggests its involvement in immune responses and inflammation, with numerous studies since the late 1990s highlighting its antimicrobial effects, as shown in Table 2.1 The expression of Hu-XO in microbial systems can offer a viable solution that allows scalable production of the enzyme. *P. pastoris*, a well-established host for recombinant protein expression, was chosen for this study because of its several advantages, including high yield, proper post translational modifications, and the ability to grow in simple media [81].

Oxidation of Hypoxanthine to Xanthine: $C_5H_4N_4O + O_2 \rightarrow C_5H_4N_4O_2 + H_2O_2$ **(Equation 1)**

Oxidation of Xanthine to Uric Acid: $C_5H_4N_4O_2 + O_2 \rightarrow C_5H_4N_4O_3 + H_2O_2$ **(Equation 2)**

Table 2. 1 Key findings from studies on the antimicrobial effects of XO

Year	Key finding(s)	Reference
1997	Xanthine oxidase (XO) and nitric oxide (NO) play crucial roles in the host defense mechanism against *Salmonella typhimurium* infection in mice.	[82]
2000	Xanthine oxidase in breastmilk inhibits the growth of *Escherichia coli* and *Salmonella enteritidis*.	[83]
2004	High expression of XO in intestinal epithelial cells suggests a barrier and microbicidal role. XOR in milk contributes to neonatal gut defense by generating ROS and reactive nitrogen species (RNS), inhibiting bacterial growth.	[84]

2019	Xanthine oxidase in raw, batch pasteurization, and high-temperature short time (HTST) milk inhibited the growth of *S. aureus*, but this property was lost in ultrahigh temperature (UHT) milk.	[85]
2020	Bovine milk xanthine oxidase (XO) exhibits antimicrobial properties like human milk XO, inhibiting both Gram-negative and Gram-positive bacteria in a dose-dependent manner.	[86]

The inherent antimicrobial properties of XO can be enhanced through a coupled Fenton reaction. The Fenton reaction involves the reaction of H_2O_2 with ferrous ions to generate hydroxyl radicals and ferric ions (Equation 3), which degrade organic pollutants and have antimicrobial properties. Both byproducts of the XO reaction can increase the efficiency of the Fenton reaction. Uric acid, produced as a result of XO catalysis, can dissociate into urate and a proton, creating a slightly acidic environment [87]. Moreover, the superoxide anions generated as byproducts in the XO reaction can accelerate the Fe^{2+}/Fe^{3+} cycle in the Fenton reaction [88]. These cascading supplementary reactions are hypothesized to address the limitations of the traditional Fenton process.

$$\boldsymbol{Fe^{2+} + H_2O_2 \rightarrow Fe^{3+} + OH + OH^-} \qquad \textbf{(Equation 3)}$$

This study investigated the potential of a Hu-XO coupled Fenton system for bioremediation, hypothesizing that the ROS generated by Hu-XO can enhance antimicrobial activity, degrade CR and reduce the organic load in wastewater when combined with the Fenton reaction. This innovative approach aims to overcome the limitations of the traditional Fenton process, such as excessive reagent use, acidic conditions, and high H_2O_2 costs [89]. A systematic approach was employed to develop and optimize the synergistic XO–Fenton reaction for enhanced antimicrobial and organic load reduction and CR degradation. The antimicrobial effects were characterized via a combination of stress assays, electron microscopy, and live/dead staining. The efficacy of the process in reducing the BOD and COD in industrial wastewater and CR degradation was also evaluated. To assess the environmental safety of the treatment, toxicity tests using *A. fischeri* and phytotoxicity assays on various seeds were conducted.

2.2 Materials and methods

2.2.1 Materials

The plasmid isolation and PCR Cleanup/Gel extraction kits were procured from Macherey-Nagel, Germany. The antibiotics Zeocine, Amplex™ Red, and SYTO™ 9 were purchased from Invitrogen, United States, and all other restriction enzymes and Gibson assembly master mixes were procured from New England Biolabs, United Kingdom. A size exclusion chromatography column (HiPrep Sephacryl S-300 HR) was purchased from Cytiva, Sweden. The protein concentrator (Amicon 30,000 molecular weight cutoff) was obtained from MilliporeSigma, United States. Xanthine oxidase activity assay kit (MAK078) and propidium iodide were purchased from Sigma–Aldrich, USA. The primary A-His-Ab and secondary GAR-IgG-HRP were obtained from Bio Bharati Life Science Pvt. Ltd., India. Congo red (sodium salt of benzidinediazo-bis-1-naphthyl-amine-4-sulfonic acid; molecular weight 696.66 g/mol; $C_{32}H_{22}N_6Na_2O_6S_2$) was procured from HiMedia, Bangalore. All other chemicals used in this study were of the finest quality and analytical grade. The chemicals were employed without further purification.

2.2.2 Strains, media, buffers and reagents

The *E. coli* 1652 DH5α 1652, *E. coli* 1302 and *B. subtilis* were procured from MTCC Chandigarh, India. *A. fischeri* was acquired from the American Type Culture Collection (ATCC) under accession number 7744. The mixture was then reconstituted on Zobell marine broth at 25°C and maintained on Zobell marine agar plates at 4°C. Photobacterium broth was used for all bioluminescence experiments. The vectors pPICZα A and *P. pastoris* were procured from Invitrogen Life Technologies, Carlsbad, USA. For the growth and maintenance of *E. coli* (1652) and *P. pastoris* strains, LSLB and YPD media were used, respectively. For expression studies, BMGY and BMMY were used. All the media compositions used in this study are presented in (Appendix A).

2.2.3 pPICZαA-Hu-XO plasmid construction and *E. coli* DH5α transformation

The Hu-XDH gene (GenBank: U39487.1) was codon optimized per the codon usage of *P. pastoris* by accessing the genome annotation by NCBI. The gene construct was synthesized by GenScript, Inc., and delivered in a pUC57 vector. Using primers containing EcoRI and SalI sites (Table 2.2), the Hu-XDH gene was PCR-amplified from pUC57. The pPICZαA shuttle vector was chosen for constructing the yeast expression vector in *E. coli* DH5α and subsequent heterologous expression in *P. pastoris*. The EcoRI and SalI-digested pPICZαA backbone was

gel-purified and ligated with the Hu-XDH fragment using Gibson assembly (50°C, 20 min) to generate pPICZαA-Hu-XDH. The vector was transformed into $CaCl_2$-$MgCl_2$ competent *E. coli* DH5α (Appendix B.5) via heat shock, and colonies were selected on LSLB plates supplemented with 25 µg/mL Zeocin. pPICZαA-Hu-XDH vector integration was confirmed by colony PCR.

Table 2. 2 The primers used for amplification of the Hu-XDH gene with EcoRI and SalI sites

Forward primer	5'- AGAGAGGCTGAAGCT**GAATTC**ATGACTGCTG ATAAGTTGGTTTTCTTTGT-3'
Reverse primer	5'- CAATGATGATGATGATGAT G**GTCGAC**ATCAACGACTCTAACAGACCAAGGCTTACAAT-3'

2.2.4 Expression of recombinant Hu-XO in *P. pastoris*

The pPICZαA-Hu-XDH plasmid was extracted from *E. coli DH5α*, linearized with PmeI, and transformed into *P. pastoris* via electroporation following the manufacturer's protocol [90]. Transformants were selected on YPD agar plates containing 100–300 µg/mL Zeocin. After 3 days of incubation at 30°C, the colonies were thermally lysed for colony PCR (using the primers listed in Table 2.2). The genomic DNA of transformed *P. pastoris* was isolated via a method adopted from Offei et al. and sent for Sanger sequencing (GeneSpec Pvt. Ltd., India), confirming the presence of the Hu-XO gene [91]. Positive clones were grown in 50 mL of BMGY (30°C, 200 RPM, 36 h), centrifuged (8000 × g, 6 min), and resuspended in 800 mL of BMMY in a 2-L baffled flask (30°C, 200 RPM, 96 h) supplemented with 1% methanol every 24 hours. Post-incubation, the pellets were stored at -20°C. For lysis, 3.2 g pellets (wild-type/transformed) were resuspended in 50 mL lysis buffer (Tris-50mM pH 6.5, Imidazole-10mM, NaCl-500mM, PMSF-1mM, Lyticase-40 U/ml), incubated (37°C, 15 min), sonicated (33% amplitude, 10s ON/30s OFF, 15 min, 4°C), and centrifuged (8000 × g, 10 min, 4°C). The SUP was stored at 4°C for further purification. Comparative protein profiles of the wild-type and transformed strains were analyzed via 12% SDS–PAGE (Appendix B.6).

2.2.5 Hu-XDH purification, conversion to Hu-XO, and Western blotting

The Ni–NTA column was equilibrated with 4 column volumes of equilibration buffer (50 mM Tris pH 6.5, 10 mM Imidazole, 500 mM NaCl). After loading 50 mL of SUP1, the column was washed with 3 column volumes of wash buffer (50 mM Tris pH 6.5, 20 mM Imidazole, 500 mM NaCl). Recombinant Hu-XO was eluted with 2.5 mL of elution buffer (50mM Tris pH-6.5, 250mM Imidazole, 500mM NaCl). The eluate was gel-filtered through a Sephacryl™ S-

300 high-resolution column pre-equilibrated with degassed baseline buffer (50 mM Sodium Phosphate buffer, pH 6.5, 50 mM NaCl). To ensure full conversion of Hu-XDH to Hu-XO, the purified protein was incubated with 100 µM 4,4′-DTPY at 25°C for 60 min [92]. Finally, Hu-XO was concentrated via a 30,000 MWCO protein concentrator (2000 × g, 4°C, 15 min) to eliminate 4,4′-DTPY.

Protein validation was conducted through Western blotting to confirm its expression and integrity. Proteins separated by SDS–PAGE (Appendix B.6) were transferred onto a nitrocellulose membrane (Bio-Rad) via precooled transfer buffer (48 mM Tris base, 39 mM Glycine, 20 % Methanol) in a semiwet transfer apparatus at 320 mA for 1 hour. After transfer, the membrane was removed with forceps, rinsed with deionized water, and incubated for 1 hour in blocking solution (5% non-fat milk in 1x phosphate-buffered saline with 0.1%Tween) at 4°C with agitation. After being washed with PBST (137 mM NaCl, 2.7 mM KCl, 10 mM Na_2HPO_4, 1.8 mM KH_2PO_4 with 0.1%Tween), the membrane was incubated overnight at 4°C with agitation in primary A-His-Ab (1:5000 dilution in PBST). After washing, the samples were incubated with secondary antibody (GAR-IgG-HRP, 5 µl) in 1x PBS (137 mM NaCl, 2.7 mM KCl, 10 mM Na_2HPO_4, 1.8 mM KH_2PO_4) containing 0.1% Tween-20 and 5% nonfat skimmed milk for 1 hour at room temperature with agitation. Finally, the membrane was treated with 1 ml of Bio-Rad's Clarity™ Western ECL substrate and visualized via a Bio-Rad ChemiDoc system (Image Lab software).

2.2.6 Hu-XO activity, stability (pH and temperature), and kinetics

The heterologous Hu-XO activity was measured via a xanthine oxidase activity assay kit (MAK078, Sigma–Aldrich, USA) with an H_2O_2 standard curve. To generate the H_2O_2 standard curve, 0, 10, 20, 30, 40, and 50 µL of 0.2 mM H_2O_2 solution were added to a 96-well plate and adjusted to 50 µL with water to yield 0 (blank), 2, 4, 6, 8, and 10 nmol/well H_2O_2. A standard curve (absorbance at 570 nm vs. H_2O_2 concentration) was plotted (Fig 2.1).

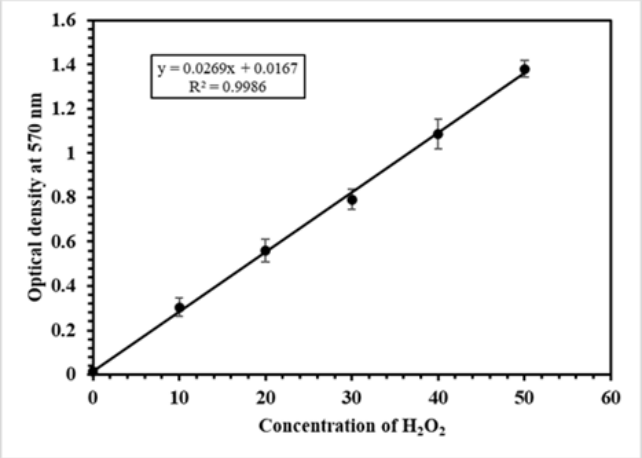

Fig 2. 1 H_2O_2 standard calibration curve

A linear regression curve depicting the fluorescence intensity at 571/585 nm versus known H_2O_2 concentrations (0–100 µM). The standard was used to quantify peroxide generation in subsequent assays.

To quantify H_2O_2 produced by heterologous Hu-XO, blank, positive control, and test samples were prepared (Table 2.3) in triplicate on a round-bottom 96-well microplate. Absorbance at 570 nm was recorded every 5 min for 60 min. Hu-XO activity was calculated using an equation (Equation 4) by comparing the absorbance of H_2O_2 generated by Hu-XO to the H_2O_2 calibration standard curve (Fig 2.1).

Table 2. 3 Reaction mixes for determining Hu-XO activity

Reagent	Blank	Positive Control	Test
Assay buffer	46 µl	44 µl	44 µl
Substrate mix	--	2 µl	2 µl
Enzyme mix (kit)	2 µl	2 µl	--
Heterologous Hu-XO	--	--	2 µl
Fluorescent peroxidase substrate	2 µl	2 µl	2 µl

$$\textbf{Hu XO Activity} = \frac{\text{B}\times\text{Sample dilution factor}}{(\text{T final}-\text{T initial})\times\text{V}} \qquad \textbf{(Equation 4)}$$

Where B is the amount (nmole) of hydrogen peroxide generated between T initial and T final, T initial is the time of first reading in minutes, T final is the time of final reading in minutes, and V is sample volume (mL) added to well. The hu-XO activity was reported as milliunit/mL, where one mU of XO is defined as the quantity of enzyme that catalyzes the oxidation of xanthine, producing 1.0 mmole of uric acid and hydrogen peroxide per minute at 25 °C.

The pH stability of Hu-XO was assayed via a xanthine oxidase activity kit (MAK078). McIlvaine's buffer (50 mM) adjusted to pH 3.5–8.5 replaced the standard assay buffer. The

activity was calculated by correlating the absorbance of H_2O_2 generated by Hu-XO relative to a calibration curve, with the results expressed as percentages with the highest activity set at 100%. The thermal stability of Hu-XO (0.2 mg/mL in 50 mM sodium phosphate buffer, pH 6.5, 50 mM NaCl) was assessed via a CD spectropolarimeter (Jasco J1500-150, Jasco Corp., Tokyo, Japan). Spectra were recorded from 190–260 nm across 25–95°C, with a scan speed of 100 nm/min, a 1–3 sec response time, and a 1 nm bandwidth. Data were processed by averaging readings and converting to molar residue ellipticity, expressed as mdeg (deg cm² $dmol^{-1}$).

Kinetic parameters (maximal reaction rate, V_{max}; Michaelis–Menten constant, K_M) were evaluated by measuring the initial reaction rate at 37°C (pH 6.5) with 20 to 200 µM xanthine. The catalytic rate of xanthine was measured spectrophotometrically by recording the initial slopes at 260 nm for 5 minutes following the initiation of the reaction with 3 units of Hu-XO. The Michaelis–Menten equation ($V = \frac{Vmax[S]}{(Km+[S])}$) was fitted directly to the experimental data to determine K_M and V_{max} via the nonlinear least-squares fitting approach with OriginPro 2021 9.8.0.200 software.

2.2.7 Designing the Fenton–xanthine oxidase coupled reaction

In this study, hydrogen peroxide produced by Hu-XO (primary reaction) was used as a substrate for the Fenton reaction (secondary reaction), generating hydroxyl radicals. These radicals are effective antimicrobial agents and can degrade organic contaminants in wastewater. The following subsection of this paper addresses the statistical optimization of the quantities of Hu-XO and Fenton reagents required to achieve optimal antimicrobial activity, as well as their application in the degradation and detoxification of water contaminated with CR.

2.2.7.1 Optimization of the Fenton-XO reaction for improved CR degradation and detoxification.

RSM was used to evaluate the influence of the enzyme dosage (X_1), Fenton reagent concentration (X_2), and reaction time (X_3) on the percent decolorization of CR dye (Y1), which was measured as a percentage on the basis of the absorbance maxima of CR at 497 nm [93]. The RSM design, featuring both coded and uncoded levels, is detailed in (Table 2.4). The experiment utilized a CCD with five levels and a quadratic model. The broad ranges for enzyme dosage, Fenton reagent concentration, and reaction time were identified through three independent tests, each conducted by varying one parameter while keeping the other two constant. The primary reaction was initiated by incubating a specific amount of Hu-XO with

100 µL of substrate mixture (0.5mM Xanthine, 100 µM Na_2MoO_4 & 100 µM FAD) in 10 mL of reaction buffer (RB; 5 mM Tris pH 5.8, 10 mM NaCl) at 37°C for 30 minutes. For the secondary reaction, 90 mL of 100 mg/L CR was subsequently added to varying concentrations of Fenton reagent ($FeSO_4$; mM) for specified durations (Table 2.7). Decolorization tests were carried out in 250 mL Erlenmeyer flasks containing 100 mL of the enzyme-CR mixture (in 50 mM PBS, pH 6.5). A CCD experimental matrix encompassing six axial points, eight fractional factorial points, and six central points were employed to determine the effects of these parameters. The experimental runs were conducted in random order (Table 2.7).

Table 2. 4 Independent variables and their corresponding levels for CR decolouration

Independent variable	Symbol	Coded levels				
		-α	**-1**	**0**	**+1**	**+α**
Amount of enzyme (U)	X_1	7.95	10.00	13.50	16.00	18.04
Concentration of Fenton reagent (mM)	X_2	0.31	1.00	2.00	3.00	3.68
Reaction time (Min)	X_3	39.55	60.00	90.00	120	140.45

Data analysis was conducted via Design Expert Software (version 13.0.5.0). Optimal polynomial models were determined through comparative assessment of various statistical parameters, including lack-of-fit, predicted and adjusted multiple correlation coefficients, and coefficients of variation. Analysis of variance, employing F values at significance levels of 0.5, 0.1, and 0.01, was used to identify significant effects. Response surface plots generated by Design Expert software facilitated visualization of the CR degradation effects on response variables. All experiments were performed in triplicate to enhance data reliability, and the results are expressed as the mean values.

2.2.7.2 Optimization of the Fenton-XO reaction for enhanced antimicrobial activity.

RSM was used to assess the effects of the amount of enzyme (X_1), Fenton reagent concentration (X_2), and reaction time (X_3) on antimicrobial activity, which was measured as the PI intensity (Y_1). PI selectively stains dead or membrane-compromised bacteria by binding to DNA/RNA but is excluded by intact cell membranes [94]. The RSM design, with coded and uncoded levels, is detailed in Table 2.5. A CCD with five levels and a quadratic model was applied. The broad ranges for enzyme dosage, Fenton reagent concentration, and reaction time were identified through three independent tests, each conducted by varying one parameter while keeping the other two constant. *E. coli* (1302) and *B. subtilis* (121) overnight cultures were standardized to 0.5 McFarland turbidity (1.5×10^8 cfu/mL). 50mL of each strain was mixed to

a final volume of 100 mL at 10^6 cfu/mL. The primary reaction involved incubating a specific amount of Hu-XO with 100 µL of substrate mixture in 10 mL of reaction buffer at 37°C for 30 minutes. For the secondary reaction, the microbial culture (100 mL, 10^6 cfu/mL) was exposed to various Fenton reagent concentrations (mM) for specified times. The samples were stained for PI intensity using 20 mM PI stock in DMSO, with a final concentration of 30 µM in PBS. The CCD matrix included six axial points, eight fractional factorial points, and six central points to evaluate these factors. The experimental runs were conducted in random order (Table 2.10).

Table 2. 5 Independent variables and their corresponding levels for antimicrobial activity

Independent variable	Symbol	Coded levels				
		-α	**-1**	**0**	**+1**	**+α**
Amount of enzyme (U)	X_1	18.30	20.00	22.50	25.00	26.70
Concentration of Fenton reagent (mM)	X_2	0.31	1.00	2.00	3.00	3.68
Reaction time (Min)	X_3	39.55	60.00	90.00	120	140.45

Data analysis was performed via Design Expert Software (version 13.0.5.0). Optimal polynomial models were selected on the basis of comparisons of lack-of-fit, predicted and adjusted multiple correlation coefficients, and coefficients of variation. Analysis of variance, with F values at significance levels of 0.5, 0.1, and 0.01, identified significant effects. Response surface plots from Design Expert software illustrated the antimicrobial effects on the response variables. All experiments were conducted in triplicate for data reliability, and the results are expressed as the mean values.

2.2.8 CR decoloration assay

Decolorization tests were performed in 250 mL Erlenmeyer flasks using 90 mL of a 100 mg/L CR solution prepared in deionized water. The primary reaction involved incubating 16 U of Hu-XO with 100 µL of a substrate mixture in 10 mL of RB at 37°C for 30 minutes. For the secondary reaction, 3 mM Fenton reagent was added to the primary reaction mixture, which was then transferred to the CR solution. The reaction proceeded for 120 minutes at 60 RPM in the dark under ambient temperature. Absorption spectra were measured across the visible range (400–800 nm) at two intervals: the optimal time of 120 minutes (T) and half that duration (T/2, 60 minutes). Decolorization percentages were calculated based on absorbance maxima at 497 nm. Control samples, processed simultaneously, contained heat-inactivated Hu-XO.

2.2.9 Analysis of CR degraded products via MS and FTIR

Treated (test) and untreated control (containing heat-denatured Hu-XO) CR samples were freeze-dried after 120 minutes of reaction and stored at -20°C until analysis. Degraded compounds were analyzed using a triple Q/TOF-MS system (Agilent G6546A, Santa Clara, USA) fitted with an ESI source. Mass spectrometric analysis was conducted in negative ion mode with the following parameters: capillary voltage, 3.5 kV; drying and sheath gas temperatures, 320–350°C; drying/sheath gas flow rates, 8 and 11 L min^{-1}, respectively; nebulizer pressure, 35 psi. Acetonitrile (10 nM CH_3CN) served as the mobile phase. Data was analyzed and visualized using MestReNova software. Functional groups in degradation products from test and control samples were characterized via ATR-FTIR spectroscopy using a Shimadzu IRAffinity-1S instrument (Shimadzu Corp., Japan) equipped with a Quest ATR GS10801-B diamond accessory (Specac Ltd., England). Spectra were recorded from 400–4000 cm^{-1} (triplicate measurements) at a resolution of 2 cm^{-1} and processed using Shimadzu LabSolution IR software.

2.2.10 Toxicity assessment of CR degradation products via bioluminescence inhibition test

Toxicity analysis of the negative control (saline), control and test samples were performed via a bioluminescence inhibition test using the bacterium *A. fischeri*. The assay was conducted following the standard operating procedure of the International Organization for Standardization [95] and was adapted to a 96-well plate format as reported previously [96,97]. In brief, the negative control, control and test samples were diluted (1:2) in saline buffer. 100 µL of each sample was mixed with 50 µL of overnight-grown *A. fischeri* solution in Photobacterium broth (with DMSO > 1%). Luminescence was measured before and after 30 minutes of incubation to quantify inhibition via a microplate reader (Varioskan™ LUX, Thermo Scientific). The relative inhibitory rate (I %) was calculated according to Equation 5.

$$\textbf{\textit{Relative inhibitory rate }}\textit{I}\ \% = \frac{Eo-E}{Eo} \times 100 \qquad \textbf{(Equation 5)}$$

where E_0 and E are the bioluminescence intensities of the control and test samples, respectively.

2.2.11 Phytotoxicity test of CR degraded products

The various toxic effects of the Hu-XO coupled Fenton reaction on the control and test CR samples were tested on the seeds of *V. mungo* (black gram), *V. radiata* (Mung bean), and *C. arietinum* (Bengal gram) in this study. Seed germination (%) and seedling growth inhibition

(%) were assessed at degraded product concentrations of 50–100% (v/v) in Petri dishes under ambient conditions. Phytotoxicity was quantified by measuring germination rates, shoot length, and root length after seven days. Seeds were surface-sterilized with 1% sodium hypochlorite for 10 minutes to eliminate microbial contamination, followed by 15 rinses with deionized water. Sterilized seeds were transferred to Petri dishes containing degraded product solutions (treated with functional or denatured Hu-XO) at concentrations of 50, 60, 70, 80, 90, and 100% (v/v). Dishes were incubated in dark for seven days, after which germination and growth inhibition rates were recorded. A negative control with tap water was included for comparison.

2.2.12 Antimicrobial effect of Hu-XO coupled Fenton reaction

E. coli and *B. subtilis* strains were selected to assess the effects of the Hu-XO coupled Fenton reaction on microbes. These models represent Gram-negative and Gram-positive bacteria, respectively, a distinction that is crucial owing to significant differences in their cell wall structures, which impact susceptibility to antimicrobial agents. Additionally, both strains are easy to culture and manage in the laboratory, with rapid growth enabling efficient and consistent antimicrobial testing [98,99]. 100 mL of control and test samples of *E. coli* and *B. subtilis* were grown overnight in Luria Bertani broth at 37°C and 180 RPM in 250 mL Erlenmeyer flasks. Two primary reactions were set up for the control (24.69 U heat-denatured Hu-XO, 100 µL substrate mix, and 10 mL RB) and two for the test samples (24.69 U Hu-XO, 100 µL substrate mix, and 10 mL RB) in 50 mL flasks by incubation at 37°C and 50 RPM. For secondary reactions, the primary mixtures were added to the respective control and test samples, along with 2.36 mM $FeSO_4$ per flask. The antimicrobial effect of the Hu–XO-coupled Fenton reaction was studied via microbial stress tests, SEM, TEM, differential live/dead fluorescence microscopy, and flow cytometry.

2.2.13 Microbial stress induced by Hu-XO coupled Fenton reaction

A microbial stress test was conducted to assess the impact of the Hu-XO-coupled Fenton reaction on the oxidative stress response of *E. coli* and *B. subtilis* by measuring hydrogen peroxide (H_2O_2) production. Microbes generate ROS, including H_2O_2, as a defense mechanism against environmental stressors. Comparative cellular stress levels were evaluated by quantifying H_2O_2 generated via the Hu-XO-coupled Fenton reaction via the Amplex® Red assay. Amplex® Red (10-acetyl-3,7-dihydroxyphenoxazine) is a nonfluorescent substrate that reacts with H_2O_2 in the presence of HRP to form resorufin, a highly fluorescent compound

(Equation 6). The fluorescence intensity of resorufin is directly proportional to the H_2O_2 concentration, enabling precise quantification of cellular stress [100].

$$C_{14}H_{11}NO_4(Amplex^{®}Red) + H_2O_2 \xrightarrow{HRP} C_{12}H_7NO_3(Resorufin) + H_2O \quad \textbf{(Equation 6)}$$

Following the secondary reaction (15 min; Section 2.2.12), 15 mL aliquots of *E. coli* and *B. subtilis* controls and test samples were centrifuged (6000 × g, 5 min, 4°C). After discarding the supernatant samples were washed four times with PBS to eliminate residual H_2O_2, resuspended in 5 mL PBS, and mixed with 0.8 g of 0.5 mm glass beads. The suspension was vortexed (15 min, 4°C) for 30-second ON/20-second OFF cycles, followed by centrifugation (8000 × g). Then, 50 µL of the supernatant was combined with 50 µL of Amplex® Red reagent (100 µM Amplex Red®, 0.4 U/mL HRP) and transferred to a Corning black-wall, clear-bottom 96-well plate, and fluorescence was measured (Varioskan™ LUX microplate reader; Thermo Scientific) at 571/585 nm excitation/emission maxima.

2.2.14 Morphological characterization of microbes after Hu-XO-Fenton treatment using SEM and TEM

Scanning and transmission electron microscopy were used to examine the impact of the Hu–XO-coupled Fenton reaction on the morphology of *E. coli* and *B. subtilis*. The drop-cast method was adopted from Su et al. with minor modifications [101]. After the secondary reaction (82.74 min, Section 2.2.12), 15 mL aliquots of *E. coli* or *B. subtilis* control/test samples were centrifuged (6000 × g, 5 min, 4°C), washed four times with PBS, and resuspended in PBS (1×10^7 CFU/mL). The cells were fixed with 2.5% glutaraldehyde (10 h, room temperature), washed repeatedly with PB (0.07541 M $Na_2HPO_4 \cdot 7H_2O$, 0.02459 M $NaH_2PO_4 \cdot H_2O$), and dehydrated in a graded ethanol series (30%, 50%, 70%, 80%, 90%, 100%; 10 min each). The dehydrated cells were drop-cast onto thin aluminum foil for SEM analysis (Zeiss-Gemini, Germany) and onto carbon-coated copper grids for TEM analysis (JEOL-2100F, Japan). For SEM analysis, samples were coated with gold to enhance morphological and structural visualization.

2.2.15 Live/dead assay of Hu-XO-Fenton-treated microbes via fluorescence microscopy

To assess the effect of the Hu-XO coupled Fenton reaction on *E. coli* and *B. subtilis* viability, a live/dead assay with SYTO™ 9 and PI was performed based on the method of Chen et al., with modifications [102]. SYTO™ 9 marks live cells by binding to DNA in intact membranes, whereas PI binds to DNA in damaged or dead cells. The samples were analyzed via

fluorescence microscopy and flow cytometry. After the reaction (82.74 min; Section 2.2.12), 5 mL samples from the *E. coli* and *B. subtilis* control and experimental groups were centrifuged (6000 × g, 5 min, 4°C), the supernatants were removed, and the pellets were washed four times with PBS. The cell suspensions were adjusted to 10^6 cfu/mL in PBS. For microscopy, samples were stained with PI (20 mM stock) and SYTO™ 9 (3.34 mM stock) in DMSO, achieving final concentrations of 30 µM PI and 5 µM SYTO™ 9 (1:1 ratio in PBS). For flow cytometry, 1 mL samples were stained with 30 µM PI. The stained samples were incubated for 15 min in the dark at room temperature before analysis. Fluorescence microscopy was conducted via an inverted fluorescence microscope (CKX53SF-OLYMPUS, Tokyo, Japan). SYTO 9 signals were acquired via a 488 nm laser with a 505–550 nm emission filter, whereas PI signals were detected via a 561 nm laser and 575 nm longpass filter. Images were analyzed via ImageJ software. Flow cytometry was performed on a BD LSR Fortessa system (BD Biosciences, San Jose, CA, USA) equipped with four laser lines (355, 405, 488, 640 nm), forward/side scatter detectors, and 16 fluorescence detectors. PI detection was specifically measured via the 695/40 channel.

2.2.16 Impact of Hu-XO coupled Fenton reaction on BOD and COD levels in industrial wastewater

BOD and COD are key water quality indicators; BOD reflects the oxygen needed by microorganisms to decompose organic matter, whereas COD represents the total oxygen required to oxidize all pollutants, indicating pollution levels and ecosystem health [103]. The potential of the Hu–XO coupled Fenton reaction to restore the BOD and COD levels of wastewater was examined via ^{UT}LIWW. Tannery wastewater was selected for this study because of its complex organic load, microbial diversity [104], and proximity to the research facility. A total of 600 mL of untreated leather industry wastewater (UTLIWW) was collected in a BOD bottle from CLC, Kolkata, West Bengal (India), with support from the CSIR–CLRI, Chennai. The initial wastewater parameters are summarized in Table 2.6. The effluent was filtered through 125 mm Whatman™ filter paper to remove solids. The control and test reactions (24.69 U of heat-denatured or active Hu-XO, respectively, with 100 µL substrate mix and 10 mL RB; 5 mM Tris pH 5.8, 10 mM NaCl) were conducted in separate 100 mL BOD bottles for 30 minutes. 90 mL of the filtered ^{UT}LIWW was poured into each bottle with 2.36 mM $FeSO_4$. The BOD and COD of the crude, control, and test samples were determined via standard methods as explained by Rice et al. [105]. BOD was measured via the dilution method by incubating samples at 20°C for 5 days and calculating DO differences. COD was assessed

via the open reflux dichromate method. A digestion solution was prepared with 3 g of pre-dried potassium dichromate, 167 mL of concentrated sulfuric acid, and 33.3 g of mercury (II) sulfate in 500 mL of distilled water. 50 mL of each sample was mixed with the digested solution and heated in a thermoformer for 2 h at 150°C. Absorbance for COD was measured at 600 nm via a spectrophotometer.

Table 2. 6 Key parameters of LIWW at the time of sampling

Wastewater parameter	Description/Value
Location	Calcutta Leather Complex
GPS Coordinates	22°29'40.3"N 88°31'28.8"E
pH	6
Color	Gray
Temperature (Collection point)	34°C

2.2.17 Toxicity analysis of treated and untreated LIWW

The toxicity analysis of ^{UT}LIWW and treated LIWW was conducted via two methods to assess their impact on microbial and plant systems. The bioluminescence inhibition test, a widely used bioassay, was performed to detect toxicants affecting aquatic microorganisms, offering critical insights into ecological risks [106]. A phytotoxicity test was also conducted to assess the effects of wastewater on plant life, with a focus on seed germination and seedling growth. Examining the impact of wastewater before and after treatment reveals potential environmental hazards and helps evaluate the effectiveness of treatment methods [107].

The toxicity of ^{UT}LIWW and treated LIWW was analyzed via a bioluminescence inhibition test with *A. fischeri*. The assay was conducted following the standard operating procedure of the International Organization for Standardization [95], and was adapted to a 96-well plate format as reported previously [96,97]. In brief, the negative control (saline), ^{UT}LIWW, ^{UT}LIWW-Hu-XO degradation products, and ^{UT}LIWW-denatured Hu-XO were diluted (1:2) in saline buffer. 100 µL of each sample was mixed with 50 µL of *A. fischeri* solution (with DMSO > 1%). Luminescence was measured before and after 30 minutes of incubation to quantify inhibition via a microplate reader (Varioskan™ LUX, Thermo Scientific). The relative inhibitory rate (I %) was calculated according to Equation 5.

The various toxic effects of untreated leather industry wastewater on seeds of *V. mungo*, *V. radiata*, and *C. arietinum* after treatment with a Fenton–XO coupled reaction (with functional and denatured Hu–XO) mixture were investigated in this study. Phytotoxicity was evaluated

on the basis of seed germination (%) and seedling growth inhibition (%) at ^{UT}LIWW concentrations ranging from 50–100% (v/v) in Petri dishes at room temperature. The effects were measured as the germination rate, shoot length, and root length after seven days. The seeds were sterilized with 1% sodium hypochlorite solution for 10 min to prevent fungal and yeast growth and were subsequently washed 15 times with deionized water. The sterilized seeds were placed in Petri dishes containing distilled water (control) and treated with ^{UT}LIWW solutions (with functional/denatured Hu-XO) at varying concentrations (50–100% v/v). The dishes were incubated in the dark for seven days, after which germination and growth inhibition rates were measured to determine phytotoxicity.

2.2.18 Statistical analysis

All measurements were performed in triplicate. The data are reported as the means ± standard deviations, and a t test or ANOVA was used to find significant differences among the means. The 5% level ($p \leq 0.05$) was used as a significance criterion unless explicitly stated in a particular section.

2.3 Results and discussion

2.3.1 Cloning, expression, and purification of Hu-XO

The Hu-XDH gene, which was amplified via PCR with EcoRI and SalI sites, was successfully ligated into the pPICZαA vector to create the pPICZαA-Hu-XDH shuttle vector (Fig 2.2 & 2.3).

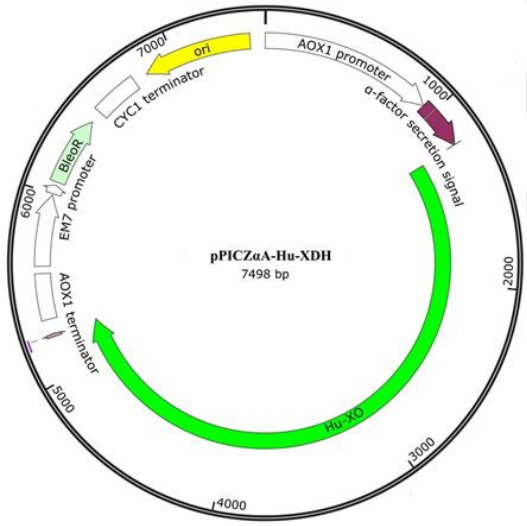

Fig 2. 2 Vector construct showing the Hu-XDH gene with vital components of the pPICZαA

The transformation of pPICZαA-Hu-XDH into *E. coli* DH5α was confirmed via colony PCR, and Sanger sequencing verified 100% nucleotide homology of the Hu-XO gene in transformed

P. pastoris. SDS–PAGE (12%) revealed a prominent 75 kDa band in the recombinant *P. pastoris* intracellular fraction, highlighting differences from the wild-type strain (Fig 2.3 E-F). The Hu-XDH protein was isolated from the intracellular fraction via Ni-NTA chromatography and further purified with AKTA Prime Plus FPLC fitted with a HiPrep Sephacryl S-300 HR column. After purification, the protein was treated with 4,4′-DTPY and concentrated via a 30,000 MWCO concentrator. While native Hu-XO has a molecular mass of 150 kDa, it appeared as a 75 kDa band via SDS–PAGE (Fig 2.3 G), indicating a homodimeric protein structure, which is consistent with the findings of Zaahkouk et al. [108].

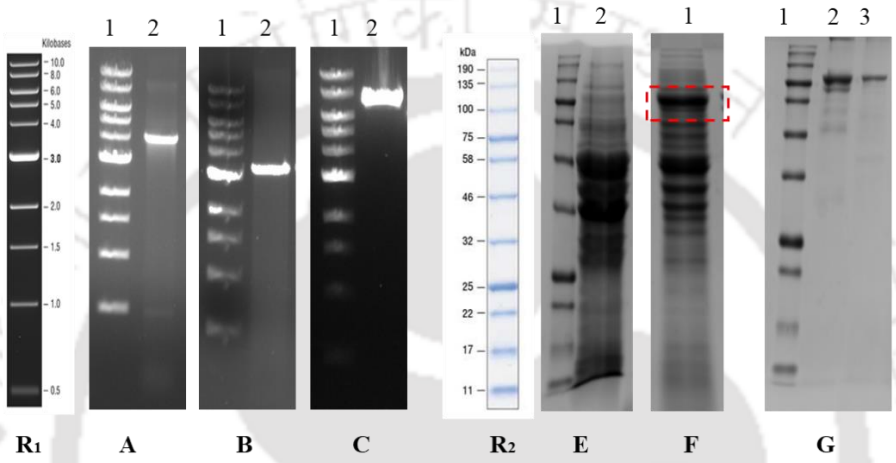

Fig 2. 3 Cloning, expression, and purification of Hu-XO

(R1) Reference 1 kb marker; (A) 1: marker, 2: Hu-XDH gene after PCR amplification (4,046 bp); (B) 1: marker, 2: pPICZαA vector after digestion (EcoRI & SalI, 3,481 bp); (C) 1: marker, 2: single digested pPICZαA-Hu-XDH (7,527 bp);(R2) reference protein marker (11–190 kDa); (E) 1: marker, 2: wild-type P. pastoris intracellular protein fraction; (F) 1: intracellular protein fraction of recombinant P. pastoris; (G) 1: Marker, 2: Ni-affinity chromatography-purified Hu-XDH, 3: SEC purified Hu-XDH

2.3.2 Western blotting, activity, kinetics, and stability of Hu-XO

The expression of recombinant Hu-XO in *P. pastoris* was confirmed through Western blot analysis, revealing a distinct 75 kDa band for the 6x-His-tagged Hu-XO protein (Fig 2.4 A). This result was consistent with earlier studies on recombinant XO expression and verified the structural integrity of the protein [108,109]. The enzymatic activity of the purified Hu-XO, determined via a H_2O_2 calibration standard curve, was found to be 337.685 mU/mL. This activity was comparable to, or even greater than, previously reported values for recombinant XO, indicating successful expression and purification of a functionally active enzyme. To further understand the enzyme's performance, kinetic analysis was performed. Kinetic analysis via a Michaelis–Menten model ($r^2 = 0.9938$) revealed a K_M of 66.13 ± 5.41 µM and a V_{max} of

5.91 ± 0.18 µmol/min, indicating strong substrate affinity and efficient catalysis (Fig 2.8 D). These findings are critical for optimizing enzyme use in biotechnological processes, ensuring efficiency and stability under various conditions [85]. The enzyme showed optimal activity at pH 7 (Fig 2.4 B), and thermal stability tests via circular dichroism spectroscopy demonstrated structural integrity at temperatures up to 45°C. Beyond this temperature, gradual distortion of the characteristic curve was observed, indicating thermal denaturation (Fig 2.4 C). Temperature and pH are key parameters that provide crucial insights into enzyme stability for potential environmental applications [110].

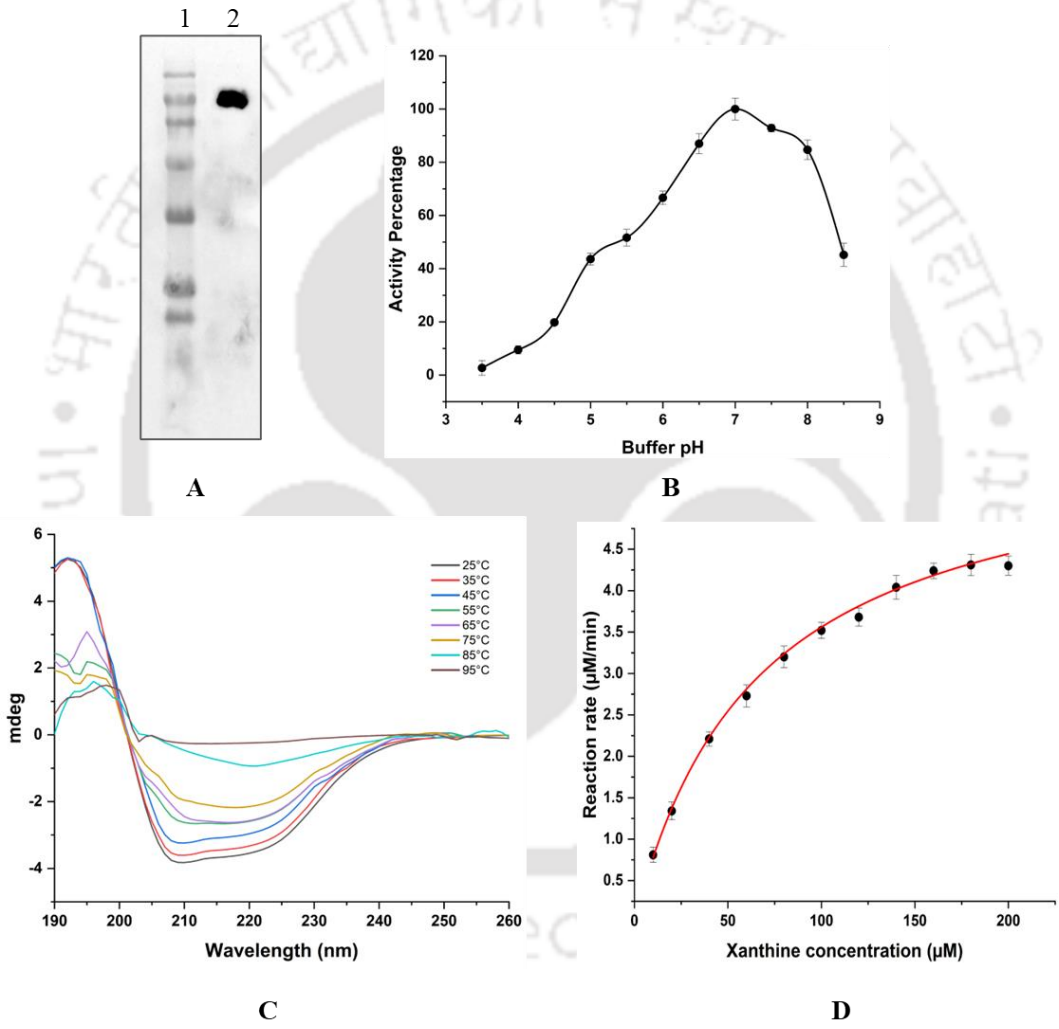

Fig 2. 4 Western blotting, kinetics, and stability of Hu-XO

(A) Western blot showing 1: Marker, 2: Hu-XDH enzyme; (B) Effect of pH on Hu-XO activity; (C) Hu-XO CD spectra obtained at different temperatures ranging from 25–95°C; (L) The initial reaction rates of Xanthine transformation was analyzed to obtain the kinetic parameters. The dots (•) represent the experimental rates, while the continuous lines were derived via the Michaelis–Menten equation ($V = \frac{Vmax[S]}{(Km+[S])}$), and the optimized parameters V_{max} (5.91 µmol/min) and K_M (66.13 µM) were added.

2.3.3 Design and optimization of Hu-XO-coupled Fenton–xanthine oxidase for enhanced CR degradation.

The Hu–XO-coupled reaction was optimized for CR degradation using RSM with a CCD. RSM, a statistical approach for modeling interactions between multiple input variables and response outputs [111], systematically evaluated three factors: enzyme amount (X_1), Fenton reagent concentration (X_2), and reaction time (X_3), on CR decolorization efficiency (Y_1). The experimental design matrix and response data are provided in Table 2.7. Decolorization percentages ranged from 40.69% to 99.14%, demonstrating significant variability across tested conditions. These results highlight the necessity of parameter optimization to achieve maximal degradation efficacy.

Table 2. 7 Experimental design for enhanced degradation of CR with independent variables and experimental and response values

Run	Enzyme amount (U)	Fenton reagent (mM)	Reaction time (Min)	Decolouration (%)
1	13	2	90	65.79
2	13	2	140.45	74.04
3	16	3	60	84.43
4	10	1	120	57.08
5	13	0.32	90	40.69
6	13	2	90	66.79
7	13	2	39.55	58.79
8	10	3	120	72.74
9	10	3	60	65.98
10	16	1	60	60.88
11	10	1	60	52.05
12	16	1	120	57.12
13	13	2	90	60.58
14	13	2	90	67.26
15	13	2	90	64.61
16	13	2	90	66.25
17	18.04	2	90	87.9
18	16	3	120	99.14
19	7.95	2	90	65.31
20	13	3.68	90	79.34

ANOVA was applied to assess the significance of the quadratic model and its terms. The model exhibited high statistical significance ($p < 0.0001$, F-value = 45.99), as detailed in Table 2.8. A

non-significant lack of fit (p = 0.3132) confirmed the model's adequacy in describing the experimental data. The coefficient of determination (R^2 = 0.97) accounted for 97% of the variability in the response, while adjusted R^2 (0.95) and predicted R^2 (0.86) values showed close alignment, further supporting the model's reliability.

Table 2. 8 Regression coefficient values of different responses for the decolorization rate via RSM

Variable	Decolouration (%)	
	Regression coefficients	**p value**
Intercept	65.18	-
A-Enzyme amount	6.71	0.0001
B-Fenton reagent	11.72	0.0001
C-Reaction time	3.54	0.0008
AB	4.49	0.0010
AC	-0.10	0.9170
BC	2.525	0.0279
A^2	4.20	0.0002
B^2	-1.65	0.0470
C^2	0.60	0.4286
Lack of fit and R^2		
Lack of Fit	0.3132 (not significant)	
R^2	0.9764	
Adjusted R^2	0.9551	
Predicted R^2	0.8602	

The quadratic polynomial equation describing the relationship between the variables and the response (Decolouration %) was determined as (Equation 7):

Decolouration (%) = 132.563 -12.80A -8.70B -0.15C + 1.50AB - 0.001AC + 0.08BC + 0.47A^2 - 1.66B^2 + 0.0006C^2 **(Equation 7)**

where A, B, and C represent the coded values for the enzyme amount, Fenton reagent concentration, and reaction time, respectively. The significance of model terms was determined based on p-values, with values <0.05 considered statistically significant. Linear terms (A, B and C), interaction terms (AB, BC), and quadratic terms (A^2, B^2) demonstrated significance ($p < 0.05$), indicating that all three variables substantially influence CR degradation both independently and interactively. Positive coefficients for A, B, and C suggest that increasing enzyme amount, Fenton reagent concentration, or reaction time enhances decolorization efficiency. In contrast, the negative coefficient for B^2 implies inhibitory effects at elevated Fenton reagent concentrations, consistent with prior reports where excess iron salts scavenge

hydroxyl radicals, reducing efficacy [112]. The significant positive interaction between enzyme amount and Fenton reagent concentration (AB) highlights synergistic behavior. This synergy likely arises from Hu-XO's role in hydrogen peroxide generation and the Fenton reagent's hydroxyl radical production, a mechanism observed in analogous enzyme-Fenton systems [113]. Contour and 3D response surface plots (Fig 2.5) illustrated the interactions between variables and their influence on CR decolorization efficiency. The plots identified optimal conditions for maximum degradation within the tested experimental range. Curved surfaces reflected significant quadratic effects of enzyme amount, Fenton reagent concentration, and reaction time.

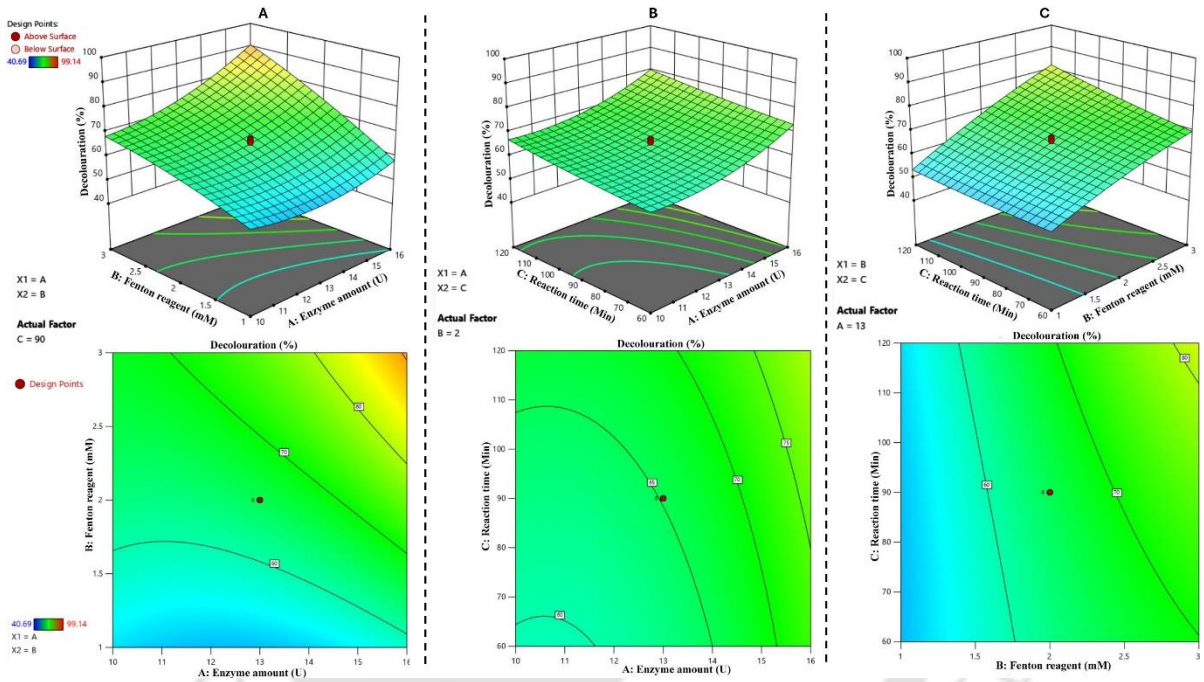

Fig 2. 5 3D surface and contour plots for the effects of variables on CR decolorization

(A) enzyme amount and concentration of Fenton reagent, (B) enzyme amount and reaction time, and (C) concentration of Fenton reagent and reaction time

Model-predicted optimal parameters included 16 U enzyme, 3 mM Fenton reagent, and 120 minutes reaction time, yielding a maximum decolorization rate of 97.24 ± 2.71%. Validation experiments under these conditions achieved a decolorization rate of 93 ± 3.24%, demonstrating 95% agreement with model predictions (Table 2.9). The close agreement between the predicted and experimental values confirmed the reliability and predictive power of the developed model.

Table 2. 9 Optimal conditions, along with the experimental and predicted response values under these optimized settings

Optimum Conditions	Coded Levels	Actual Levels
Amount of enzyme (U)	1.21	16
Concentration of Fenton reagent (mM)	1	3
Reaction time (Min)	1	120

Response	Predicted Value	Experimental Value
Decolouration (%)	97.24±2.71	93±3.24

The enhanced decolorization percentage observed under optimized conditions was likely due to several factors. The optimal enzyme amount ensures sufficient H_2O_2 production, which is essential for the Fenton reaction, whereas a moderate Fenton reagent concentration allows efficient hydroxyl radical generation without excessive scavenging. Additionally, the optimal reaction time enabled the full development of synergistic effects between Hu-XO and the Fenton reaction, maximizing the amount of reactive oxygen species needed for the degradation of CR. These findings demonstrated the successful optimization of the Fenton-xanthine oxidase reaction and provided valuable insights into the complex interactions between reaction parameters, offering a robust predictive model for improving CR degradation efficacy in wastewater treatment applications.

2.3.4 Designing and optimization of the Fenton-XO coupled reaction for enhanced antimicrobial activity

The Hu-XO coupled reaction was optimized for enhanced antimicrobial activity using RSM with a CCD. RSM, an advanced statistical technique for optimizing complex processes by analyzing relationships between multiple input factors and response variables [114], enabled systematic evaluation of three key variables enzyme amount (X_1), Fenton reagent concentration (X_2), and reaction time (X_3), on antimicrobial activity, measured as PI intensity (Y_1). The experimental design matrix and corresponding response values are presented in (Table 2.10).

Table 2. 10 Experimental design for enhanced antimicrobial activity with independent variables, experimental and response values

Run	Independent Variables			Response Values
	Enzyme amount (U)	Concentration of Fenton reagent (mM)	Reaction time (Min)	PI Intensity (RFU)
1	20	3	60	2401
2	20	1	120	2105
3	25	3	120	4294
4	22.5	3.68	90	3379
5	25	1	120	2301
6	22.5	2	90	3119
7	22.5	2	90	3227
8	25	3	60	3972
9	25	1	60	1910
10	18.29	2	90	2036
11	22.5	2	140.45	3211
12	22.5	2	90	3241
13	20	3	120	2642
14	22.5	2	90	3318
15	22.5	2	39.54	2697
16	22.5	2	90	3429
17	22.5	0.31	90	1361
18	22.5	2	90	3550
19	26.70	2	90	3611
20	20	1	60	1780

The PI intensity values ranged from 1361 to 4294 RFU, indicating a wide range of antimicrobial effects under different conditions. This variability underscores the importance of optimizing the reaction parameters for maximum efficacy. ANOVA revealed a highly significant quadratic model ($p < 0.0001$, F value of 98.67) with a nonsignificant lack of fit ($p = 0.9897$), confirming the model's adequacy (Table 2.11). The model explained 98% of the response variability ($R^2 = 0.98$), with adjusted and predicted R^2 values (both 0.97) showing close agreement, further validating its reliability.

Table 2. 11 Regression coefficient values of different responses for antimicrobial activity (measured as PI intensity) via RSM

Variable	PI Intensity (RFU)	
	Regression coefficients	**p value**
A-Enzyme amount	453.83	0.0001
B-Concentration of Fenton reagent	630.22	0.0001
C-Reaction time	156.95	0.0005
AB	362.13	0.0001
AC	18.37	0.6594
BC	-19.13	0.6466
A^2	-174.25	0.0002
B^2	-334.58	0.0001
C^2	-128.11	0.0017
Lack of fit and R^2		
Lack of Fit	0.9897 (not significant)	
R^2	0.9822	
Adjusted R^2	0.9731	
Predicted R^2	0.9742	

The quadratic polynomial equation describing the relationship between the variables and the response (PI intensity) was determined as (Equation 8):

PI intensity = -12207.2 + 1124.35A - 1233.2B + 26.6156C + 144.85AB + 0.245AC - 0.6375BC - 27.8793A^2 + -334.582B^2 - 0.142341C^2 **(Equation 8)**

where A, B, and C represent the coded values for the enzyme amount, Fenton reagent concentration, and reaction time, respectively. The significance of the model terms was determined via p values (with <0.05 considered significant). The significant terms included the linear factors A, B, and C; the interaction term AB; and the quadratic terms A^2, B^2, and C^2 ($p < 0.05$). These results highlight the individual and combined influences of all three variables on antimicrobial activity. The positive coefficients for A and C suggest that increasing the enzyme amount and reaction time enhances antimicrobial activity, whereas the negative coefficient for B implies that higher Fenton reagent concentrations may inhibit efficacy. This aligns with prior research showing that excess iron salts in Fenton systems scavenge hydroxyl radicals, reducing overall efficacy [112]. The interaction effect between A and B was significant and positive, suggesting a synergistic effect. This synergy likely arises from the complementary roles of Hu-XO in producing hydrogen peroxide and the Fenton reagent in generating hydroxyl radicals, as noted in similar coupled enzyme–Fenton systems [113]. Contour and 3D response surface plots

(Fig 2.6) demonstrated that the maximum antimicrobial activity occurred within the tested ranges, with surface curvature confirming notable quadratic effects for the enzyme amount and Fenton reagent concentration.

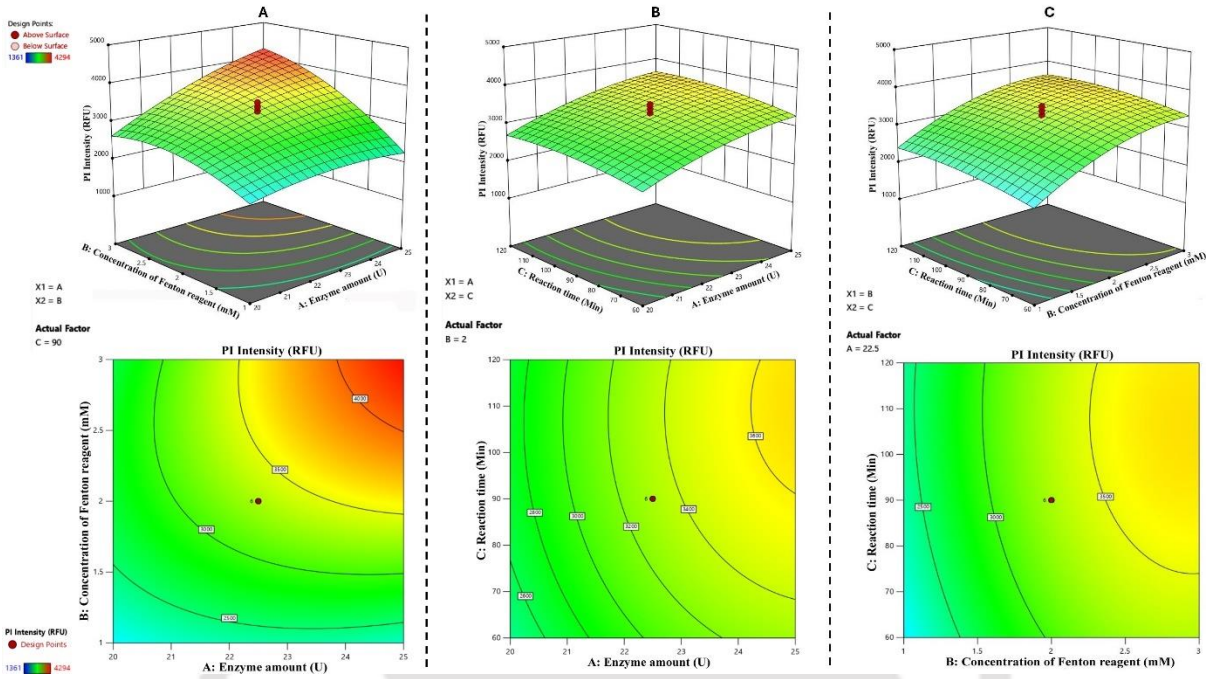

Fig 2. 6 3D surface and contour plots for the effects of variables on antimicrobial activity measured as PI intensity

(A) enzyme amount and concentration of Fenton reagent, (B) enzyme amount and reaction time, and (C) concentration of Fenton reagent and reaction time

The model predicted optimal conditions of 24.69 U of enzyme, 2.36 mM Fenton reagent, and 82.74 min of reaction time, yielding a maximum PI intensity of 3827. Experimental validation under these conditions achieved 3748 ± 3.24 PI intensity, showing 95% agreement with the predictions and confirming model reliability (Table 2.12).

Table 2. 12 Optimal conditions, along with the experimental and predicted response values under these optimized settings

Optimum Conditions	Coded Levels	Actual Levels
Amount of enzyme (U)	0.876	24.69
Concentration of Fenton reagent (mM)	0.36	2.36
Reaction time (Min)	-0.242	82.74

Response	Predicted Value	Experimental Value
Optimized PI Intensity	3827	3635±3.24

The enhanced antimicrobial activity under optimized conditions was likely due to several factors. An optimal enzyme amount ensures sufficient hydrogen peroxide production, which is essential for the Fenton reaction, whereas a moderate concentration of Fenton reagent allowed efficient hydroxyl radical generation without excessive scavenging. Additionally, an optimal reaction time enabled the full development of synergistic effects between Hu-XO and the Fenton reaction, maximizing the amount of reactive oxygen species needed for antimicrobial action. These findings demonstrated the effective optimization of the Fenton-xanthine oxidase reaction and provided valuable insights into the complex interactions among reaction parameters, offering a robust predictive model for enhancing antimicrobial efficacy in wastewater treatment applications.

2.3.5 CR decoloration assay using Hu–XO coupled Fenton reaction

The Hu–XO coupled Fenton reaction was found to be highly efficient in degrading CR in wastewater. The choice of pH 6.5 was due to the pI of the protein (pI 7.6; at a pH above or below the pI, the protein has a net charge and remains more stable) and the nature of CR, as CR turns blue at lower pH [115,116]. The initial absorbance at 497 nm was reduced to 74.02% at time $\frac{T}{2}$ of the T optimum and 99.61% at time T optimum (Fig 3A). An experiment in which a heat denatured enzyme was used as a point of comparison revealed no change in color.

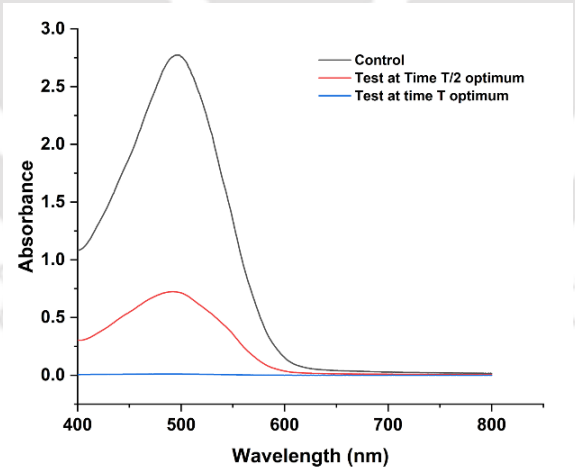

Fig 2. 7 Spectral analysis of CR degradation

Changes in the visible spectra (400–800 nm) of CR after time $\frac{T}{2}$ of the T optimum and at time T optimum along with the control

2.3.6 Analysis of degradation products via MS and FTIR

MS and FTIR spectroscopy provided critical insights into the structural breakdown of CR during the Hu-XO-Fenton reaction. The detection of fragments at m/z 197, 341, 441, and 569 in the test sample indicates progressive degradation of CR (Fig 2.8). Larger fragments (m/z 441 and 569) suggest partial breakdown of CR, retaining core structural elements such as naphthalene rings, sulfonic acid groups, and some azo bonds, albeit with functional group modifications.

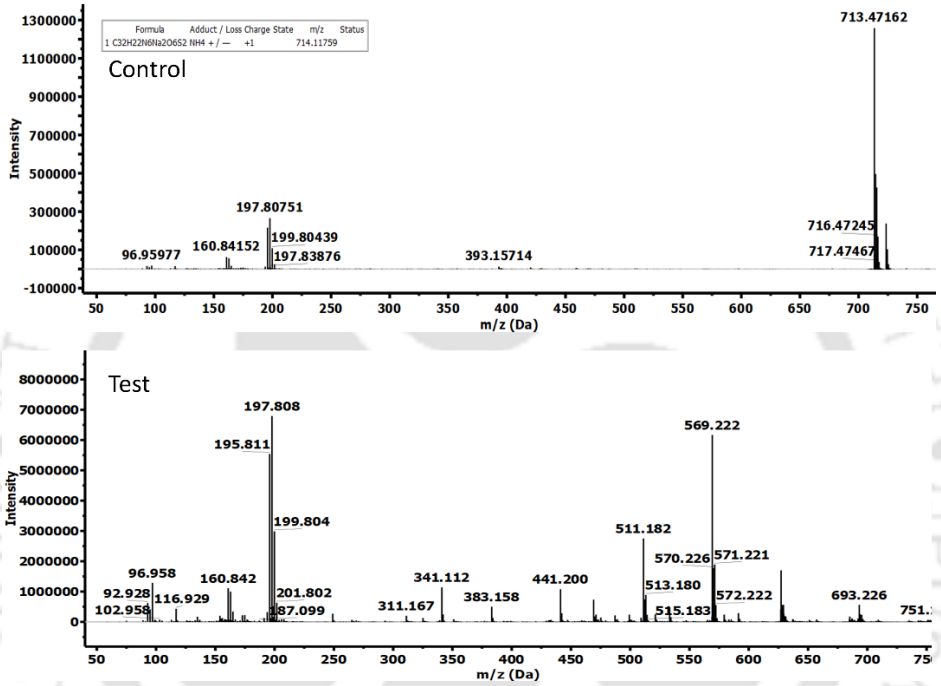

Fig 2. 8 MS spectrum of control and treated CR sample

FTIR analysis supported this observation: peaks at 3153, 2968, 2819, 1546, 1037, and 837 cm^{-1} corresponded to amino, sulfonate, nitro, and oxygen-containing groups (Fig 2.9). The smaller fragment (m/z 341) points to further breakdown of larger structures, likely involving loss of naphthalene rings or cleavage of azo bonds, producing aromatic byproducts. FTIR peaks at 3153, 2968, 2819, and 1546 cm^{-1} (O–H, N–H, and nitro group vibrations) reinforce this.

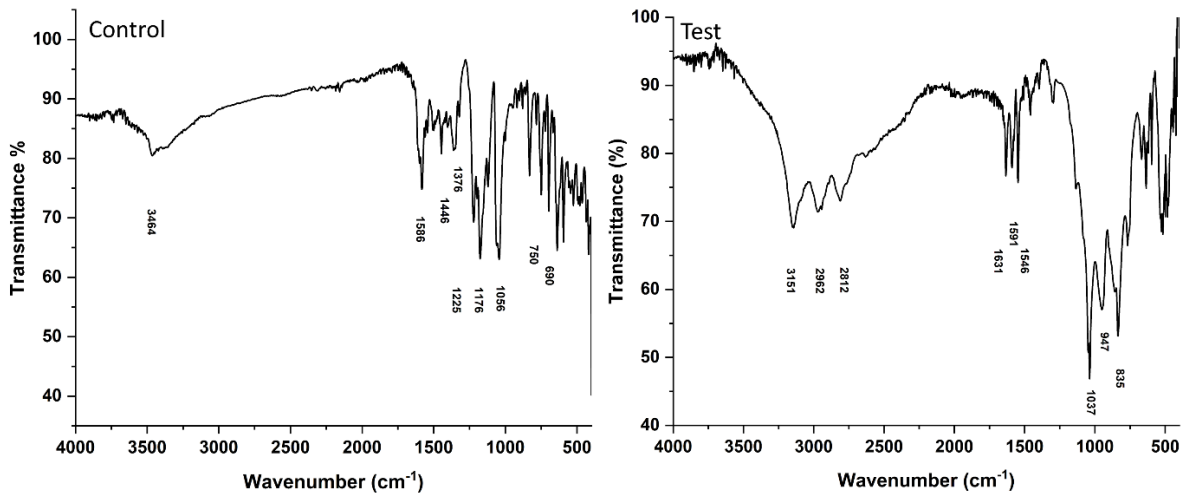

Fig 2. 9 FTIR spectrum of control and treated CR sample

The m/z 197 fragment suggests continued aromatic framework breakdown, potentially via nitrogen loss (e.g., –N=N– to –NH_2 conversion) or sulfonic acid group removal, yielding simpler oxygen-containing aromatic structures. A carbonyl group (C=O) was confirmed by the FTIR peak at 1633 cm^{-1}. Additional fragments (m/z 693, 511, 96) likely arose from hydroxyl radical-driven fragmentation (via Fenton reactions). The m/z 511 fragment aligns with the FTIR peak at 1546 cm^{-1} (N–O stretching, indicating nitro compounds), while m/z 96 corresponds to peaks at 2962 and 2812 cm^{-1} (N–H stretching, suggesting amines). Fig 2.10 proposes a CR degradation pathway based on these findings.

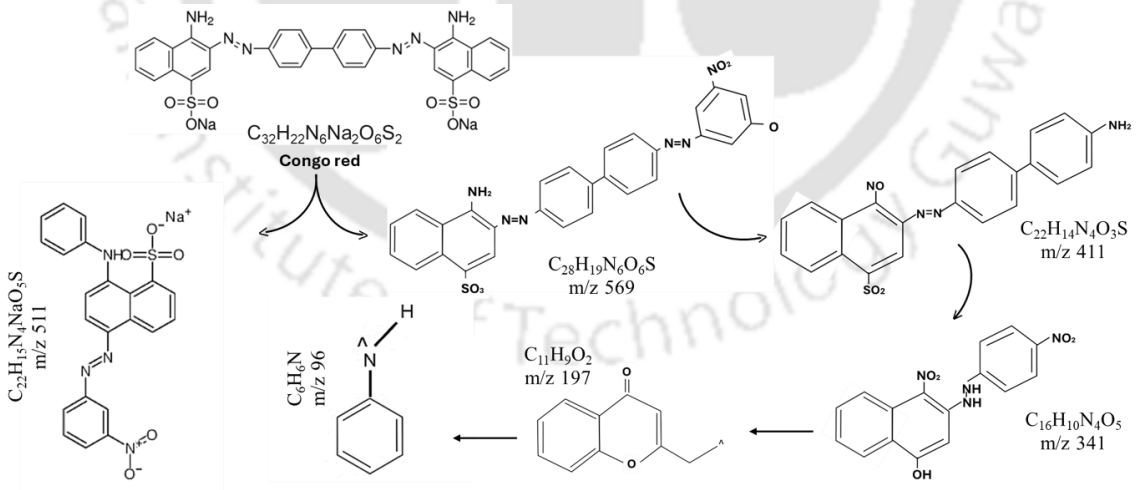

Fig 2. 10 Proposed degradation path of CR degradation

2.3.7 Toxicity analysis of CR degraded products via bioluminescence inhibition tests

The bioluminescence inhibition test measures toxicity by assessing reduced light emission from *A. fischeri* bacteria. This rapid, sensitive method is widely used to detect harmful

substances in water. This test is known for its sensitivity and rapid results, making it effective for detecting toxic substances that can affect aquatic microorganisms. It provides critical data on the potential impact of wastewater on microbial life, which is essential for understanding broader ecological consequences [106]. The toxicity of CR samples was evaluated before and after degradation using the Hu-XO-coupled Fenton reaction. The negative control showed only 4% inhibition, confirming *A. fischeri* viability and validating our analysis. In contrast, samples treated with the active Hu–XO-coupled Fenton reaction exhibited just 16% inhibition (Fig 2.11). Meanwhile, the control sample treated with heat-denatured Hu-XO and Fenton reagents showed 98% inhibition similar to the untreated sample ($p \geq 0.05$). This result confirmed that the detoxification effect was due to enzymatic activity of Hu-XO. Overall, the treated samples had significantly lower toxicity, indicating that the breakdown products were much less harmful than the original pollutants. The observed less toxicity of the treated sample was probably due to the conversion of toxic groups such as sulfonic acid (–SO_3H) and azo (–N=N–) bonds into less harmful derivatives. For example, through oxidation and reduction processes, these groups were transformed into –NH_2, –OH, or –COOH. These findings align with previous studies showing that Fenton-based treatments can greatly reduce toxicity in various industrial effluents [117].

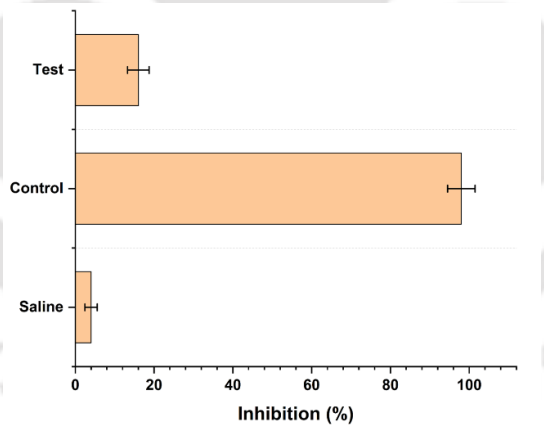

Fig 2. 11 Toxicity analysis of CR degraded products via bioluminescence inhibition tests

Changes in the percent luminescence of *A. fischeri* exposed to saline, treated, and untreated CR with functional or denatured Hu-XO coupled Fenton reactions

2.3.8 Phytotoxicity test of CR degraded products

The phytotoxic effects of the treated and untreated CR samples via the Hu–XO-coupled Fenton reaction was assessed on the basis of seed germination and seedling growth inhibition of *C. arietinum*, *V. radiata*, and *V. mungo*. The results reveal a clear concentration-dependent toxicity

for both sample types. In the germination tests, the negative control (distilled water) achieved 100% germination across all three species, confirming viability of the seeds under optimal conditions. However, increasing concentrations of CR samples led to reduced germination rates. For *C. arietinum*, germination dropped from 100% at 50% concentration to 75% in test samples and 69% in control samples at 100% concentration (Fig 2.12). Similarly, *V. mungo's* germination declined from 100% at 50% to 81% in test samples and from 100% to 73% in control samples at 100% (Fig 2.12). *V. radiata* showed higher tolerance, with test samples maintaining 100% germination up to 70% concentration before decreasing to 86% at 100%, while control samples dropped from 96% at 60% to 78% at 100% (Fig 2.12). These variations suggest that the species exhibit different tolerance levels to the degraded CR products.

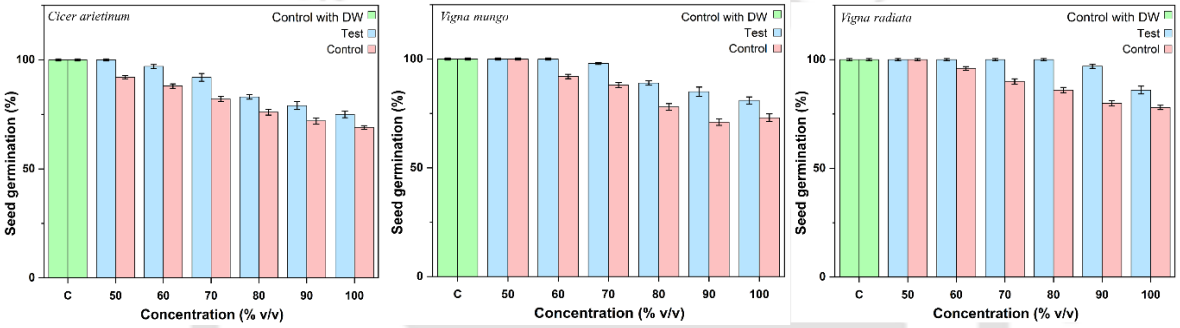

Fig 2. 12 Phytotoxicity assessment of treated and untreated CR based on seed germination rate.

Seed germination percentages of *C. arietinum*, *V. mungo*, and *V. radiata* with increasing concentrations in the control and test samples treated with functional and denatured Hu–XO coupled with the Fenton reaction

Growth inhibition, measured in terms of root and shoot length reduction, also demonstrated a concentration-dependent effect. For *C. arietinum*, the test sample showed growth inhibition increasing from 2% at a 50% concentration to 15% at 100%. The control samples presented significantly greater inhibition under similar conditions, ranging from 12% at 50% to 62% at 100% (Fig 2.13). A similar trend was observed for *V. mungo*, where the test sample inhibition ranged from 1% to 15%, and the control sample inhibition ranged from 7% to 48% (Fig 2.13). *V. radiata*, once again, presented the lowest inhibition rates, with the inhibition rates of the test samples increasing from 1% at 50% to 14% at 100%, whereas those of the control samples ranged from 6% at 50% to 39% at 100% (Fig 2.13). The higher inhibition rates in the control samples than in the test samples across all species suggested the successful degradation of CR by the Hu–XO-coupled Fenton reaction, reducing its toxicity. These results were consistent with previous observations of a similar reduction in toxicity following the degradation of CR via various methods [118,119].

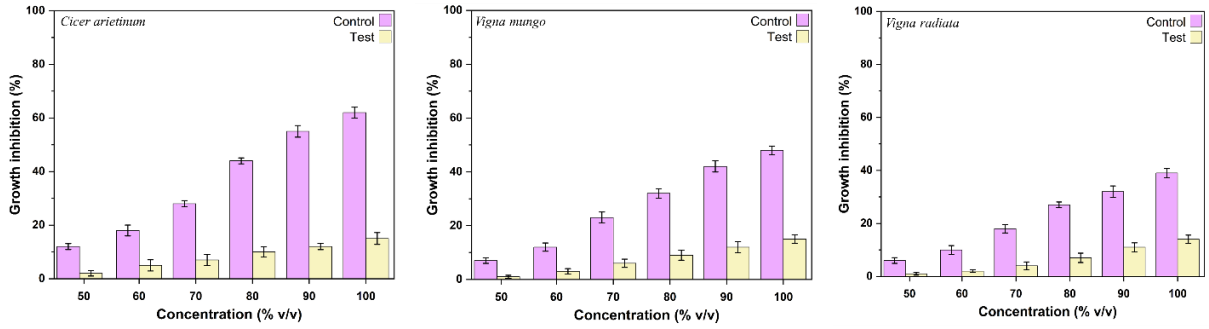

Fig 2. 13 Phytotoxicity assessment of treated and untreated CR based on growth inhibition

Growth inhibition percentages of *C. arietinum*, *V. mungo*, and *V. radiata* with increasing concentrations in the control and test samples treated with functional and denatured Hu–XO coupled with the Fenton reaction

2.3.9 Morphological characterization of microbes after Hu-XO-Fenton treatment using SEM and TEM

SEM analysis revealed substantial morphological changes in *E. coli* and *B. subtilis* following treatment with the Hu–XO-coupled Fenton reaction. Untreated *E. coli* cells retained their characteristic rod-shaped morphology with smooth surfaces (Fig 2.14 A-B). In contrast, the treated cells exhibited severe surface roughness, irregular shapes, membrane ruptures, and compromised integrity, with some appearing collapsed or flattened (Fig 2.14 C-D).

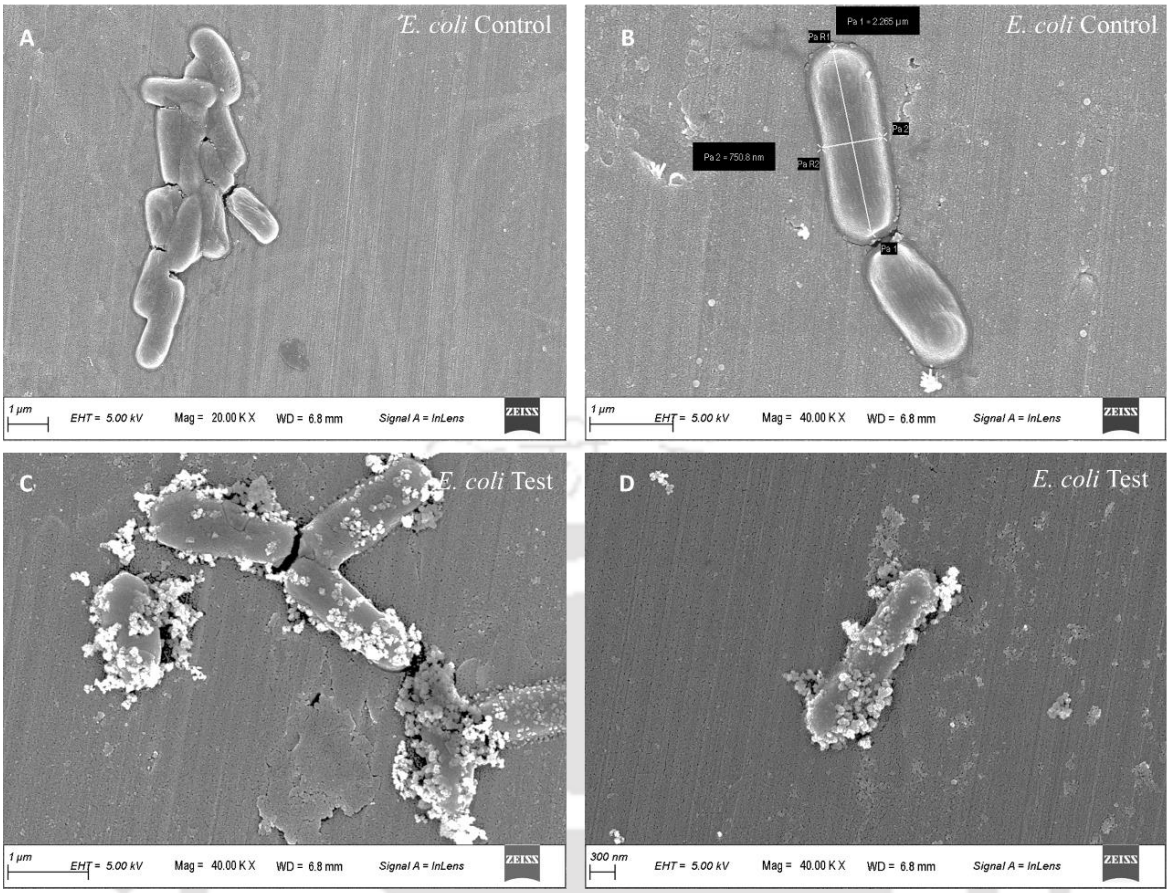

Fig 2. 14 SEM micrographs of *E. coli* cells treated with the Hu–XO-coupled Fenton reaction

(A & B) Control *E. coli* cells with smooth, rod-shaped morphology. (C & D) *E. coli* cells with rough surfaces, irregular shapes, and ruptured membranes were treated

Similarly, control *B. subtilis* cells presented typical rod-shaped structures with smooth surfaces (Fig 2.15 A-B), but treated cells presented exacerbated damage, including distorted morphology and surface blebbing (Fig 2.15 C-D). The TEM images provided additional insights into internal structural changes. The control *E. coli* cells maintained intact outer membranes (Fig 2.16 A), whereas the treated cells displayed membrane disruption and electron-dense aggregates (Fig 2.16 B). In *B. subtilis*, control cells presented a thick, uniform cell wall typical of Gram-positive bacteria (Fig 2.16 C), but treated cells presented severe wall degradation with bulging lesions (Fig 2.16 D).

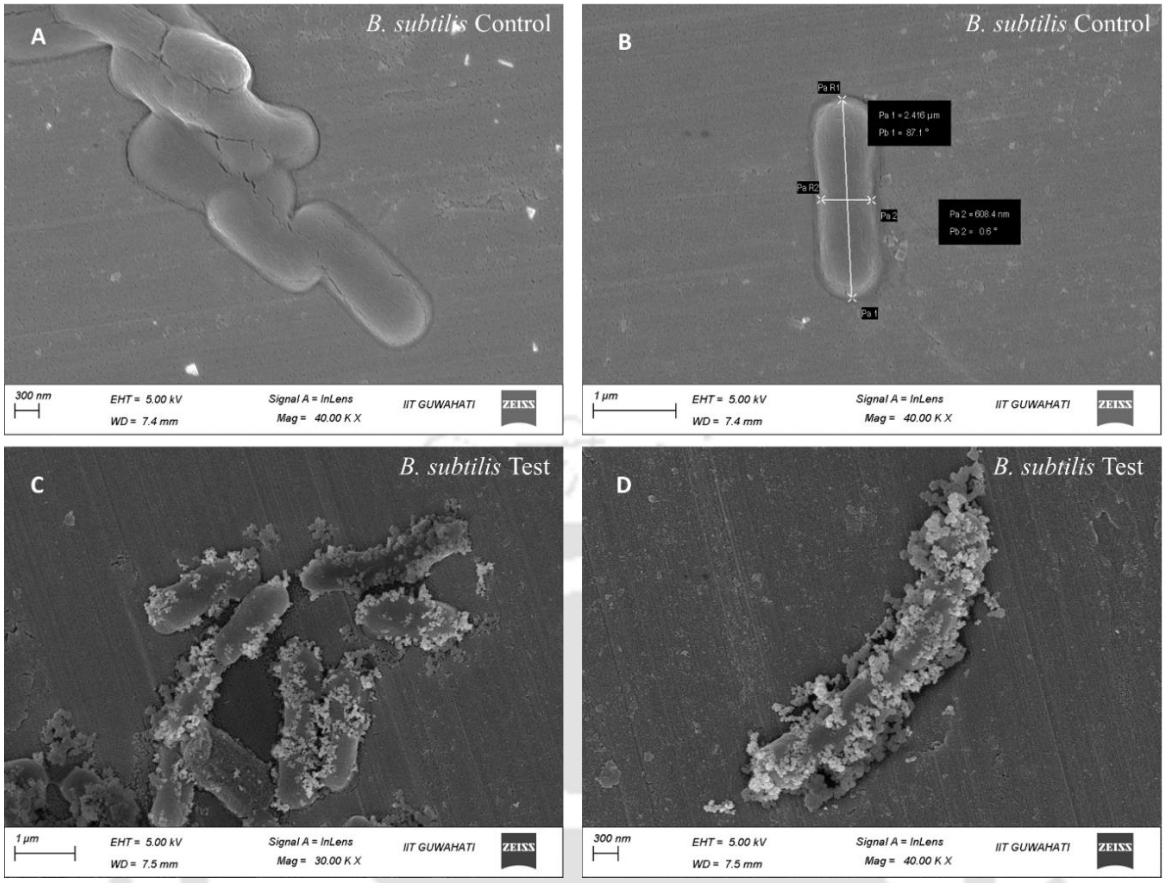

Fig 2. 15 SEM micrographs of *B. subtilis* cells treated with the Hu–XO-coupled Fenton reaction

(A & B) Control *B. subtilis* cells with smooth, rod-shaped structures. (C & D) Treated *B. subtilis* cells exhibited surface distortions and blebbing

The observed surface impairment in *E. coli* cells, characterized by irregular shapes and small, ruptured membranes, likely resulted from ROS-induced lipid oxidation in the outer membrane. This oxidative damage caused increased membrane permeability, culminating in the leakage of cellular contents. In contrast, *B. subtilis* cells exhibited severe distortions, wall ruptures, and blebbing, indicating a failure of the cell wall to withstand oxidative stress. Additionally, bulged lesions in certain regions suggest turgor pressure loss attributed to cytoplasmic leakage from compromised membrane integrity. These findings align with prior studies demonstrating ROS-mediated structural damage in diverse microbes under similar stress conditions [120,121]. The results confirmed that enhanced antimicrobial activity of the system arose from severe oxidative stress, which disrupted cell wall integrity and ultimately induced cell death.

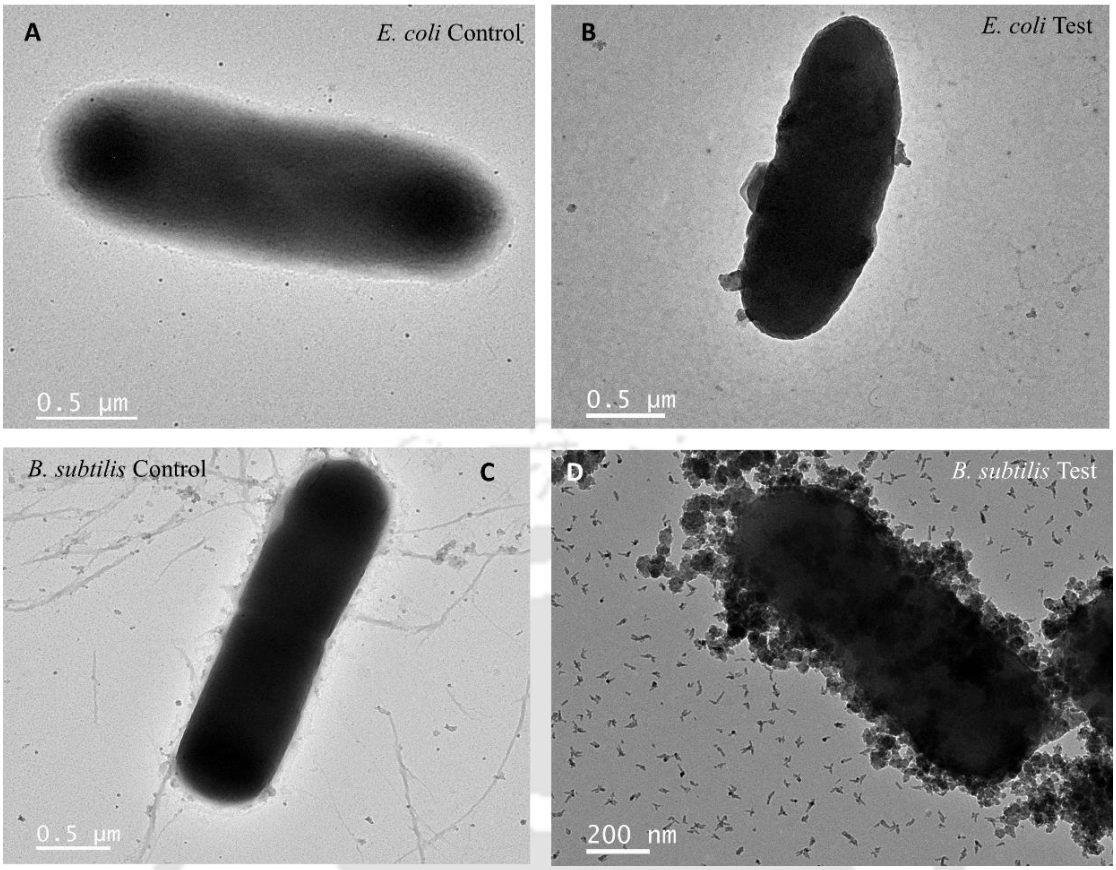

Fig 2. 16 TEM micrographs of *E. coli* and *B. subtilis* cells treated with the Hu–XO-coupled Fenton reaction

(A) TEM image of control *E. coli* cells with intact outer membranes, while (B) treated cells exhibited disrupted membranes and electron-dense aggregates. (C) Control *B. subtilis* cells with uniform cell walls and (D) treated cells with damaged walls

2.3.10 Live/dead assay of Hu-XO-Fenton-treated microbes via fluorescence microscopy

Fluorescence microscopy also confirmed the antimicrobial efficacy of the Hu-XO-coupled Fenton reaction against Gram-negative and Gram-positive bacteria. In the control samples of *E. coli* and *B. subtilis*, the presence of predominantly green fluorescent cells indicated that heat-denatured Hu-XO combined with the Fenton reagent had no significant effect on cell viability (Fig 2.17). SYTO™ 9, a membrane-permeant nucleic acid stain, entered and bound to cellular DNA, producing green fluorescence that confirmed intact membranes. In contrast, the test samples exhibited predominantly red fluorescence due to PI uptake, with smudged, irregularly shaped cells indicating severe membrane damage (Fig 2.17). The intense red fluorescence indicated widespread PI entry, a phenomenon exclusive to cells with compromised membranes, confirming that the Hu–XO-coupled Fenton reaction caused membrane damage, enabling PI to intercalate with DNA. These findings are consistent with prior studies on Fenton-based

antimicrobial systems, which documented analogous membrane damage and bacterial viability loss via fluorescence microscopy [122].

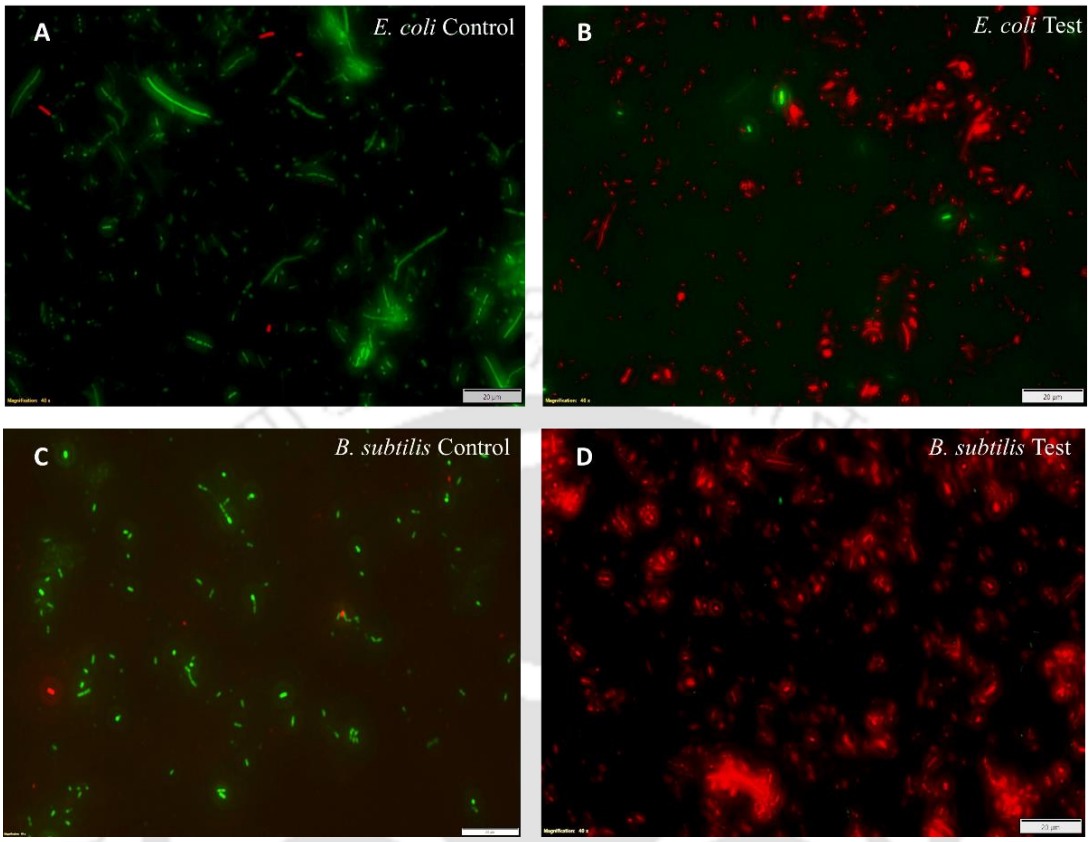

Fig 2. 17 Fluorescence microscopy of *E. coli* and *B. subtilis* cells treated with the Hu–XO-coupled Fenton reaction

(A & C) Fluorescence microscopy of control cells with green fluorescence (intact membranes), while (B & D)-treated cells exhibited red fluorescence, indicating membrane damage and PI uptake.

2.3.11 Microbial stress assay of Hu-XO-Fenton-treated microbial samples

The role of the Hu-XO-coupled Fenton reaction in the cellular stress response was investigated in *E. coli* and *B. subtilis* via stress tests. To minimize complete cell disruption, the exposure time to the reaction mixture was kept brief. The residual H_2O_2 and ROS were thoroughly washed prior to intracellular fraction extraction, preventing interference between Amplex® Red and the reaction reagents. The results revealed elevated oxidative stress in both *E. coli* (22.34%) and *B. subtilis* (36.41%) post-exposure (Fig 2.18 A-D). The elevated oxidative stress in both bacterial strains was likely caused by increased ROS levels, particularly hydroxyl radicals, leading to lipid peroxidation, membrane damage, and higher permeability. The surge in ROS likely overwhelmed antioxidant defenses like catalase and superoxide dismutase. The Fenton reaction, involving Fe^{2+} and Fe^{3+} cycling, likely disrupted cellular redox balance [123].

Elevated oxidative stress in both Gram-negative and Gram-positive bacteria highlights the potential of this system as a broad-spectrum antimicrobial process for wastewater treatment.

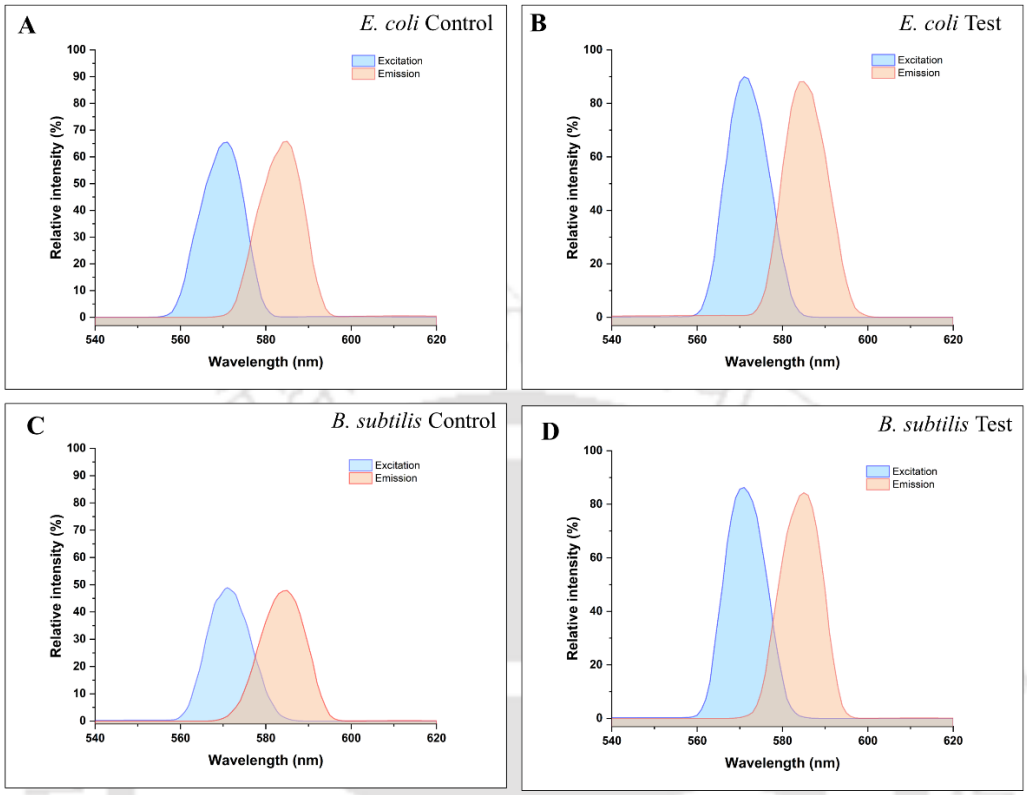

Fig 2. 18 Oxidative stress in *E. coli* and *B. subtilis* exposed to the Hu-XO coupled Fenton reaction

(A-D) Excitation/emission wavelength scan of the "Intracellular fraction- Amplex™ red" mixture. Cellular stress levels in control and test samples of *E. coli* and *B. subtilis*, respectively

2.3.12 Flow cytometric analysis of Hu-XO-Fenton-treated microbes

Flow cytometry was used to quantitatively evaluate the impact of the Hu–XO-coupled Fenton reaction on the viability of *E. coli* and *B. subtilis* populations. This technique offers a high-throughput method to assess cell membrane integrity, complementing the qualitative observations from fluorescence microscopy. PI was used as the sole fluorescent dye for the analysis. The PI-A vs. FSC-A scatter plot for the control samples revealed a tight cluster of events with low PI fluorescence intensity, indicating a predominantly viable population with intact membranes (Fig 2.19 A & C). In contrast, the scatter plot for the test samples displayed a significant shift toward higher PI fluorescence intensity and a broader distribution of events, suggesting extensive membrane damage in the treated *E. coli* and *B. subtilis* populations (Fig 2.19 B & D). The overlaid histogram of PI-A for the control and test samples exhibited a clear rightward shift in fluorescence intensity for the test samples (Fig 2.19 E & F). The percentage of PI-positive cells rose markedly for *E. coli* (from 0.4% to 89.2%) and *B. subtilis* (from 0.25%

to 91.2%) in the test samples compared with the controls, indicating significant membrane damage in both species. This substantial increase in PI-positive cells highlights the efficacy of the Hu-XO-coupled Fenton reaction in compromising bacterial membrane integrity. The flow cytometry results provide robust quantitative support for this mechanism, reinforcing the fluorescence microscopy findings. While microscopy visually reveals membrane damage, flow cytometry offers a comprehensive view of the entire population, allowing for precise quantification of treatment efficiency. A similar approach was employed by Li et al. to quantify viable cells following treatment with antimicrobial compounds [124].

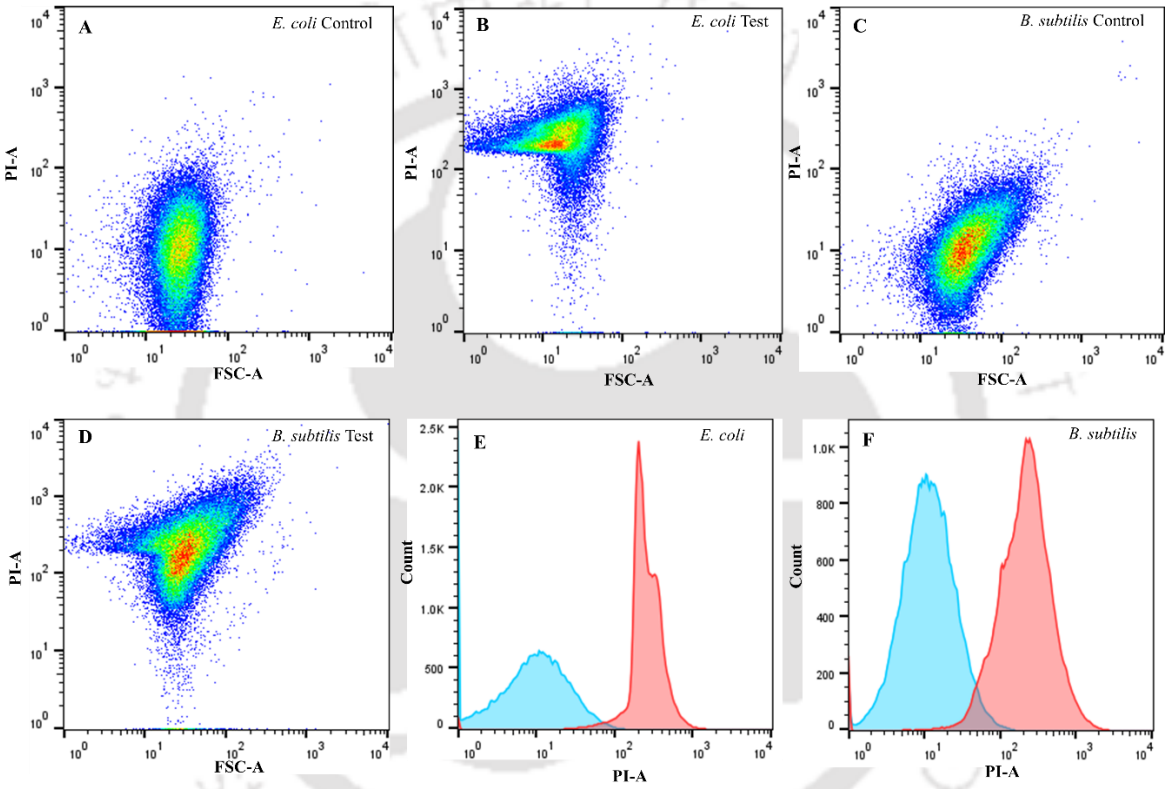

Fig 2. 19 Assessment of cell mortality in *E. coli* and *B. subtilis* exposed to the Hu-XO coupled Fenton reaction

(A-D) The PI-A vs. FSC-A graph shows the populations of the PI-stained control and test samples of *E. coli* and *B. subtilis*, respectively. (E-F) Cell count vs. PI-A overlaid histogram showing the wavelength shift in the control and test samples of *E. coli* and *B. subtilis*.

2.3.13 Impact of Hu-XO coupled Fenton reaction on the BOD and COD levels in industrial wastewater

The BOD of treated wastewater was reduced from 623 mg/L to 51 mg/L, achieving a 91.8% reduction, whereas the COD decreased from 1015 mg/L to 142 mg/L, indicating an 86.0% reduction (Table 2.13). This substantial decline in BOD and COD demonstrates the effective removal of both biodegradable and nonbiodegradable organic matter. The pronounced drop in

BOD suggests that the Fenton-Hu-XO coupled reaction efficiently oxidizes organic compounds, breaking them into simpler forms with lower oxygen demand or completely mineralizing them into CO_2 and H_2O [125]. Additionally, the strong antimicrobial effect of the reaction likely eliminated a significant portion of the microbial population, further reducing BOD by minimizing oxygen consumption by microbes [126]. The COD reduction underscored the capacity of the system to degrade recalcitrant organic matter, offering a distinct advantage over conventional biological treatments, as noted in the conventional Fenton process by Mahtab et al [127]. The efficacy of this treatment method was further supported by a visual transition of the wastewater from a cloudy grayish-white to a clear solution with accumulated debris, indicative of effective organic removal. This transformation likely stemmed from the iron salts in the Fenton reaction promoting coagulation and flocculation of the suspended particles. The debris, possibly consisting of oxidized organic matter and iron hydroxide precipitates, could be easily removed through filtration or settling. The formation of debris is a common phenomenon associated with Fenton processes [128].

Table 2. 13 Quality parameters of tannery industry wastewater before and after treatment with Hu–XO-coupled Fenton reaction

Parameters	Crude sample	Control (Heat denatured Hu-XO+ Fenton)	Test (Hu-XO+ Fenton)
BOD (mg/L)	623±4.33	617±5.22	51±3.31
COD (mg/L)	1015±8.76	997±7.21	142±5.62
Color	Cloudy greyish white (after filter)	Cloudy greyish white	Transparent with accumulated debris

2.3.14 Bioluminescence inhibition test of treated and untreated LIWW sample for toxicity analysis

Tannery wastewater is known for containing high levels of toxic organic and inorganic pollutants [104]. To assess toxicity reduction, the effectiveness of the Hu-XO coupled Fenton reaction was evaluated via a bioluminescence inhibition assay using *A. fischeri*. This assay provides insights into the environmental impact of wastewater and the efficacy of the proposed treatment process. Untreated wastewater displayed severe toxicity (98% bioluminescence inhibition), whereas the Hu-XO-coupled Fenton-treated sample showed drastically lower toxicity (18% inhibition), resulting in an 80% reduction (Figure 4A). The control sample, which was treated with heat-denatured Hu-XO and Fenton reagents, showed 96% inhibition,

similar to that of the untreated sample ($p \geq 0.05$), indicating that the detoxification effect was primarily due to the enzymatic activity of Hu-XO (Fig 2.20). The significantly lower toxicity of the treated sample suggested that the breakdown products formed during the Hu–XO coupled Fenton reaction were substantially less harmful than the original pollutants were, a key consideration for any effective wastewater treatment process.

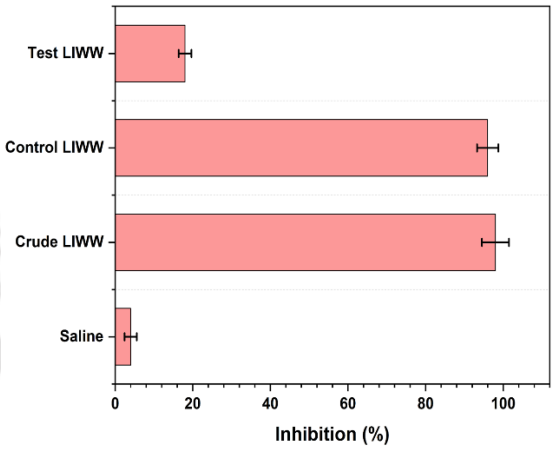

Fig 2. 20 Toxicity analysis of treated and untreated LIWW via bioluminescence inhibition test

Changes in the percent luminescence of *A. fischeri* exposed to saline, crude LIWW, and the control and test LIWW treated with functional and denatured Hu-XO coupled with Fenton reactions

2.3.15 Phytotoxicity test of treated and untreated LIWW sample

The phytotoxicity of ^{UT}LIWW and treated LIWW was assessed via seed germination and growth inhibition tests on *V. mungo*, *V. radiata*, and *C. arietinum*. The control seeds treated with distilled water exhibited 100% germination in all the species, whereas the germination rates decreased with increasing wastewater concentration, with a more pronounced effect on the untreated samples (Fig 2.21). For example, in *V. mungo*, the control samples presented germination rates of 100%, 100%, 96%, 92%, 88%, and 84% at 50–100% v/v LIWW concentrations, compared to 100%, 100%, 100%, 96%, 96%, and 92% in test samples. *V. radiata* displayed 100%, 100%, 100%, 96%, 92%, and 88% germination in controls versus 100%, 100%, 100%, 100%, 96%, and 92% in the treated samples. Similarly, the *C. arietinum* controls had 100%, 100%, 100%, 92%, 88%, and 84% germination, while test samples achieved 100%, 100%, 100%, 100%, 100%, and 92%. The decline in germination rates with increasing concentrations in the control samples likely stemmed from pollutants inhibiting enzyme activity, disrupting metabolic pathways, and damaging seed membranes. Enhanced germination in treated samples confirmed that the Hu-XO-coupled Fenton reaction mitigated phytotoxicity, even at high concentrations, by degrading harmful components.

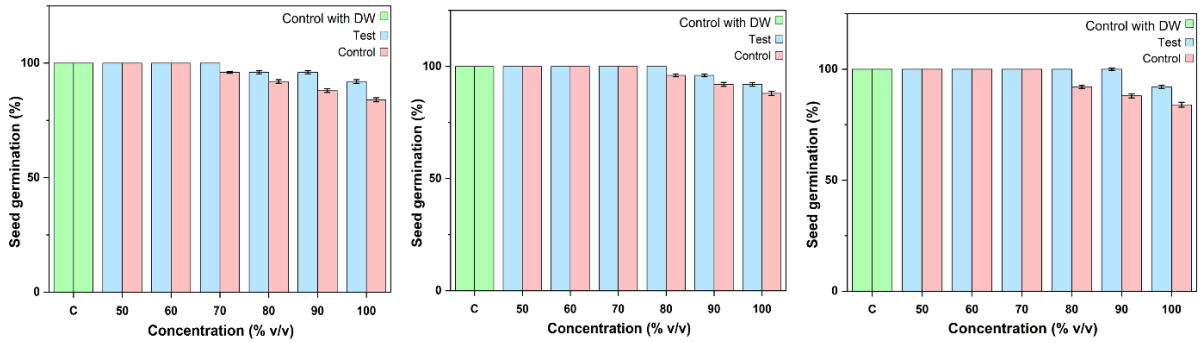

Fig 2. 21 Phytotoxicity assessment of treated and untreated LIWW based on seed germination rate

Seed germination percentages of *V. mungo*, *V. radiata*, and *C. arietinum* with increasing concentrations of control and test LIWW treated with functional and denatured Hu–XO coupled with Fenton reactions

Phytotoxicity assessments also demonstrated pronounced effects of untreated and treated LIWW on plant growth. The growth inhibition increased progressively with increasing wastewater concentration, peaking in the untreated samples. For example, the *V. mungo* control samples exhibited inhibition rates of 12.26–45.37%, versus 5.61–21.17% in treated samples. Similarly, *V. radiata* showed 20.04–50.38% inhibition in controls compared to 9.15–27.24% in the test samples, whereas the percentage of *C. arietinum* controls ranged from 10.33–52.47% inhibition, dropping to 5.26–23.26% post-treatment (Fig 2.22). These results confirmed the phytotoxic effects of untreated wastewater and the efficacy of the treatment. The substantial decline in growth inhibition rates indicates that the Hu–XO-coupled Fenton treatment effectively degraded plant growth-inhibiting pollutants. The reduced phytotoxicity aligns with previous studies showing the harmful effects of toxic components in untreated wastewater on seed germination and plant growth [129]. This dual-method approach combining *A. fischeri* bioluminescence assays with seed-based tests not only identified environmental hazards in untreated wastewater but also validated treatment efficiency through biological endpoints.

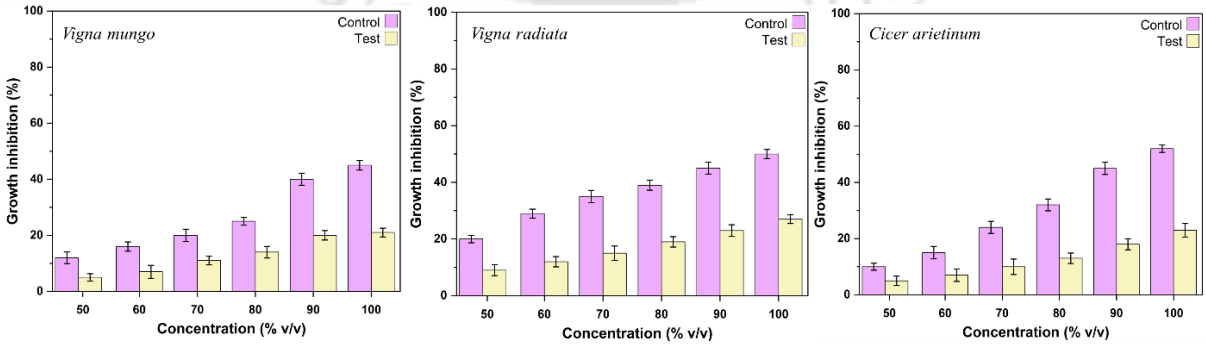

Fig 2. 22 Phytotoxicity assessment of treated and untreated LIWW based on growth inhibition

Growth inhibition percentages of *V. mungo*, *V. radiata*, and *C. arietinum* with increasing concentrations of control and test LIWW treated with functional and denatured Hu-XO coupled Fenton reactions.

2.4 Techno-economic analysis of Hu-XO driven bio-Fenton reaction for wastewater remediation

P. pastoris is a highly desirable and economical host for the production of extracellular heterologous enzymes, offering significant advantages for industrial applications. Its ability to perform proper post-translational modifications and produce enzymes extracellularly can simplify downstream processing, reducing overall production costs [130]. Furthermore, the scalability of *P. pastoris* fermentation systems to industrial-grade reactors makes it a practical choice for large-scale enzyme production [131]. The potential for enzyme immobilization adds another layer of economic efficiency by enabling enzyme reuse and increasing operational stability, which are critical for continuous industrial processes [132]. The present study also demonstrated the potential to overcome the conventional bottlenecks associated with the Fenton reaction, such as dependency on external H_2O_2, high reagent costs, and the need for highly acidic conditions. By leveraging enzyme-driven in situ H_2O_2 generation, this approach eliminates the reliance on expensive reagents and operates under mild and eco-friendly conditions. These advancements not only enhance the economic viability of the process but also contribute to sustainability, aligning with the principles of green chemistry. With further optimization, the enzyme-assisted Fenton reaction has the potential to offer a scalable and cost-effective framework for industries, enabling them to meet environmental regulations while maintaining economic competitiveness.

2.5 Conclusion

The traditional Fenton process, while effective in degrading organic pollutants, faces significant challenges such as reliance on external H_2O_2, which increases operational costs, and the requirement for acidic conditions, making it less sustainable and eco-friendly. This study emphasizes the potential of the Hu-XO coupled Fenton reaction as a sustainable solution for addressing the challenges of wastewater remediation. The optimized system achieved significant results in pollutant degradation and microbial load reduction, demonstrating its efficacy. Through a systematic investigation, the synergistic interaction between Hu-XO and the Fenton reaction was characterized and fine-tuned. This led to remarkable outcomes, including over 99% degradation efficiency of CR at a concentration of 100 mg/L, showcasing its potential to tackle azo dye pollutants. The antimicrobial activity was equally impressive, effectively reducing microbial loads of *E. coli* and *B. subtilis* at 10^6 CFU/mL, as validated by PI intensity analyses and stress assays. The treated wastewater exhibited significant reductions in BOD by 91.8% and chemical oxygen demand COD by 86%, reflecting the robustness of the

system in reducing organic loads in industrial effluents. The toxicity evaluation using *A. fischeri* demonstrated substantial reductions in luminescence inhibition, underscoring the system's effectiveness in mitigating environmental toxicity. For CR degradation products, luminescence inhibition was reduced by 82%, indicating a significant decrease in toxicity. Similarly, for treated LIWW, the luminescence inhibition was reduced by 84% after treatment with the Hu-XO coupled Fenton reaction. Phytotoxicity assays confirmed minimal adverse effects on seed germination and plant growth. These results highlight the ability of the system to convert highly toxic effluents into safer forms, rendering them less harmful to aquatic microbial life. The integrated approach effectively addresses limitations of traditional Fenton processes, such as dependency on external H_2O_2 and acidic conditions, by harnessing enzyme-driven in situ H_2O_2 generation. This study lays a strong foundation for adopting enzyme-assisted advanced oxidation processes in wastewater treatment, bridging the gap between efficiency and environmental sustainability.

Chapter 3. Engineered Mors1 enzyme from Antarctic bacteria *Moraxella* TA144 for enhanced thermal stability and activity for polyethylene terephthalate degradation

Abstract

Plastic pollution, particularly from PET, is a significant environmental concern due to its persistence in ecosystems and extensive use in packaging and textiles. Conventional recycling methods, such as thermo-mechanical and chemical processes, are hindered by inefficiencies, high costs, and limited scalability, highlighting the need for sustainable alternatives. Biodegradation using PET hydrolases offers a promising and eco-friendly solution. However, most natural PET-degrading enzymes are thermophilic, requiring high temperatures near PET's glass transition point, which makes the process energy-intensive and less practical. In this study, the Mors1 PETase from the Antarctic bacterium *Moraxella* TA144 was engineered to improve its thermal stability and catalytic efficiency. Strategic mutations involving three hydrophobic amino acid substitutions (K93I, E221I, and R235F) in the enzyme's near-turn regions yielded the mutant variant Mors1^{MUT}. Comparative analyses revealed that Mors1^{MUT} exhibited superior pH and thermal stability, retaining 98% activity at pH 9 and demonstrating improved performance across both acidic and alkaline conditions compared to the wild-type enzyme. Additionally, Mors1^{MUT} displayed enhanced thermal resilience, retaining 61% activity at 40°C and 14% at 50°C, where the wild type was completely inactivated. PET hydrolysis by Mors1^{MUT} showed a 4.16-fold improvement over the wild-type enzyme, confirmed by gravimetric weight loss and ATR-FTIR analysis.

3.1 Background

Plastic pollution has become one of the most pressing environmental issues of our time, with its pervasive presence extending even to the most remote corners of the planet. Aquatic ecosystems, from the depths of the oceans to the freshwater streams that flow through our landscapes, are particularly vulnerable to the escalating accumulation of plastic waste [133]. Plastics, primarily composed of long-chain synthetic polymers synthesized from petroleum-based monomers, are widely used in modern applications such as clothing fibers and containers for food and liquids. Their popularity is due to their affordability, versatility, durability, resistance to leaching, and non-corrosive properties, making them indispensable in industries like packaging, pharmaceuticals, and textiles[134]. However, this persistent material, designed for longevity, often fragments into microplastics and nanoplastics, which infiltrate the food chain and pose significant risks to aquatic organisms and human health. The improper disposal of PET waste, combined with its resistance to natural degradation, exacerbates these challenges, threatening the balance of ecosystems and raising critical environmental and health concerns [135]. Managing the growing accumulation of plastic waste has primarily relied on physical and chemical recycling methods, each with distinct limitations, particularly for PET. Thermo-mechanical recycling, a commonly used physical approach, involves melting and remolding PET but often results in the production of lower-quality materials due to polymer degradation during processing [136]. Chemical recycling, which breaks down PET into its monomers such as TPA and MHET/BHET via hydrolysis, glycolysis, or methanolysis, allows for the recovery of high-purity components that can be repolymerized into virgin-grade PET. However, this process is energy-intensive, requires expensive reagents, and has yet to achieve widespread economic feasibility [137].

In contrast, biological recycling has emerged as a promising alternative, leveraging PET hydrolases (PETases) to enzymatically degrade PET into EG and TPA under ambient temperature conditions, offering a more sustainable and environmentally friendly solution [138]. Most known PETases are thermophilic, exhibiting optimal activity near glass transition temperature of PET (~65°C), where the polymer chains gain flexibility and become more susceptible to hydrolysis. Despite the compatibility of these enzymes with physical properties of PET, their high-temperature requirements necessitate significant energy inputs, limiting their practicality [139]. Recent advancements, however, have discovered several PETases capable of functioning at moderate temperatures, significantly improving the feasibility of enzymatic recycling. For instance, Mors1 from *Moraxella* sp. TA144 can degrade PET at 25°C, while

Ple628 and Ple629 from a marine microbial consortium and PE-H from *Pseudomonas aestusnigri* exhibit activity at 30°C [140]. IsPETase, derived from *Ideonella sakaiensis* 201-F6, operates efficiently at 40°C, representing a significant step forward in enzymatic PET recycling. These moderate-temperature enzymes reduce energy demands and broaden the applicability of biological recycling methods [141].

Protein engineering has significantly enhanced the activity of these enzymes at ambient temperatures. For instance, rational design improved the thermal stability of IsPETase, resulting in a triple mutant (IsPETaseTS) with 14-fold increased activity and an enhanced melting temperature compared to the wild-type enzyme [142]. A computational design strategy known as GRAPE identified single-point mutations to enhance thermal stability, producing DuraPETase with ten substitutions and a comparatively higher melting temperature than IsPETase [143]. Advancements in PET enzyme engineering have leveraged both directed evolution and machine learning to improve the efficiency and stability of IsPETase for PET degradation. Directed evolution, a method involving iterative rounds of mutation and selection, enabled the screening of over 13,000 IsPETaseTS variants, leading to the development of HotPETase. This engineered enzyme exhibited a 36°C higher melting temperature and a 43-fold increase in activity at 65°C, significantly enhancing its thermal stability and catalytic efficiency [144]. Complementing this, machine learning has emerged as a powerful tool for enzyme optimization by predicting beneficial mutations. Using computational algorithms, researchers identified three key substitutions in IsPETaseTS, resulting in the creation of FAST-PETase, which demonstrated a 38-fold improvement in activity at 50°C. These approaches highlight the transformative potential of combining experimental and computational strategies to develop robust PET-degrading enzymes [145].

This study conducted a comprehensive comparative analysis between the native Mors1 mesophilic enzyme and its engineered variant, which was mutated to enhance its performance. The mutations targeted three specific near-turn regions, where hydrophobic amino acids were strategically introduced. These modifications were meticulously chosen using the DDMut server, ensuring that the substitutions were structurally constructive without compromising the three-dimensional conformation of the enzyme. The study evaluated several critical parameters, including enzyme kinetics, secondary structure integrity, thermal and pH stability, PET film degradation efficiency, and the composition of degradation by-products. This systematic analysis aimed to assess the impact of the engineered mutations on the enzyme's

functional properties, providing valuable insights into the optimization of PET-degrading enzymes.

3.2 Materials and methods

3.2.1 Materials

The plasmid isolation and PCR Cleanup/Gel extraction kits were procured from Macherey-Nagel, Germany. The antibiotics Zeocine and SYPRO™ Orange was purchased from Invitrogen, United States, and all other restriction enzymes and Gibson assembly master mixes were procured from New England Biolabs, United Kingdom. A size exclusion chromatography column (HiPrep Sephacryl S-200 HR) was purchased from Cytiva, Sweden. The protein concentrator, Amicon 10,000 MWCO and PCL was obtained from MilliporeSigma, United States. The primary A-His-Ab and secondary GAR-IgG-HRP were obtained from Bio Bharati Life Science Pvt. Ltd., India. Amorphous PET film was procured from Kuber Metpack Pvt. Ltd., Delhi. All other chemicals used in this study were of the finest quality and analytical grade. The chemicals were employed without further purification.

3.2.2 Strains and media

E. coli DH5α 1652 was procured from MTCC Chandigarh, India. The vector pPICZαA and *P. pastoris* was procured from Invitrogen Life Technologies, Carlsbad, USA. For the growth and maintenance of *E. coli* (1652) and *P. pastoris* strains, LSLB and YPD media were used, respectively. For expression studies, BMGY and BMMY media were used. All the media compositions used in this study are presented in (Appendix A.1).

3.2.3 Construction and *E. coli* DH5α transformation of pPICZαA-Mors1$^{WT/MUT}$ plasmid.

The Mors1^{WT} gene (GenBank: X53053.1) was codon optimized per the codon usage of *P. pastoris* by accessing the genome annotation by NCBI. The gene construct was synthesized by GenScript, Inc., and delivered in a pEX-A128-PET vector. The Mors1^{WT} gene from pEX-A128-PET was amplified via PCR with primers with EcoRI and SalI sites (Appendix B.1). The sequences of the primers used to amplify the Mors1^{WT} gene are listed in (Table 3.1). For the Mors1^{MUT} construct, four distinct fragments were amplified using primers (detailed in Table 2) designed with EcoRI and SalI restriction sites. These primers incorporated specific codon mutations (indicated in Fig 3.1) and utilized the pEX-A128-PET as template.

Table 3. 1 The primers used for amplification of the Mors1$^{WT/Mut}$ gene with restriction sites (black, bold) and mutated codon (red, bold).

Clone	Type	Primer
Wild	Forward	AGAGAGGCTGAAGCT**GAATTC**ATGTTCATCATGATTAA GAAATCTGAATTGGC
	Reverse	CAATGATGATGATGATGATG**GTCGAC**AGGACAATCCTT ATAATCGTAAGCAGAGATTCT
Mutant	Forward	AGAGAGGCTGAAGCT**GAATTC**ATGTTCATCATGATTAA GAAATCTGAATTGGC
	Reverse	ACCGAAACC**AAT**AGCAGATTGTCTAGAG
	Forward	CTGCT**ATT**GGTTTCGGTGGTG
	Reverse	GGAGTTTTAAC**AAT**TCCATAAGACTTATCAT
	Forward	TTATGGA**ATT**GTTAAAACTCCAACTTTGGT
	Reverse	GTATTTCTTAGTCTCAGCAAT**GAA**ATCATCTTCACAAG
	Forward	**TTC**ATTGCTGAGACTAAGAAATACGCTAACG
	Reverse	CAATGATGATGATGATGATG**GTCGAC**AGGACAATCCTT ATAATCGTAAGCAGAGATTCT

The highlighted mutations (Fig 3.1) were strategically chosen by introducing hydrophobic amino acids into the near-turn region, a critical area for maintaining protein functionality. Hydrophobic amino acids are well-documented for their ability to enhance the structural integrity of proteins, particularly under thermal and osmolar stress conditions [146]. To identify the most suitable substitutions, the Gibbs free energy changes (ΔΔG) associated with the mutations were analyzed using the advanced DDMut server. DDMut utilizes advanced deep learning techniques, combining 3D graph-based representations with convolutional layers and transformer encoders, to accurately predict Gibbs free energy changes (ΔΔG) for stabilizing and destabilizing mutations [147]. By applying DDMut, the unfolding Gibbs free energy changes (ΔΔGU) were calculated, enabling a precise distinction between stabilizing (positive ΔΔGU) and destabilizing (negative ΔΔGU) mutations [148]. The three most stabilizing mutations (K93I, E221I and R235F), offering significant contributions to protein stability, were selected to develop the enhanced Mors1^{MUT} enzyme having ΔΔGU values 0.09, 0.29 and 0.63 respectively.

For this study, pPICZαA was selected as a shuttle vector for creating the final vector construct in *E. coli* DH5α, which expressed heterologous Mors1$^{WT/Mut}$ in *P. pastoris*. Restriction digestion of pPICZαA with EcoRI and SalI followed by gel extraction yielded a backbone for synthesizing the yeast expression vector (Appendix B.3).

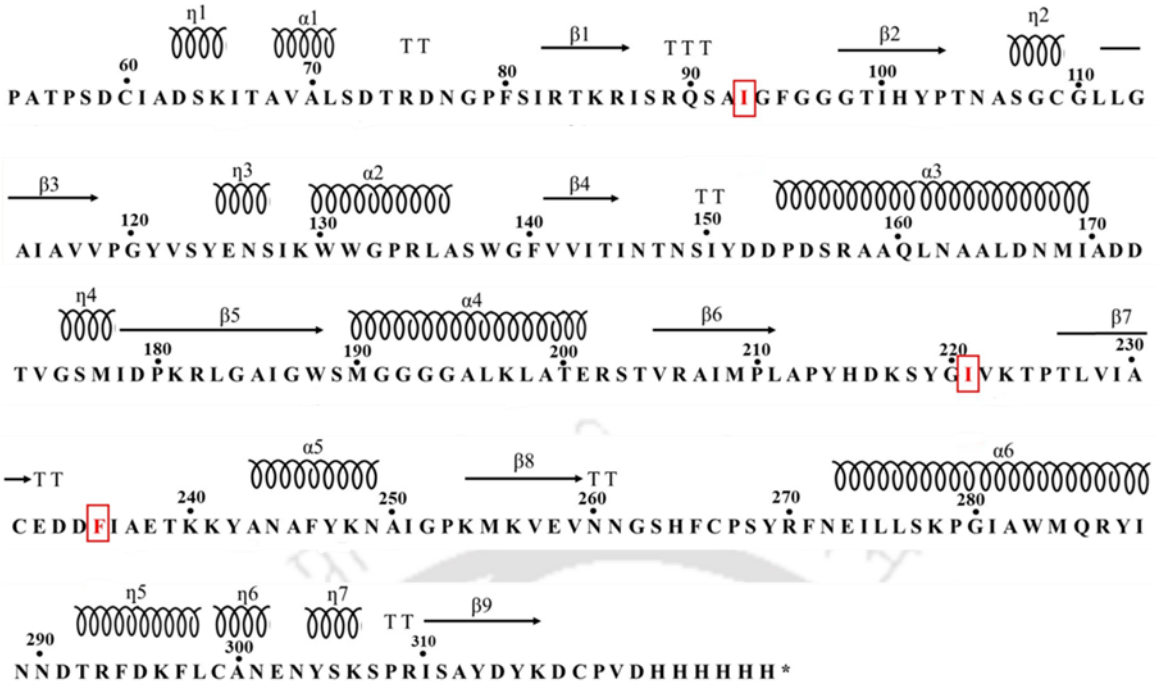

Fig 3. 1 Secondary structure of the Mors1 enzyme with induced mutations marked in red

3.2.4 Expression of recombinant Mors1$^{WT/MUT}$ in *P. pastoris*

The Mors1$^{WT/MUT}$ plasmid was extracted from an *E. coli* DH5α clone and digested with PmeI. The linearized pPICZαA-Mors1$^{WT/MUT}$ vector was transformed into *P. pastoris* by electroporation according to the Invitrogen EasySelect™ Pichia expression kit user manual [90]. To select transformants, electroporated *P. pastoris* was inoculated on YPD agar plates supplemented with 100–300 µg/mL Zeocin. After three days of incubation at 30°C, the colonies were thermally lysed, and colony PCR was performed via the primers listed in the (Table 3.1). The genomic DNA of the transformed *P. pastoris* was isolated via a method adopted from [91] and sent for Sanger sequencing (GeneSpec Pvt. Ltd., Kerala, India). The presence of the pPICZαA-Mors1$^{WT/MUT}$ vector was sequence verified. The positive Mors1$^{WT/MUT}$ clones were inoculated in 50 mL of BMGY media and incubated at 30°C and 200 RPM. After 36 hours of incubation, the cells were centrifuged at 8000 × g for 6 minutes. The supernatant was discarded, and the pellet was resuspended in 800 mL of BMMY media. The media was carefully transferred to a sterile 2-L baffled flask and incubated at 30°C and 200 RPM for 96 hours. Then, 1% (vol/vol) methanol was added to the medium every 24 hours. After 96 hours of incubation, the cells were centrifuged at 8000 × g for 6 minutes, and the pellet was stored at -20°C until use. A 3.2 g cell pellet of both x-33 and transformed Mors1$^{WT/MUT}$ *Pichia pastoris* were resuspended in 50 mL of lysis buffer (Tris-50mM pH 7, Imidazole-10mM, NaCl-500mM, PMSF-1mM, Lyticase-40 U/ml) and incubated separately at 37°C for 15 minutes. The

lysis solution was sonicated at 33% amplitude (pulse 10 sec ON & 30 sec OFF) for 15 minutes at 4°C. The lysed cells were centrifuged at 8000 × g (4°C) for 10 min, and the supernatant was stored at 4°C for further purification. For comparative protein profile analysis, 25 µL of supernatant from x-33 and transformed Mors1$^{WT/MUT}$ *P. pastoris* strains were analyzed via 12% SDS–PAGE (Appendix B.6).

3.2.5 Purification and Western blotting of Mors1$^{WT/MUT}$

The Ni–NTA columns were equilibrated with 4 column volumes of equilibration buffer (50 mM Tris pH 7, 10 mM Imidazole, 500 mM NaCl). 50 mL of supernatant from Mors1$^{WT/MUT}$ *P. pastoris* was loaded into respective columns. The Ni-NTA columns were washed with 3 column volumes of wash buffer (50 mM Tris pH 7, 20 mM Imidazole, 500 mM NaCl). Recombinant Mors1$^{WT/MUT}$ were eluted with 2.5 mL of elution buffer (50mM Tris pH 7, 250mM Imidazole, 500mM NaCl). The proteins were then buffer exchanged and purified using SEC via a Sephacryl™ S-200 high-resolution column using degassed baseline buffer (50 mM Sodium Phosphate buffer, pH 7, 200 mM NaCl).

The enzymes Mors1$^{WT/MUT}$ separated via SDS–PAGE were transferred onto a nitrocellulose membrane (Bio-Rad) via precooled transfer buffer (48 mM Tris base, 39 mM Glycine, 20 % Methanol) and a semiwet transfer apparatus. The transfer unit was run at 320 mA for 45 mins. After the run, the membranes were removed via forceps, rinsed with deionized water, and incubated for 1 hour in membrane-blocking solution (5% non-fat milk in 1x phosphate-buffered saline with 0.1%Tween) at 4°C under agitation. The membranes were washed with PBST (137 mM NaCl, 2.7 mM KCl, 10 mM Na_2HPO_4, 1.8 mM KH_2PO_4 with 0.1%Tween), and primary A-His-Ab was mixed with 10 ml of PBST buffer at a ratio of 1:5000 and incubated overnight at 4°C under agitation. The membranes were washed with PBST for 10 min and incubated with 1x PBS (137 mM NaCl, 2.7 mM KCl, 10 mM Na_2HPO_4, 1.8 mM KH_2PO_4), 0.1% Tween-20 with 5% nonfat milk, and 5 µl of GAR-IgG-HRP-conjugated secondary antibody. The membranes were agitated at room temperature for 1 hour. The washed membranes were treated with 1 ml of Bio-Rad's Clarity™ Western ECL Substrate. The membranes were visualized with a Bio-Rad ChemiDoc system via Image Lab software.

3.2.6 Characterization and stability (pH and thermal) of Mors1$^{WT/MUT}$

The secondary structure of Mors1^{WT} and Mors1^{MUT} (0.2mg/mL protein in 50 mM Sodium Phosphate buffer, pH 8, 50 mM NaCl) was analyzed using a CD spectropolarimeter (Jasco J1500-150, Jasco Corp., Tokyo, Japan). Spectral data were collected over the wavelength range

of 190–260 nm at 25°C to evaluate the characteristic secondary structural elements of the proteins. The measurements were performed using a scan speed of 100 nm/min, a response time of 1–3 seconds, and a bandwidth of 1 nm to ensure high-resolution spectral acquisition. The recorded CD signals were converted to molar residue ellipticity and expressed in units of millidegrees (mdeg; deg·cm²·dmol⁻¹) for quantitative analysis. To improve accuracy, the spectral data from multiple scans were averaged before further interpretation. This approach allowed for the reliable assessment of structural differences between the wild-type and mutant enzyme forms. The data was analyzed using the CD data analysis tool BeStSel, which estimated the fraction of secondary structure in Mors1 $^{WT/MUT}$ [149].

The kinetic parameters, including the maximal reaction rate (V_{max}) and the Michaelis–Menten constant (K_M), were determined by measuring the initial reaction rates at 25°C under optimized reaction conditions (Tris buffer, pH 9, containing 200 mM NaCl). PCL nanoparticles, used as the substrate, were prepared at varying concentrations (3–30 µg/mL). The catalytic activity was assessed spectrophotometrically by monitoring the optical density at 600 nm over a ten-minute period following the initiation of the reaction with 8 µg/mL of either Mors1^{WT} or Mors1^{MUT}. The kinetic data were analyzed by directly fitting the Michaelis–Menten equation, ($V = \frac{Vmax[S]}{(Km+[S])}$), to the experimental measurements using a nonlinear least-squares fitting approach. The analysis was performed using OriginPro 2021 (version 9.8.0.200).

The pH stability of the enzyme was assessed using a range of buffers prepared at different pH values. Buffers from pH 3 to 8 were prepared using 50 mM McIlvaine's buffer, while pH 9 was prepared using 50 mM Tris. The stability test was performed in a clear-bottom 96-well plate (Corning, USA). For each pH condition, 200 µL of buffer (pH 3–9) containing 0.12 mg/mL PCL nanoparticles, 8 µg/mL of respective Mors1^{WT} or Mors1^{MUT} and 200 mM NaCl was pipetted into separate wells. The hydrolysis rate was monitored by measuring the decrease in OD_{600} over time using a microplate reader (Varioskan™ LUX, Thermo Scientific). To determine the optimal reaction temperature for PCL hydrolysis catalyzed by Mors1^{WT} and Mors1^{MUT}, initial hydrolysis rates were measured at temperatures ranging from 5°C to 50°C. The reactions were conducted in a buffer containing 50 mM Tris (pH 9), 200 mM NaCl, and 0.12 mg/mL PCL, with 8 µg/mL of the Mors1$^{WT/MUT}$ enzyme. The reaction progress was monitored every 5 seconds using microplate reader. Thermal inactivation (residual activity) studies were conducted by incubating purified enzymes at temperatures of 20-80 °C for up to 6 hours. Aliquots were withdrawn at predetermined time intervals, and the residual enzymatic

activity was measured under standardized assay conditions. In both the pH and thermal stability assays, a reference reaction conducted at 25°C in 50 mM Tris (pH 9) containing 200 mM NaCl, 0.12 mg/mL PCL, and 8 µg/mL of Mors1^{WT} or Mors1^{MUT} was used as a standard to define 100% activity. The reagent composition and experimental setup were selected based on previously reported findings on Mors1 activity [150].

3.2.7 Degradation of PET by Mors1$^{WT/MUT}$ and characterization of degraded products

Amorphous PET films (dimensions: 0.8 cm × 0.8 cm; weight: ~52 mg; thickness: 250 µm) were incubated in a reaction mixture containing 250 mM potassium phosphate buffer (pH 8.0), 200 mM NaCl, and 8 µg/mL of either Mors1^{WT} or Mors1^{MUT} at 25°C for 12 days with continuous shaking (90 RPM). After incubation, the PET films were retrieved, thoroughly washed with deionized water containing 20% ethanol to remove residual reaction components and dried at 40°C overnight. The dried films were weighed to determine gravimetric weight loss, which served as an indicator of enzymatic hydrolysis efficiency. The soluble hydrolysis products, present in the supernatants of 12 days reactions, were separated from the enzyme using 10,000 MWCO and concentrated using vacuum evaporator at 60 RPM at 25°C. The hydrolysis products were analyzed using ATR-FTIR spectroscopy. ATR-FTIR analysis was performed with a Shimadzu IRAffinity-1S spectrometer (Shimadzu Corp., Japan) equipped with a Quest ATR GS10801-B single-bounce diamond accessory (Specac Ltd., England). Spectral data were recorded in the wavenumber range of 400–4000 cm^{-1} with a resolution of 1 cm^{-1}, and three replicates were collected for each sample. The spectral data were processed using LabSolution IR software (Shimadzu) to identify the functional groups associated with degradation products in both control and enzymatically treated samples.

SEM was utilized to evaluate the morphological changes in PET film surfaces following 12 days of treatment with Mors1^{WT} and Mors1^{MUT}. The treated PET samples were sputter-coated with a thin layer of gold to improve the morphological and structural visualization of surface structures during imaging. SEM analysis was conducted using a Zeiss-Gemini microscope (Zeiss, Germany) under high-vacuum conditions to capture high-resolution images of the treated film surfaces. Images were recorded to assess the extent of surface degradation or alteration induced by enzymatic activity. Surface topography and nanoscale structural modifications of the treated PET films were further analyzed using an AFM, Cypher S (Asylum Research, Oxford Instruments, Santa Barbara, CA, USA). Samples were mounted securely onto the AFM sample holder using double-sided carbon adhesive tape. The scanning was

performed in non-contact mode under ambient laboratory conditions to minimize sample deformation and ensure high-resolution imaging of the film surface. AFM measurements provided quantitative data on surface roughness and textural changes induced by enzymatic hydrolysis.

3.2. 8 Statistical analysis

All measurements were performed in triplicate. The data are reported as the means ± standard deviations, and a t test or ANOVA was used to find significant differences among the means. The 5% level ($p \leq 0.05$) was used as a significance criterion unless explicitly stated in a particular section.

3.3 Results and discussion

3.3.1 Cloning, expression, purification and functional validation of Mors1$^{WT/MUT}$

The generation of Mors1^{MUT} involved assembling four amplified fragments (73 bp, 280 bp, 309 bp, and 403 bp; Fig 3.3, L1-L4) via Gibson assembly. The expected sizes of these fragments aligned with the primer design and mutation sites, indicating precise amplification and successful introduction of codon mutations. The Mors1^{WT} gene was amplified as a 990 bp fragment (Fig 3.3, L5), consistent with its expected size. Fig 3.2 illustrates the pPICZαA vector construct containing the Mors1$^{WT/MUT}$ gene along with its essential regulatory elements.

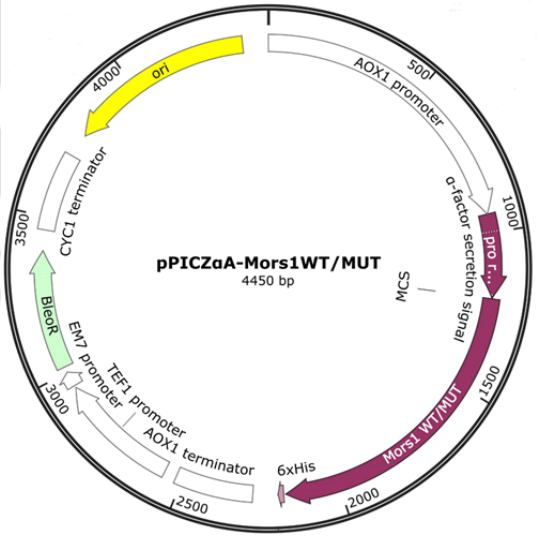

Fig 3. 2 Vector construct showing the Mors1$^{WT/MUT}$ gene with vital components of the pPICZαA vector

Restriction digestion of the pPICZαA vector with EcoRI and SalI yielded a linearized backbone of 3,481 bp (Fig 3.3, L6). The assembly of the Mors1$^{WT/MUT}$ constructs into the vector was validated by single digestion, producing a band corresponding to the size of the recombinant

vector at 4,450 bp (Fig 3.3, L7-8). Colony PCR further confirmed the presence of the Mors1$^{WT/MUT}$ genes in transformed *E. coli* clones (Fig 3.3, L9-10). Sanger sequencing confirmed the homologous recombination-based insertion of Mors1$^{WT/MUT}$ gene in transformed *P. pastoris*.

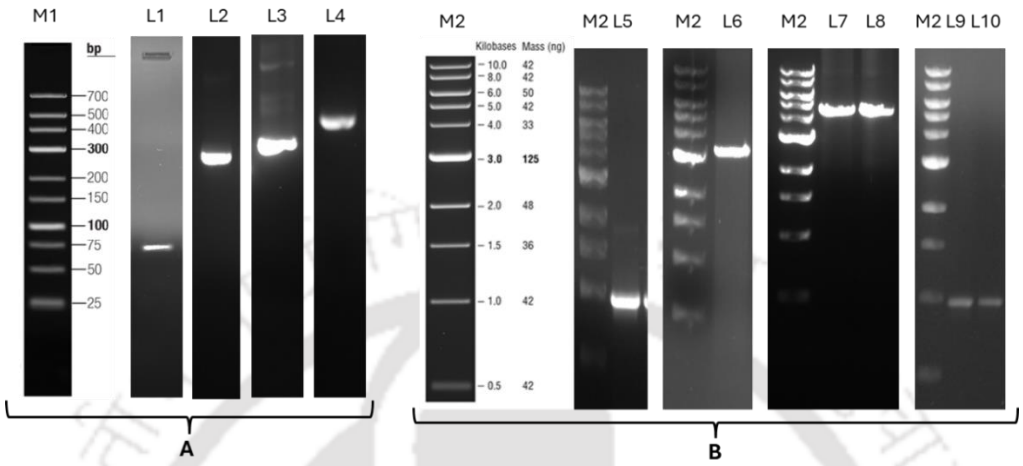

Fig 3. 3 PCR and restriction digestion products for cloning of Mors1$^{WT/MUT}$

(A) PCR amplified fragments for Mors1MUT assembly, M1: Reference LR DNA maker, L1: fragment1 73bp, L2: fragment2 280bp, L3: fragment4 309bp, L4: fragment 4 403bp; (B) Mors1WT gene, vector backbone and validation, M2: Reference 1kb marker, L5: Mors1WT gene after PCR amplification 990bp, L6: pPICZαA vector after digestion with EcoRI & SalI 3,481 bp, L7-8: pPICZαA- Mors1WT/MUT plasmid after single digestion 4450bp, L9-10: colony PCR showing presence of Mors1WT/MUT gene

SDS-PAGE analysis demonstrated distinct protein expression profiles between wild-type *P. pastoris* and recombinant strains expressing Mors1^{WT} and Mors1^{MUT} (Fig 3.4, L11-13). The recombinant strains showed the presence of the target proteins. Ni-affinity chromatography provided partially purified protein (Fig 3.4, L14-L15), while SEC yielded highly purified fractions (~35 kDa) for both constructs (Fig 3.4, L16-L17). Western blotting (Fig 3.4, L18-L19) confirmed the expression of the 6x-His-tagged recombinant enzymes, as indicated by clear ~35 kDa bands corresponding to Mors1^{WT} and Mors1^{MUT}. Overlapping SEC elution profiles were observed for Mors1^{WT} and Mors1^{MUT} (Fig 3.4 C), indicating that both the enzymes maintained similar structural integrity and folding patterns.

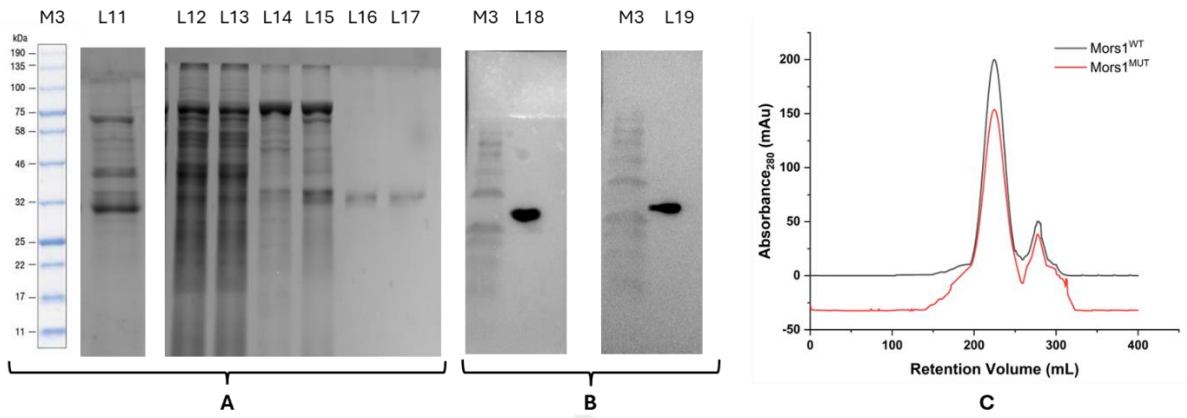

Fig 3. 4 Enzyme expression and validation of Mors1$^{WT/MUT}$

(A) Mors1$^{WT/MUT}$ enzyme expression and purification, M3: reference protein marker, L11: intracellular protein fraction of wild-type *P. pastoris,* L12-13: intracellular protein fraction of recombinant *P. pastoris* Mors1$^{WT/MUT}$ respectively, L14-15: Ni-affinity chromatography-purified Mors1$^{WT/MUT}$ respectively, L16-17: SEC purified Mors1$^{WT/MUT}$ (~35kDa) respectively; (E) Western blotting, L18: Mors1^{WT}, L19: Mors1^{MUT}; (F) SEC profile of Mors1$^{WT/MUT}$

3.3.2 Comparative analysis of Mors1$^{WT/MUT}$ secondary structure

The secondary structure of Mors1 (PDB: 8SPK; UniProt: P19833) was analyzed using CD spectroscopy to evaluate potential structural differences between the Mors1^{WT} and Mors1^{MUT} forms. Spectral data processed via BeStSel provided quantitative insights into the fractions of key secondary structural elements. Mors1^{WT} exhibited secondary structure composition with 18.2% α-helix, 16% β-strand, 16.5% turns, and 39.1% other structural elements. In comparison, the mutant variant, Mors1^{MUT}, displayed 19.7% α-helix, 14% β-strand, 15.8% turns, and 38% other secondary structures. These values suggest that the mutation induced very minute changes in secondary structure, particularly in the β-strand content, which decreased slightly in the mutant form. The CD spectra of Mors1^{WT} and Mors1^{MUT} (Fig 3.5) showed significant overlap, indicating a high degree of structural similarity between the two protein variants. This observation aligns with the quantitative analysis, where only minor deviations were detected in the secondary structure composition. The predominance of the α-helix and β-strand fractions is consistent with the typical secondary structure reported for the native Mors1 protein, which comprises approximately 19.8% α-helix, 23.8% β-strand, 16.3% turns, and 40.1% other elements [151]. The structural integrity of Mors1^{MUT} appears largely conserved despite the mutation, as evidenced by both spectral overlap and BeStSel-derived secondary structure fractions. This finding suggests that the mutation may not significantly impact the global fold of the protein.

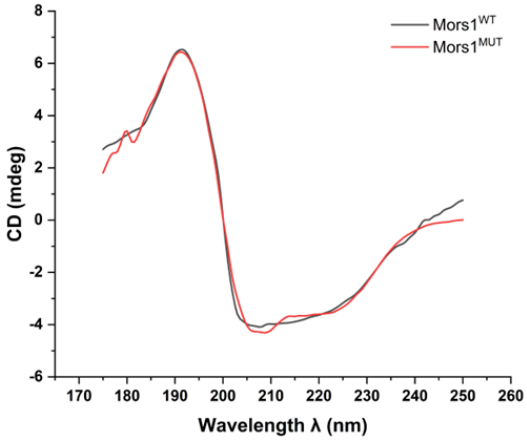

Fig 3. 5 CD spectra of Mors1$^{WT/MUT}$ in sodium phosphate buffer, pH 8 at 25 °C

The overlaid CD spectra of Mors1WT and Mors1^{MUT} indicate nearly identical secondary structures, suggesting that the mutation did not significantly disrupt the overall protein fold.

3.3.3 Comparative analysis of Mors1$^{WT/MUT}$ catalytic kinetics

The kinetic parameters for the enzymatic transformation of PCL nanoparticles by Mors1^{WT} and Mors1^{MUT} were determined using Michaelis-Menten kinetics. The wild-type enzyme exhibited V_{max} of 21.26 ± 0.61 µg mL^{-1} min^{-1} and a K_M of 6.74 ± 0.73 µg mL^{-1}, with an r² of 0.9822 and an adjusted r² of 0.9800 (Fig 36 A). In contrast, the mutant enzyme demonstrated a higher V_{max} of 30.77 ± 0.56 µg mL^{-1} and a lower K_M of 5.52 ± 0.38 µg mL^{-1}, with an r² of 0.9889 and an adjusted r² of 0.9875 (Fig 3.6 B). The observed differences in kinetic parameters between Mors1^{WT} and Mors1^{MUT} underscore the impact of the mutation on catalytic properties of the enzyme. The higher V_{max} of Mors1^{MUT} indicates an improved capacity to catalyze the substrate under saturated conditions, while the lower K_M reflects a greater substrate affinity. The enhanced performance of Mors1^{MUT} could be attributed to mutational changes that facilitate substrate binding and product release, leading to higher catalytic efficiency. These findings align with previous studies that reported improved enzymatic activity through targeted mutations, emphasizing the potential of rational enzyme engineering for optimizing biocatalysts [152,153].

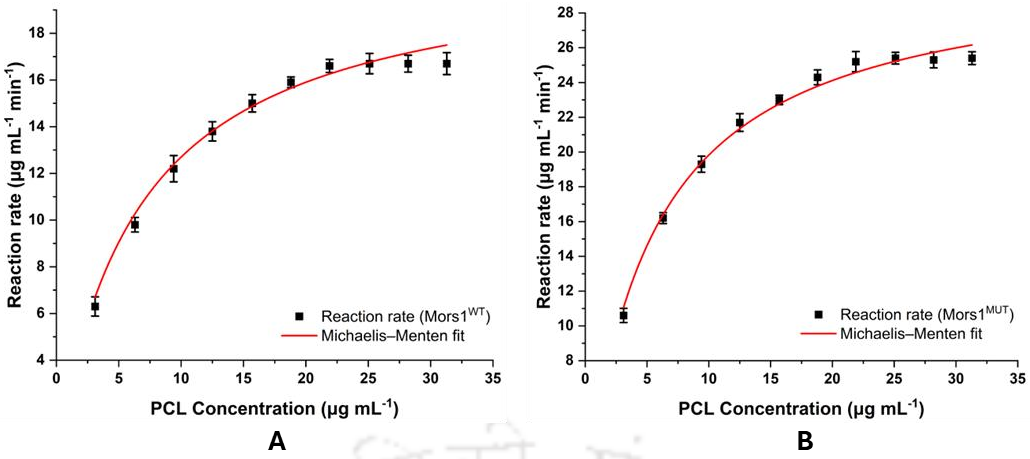

Fig 3. 6 Kinetic analysis of PCL nanoparticle transformation by Mors1$^{WT/MUT}$

(•) Symbols represent experimental reaction rates, and continuous lines are fitted using the Michaelis-Menten equation ($V = \frac{Vmax[S]}{(Km+[S])}$). Optimized parameters: V_{max} (Mors1^{WT}: 21.26±0.61 μg mL^{-1} min^{-1}; Mors1^{MUT}: 30.77±0.56 μg mL^{-1} min^{-1}) and K_M (Mors1^{WT}: 6.74±0.73 μg mL^{-1}; Mors1^{MUT}: 5.52±0.38 μg mL^{-1})

3.3.4 Comparative analysis of Mors1$^{WT/MUT}$ pH stability

The pH stability of the enzyme was evaluated across a range of pH conditions (3–9) using the hydrolysis rate as a measure of activity (Fig 3.7). The activity of both Mors1^{WT} and Mors1^{MUT} was observed to increase with pH, achieving peak performance at pH 8 and 9. Specifically, Mors1^{WT} exhibited its highest activity at pH 9, with 93% relative activity (±2.31), while Mors1^{MUT} demonstrated even greater stability, reaching 98% relative activity (±1.55) under the same conditions. At lower pH values (pH 3–5), Mors1^{MUT} consistently outperformed Mors1^{WT}. For instance, at pH 3, Mors1^{MUT} retained 8% activity (±1.5) compared to only 4% (±1.8) for Mors1^{WT}. Similarly, at pH 5, Mors1^{MUT} exhibited 68% activity (±2.41), significantly higher than the 58% (±2.51) observed for Mors1^{WT}. This trend suggests that the mutation conferred improved stability under acidic conditions. Between pH 6 and 8, both enzymes demonstrated robust activity, with Mors1^{MUT} maintaining consistently higher activity levels. At pH 8, Mors1^{MUT} achieved 95% activity (±2.11), compared to 90% (±1.81) for Mors1^{WT}. These results indicate that while both enzymes exhibit optimal stability in neutral to slightly alkaline conditions, Mors1^{MUT} has superior tolerance across the tested pH spectrum. The findings highlight the potential of Mors1^{MUT} for applications requiring enzyme functionality in diverse pH environments. The improved stability of Mors1^{MUT} under both acidic and alkaline conditions suggested mutational modifications that enhanced resilience to pH-induced denaturation.

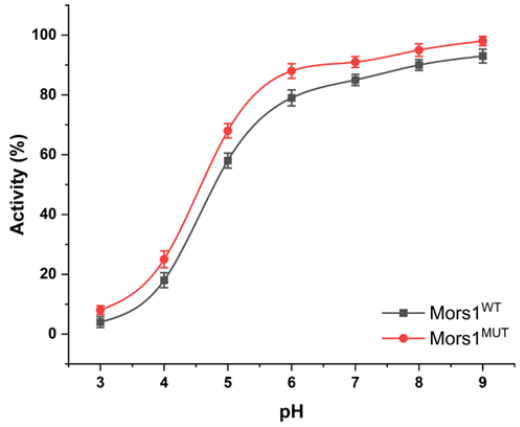

Fig 3. 7 Effect of pH on Mors1$^{WT/MUT}$ activity

This pH profile reveals that while both enzymes perform best at alkaline conditions, Mors1^{MUT} maintains higher activity across a broader pH range, particularly in acidic environments

3.3.5 Comparative analysis of Mors1$^{WT/MUT}$ thermal stability

The effect of temperature on the catalytic activity of Mors1^{WT} and Mors1^{MUT} for PCL hydrolysis was evaluated across a temperature range of 5-50°C (Fig 3.8). Both enzymes exhibited a bell-shaped activity profile, with optimal performance at 25°C. The observed optimal activity of the wild-type enzyme was consistent with previously reported findings [154]. At this temperature, Mors1^{WT} achieved 97% relative activity (±1.5), while Mors1^{MUT} showed higher activity, reaching 99% (±0.53). At lower temperatures (5–20°C), Mors1^{MUT} consistently demonstrated marginally higher activity compared to Mors1^{WT}. For instance, at 5°C, Mors1^{MUT} retained 75% activity (±2.17) compared to 74% (±1.21) for Mors1^{WT}, and at 20°C, Mors1^{MUT} achieved 96% activity (±2.61) versus 93% (±1.43) for Mors1^{WT}. This trend suggests that the mutation conferred a modest enhancement in catalytic efficiency at sub-optimal temperatures. Beyond the optimal temperature of 25°C, both enzymes displayed a gradual decline in activity. At 30°C, Mors1^{WT} retained 89% activity (±2.41) compared to 91% (±1.87) for Mors1^{MUT}, while at 35°C, the decline was more pronounced, with Mors1^{WT} showing 78% activity (±2.11) and Mors1^{MUT} retaining 86% (±1.92). At higher temperatures, the activity of both enzymes decreased sharply. At 40°C, Mors1^{WT} retained only 40% activity (±1.8) compared to 61% (±2.38) for Mors1^{MUT}, highlighting the latter's superior thermal stability. At 45°C, Mors1^{WT} retained merely 4% activity (±1.81), while Mors1^{MUT} showed 35% activity (±2.11). By 50°C, the activity of Mors1^{WT} was negligible (0%), whereas Mors1^{MUT} retained 14% activity (±1.89). These findings highlight the improved thermal stability of Mors1^{MUT} over Mors1^{WT}, particularly at elevated temperatures, likely due to structural modifications that enhance its resistance to thermal denaturation. Although both enzymes

exhibited optimal performance at 25°C, the enhanced temperature tolerance of Mors1^{MUT} makes it particularly well-suited for industrial applications. Enzymes with such versatility are preferred due to their ability to maintain stability and functionality under varying process conditions. [155].

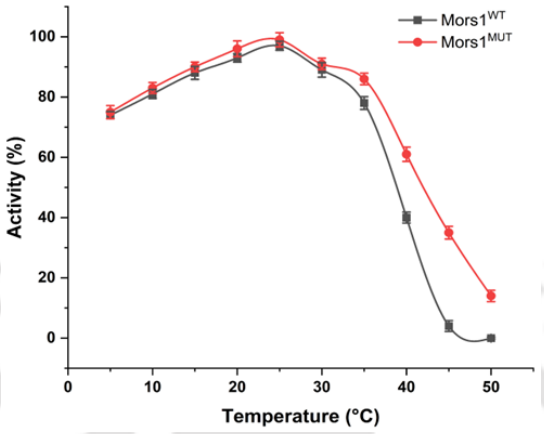

Fig 3. 8 Effect of temperature on Mors1$^{WT/MUT}$ activity

Both enzymes display peak catalytic activity at 25°C, but Mors1^{MUT} consistently shows slightly enhanced activity at suboptimal temperatures, indicating better cold-adaptation

The thermal inactivation profiles of Mors1^{WT} and Mors1^{MUT} were evaluated by measuring residual activity after incubation at various temperatures (20–80°C) for up to 6 hours (Fig 3.9). Both enzymes exhibited high thermal stability at lower temperatures (20-30°C) but showed significant differences in stability as the temperature increased beyond 40°C. At 20°C, Mors1^{WT} retained 98% residual activity (±1.8), while Mors1^{MUT} retained 97% (±1.5). Similarly, at 30°C, both enzymes demonstrated excellent thermal stability, with Mors1^{MUT} showing slightly higher residual activity (99% ± 0.5) compared to Mors1^{WT} (97% ± 1.5). However, at 40°C, Mors1^{WT} retained only 75% residual activity (±2.13), whereas Mors1^{MUT} displayed enhanced stability, maintaining 80% activity (±2.31). The disparity between the enzymes became more pronounced at higher temperatures. At 50°C, Mors1^{WT} was completely inactivated, showing 0% residual activity, whereas Mors1^{MUT} retained 26% residual activity (±2.17). Both enzymes were entirely inactivated at 60°C and above, with no measurable residual activity at 60°C, 70°C, or 80°C. These findings highlight the superior thermal resilience of Mors1^{MUT} compared to Mors1^{WT}, particularly at moderately elevated temperatures (40°C–50°C). The enhanced stability of Mors1^{MUT} suggests potential amino acid replacements that confer resistance to thermal denaturation, making it a more suitable option for industrial applications requiring stability under fluctuating or moderately elevated temperatures.

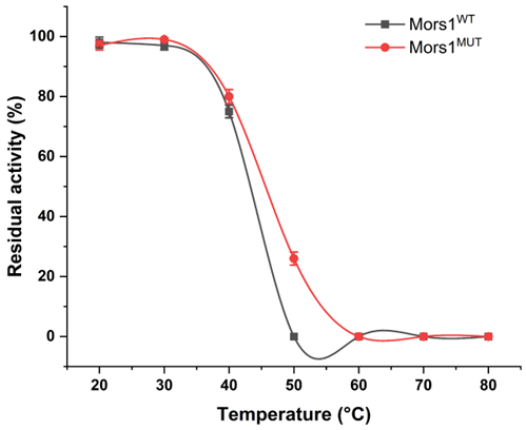

Fig 3. 9 Residual thermal stability of Mors1$^{WT/MUT}$ across 20-80°C

Residual activity trends show that Mors1^{MUT} is notably more heat-resistant than Mors1^{WT}, especially at moderately high temperatures (40–50°C), hinting at improved structural stability

3.3.6 Surface characterization of Mors1$^{WT/MUT}$ treated PET film via SEM and AFM

SEM micrographs (Fig 3.10 A-C) revealed distinct surface morphologies among untreated (control) and treated PET films. The control PET film (Fig 3.10 A) exhibited a relatively smooth surface with minimal irregularities, indicative of a lack of enzymatic activity. In contrast, the surface of the PET film treated with Mors1^{WT} (Fig 3.10 B) displayed notable grooves and pits, reflecting moderate enzymatic degradation. These features suggest partial hydrolysis of the polymer, resulting in localized surface erosion. Furthermore, the PET film treated with Mors1^{MUT} (Fig 3.10 C) exhibited even more pronounced surface roughness, characterized by deeper and more widespread grooves and pits compared to the wild-type enzyme treatment. These observations indicate that the mutant variant possessed enhanced enzymatic activity, leading to a greater degree of surface degradation.

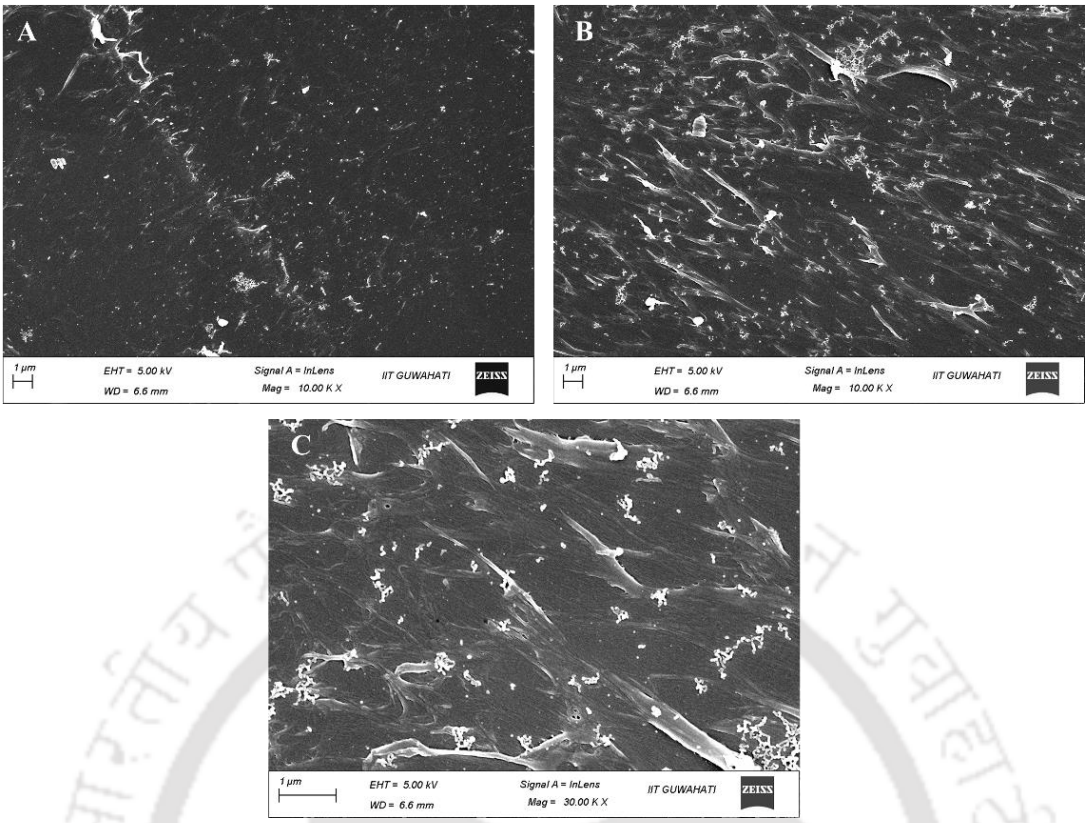

Fig 3. 10 SEM micrographs of treated and untreated PET films showing surface morphology

(A) control PET film, (B) PET film treated with Mors1^{WT}, and (C) PET film treated with Mors1^{MUT}

AFM imaging provided quantitative data on surface topography and roughness, supplementing the qualitative insights from SEM. The control PET film (Fig 3.11 A, D) displayed a smooth surface with minimal roughness, as confirmed by its RMS roughness of 2.80 nm and roughness average of 2.16 nm. Other parameters, including peak-to-peak height (31.14 nm) and surface skewness (0.68), further validated the uniform and unaltered surface texture. The PET film treated with Mors1^{WT} (Fig 3.11 B, E) demonstrated an increase in surface roughness, with an RMS roughness of 4.82 nm and a roughness average of 3.43 nm. The peak-to-peak height increased to 68.34 nm, and surface skewness (1.13) indicated the presence of asymmetrical surface features such as grooves and pits. These changes are consistent with partial hydrolytic degradation induced by the wild-type enzyme. The PET film treated with Mors1^{MUT} (Fig 3.11 C, F) exhibited the highest surface roughness among the samples, with an RMS roughness of 7.87 nm and a roughness average of 4.50 nm. The peak-to-peak height reached 134.63 nm, while the surface skewness value (3.86) and surface kurtosis (33.76) highlighted the presence of deep, sharp features. These data confirm that Mors1^{MUT} significantly enhanced enzymatic hydrolysis, resulting in substantial surface erosion and nanoscale structural modifications.

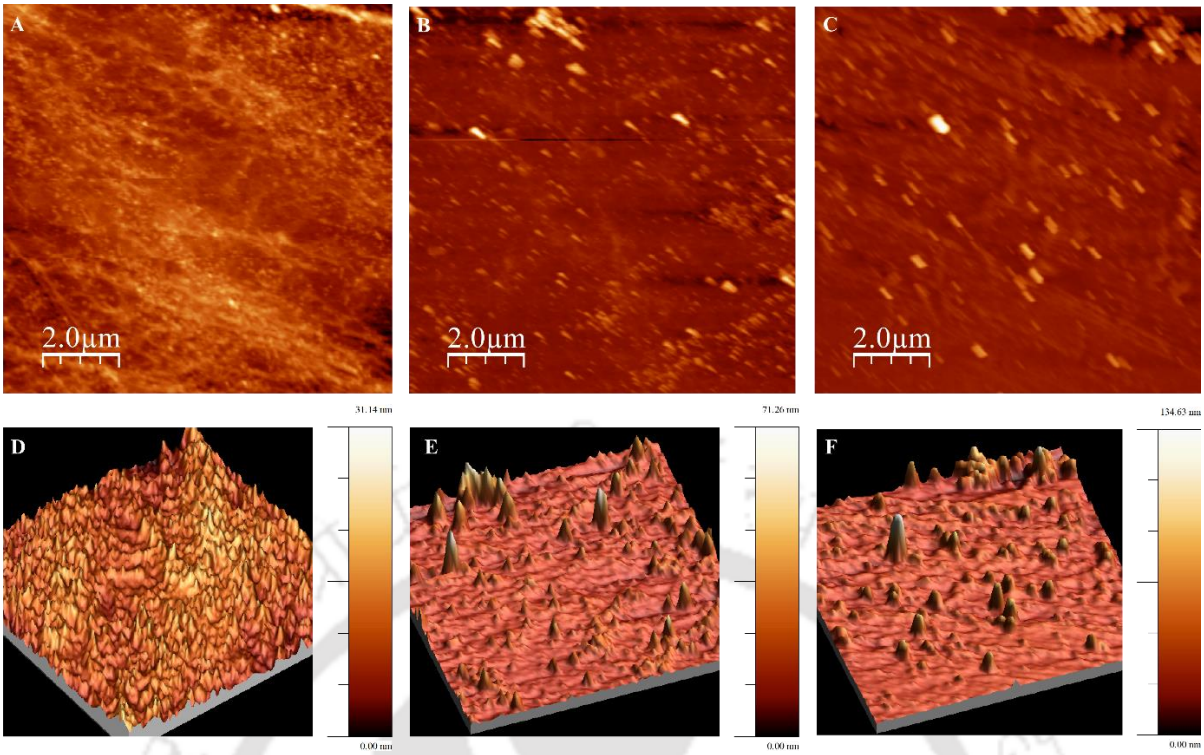

Fig 3. 11 AFM micrographs of treated and untreated PET films showing surface roughness

2D and 3D AFM images of (A, D) control PET film, (B, E) PET film treated with Mors1^{WT}, and (C, F) PET film treated with Mors1^{MUT}, respectively.

3.3.7 Hydrolysis product analysis of Mors1$^{WT/MUT}$ treated PET films

The enzymatic hydrolysis of PET films was evaluated using both the wild-type and mutant enzymes. The gravimetric analysis revealed weight losses of 0.83% for Mors1^{WT} and 3.46% for Mors1^{MUT} after a 12-day incubation period. This data suggests that the Mors1^{MUT} enzyme exhibited a 4.16-fold increase in hydrolysis efficiency compared to the wild-type enzyme, demonstrating the enhanced catalytic activity of the mutant variant. The extended hydrolysis reaction over 12 days corroborated the higher efficiency of Mors1^{MUT}, resulting in increased production of soluble degradation products. The ATR-FTIR spectra of untreated PET films (Fig 3.12) exhibited characteristic peaks at 2918 cm^{-1} (C-H stretching in the methylene group), 1713 cm^{-1} (C=O stretching in ester groups), 1407 cm^{-1} (C-H bending), 1243 cm^{-1} (C-O stretching in ester groups), 1095 cm^{-1} (C-O stretching), 1016 cm^{-1} (aromatic C-H in-plane bending), 872 cm^{-1} (C-H out-of-plane bending in benzene rings), 724 cm^{-1} (C-H deformation), and 493 cm^{-1} (aromatic ring vibrations). These findings align with previously reported spectral data, confirming the structural integrity of untreated PET [156]. The ATR-FTIR spectra of the hydrolysis products from both Mors1^{WT} and Mors1^{MUT} enzymes (Figure 5) displayed distinct peaks at 3290 cm^{-1} (O-H stretching in carboxylic acids), 1850 cm^{-1} (aromatic overtones), 1714

cm^{-1} (C=O stretching in carboxylic acids), 1638 cm^{-1} (C=C stretching in aromatic rings), 1408 cm^{-1} (C-H bending), 1339 cm^{-1} (O-H bending in phenolic groups), 1239 cm^{-1} (C-O stretching in esters), 1087 cm^{-1} (C-O stretching), 1017 cm^{-1} (aromatic C-H in-plane bending), and 722 cm^{-1} (C-H deformation in aromatic rings). These peaks confirmed the presence of TPA and MHET/BHET a major product of PET depolymerization [150]. Specifically, the peak at 1714 cm^{-1} corroborated the formation of TPA, while the peaks at 1239 cm^{-1} and 1087 cm^{-1} corresponded to MHET/BHET. The intense O-H stretching observed at 3290 cm^{-1} provided additional evidence of the accumulation of carboxylic acids during hydrolysis. The gravimetric weight loss and ATR-FTIR analysis clearly demonstrated that Mors1^{MUT} had a significantly enhanced capacity for PET hydrolysis compared to the wild-type enzyme. The ability of Mors1^{MUT} to cleave PET more efficiently likely stemmed from the integration of hydrophobic amino acids, which improved substrate binding or catalytic turnover. The production of TPA and MHET/BHET as hydrolysis products aligned with the enzymatic depolymerization pathways of PET, confirming the specificity and effectiveness of the enzymes.

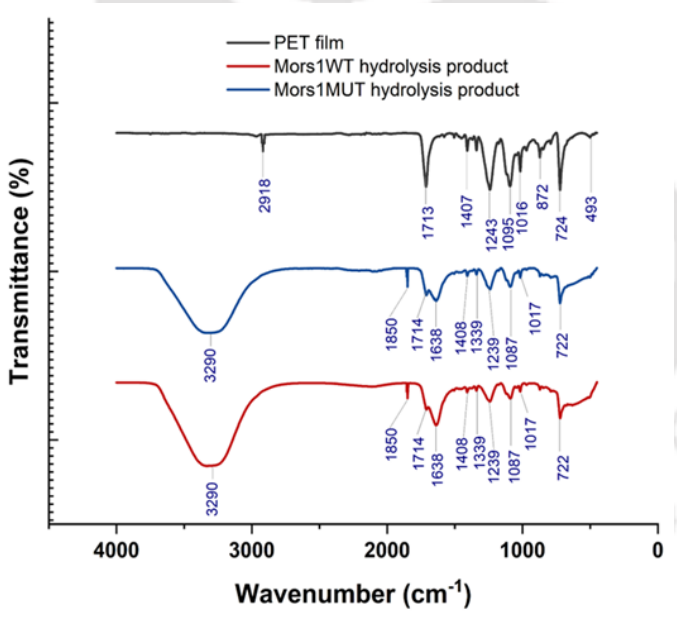

Fig 3. 12 FTIR spectra of PET and its hydrolysis products by Mors1^{WT} and Mors1^{MUT}, respectively.

3.4 Techno-economic analysis of using Mors1^{MUT} for PET degradation

The use of *P. pastoris* as the host for Mors1 expression can offers a highly economical and scalable solution for producing recombinant enzymes. Its ability to secrete enzymes extracellularly (intracellular enzyme was used in this study) can simplify downstream purification processes, reducing overall costs and enabling large-scale industrial applications [130]. The engineered Mors1^{MUT} enzyme further enhances economic viability by exhibiting

improved thermal stability and catalytic efficiency, which are critical for sustained enzymatic PET hydrolysis under diverse operational conditions. The production of Mors1^{MUT} in *P. pastoris* using cost-effective media and scalable fermentation systems underscores its practicality for industrial adoption. The enhanced stability and activity of Mors1MUT at moderate temperatures, particularly its capacity to function efficiently at ambient conditions, significantly lower energy demands compared to thermophilic PETases requiring higher temperatures. This energy efficiency aligns with the goals of sustainable industrial processes, making the enzyme suitable for energy-conscious industries. Additionally, the improved catalytic performance of Mors1^{MUT}, which achieved a 4.16-fold enhancement in PET degradation compared to the wild type, translates into reduced enzyme load requirements and lower operational costs for industrial-scale biodegradation. The integration of rational protein engineering with scalable enzyme production in *P. pastoris* addresses critical bottlenecks of conventional chemical recycling, such as high energy costs and limited economic feasibility. By leveraging these advantages, the engineered Mors1^{MUT} enzyme provides a compelling framework for biological PET recycling, aligning cost-effectiveness with environmental sustainability for tackling the growing challenge of plastic pollution.

3.5 Conclusion

Plastic pollution has emerged as a critical environmental issue, PET contributing significantly due to its widespread use and persistence in ecosystems. Despite its utility in industries such as packaging and textiles, PET's resistance to natural degradation exacerbates environmental harm, particularly in aquatic ecosystems. Current recycling methods, including thermo-mechanical and chemical approaches, face challenges such as energy inefficiency, high costs, and limited scalability. These limitations underscore the urgent need for alternative strategies to manage PET waste sustainably. Biodegradation, leveraging PET hydrolases for enzymatic degradation, has shown promise as a more sustainable solution. However, many naturally occurring PETases require high temperatures for optimal activity, which increases energy demand. While some PETases have demonstrated moderate-temperature activity, they often lack the thermal stability or catalytic efficiency required for practical applications. This gap highlights the need for engineered enzymes that combine high activity, stability, and compatibility with energy-efficient processes. This study focused on engineering Mors1, a PETase derived from the Antarctic bacterium *Moraxella* TA144, to enhance its thermal stability and activity. Using DDMut server, three strategic hydrophobic amino acid substitutions (K93I, E221I, and R235F) were introduced into near-turn regions of the enzyme. The modified

enzyme, Mors1^{MUT}, was systematically analyzed and compared to the wild-type enzyme (Mors1^{WT}). Experimental evaluations included secondary structure analysis, enzyme kinetics, pH and thermal stability assessments, and the hydrolysis efficiency of PET films. The mutant variant exhibited broader pH and temperature tolerance compared to the wild-type enzyme, demonstrating enhanced stability and activity across diverse conditions. Gravimetric weight loss and ATR-FTIR analyses confirmed the enhanced PET degradation capacity of Mors1^{MUT}, with a 4.16-fold improvement in efficiency compared to Mors1^{WT}. This study demonstrated the potential of protein engineering to overcome the limitations of natural PET hydrolases, offering a sustainable pathway for managing plastic pollution. By enhancing the catalytic efficiency and stability of enzymes like Mors1, biological recycling could become a practical and eco-friendly solution to one of the most pressing environmental challenges of our time.

Chapter 4. Development of an energy-efficient water distillation unit using Piezoelectric and Peltier technologies

Abstract

The rapid urbanization, industrialization, and agricultural expansion have significantly deteriorated water quality, challenging municipalities' ability to provide safe drinking water. Municipal treatment facilities are often limited in addressing contaminants introduced through aging infrastructure and distribution systems, resulting in public distrust and increased reliance on household water purification systems. Conventional techniques, such as RO and distillation, although effective, present challenges related to energy consumption and waste generation. In this study, we developed an energy-efficient, distillation-based water purification system integrating piezoelectric ultrasonic mist technology, thermoelectric Peltier modules, and UV-C sterilization. The system was designed using biodegradable PLA materials and evaluated for its capacity to remove dissolved salts, microbial contaminants, dyes, and VOCs. The system achieved 83% water recovery efficiency under optimal conditions and demonstrated high efficacy in removing NaCl (up to 490 mg/L), E. coli (1.5×10^8 CFU/mL), Congo red dye (up to 50 mg/L), and VOCs (toluene and o-xylene at 60 µL/L). This innovative approach effectively addresses the limitations of traditional water purification methods by reducing energy consumption while enhancing contaminant removal, offering a sustainable alternative for domestic water purification.

4.1 Background

The rapid expansion of industrial activities, agriculture, and urban settlements has led to considerable environmental transformations, particularly in water resources. Anthropogenic disturbances, such as chemical runoffs, untreated sewage, and other pollutants from these activities, significantly impact both surface and groundwater quality [157]. With over half of the world's population now residing in urban areas, the demand for potable water has surged, placing pressure on municipalities to deliver clean water reliably and efficiently. To cope with these challenges, municipalities have implemented water treatment protocols aimed at meeting baseline safety standards. These processes typically include sedimentation, filtration, and disinfection to remove suspended solids, pathogens, and a limited range of chemical contaminants [158].

However, municipal water treatment is often designed to meet basic regulatory requirements rather than addressing the full spectrum of contaminants present due to industrial and agricultural activities. Municipalities face the additional challenge of delivering water through aging infrastructure, which can introduce contaminants in-route to consumers [159]. For instance, lead and other metals can leach from old pipes, or microbial growth can occur if biofilm accumulates in distribution systems. Despite initial water treatment, these distribution system-related issues may compromise water quality by the time it reaches households. A critical oversight in many municipal water systems is the lack of quality assurance at the point of consumption. Municipalities generally monitor and regulate water quality at the treatment facility or immediately upon release into the distribution network but testing at the household level is often minimal or absent [160]. As a result, consumers may receive water that, while meeting regulatory standards at the source, does not meet these standards at the tap due to contamination introduced during transit. This inconsistency has led to a lack of public trust, with many individuals doubting the safety of municipal water for direct consumption [161].

In response to this uncertainty, there has been an increased reliance on domestic water purification systems. In countries where water infrastructure may be less developed, or regulations less stringent, households with these purification systems report higher satisfaction and confidence in water quality, underscoring the role of domestic purification as a response to perceived inadequacies in public water systems [162,163]. Common household water purification techniques include ceramic candle filters, activated charcoal, ultrafiltration, UV disinfection, reverse osmosis, and distillation, all of which are covered in detail in Chapter 1.

Among these, RO and distillation are the most powerful solutions, capable of removing most pollutants, but they also have some limitations. RO systems generate a large amount of wastewater and have lower recovery rates than the other methods mentioned. Additionally, RO requires specific water pressure for installation, electricity, regular maintenance, and servicing by a qualified technician. Distillation, on the other hand, is a highly energy-intensive process, and the removal of VOCs remains a challenge [164,165].

This study involves designing an energy-efficient distillation-based water purification system using a piezoelectric ultrasonic mist maker and a Peltier system. The system was constructed with biodegradable PLA material and validated under specific ambient conditions for the effective removal of dyes, dissolved salts, microbes, and VOCs. This device addresses the primary limitations of conventional water distillation units by utilizing a less energy-intensive process and effectively removing VOCs from water.

4.2 Materials and methods

4.2.1 Materials

Ultrasonic piezoelectric transducer module and thermoelectric Peltier was procured from Xcluma, China. UV-C led strip was purchased from PPX-max, India. Motor speed regulator was procured from Robodo, India. All 3D printing was conducted using 1.75 mm PLA filament on a WOL3D Ender 3 printer (Shenzhen Creality 3D Technology Co., Ltd, China). *E. coli* 1302 was procured from MTCC Chandigarh, India. Congo red (Sodium salt of benzidinediazo-bis-1-naphthyl-amine-4-sulfonic acid; molecular weight 696.66 g/mol; $C_{32}H_{22}N_6Na_2O_6S_2$) was procured from HiMedia, Bangalore. Toluene and o-xylene were purchased from (Merk Co., Germany). The schematic illustration of all components used in this work is presented in (Fig. 4.1). All remaining accessories and components used in this research were of industrial grade, while all other reagents and chemicals were of analytical grade. (Table 4.1) delineates workable ranges for all the parameters involved in this work.

Table 4. 1 Range for all dimensions, input and output parameters involved in this development

Parameter/Component	Workable Range/Specification	Remarks
Ultrasonic Piezoelectric Transducer	Frequency: 108–110 kHz	Generates mist for evaporation.
	Voltage: 5V, Current: 300 mA	Converts electrical energy to sound waves.
	Power: 2W, Temperature: 0–85°C	Operates efficiently within this temperature range.
	Humidity: 10%–90%	Suitable for varying ambient conditions.
Peltier Module	Input Voltage: 12V DC	Thermoelectric cooling and heating.
	Operating Temperature Range: -10°C to 65°C	Ensures effective phase changes.
	Power Consumption: 60 Watts	Measured under ambient conditions.
Circulating Fan	Speed: 250-2500 RPM (250 RPM fixed for testing)	Ensures consistent airflow in the system.
Fan Speed Regulator	Input Voltage: 12V DC, Adjustable Speed Range	Allows precise adjustment of fan speed.
VOC Escape Valve	Area per valve: 78.54 mm^2	Used to control VOC release.
	Open Valves: 1–3	Adjusts water recovery rates.
UV-C Light Strip	Voltage: 12V DC	Provides sterilization.
	Wavelength: ~254 nm	Effective for microbial deactivation.
Desalination (NaCl Concentration)	Input: 0–490 mg/L	Tested for salt removal efficiency.
Dye Concentration (Congo Red)	Input: 0–50 mg/L	Evaluated for dye removal.
Microbial Load (E. coli)	Initial Concentration: 1.5×10^8 CFU/mL	Validated using fluorescence microscopy.
Water Recovery Efficiency	Closed Valve: ~83%	Without VOC escape.
	1 Valve Open: ~14%, 2 Valves Open: ~22%	Reduces with more VOC valves open.
Dimensions		

Component	Dimensions (Length × Width × Height)	Material
Water Inlet & Mist Making Chamber	93 mm × 53 mm × 40 mm	Biodegradable PLA
Central Circulation Chamber	265 mm × 90 mm × 230 mm	Biodegradable PLA
Collection Chamber	93 mm × 53 mm × 40 mm	Biodegradable PLA
Piezoelectric Transducer Disc	Diameter: 16 mm (steel sheet)	Stainless Steel
VOC Escape Valve	Area per opening: 78.54 mm²	Rubber stoppers for sealing
Copper Heat Pipes (in Evaporation Chamber)	Standard diameter: 8 mm	Copper

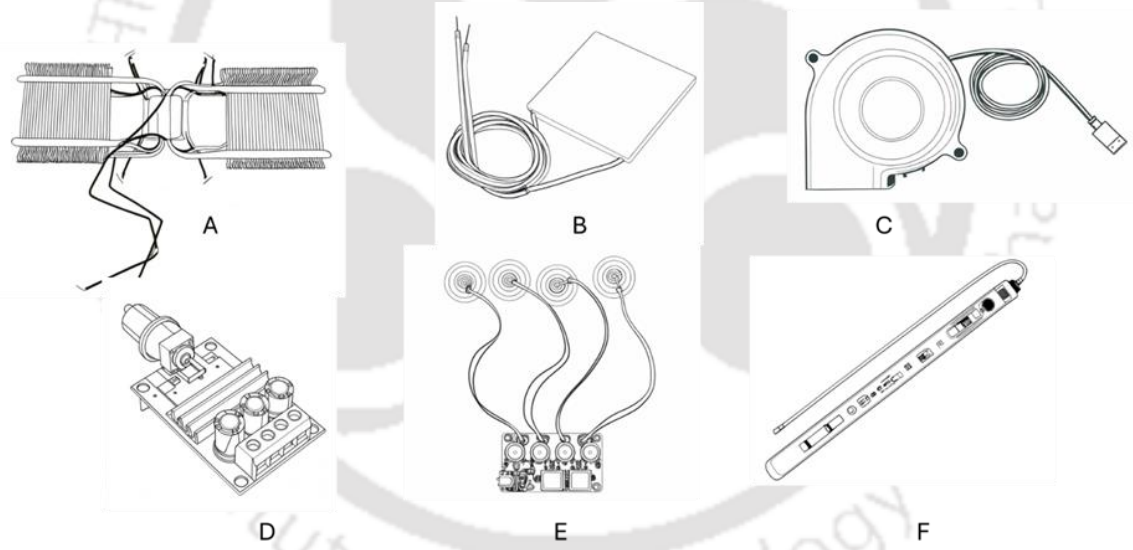

Fig 4. 1 Schematic illustration of components used in this work

(A) heat sink (B) Peltier module (C) turbine fan (D) motor speed controller (E) Piezoelectric transducer module (F) UV-C module

4.2.2 Components and assembly of the distillation unit

The system consists of a water inlet and mist-making chamber, a VOC escape valve, a central circulation chamber with UV-C disinfection, and a collection chamber. All of these components are described in the subsections below.

4.2.2.1 Water inlet and mist making chamber of the distillation unit

The inlet chamber was constructed using biodegradable PLA with dimensions of 93 mm in length, 53 mm in width, and 40 mm in height. This chamber was equipped with three ultrasonic piezoelectric transducer discs, each specified with a direct voltage of 5V, a current of 300 mA, a power output of 2W, and a frequency range of 108–110 kHz. The transducers are fitted with a steel sheet diameter of approximately 16 mm and operate within a temperature range of 0°C to 85°C and a relative humidity range of 10% to 90%. To prevent leakage, all wiring is securely encapsulated in epoxy. The ultrasonic piezoelectric transducers function by converting electrical energy into high-frequency sound waves, producing oscillations that generate thrust and create a fine mist of water [166]. Water enters the chamber via an attached pipe. A schematic representation of the inlet chamber and components of the transducer is provided in Fig 4.2.

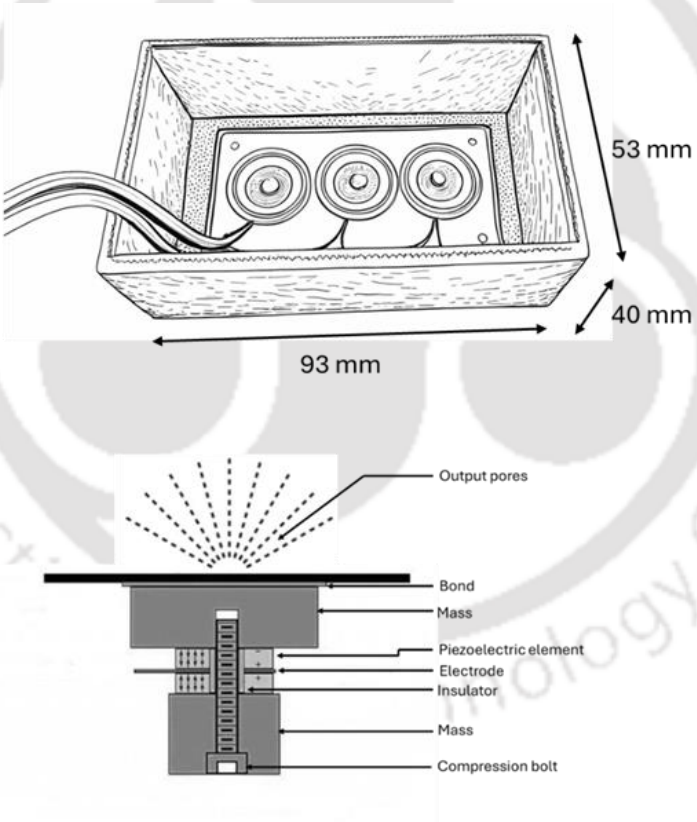

Fig 4. 2 Schematic illustration of water inlet chamber and working mechanism of ultrasonic piezoelectric transducer

4.2.2.2 VOC escape valve of the distillation unit

Conventional distillation units are typically ineffective in removing VOCs from water due to their enclosed design. To address this limitation, we incorporated a VOC escape valve at the

top of the evaporation chamber, enabling controlled release of VOCs during the distillation process. The setup includes three separate openings, each with an area of 78.54 mm², which can be opened or closed depending on the VOC concentration in the water being treated. These valves can be sealed with rubber stoppers when VOC removal is unnecessary, as keeping them open may decrease water recovery efficiency. A schematic illustration of the VOC escape valve is shown in Fig 4.3.

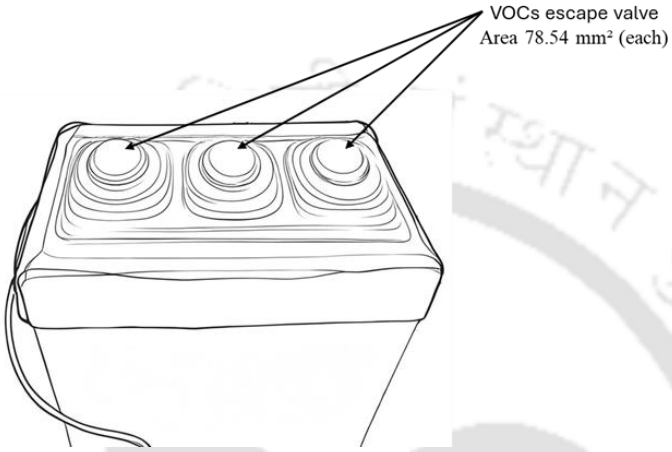

Fig 4. 3 Schematic illustration of VOC escape valve

4.2.2.3 Central circulation chamber with UV-C disinfection

The central circulation chamber was constructed from PLA material and designed with dedicated evaporation and condensation chambers, each measuring 265 mm in length, 90 mm in width, and 230 mm in height. These two chambers were linked through a single steam transfer unit that incorporated a turbine fan to maintain continuous airflow.

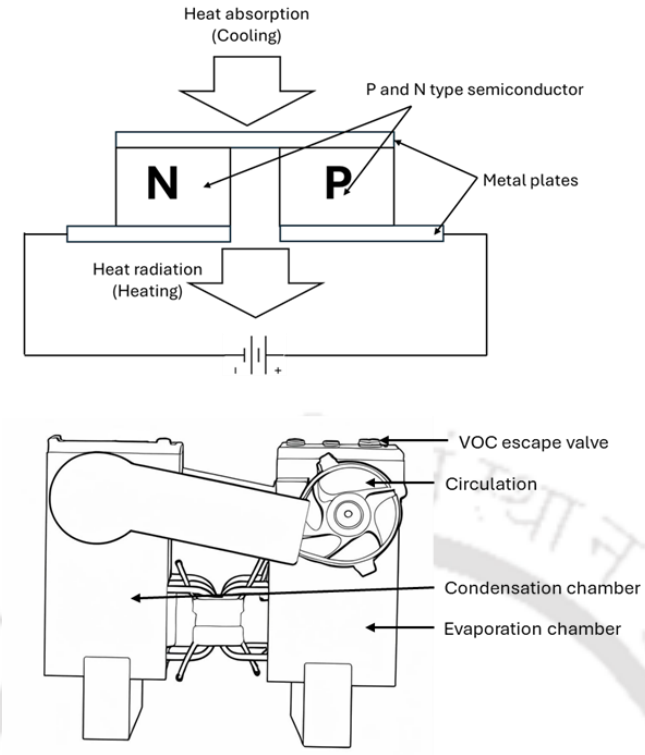

Fig 4. 4 Schematic illustration of the central circulation chamber and components of Peltier module

To uphold a sterile environment within the system, the steam transfer pathway was equipped with a UV-C light strip. Each of the chambers was also fitted with radiators featuring copper heat-conducting pipes. These pipes facilitated efficient transfer of heat or cold between the evaporation and condensation chambers. Positioned centrally within the system, a Peltier module was connected to the copper heat pipes, acting as the core temperature control component. The Peltier module operates based on the thermoelectric effect: when an electric current passes through it, one side absorbs heat, creating a cooling effect, while the opposite side releases heat, generating warmth. This allows for precise temperature control, directing heat or cooling as needed to regulate the chamber environment. A schematic illustration of the central circulation chamber and the Peltier module, detailing the working principle, is presented in Fig 4.4.

4.2.2.4 Collection chamber of the distillation unit

The collection chamber was constructed from biodegradable PLA, with dimensions of 93 mm in length, 53 mm in width, and 40 mm in height, designed to securely collect water from the condensation chamber. This chamber is tightly connected to the condensation chamber without any gaps, ensuring that no contaminants enter the purified water. Additionally, a pipe can be

attached to the chamber for the continuous delivery of purified water. A schematic illustration of the collection chamber is presented in Fig 4.5.

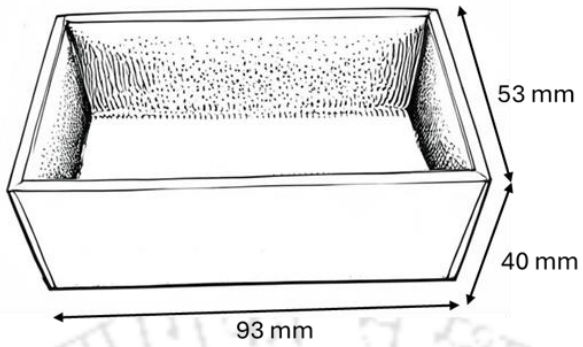

Fig 4. 5 Schematic illustration of the water collection chamber

4.2.3 Wiring configuration of the distillation unit

The machine was equipped with five key electrical components: a turbine fan, UV-C light, motor speed controller, Peltier module, and a piezoelectric transducer module. The turbine fan was connected to a motor speed controller, allowing precise adjustment of the circulation speed, with the controller powered by a 12V DC supply. Both the UV-C light and Peltier module were also connected to the 12V DC power source, ensuring consistent operation. The piezoelectric transducer module, designed to operate at a lower voltage, was connected to a 5V DC supply. A complete schematic illustration of the wiring configuration is shown in Fig 4.6.

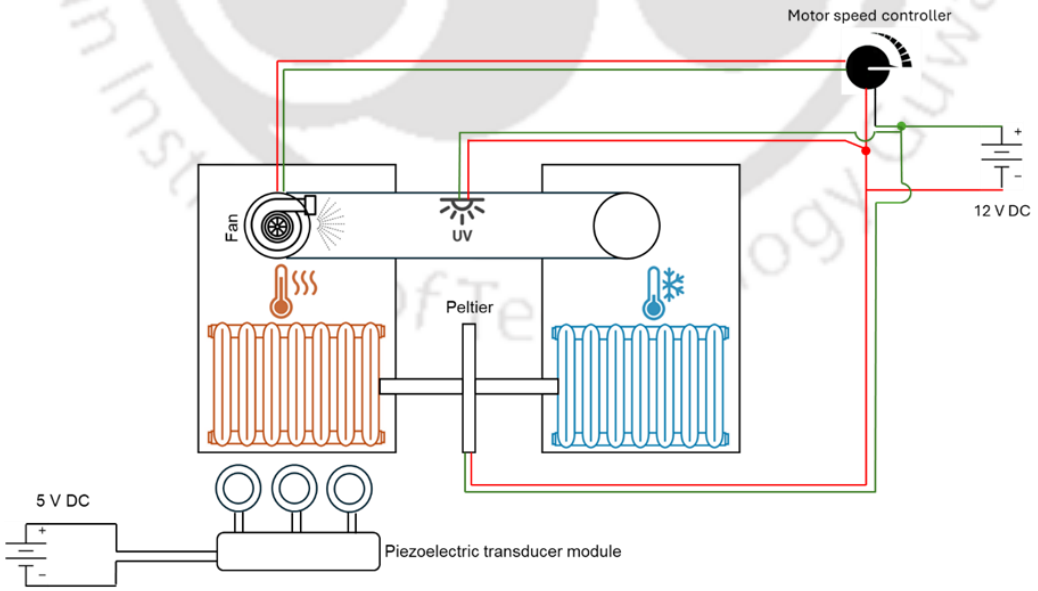

Fig 4. 6 Schematic illustration of the wiring configuration

4.2.4 Assessment of desalination efficiency of the distillation system

The efficiency of the device for salt removal (desalination) was evaluated using NaCl solutions at varying concentrations. To test its desalination capability, NaCl solutions of 0-490 mg/L concentrations were prepared, and the salt removal efficiency was monitored by measuring the conductivity of the input water across various concentrations and comparing it with the conductivity of the treated output water. The 0–490 mg/L range was selected to encompass both low-salinity conditions (e.g., freshwater) and concentrations approaching brackish water thresholds (typically ≥500 mg/L), thereby evaluating performance of the device across a practical and environmentally relevant spectrum. Similar technique was applied by Le et al. for estimating the desalination efficiency of carbon aerogel electrodes (Le et al., 2016). The circulating fan speed was kept constant at 250 RPM throughout the experiment. A graph of conductivity versus concentration was then plotted for the input and output water, providing a clear assessment of the device in terms of desalination performance.

4.2.5 Assessment of the decontamination efficiency of the distillation system

To assess the decontamination efficiency of the device, a live/dead assay was performed using SYTO™ 9 and PI dyes, which offer a clear distinction between viable and non-viable cells based on membrane integrity. SYTO™ 9 is a green-fluorescent nucleic acid stain that binds to intact cell membranes. In contrast, PI is a red-fluorescent dye that only enters cells with compromised membranes, selectively labelling dead or damaged cells by binding to their DNA. This complementary staining approach allows for a reliable differentiation between viable and non-viable cells [167]. The assay was prepared by inoculating 100 mL of Luria Bertani broth with *E. coli*, incubating it overnight at 37°C with agitation at 180 RPM in 500 mL Erlenmeyer flasks. After incubation, the culture was washed three times with phosphate-buffered saline (PBS; 137 mM NaCl, 2.7 mM KCl, 10 mM Na_2HPO_4, 1.8 mM KH_2PO_4) and standardized to a turbidity of 0.5 McFarland (1.5×10^8 CFU/mL) to ensure consistent cell density across samples. 50 ml of this sample was used as the input water. The water was purified at circulating fan speed of 250 RPM. Both input and output water sample were analysed using fluorescence microscopy. For fluorescence staining, stock solutions of 20 mM PI and 3.34 mM SYTO™ 9 in DMSO were prepared, with final staining concentrations in PBS of 30 µM for PI and 5 µM for SYTO™ 9 at a 1:1 ratio. This combination enabled the simultaneous visualization of live and dead cells under fluorescence microscopy [168]. Fluorescence microscopy was performed using an inverted fluorescence microscope (CKX53SF-OLYMPUS, Tokyo, Japan). SYTO™ 9 signals were detected using a 488 nm excitation laser with a 505–550 nm emission filter, while

PI signals were captured with a 561 nm excitation laser and a 575 nm longpass emission filter, ensuring clear distinction between the two fluorescence signals. Image analysis was conducted using ImageJ software, allowing for quantification of live/dead cell populations and providing insights into the device's decontamination effectiveness. The microbial load in tap water is generally low due to regulatory standards and treatment processes. Typical HPC in treated tap water range from <1 to 500 CFU/mL, with coliform bacteria (e.g., *E. coli*) required to be undetectable (i.e., <1 CFU/100 mL) in potable water as per WHO and EPA guidelines (WHO, 2017; EPA, 2023). The 1.5×10^8 CFU/mL range was selected to stress-test the device's efficacy under extreme contamination scenarios, simulating severe faecal or environmental contamination (e.g., 10^6–10^8 CFU/mL in untreated wastewater).

4.2.6 Assessment of the dye removal efficiency of the distillation system

The efficiency of the device in removing highly miscible dye compounds from water was evaluated using Congo red dye across a range of concentrations from 0 to 50 mg/L. This range was chosen as it represents a standard benchmark commonly used in both industrial and academic settings for evaluating various remediation techniques for CR degradation [116,119]. To assess dye removal, solutions with increasing concentrations of Congo red were prepared, and a graph of absorbance at 497 nm versus concentration was plotted to monitor the input and output water. Congo red dye has a strong absorbance at 497 nm, providing a reliable measure of dye presence and removal efficiency [116].

4.2.7 Assessment of the VOC removal efficiency of the distillation system

Aqueous solutions containing 60 µL/L of toluene and o-xylene were prepared to evaluate their removal, monitored spectrophotometrically with modifications based on the method described by Ozerova et al. The 60 µL/L concentration was selected to reflect environmentally relevant levels of VOCs typically detected in contaminated groundwater and, on rare occasions, in tap water. The solutions were prepared in airtight glass vials with secure, leak-proof caps to prevent any gas exchange. Care was taken to fill the vials completely to eliminate air gaps, followed by sonication to ensure thorough homogenization [169]. The treated mixtures were filtered using a device equipped with a single VOC escape valve, operated at a fan speed of 250 RPM to facilitate the removal of volatile compounds. The UV spectra of both treated and untreated samples were recorded in the wavelength range of 200 to 350 nm using a Varioskan™ LUX plate reader (Thermo Scientific).

4.3 Results and discussion

4.3.1 Assessment of desalination efficiency of the distillation system

The conductivity-concentration profile for the input samples demonstrated a pronounced increase in conductivity with escalating salt concentrations, while the output (purified water) maintained consistently low conductivity levels, as illustrated in Fig 4.7. This indicates the effectiveness of the device in removing salt from water. However, at higher salt concentrations, fine salt precipitation can accumulate in the evaporation and water inlet chambers. To maintain optimal purification efficiency, these salt deposits can be periodically removed with high-pressure water rinsing.

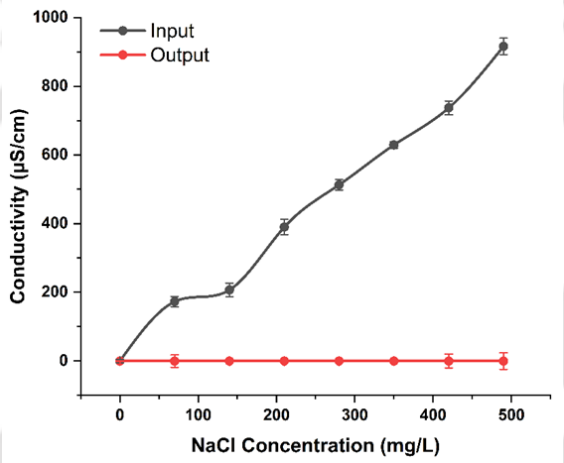

Fig 4. 7 Conductivity vs NaCl concentration graph of untreated and treated water sample

Difference between input and output conductivity, validating capability of the device to desalinate even at elevated NaCl concentrations without performance compromise

4.3.2 Assessment of the decontamination efficiency of the distillation system

Fluorescence microscopy images visually confirmed the antibacterial efficacy of the device when operating with a circulating fan speed of 250 RPM. Untreated water showed numerous viable cells under fluorescence microscopy, while treated water showed no visible live cells. The few dead cells observed in the treated water could be due to residual microbes within the chamber, as shown in Fig 4.8. The device is designed with foam pads that filter water before it reaches the piezoelectric transducer, effectively preventing most bacterial cells from entering the evaporation chamber. Any microbes that do pass through are exposed to heat in the chamber, acting as a secondary antimicrobial barrier. Additionally, UV-C light installed at the transfer junction provides a final layer of disinfection. As supported in the literature, UV-C

light is a well-established tool for microbial decontamination, enhancing the overall antimicrobial effectiveness of the system.

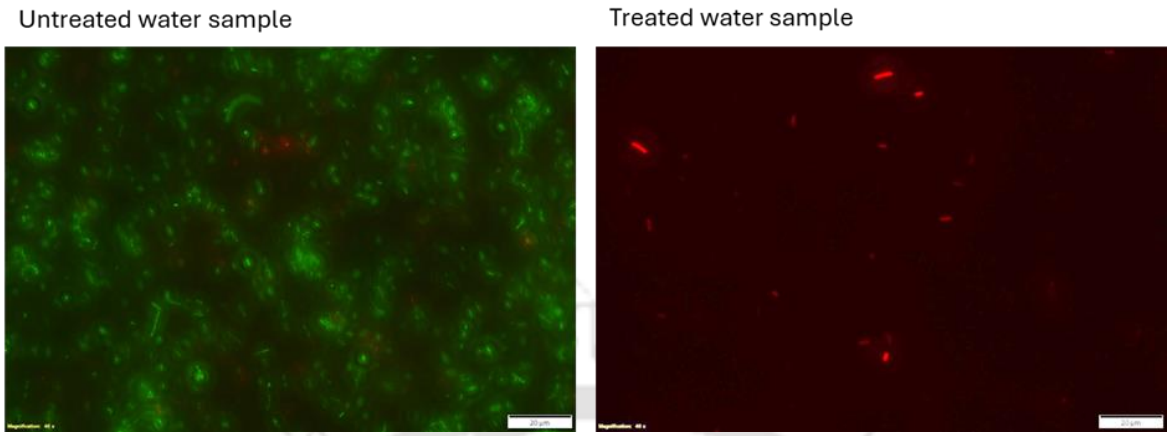

Fig 4. 8 Fluorescence microscopy showing live microbes in untreated water and mostly dead ones in the treated sample

4.3.3 Assessment of the dye removal efficiency of the distillation system

The absorbance versus concentration graph for input and output samples revealed that the absorption of dye increased as the dye concentration in the input samples was raised. However, the system demonstrated high efficiency in removing dye up to a concentration of 50 mg/L when operated at a circulating fan speed of 250 RPM as illustrated in Fig 4.9. As a result, the absorbance of the output water remained consistently low throughout the analysis, indicating effective dye removal. This suggests that the system can efficiently purify water by removing significant amounts of dye, especially at lower concentrations, while maintaining minimal dye levels in the treated water.

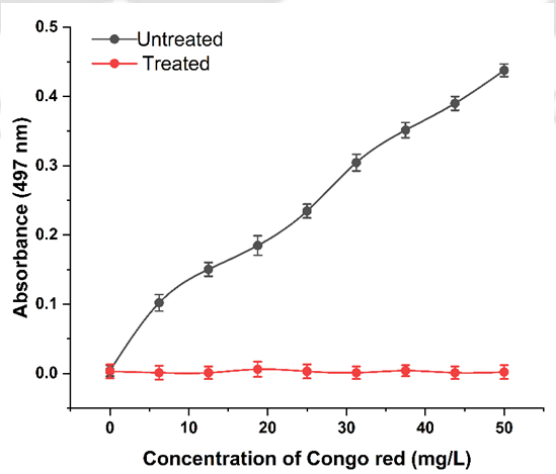

Fig 4. 9 Absorbance vs CR concentration graph of untreated and treated water sample

The system effectively maintained minimal absorbance in output samples across dye concentrations, suggesting strong retention or degradation of CR even at higher loads

4.3.5 Assessment of the VOC removal efficiency of the distillation system

The UV absorption spectra of both untreated and treated water samples are depicted in Fig. 4.10. Toluene and o-xylene exhibited strong absorbance within the wavelength range of 200 to 220 nm. The disappearance of these peaks in the treated samples indicated the effective removal of these compounds from the water, demonstrating the efficacy of the system in eliminating VOCs. However, given the diverse chemical properties of VOCs, the system's removal efficiency may vary for different compounds. Optimization of operational parameters, such as fan speed and the configuration of VOC escape valves, may be necessary to achieve efficient removal of other VOC species.

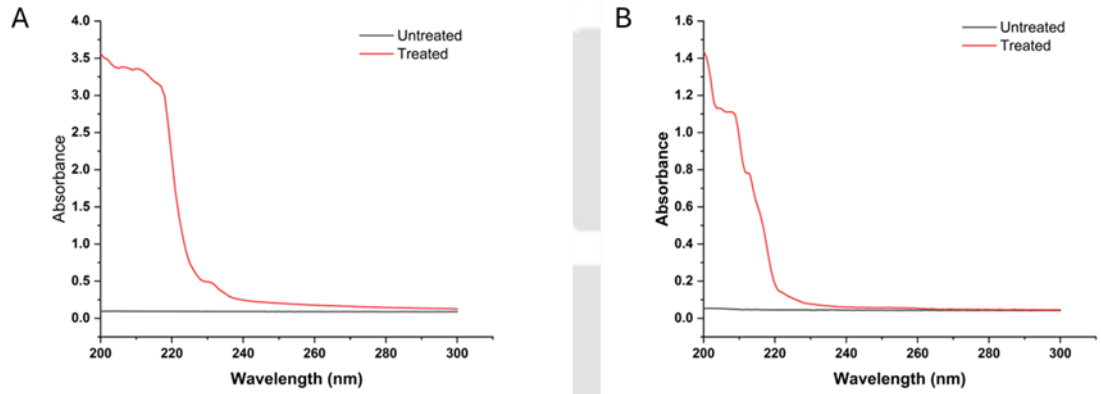

Fig 4. 10 UV absorption spectra of (A) toluene and (B) o-xylene untreated and treated water samples

The absence of characteristic UV absorption peaks for toluene and o-xylene in treated samples confirms substantial VOC elimination, underscoring the system's applicability for chemical contaminant removal

4.3.6 Working principle of the prototype

The system employed in this study demonstrated advanced water purification capabilities by integrating multiple technological components. Water entered the system through the inlet chamber, equipped with ultrasonic piezoelectric transducers. Upon activation, these transducers generated high-frequency sound waves, which vibrated the water to produce a fine mist. This mist, composed of microdroplets with a high surface area-to-volume ratio, facilitated rapid evaporation. The piezoelectric transducers efficiently converted electrical energy into mechanical vibrations, which were transmitted into the water to produce the desired mist [170]. The generated mist was subsequently directed by a turbine fan situated in the central chamber. This fan ensured a continuous flow, propelling the mist toward the evaporation and condensation chambers. Within the evaporation chamber, precise temperature control proved critical for optimizing the mist's phase changes. A Peltier module, leveraging the thermoelectric

effect, managed this process. When a current passed through the Peltier module, one side absorbed heat, generating a cooling effect, while the opposite side emitted heat [171]. By positioning the heated side of the module in contact with the evaporation chamber, it established a warm environment conducive to mist evaporation. Simultaneously, copper heat pipes connected to the cooled side directed excess heat away, maintaining system stability and supporting condensation.

During the evaporation process, contaminants such as salts, dyes, and microbial residues were effectively separated from the water vapor. The purified vapor then advanced to the condensation chamber, where the cooler side of the Peltier module facilitated its condensation back into liquid form. This phase was critical for collecting purified water, which was subsequently stored in a sealed collection chamber to prevent external contamination. A UV-C light strip, installed within the system, provided an additional sterilization step. As vaporized water traversed this section, the UV-C light disrupted the DNA of residual bacteria and microorganisms, rendering them inactive. This sterilization process enhanced the purity of the final output, further safeguarding it against microbial contamination [172]. Additionally, the system effectively addressed VOCs, which could otherwise vaporize and condense with purified water. An escape valve located at the top of the evaporation chamber enabled the release of VOCs prior to their entry into the collection chamber, thereby achieving a level of purification that surpassed traditional distillation systems (Fig 4.11).

The system was rigorously tested under various contamination conditions, exhibiting high removal efficiencies and demonstrating versatility in water purification. For dye removal, it achieved complete elimination of Congo red at concentrations of up to 50 mg/L. In salinity reduction trials, the system successfully removed salt from solutions containing concentrations as high as 490 mg/L. When loaded with a microbial load of 1.5×10^8 CFU/mL, the system effectively decontaminated the water, ensuring pathogen-free output. Furthermore, the system successfully removed 60 µL/L of toluene and o-xylene, underscoring its comprehensive purification capabilities. The water recovery efficiency, defined as the proportion of purified water obtained relative to the initial input volume, was notably high. For every 100 mL of water introduced into the inlet chamber, 83% was recovered as purified water, surpassing the typical recovery rates observed in conventional RO systems [173]. This impressive recovery rate, coupled with effective contaminant removal, positioned the system as a resource-efficient alternative to RO technology. However, opening a single VOC escape valve reduced the

recovery efficiency to approximately 14%, while opening two valves decreased it to 22%. Under ambient conditions, the system's power consumption was measured at 60 watts.

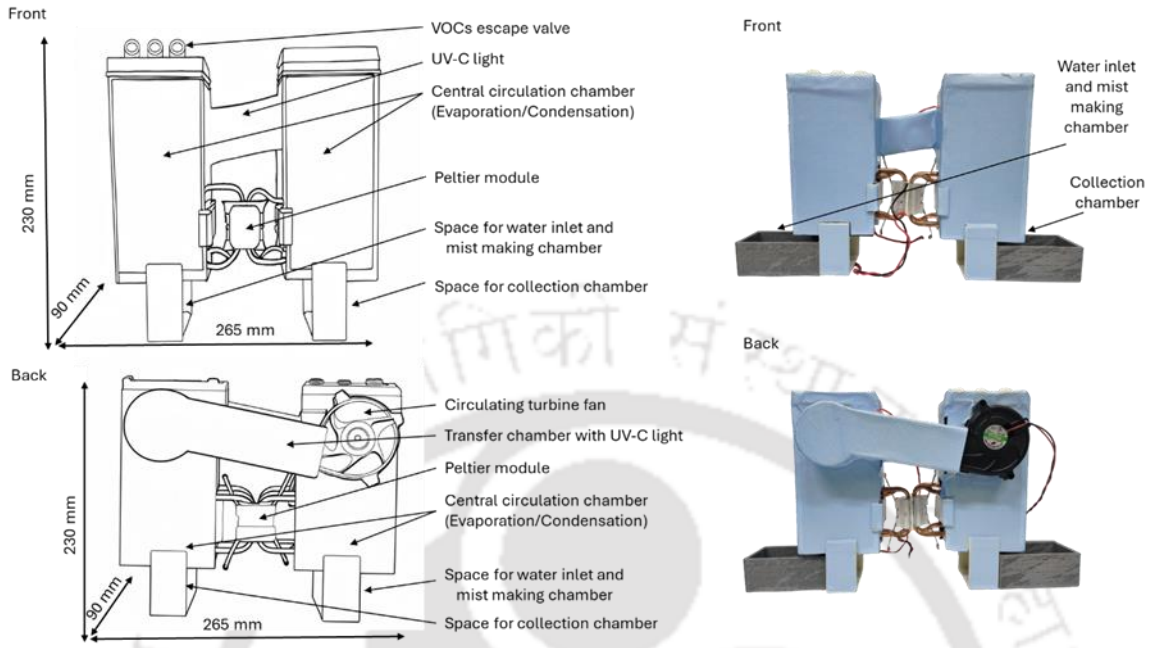

Fig 4. 11 Schematic and real illustration of the final assembled product

Given the variable nature of wastewater characteristics, the system offered adaptability by allowing adjustments to the circulating fan speed and the VOC escape valve settings. This tunable functionality optimized purification and recovery according to specific conditions, thereby ensuring maximum purification efficiency. The system demonstrated consistent performance across diverse water quality challenges, highlighting its flexibility and robustness in practical applications.

4.4 Techno-economic analysis of the distillation system

The developed energy-efficient water distillation system was designed with a focus on cost-effectiveness and practicality for domestic use. Key components, including the piezoelectric ultrasonic mist maker, thermoelectric Peltier modules, and UV-C sterilization unit, were selected to achieve optimal energy efficiency and affordability. The system consumed 60 watts under ambient conditions, significantly lower than traditional distillation units and RO systems, which typically consume 300 to 3000 watts. This considerable reduction in power consumption highlights the suitability of this system for sustainable water purification. Furthermore, the use of biodegradable PLA material in constructing the chambers contributed to reduced production costs while ensuring environmental sustainability. The high water recovery rate of 83 percent, compared to the lower recovery rates of RO systems, minimized water wastage and enhanced

economic appeal. The modular design allowed for operational flexibility, enabling adjustments to fan speed and VOC escape valve settings to optimize energy usage based on varying water quality. The ability to effectively remove dissolved salts, microbial contaminants, dyes, and VOCs while maintaining a low energy footprint positions it as a viable and sustainable alternative to traditional systems, particularly in regions with poor municipal water quality or limited access to advanced purification methods.

4.5 Conclusion

Water quality challenges stemming from urbanization, industrialization, and agricultural activities have necessitated the development of advanced domestic purification technologies to supplement traditional municipal systems. Existing purification methods, particularly reverse osmosis and distillation, while effective in removing a broad range of contaminants, are often limited by high energy consumption, low water recovery rates, and inefficiencies in removing VOCs. In view of these limitations, this study developed an energy-efficient distillation-based water purification system integrating piezoelectric ultrasonic mist technology, thermoelectric Peltier modules, and UV-C sterilization, constructed from biodegradable PLA materials. The system demonstrated robust performance across various purification metrics. It achieved up to 83% water recovery efficiency, outperforming traditional reverse osmosis systems. The removal rates for NaCl, microbial contaminants (*E. coli*), CR dye, and VOCs (toluene and o-xylene) were consistently high, with reductions of 490 mg/L, 1.5×10^8 CFU/mL, 50 mg/L, and 60 µL/L, respectively. The incorporation of VOC escape valves and the Peltier module's precise temperature control ensured effective separation of contaminants while maintaining energy efficiency. Additionally, UV-C sterilization provided a final layer of microbial decontamination, enhancing the purity of the output water. The modular design and tunable parameters of this device allowed adaptability to diverse contamination scenarios, underscoring its practical applicability for domestic use. Although the system achieved significant advancements, further optimization of VOC removal and long-term durability testing could enhance its utility. By combining advanced technologies within an environmentally friendly framework, this study contributes to the advancement of domestic water purification systems, offering a pathway toward ensuring safe and reliable access to clean water.

Chapter 5. Development of IoT enabled real-time water monitoring system with hybrid power management and remote data accessibility

Abstract

Traditional water monitoring methods, reliant on handheld devices and laboratory analyses, present limitations in terms of efficiency, cost, and responsiveness to dynamic water conditions. Proprietary systems, while offering advanced features, often impose significant financial burdens and may lack flexibility. Open-source solutions provide a cost-effective alternative but often require technical expertise. To address these challenges, this work presents the development of a real-time water monitoring device that integrated multiple sensors, a hybrid power system, and a web-based interface for comprehensive water quality analysis. The device, housed in a compact and buoyant casing, incorporated a microcontroller, sensors for temperature, humidity, dissolved oxygen, turbidity, and total dissolved solids, a GPS module, and a combined rechargeable battery and solar power system. This system enabled real-time data collection, processing, and transmission, with AI and ML readiness. A user-friendly web interface, utilizing Firebase, Plotly.js, and Leaflet.js, provided dynamic data visualization and analysis. The use of open-source Firebase hosting eliminated recurring server costs, ensuring affordability and sustainability, particularly in resource-constrained environments.

5.1 Background

The field of water monitoring experienced substantial advancements, evolving from traditional methods to sophisticated, integrated technologies that significantly improved the accuracy and efficiency of water quality assessments. Historically, water monitoring depended on handheld devices and laboratory analyses, requiring skilled personnel for sample collection and measurement. While handheld devices offered portability, they demanded frequent calibration and manual operation, making the process both labour-intensive and time-consuming. Laboratory analyses, although highly accurate, often introduced delays, limiting the ability to respond promptly to emerging water quality concerns. These limitations highlighted the need for innovative solutions, driving the shift toward real-time, automated monitoring systems that offer enhanced precision and responsiveness [174]. Modern water pollution challenges have become increasingly complex, largely due to the dynamic nature of industrial wastewater. As industries evolved, the characteristics of wastewater shifted rapidly, creating a need for adaptable monitoring systems capable of responding to these fluctuations. Effective water quality management now requires real-time sensors that can continuously monitor various parameters, including pH, turbidity, dissolved oxygen, and chemical contaminants. This requires not only advanced sensor technology but also a comprehensive framework that allows for remote monitoring and data analysis [175].

Proprietary systems for water quality monitoring typically come with significant financial burdens. These systems often involve high research and development costs, which are passed on to consumers through expensive hardware and software solutions. Additionally, users face recurring costs associated with software licenses, server maintenance, and data storage. For instance, commercial telemetry systems can cost between three to four times more than open-source alternatives, making them less accessible for municipalities and organizations with limited budgets. Moreover, proprietary systems may lack the flexibility needed to adapt to specific monitoring needs, as they are often designed for general applications rather than tailored solutions. This financial barrier often limits access for users in developing countries where affordable solutions are crucial for effective water management [176]. In contrast, open-source solutions present a cost-effective and adaptable alternative for water quality monitoring. LCSNs demonstrate that real-time groundwater monitoring can be achieved at a fraction of traditional system costs. These frameworks reduce initial investments and eliminate recurring software fees, as users can host and modify the software to fit their needs. This flexibility allows for seamless integration of various sensors and data types, enabling comprehensive, real-time

monitoring of water quality parameters [177]. Despite these advantages, open-source systems require technical expertise for setup and maintenance. However, this challenge is mitigated by community collaboration, as developers and researchers contribute to enhancing system robustness and functionality. Extensive online resources, tutorials, and forums also empower users to troubleshoot and optimize systems independently, reducing the need for costly support. Through collaborative development, open-source solutions can continually incorporate the latest advances in sensor technology and data analysis [178].

The emergence of open-source SBCs like the ESP32 has further transformed water monitoring systems. The ESP32 platform supports diverse sensor types and facilitates wireless communication with built-in Wi-Fi and Bluetooth, allowing seamless data transmission to cloud platforms for remote monitoring. This cost-effective integration of multiparametric sensors makes advanced water monitoring accessible even in resource-limited settings, though remote, real-time sensing may still incur server and hosting costs [179]. Present work involves development of a real-time water monitoring device that integrates a variety of sensors, a hybrid power system, and a web-based interface to provide comprehensive water quality data. Housed in a compact, buoyant casing, the device includes a microcontroller, multiple sensors (for temperature, component area humidity, DO, turbidity, and TDS), a GPS module, and a power system combining rechargeable batteries with solar energy. This design enabled real-time data collection, processing, and transmission, with AI and ML readiness for data analysis. A web-based interface was developed using Firebase, Plotly.js, and Leaflet.js, providing dynamic, user-friendly visualization. By using open-source Firebase hosting, recurring server costs were eliminated, making it an economically viable solution for resource-limited environments.

5.2 Materials and methods

5.2.1 Materials

The ESP32 microcontroller, turbidity module, and NEO-6M GPS module were procured from Xcluma, China. The TP4056 battery charging module and solar panel were purchased from Electronic Spices, India. The BME280 module was obtained from Bosch Sensortec, Germany. An analog TDS module was sourced from Techtonics, China, while the DO sensor was acquired from Graylogix, India. A 5000 mAh Lithium polymer battery was purchased from Ganzhou Novel Battery Technology Co. Ltd, China. All 3D printing was conducted using 1.75 mm PLA filament on a WOL3D Ender 3 printer (Shenzhen Creality 3D Technology Co., Ltd, China). The schematic illustration of all components used in this work is presented in (Fig.

5.1). All remaining accessories and components utilized in this research were of industrial grade. (Table 5.1) delineates workable ranges for all the parameters involved in this work.

Table 5. 1 Ranges for all dimensions, input and output parameters involved in this development

Component	Parameter	Range
ESP32 Microcontroller	Operating Frequency	Up to 240 MHz
	Operating Voltage	3.3-5V
Battery Charging Module (TP4056)	Input Voltage	4.5V to 5.5V
	Output Voltage	5V
GPS Module (NEO-6M)	Supply Voltage	3V to 5V
	Power Consumption	45 mA (normal), 11 mA (power save)
	Position Accuracy	2.5 meters
BME280 Sensor Module	Operating Voltage	1.8V to 3.6V
	Temperature Range	-40°C to +85°C
	Humidity Range	0% to 100%
Analog TDS Module	Input Voltage	3.3V to 5.5V
	TDS Measurement Range	0 to 1000 ppm
Turbidity Module	Operating Voltage	5V
	Operating Temperature Range	5°C to 90°C
	Analog Output Voltage	0V to 4.5V
DO Module	Dissolved Oxygen Measurement Range	0 to 20.0 ppm
	Resolution	0.1 ppm
Solar Panel	Output Voltage	6V per panel
	Current Capacity	100 mAh per panel
Battery	Battery Capacity	5000 mAh (each), 20000 mAh (total)
Housing	Dimensions (Base)	130 mm (L) x 130 mm (W) x 100 mm (H)
	Material	PLA (Polylactic Acid)

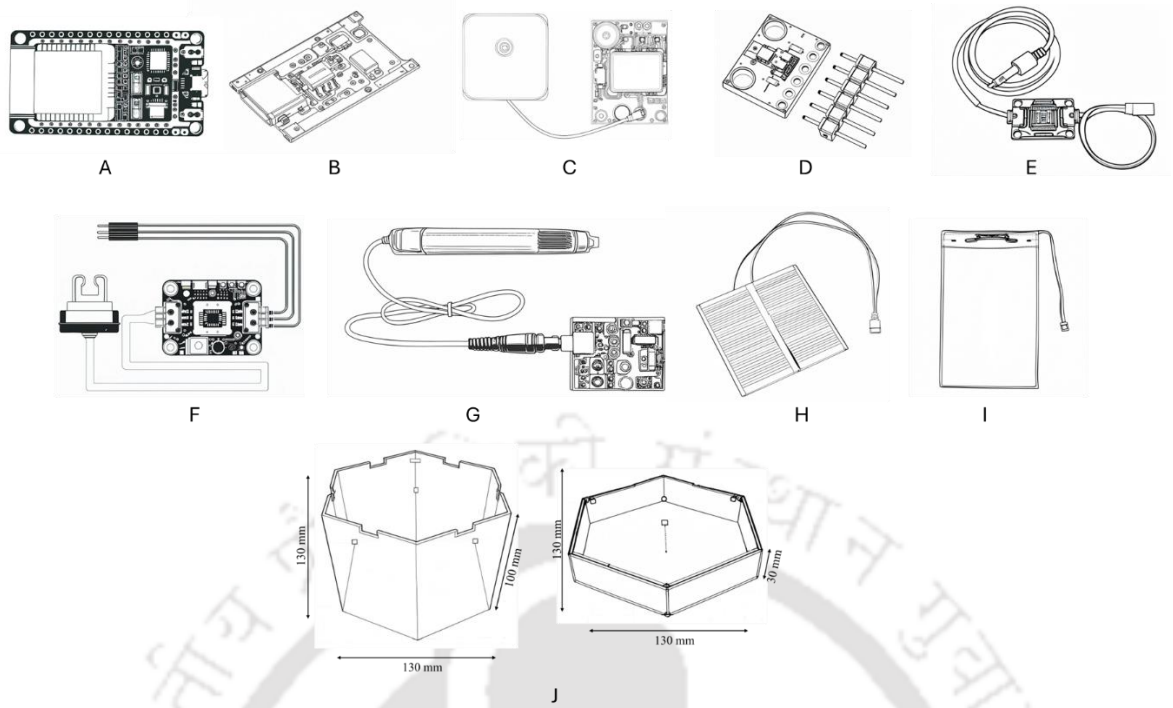

Fig 5. 1 Schematic illustration of components used in this work

(A) microcontroller ESP32 (B) battery charging module TP4056 (C) GPS module NEO-6M (D) BME280 module (E) analog TDS module (F) turbidity module (G) DO module(H) solar panel(I) battery (J) housing

5.2.2 Wiring configuration of the monitoring device

The wiring configuration of the system involved connecting the TP4056 battery connector to a 20,000mAh, 3.7V Lithium polymer battery. The charge input connector was connected to six solar panels wired in parallel. To prevent voltage backflow, each solar panel's positive terminal was equipped with a blocking diode. The output of the TP4056 was connected to the ESP32 microcontroller, with a switch installed to control the system's power. All circuit boards, except the BME280 module, were connected to their respective sensors via input pins. Since the BME280 had built-in onboard sensors, no additional connections were necessary. The power terminals (+5V) of all components, excluding the BME280 and GPS module, were connected to the +5V output from the TP4056 module, while the ground terminals (-5V) of all components, including the BME280 and GPS module, were connected to the -5V output from the TP4056. The VCC of the ESP32 and GPS module was connected to the ESP32's 3.3V terminal. The SCK and SDI pins of the BME280 were connected to the D22 and D21 pins of the ESP32, respectively. The TX and RX pins of the GPS module were wired to the DX2 and RX2 pins of the ESP32. Additionally, the analog output pins of the DO sensor, turbidity sensor, and TDS sensor were connected to the D34, D35, and D32 pins of the ESP32, respectively. The schematic illustration of the wiring/connection is depicted in (Fig 5.2).

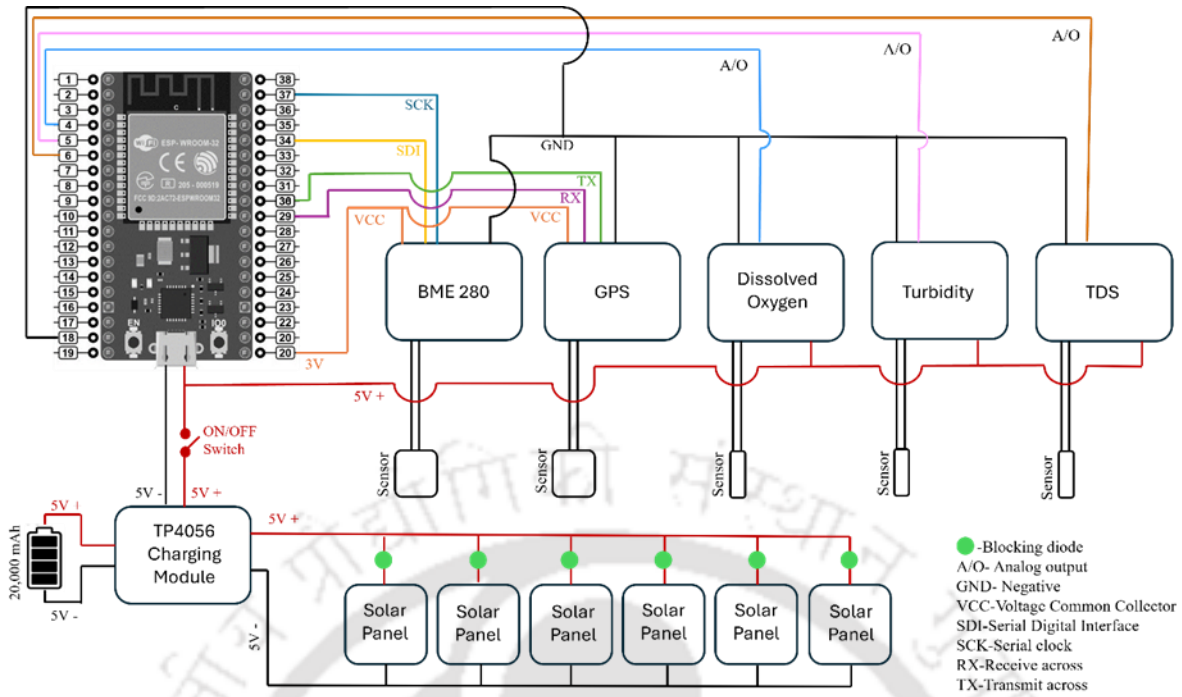

Fig 5. 2 Schematic illustration of wiring/connection

The wiring schematic integrates diverse sensors and modules with efficient power routing, illustrating the thoughtful layout required for seamless, solar-powered IoT water monitoring

5.2.3 Programming ESP32 and web interface of the water monitoring system

The source code for the ESP32 and web interface was made publicly available and can be accessed using this link:

- *https://github.com/krsatyamiitr/IoT-R-SAM-PRO*
- *https://drive.google.com/drive/folders/1nQD4GiAEuBZWKL2VPnjLpa0T80UZiDP_?usp=sharing*

The source code used in this research is delineate in Appendix D.1

The role and function of libraries used in this project are explained below:

- **Arduino.h:** This library provided essential support for controlling the ESP32's hardware and input/output pins, serving as the foundation of the microcontroller's operation.
- **TinyGPSPlus.h:** This library extracted latitude and longitude from GPS signals, allowing the device to log geographical location data by parsing raw GPS data into usable coordinates.
- **WiFi.h / ESP8266WiFi.h:** This library managed the device's Wi-Fi connection. For this project, WiFi.h was used for the ESP32, facilitating connection to a wireless network to enable communication with the Firebase database.

- **Firebase_ESP_Client.h:** This library connected the ESP32 to the Firebase Realtime Database, enabling secure authentication and transmission of real-time water quality data between the device and the cloud platform.
- **Wire.h:** This library enabled communication through the I2C protocol, which was used by the BME280 sensor to send environmental data (temperature, humidity, and pressure) to the ESP32.
- **Adafruit_Sensor.h / Adafruit_BME280.h:** These libraries facilitated data collection from the BME280 sensor, which measures atmospheric conditions, ensuring accurate readings of environmental parameters.
- **TokenHelper.h / RTDBHelper.h:** These libraries managed Firebase authentication tokens, maintaining a valid connection by handling token retries and session validation.

The web interface incorporated the following APIs to enhance functionality:

- **Firebase® API:** Supported real-time data storage and retrieval from the Firebase Realtime Database, facilitating synchronization between the ESP32 and web interface.
- **Plotly® API:** Enabled dynamic visualization of water quality data in the form of interactive graphs, allowing real-time monitoring and historical data analysis.
- **Leaflet® API:** Provided mapping capabilities, enabling the display of geographical data from the GPS module on an interactive map, which helped in tracking location-based water quality data effectively.

5.2.4 Realtime database setup of the water monitoring system

The Firebase® realtime database was set up for this project using Google's Firebase® platform, enabling real-time data synchronization and storage. To initiate the setup, a Firebase® project was created or accessed in the Firebase® console. The realtime database option was selected from the project's console, and the database was activated in "Test Mode" to allow unrestricted read and write access during development. Firebase®-CLI was configured within the project directory by running firebase login to authenticate the project. The database structure and initial data entries were configured directly in the Firebase® console or through custom scripts as needed. Following this setup, Firebase SDKs for JavaScript were added to the project codebase to enable seamless interaction with the realtime database [180]. With the Firebase® realtime database connected, data could be stored and accessed from the web application, supporting real-time updates as new information was added or modified.

5.2.5 Configuring web hosting for IoT framework

The website for this project was hosted on Google's Firebase® web hosting, which provided 1GB of data storage and 10GB of network bandwidth. To deploy the website, a Google account was used to log in to the Firebase® console, and Firebase®-CLI was installed, requiring Node.js installation beforehand. The Firebase®-CLI was then installed using the command. The process began by creating a Firebase® project in the Firebase console, accessed by logging in and selecting "Create Project" to enter the project name. Firebase® was accessed via the command line within the project directory and the project was initialized for deployment with the command [181]. Finally, the project was deployed, which generated the hosting URL *https://sensor-952c1.web.app/index.html*

5.3 Result and discussion

5.3.1 Workflow of ESP32 for input/output operations

The device begins by initializing the BME280 sensor and connecting to a Wi-Fi network using the provided credentials. The Firebase® client was then configured with API keys and user authentication details, establishing communication with the cloud database. Environmental sensors, including those for DO, turbidity, and TDS, were read using the respective analog pins.

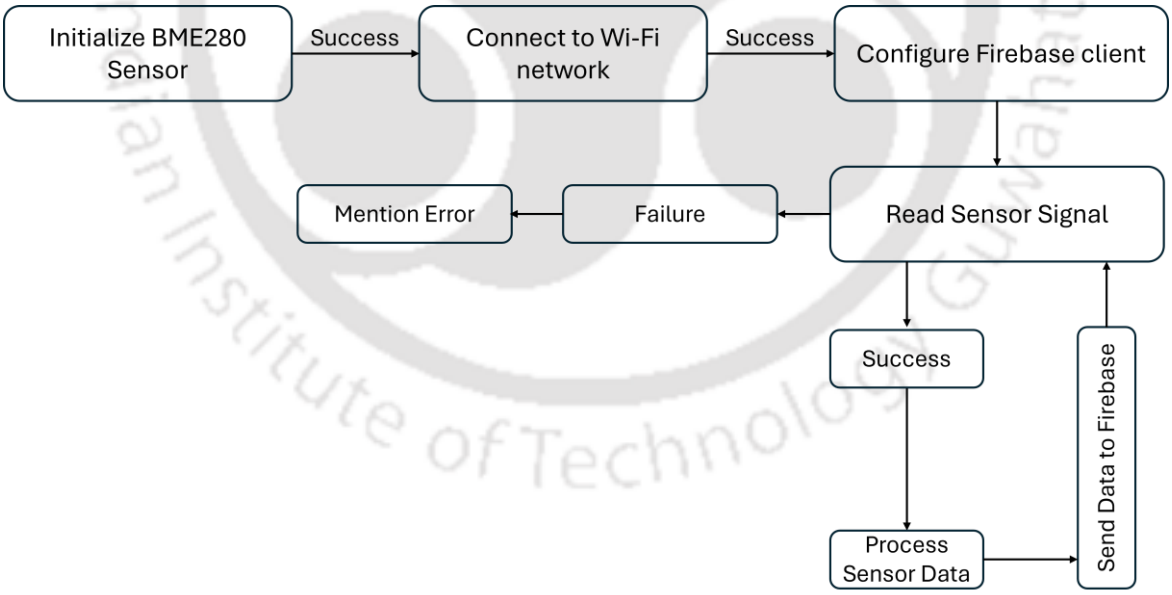

Fig 5. 3 Schematic illustration of the ESP32 workflow

Data acquisition from sensors and wireless transmission to the cloud via Wi-Fi

The data from the sensors is processed and sent to the Firebase® realtime database at regular intervals. The GPS module collects and transmits location data if a valid signal is received. The device operates in a loop, with sensor data continuously read, processed, and uploaded to

Firebase. Real-time communication with Firebase is maintained by the device, ensuring remote monitoring of water quality parameters. The schematic illustration of the ESP32 workflow is presented in (Fig 5.3).

5.3.2 Workflow of web interface for end-user

The real-time water monitoring device was seamlessly integrated into an IoT framework, where a hosted web interface plays a pivotal role in data visualization and user interaction. This device collected sensor data such as temperature, component area humidity, atmospheric pressure, TDS, turbidity, DO, and GPS coordinates and transmitted it to a real-time database. The web interface retrieves this data and presents it to the user in an interactive and visually appealing format, utilizing numbers, tables, and charts for ease of interpretation. The system operates by establishing a connection with a Firebase® realtime database, which continuously fetches and updates sensor data. The database references various data paths, ensuring that as new sensor readings are recorded, the corresponding HTML elements on the web interface update dynamically. For instance, the temperature, humidity, and other water quality parameters are displayed in real time, allowing users to monitor changes instantly. A key component of this system is the use of the Plotly.js library, which enhances data visualization by generating real-time line charts for TDS and turbidity. These charts update automatically as new data is pushed from the sensors to the database, giving users a clear view of trends and fluctuations in water quality metrics. In addition to data charts, the web interface integrates the Leaflet.js library to visualize GPS data. The device's current location, tracked through GPS coordinates, is displayed on a live map, which updates as the device moves or its location changes. This feature provides users with geographical insights into where the water monitoring is being conducted, further enhancing situational awareness. The web dashboard offers a holistic view of the water quality data, presenting it in various formats such as numerical values, interactive charts, and geographic maps enabling users to analyze the information according to their preferences. This flexibility in data display empowers users to make well-informed decisions regarding water quality based on real-time data. In summary, the web interface serves as an interactive dashboard, leveraging modern APIs and visualization tools like Firebase®, Plotly®, and Leaflet® to provide a comprehensive and dynamic water monitoring solution. It ensures real-time data is displayed efficiently, allowing users to access and interpret critical water quality information at a glance. The schematic illustration of the web interface workflow is depicted in (Fig 5.4).

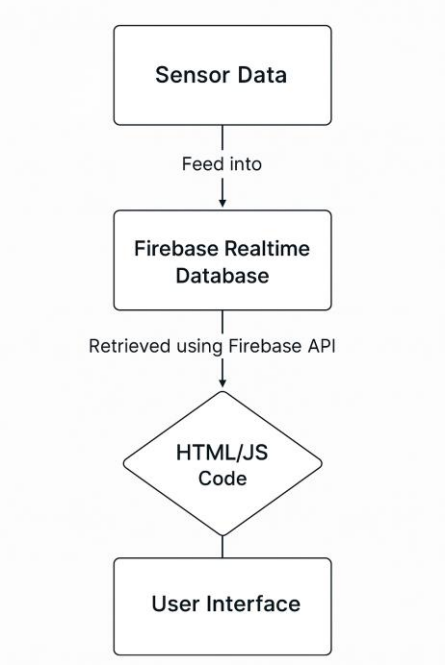

Fig 5. 4 Schematic illustration of the web interface workflow

ESP32 microcontroller receives data from sensors, processes it, and transmits it wirelessly to the Firebase cloud, which then updates the user interface in real-time.

5.3.3 End-user product and specifications

The fabricated real-time water monitoring device was a compact, self-contained system that integrated various sensors and components to provide comprehensive water quality data. The device was housed in a sturdy and buoyant PLA enclosure, measuring 130mm x 130mm x 130mm, designed to protect the internal components from environmental factors such as dust, moisture, and temperature fluctuations. At the heart of the system was the highly integrated ESP32 microcontroller, which served as the central processing unit and communication hub. The ESP32 collected and processed data from an array of sensors, including a BME280 module for measuring temperature, component area humidity, and atmospheric pressure, a DO sensor, a turbidity sensor, and a TDS sensor. These sensors were strategically integrated into the device, ensuring accurate and reliable measurements of various water quality parameters. The device was equipped with a GPS module, the NEO-6M, which provided location data, enabling users to associate the water quality information with specific geographical coordinates. This feature was particularly valuable for monitoring water sources across different locations. The power system of the device was designed for autonomous operation, combining a set of four rechargeable Lithium Polymer batteries (20,000mAh total capacity) with a solar energy harvesting system. Six solar panels, strategically mounted on the external walls of the PLA housing, collected solar energy to charge the batteries and directly power the device when

sufficient sunlight was available. This hybrid power system ensured the device could operate for extended periods without the need for external power sources, making it well-suited for remote or off-grid deployments. The device seamlessly integrated with a web-based interface, leveraging modern web technologies and libraries like Firebase®, Plotly.js, and Leaflet.js to provide a dynamic and user-friendly platform for data visualization and analysis. The web interface displayed real-time water quality data, including numerical values, interactive charts, and geographical maps, enabling users to monitor and assess the water conditions remotely.

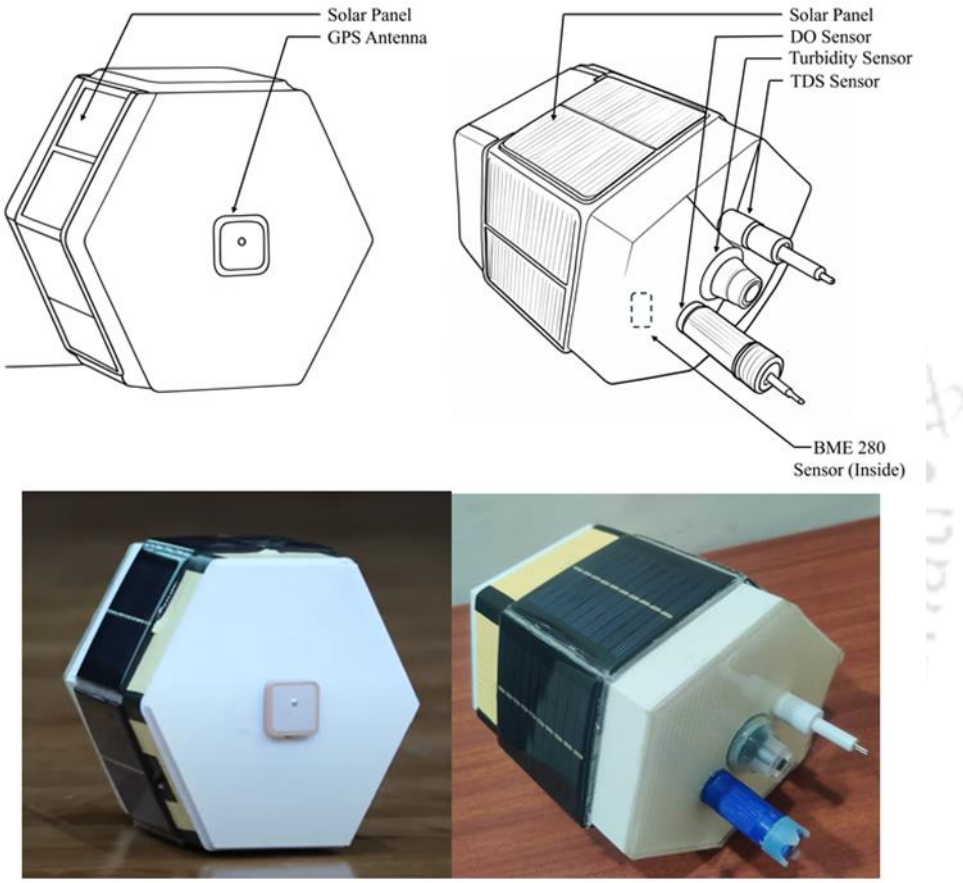

Fig 5. 5 Schematic & real illustration of final assembled product

Moreover, the nature of the data retrieval system made it AI and ML ready, facilitating the development of predictive models to regulate wastewater ejection into natural water bodies. The system ensured that the collected data was well-structured, accurate, and properly governed, adhering to the principles of AI-ready data. This enabled the development of predictive models that could learn patterns in water parameters, recognize trends, and trigger alerts and automated responses to adjust wastewater treatment processes accordingly. By leveraging RAG techniques, the models could also incorporate external knowledge and real-time data to provide more accurate and contextually relevant predictions. The schematic and

real illustration of the final assembled product is depicted in (Fig 5.5). The web interface of this framework is shown in (Fig 5.6).

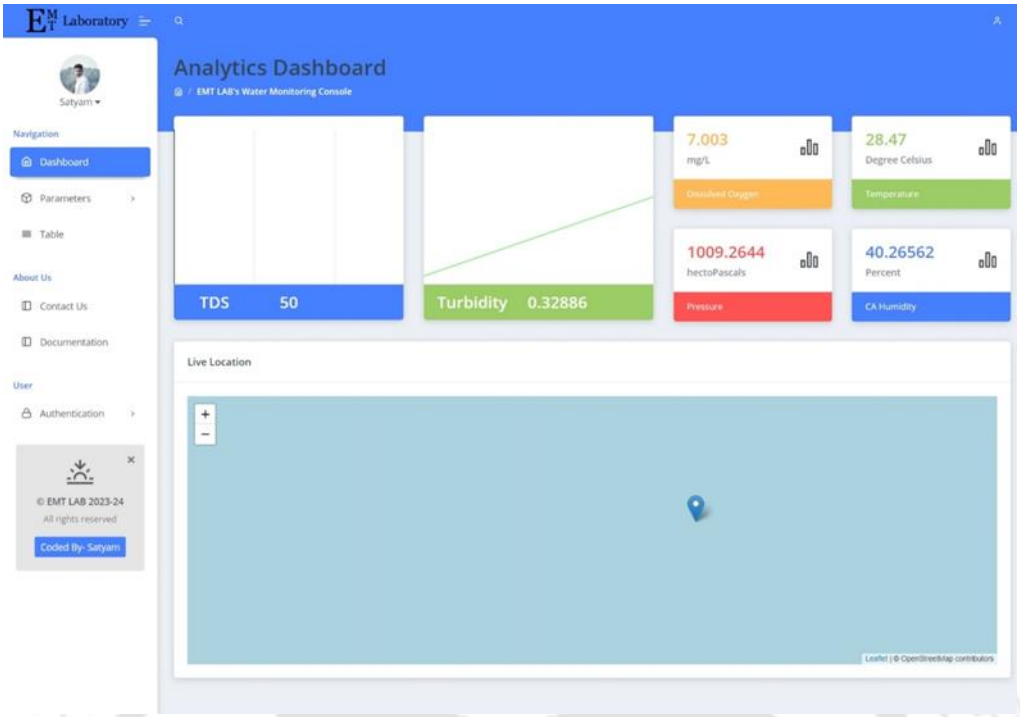

Fig 5. 6 Web interface of the IoT enabled realtime water monitoring system

5.4 Techno-economic analysis

The economic and technical feasibility of the developed real-time water monitoring system was a critical aspect of its design. Existing real-time monitoring solutions, though technologically advanced, are often burdened by high recurring costs such as subscription fees, server maintenance, and data storage, which make them inaccessible to many users. By utilizing open-source components and platforms, this system significantly reduced these costs. The integration of Firebase for real-time data management eliminated recurring server fees, while the use of affordable components like the ESP32 microcontroller and off-the-shelf sensors ensured cost-effectiveness without compromising performance. The hybrid power management approach of this system, combining solar panels and rechargeable lithium polymer batteries, further enhanced its economic appeal. This setup allowed for autonomous operation in remote or off-grid areas, reducing the need for external power sources and associated costs. The use of PLA for the device housing not only ensured durability but also minimized manufacturing costs while maintaining environmental sustainability. From a technical perspective, the system delivered high performance by continuously monitoring key water quality parameters such as temperature, dissolved oxygen, turbidity, and total dissolved solids, alongside geolocation data. Unlike proprietary systems, this device provided flexibility,

allowing users to adapt its configuration to specific monitoring needs. The AI and ML readiness of the system can add value by enabling predictive modeling for proactive water management, potentially reducing long-term operational costs. The combination of affordability, adaptability, and low operational costs positions this system as a sustainable alternative to existing real-time monitoring solutions, particularly in resource-constrained regions where access to advanced technologies is limited

5.5 Conclusion

Traditional water quality monitoring methods, reliant on manual sampling, laboratory analysis, and handheld devices, are labour-intensive, slow, and inadequate for dynamic water pollution challenges. While real-time sensors offer advanced capabilities, their high recurring costs, including subscription fees and server maintenance, hinder widespread adoption. The inflexibility of proprietary systems further limits their use, especially in resource-constrained regions. These challenges highlight the need for an affordable, adaptable, and energy-efficient real-time monitoring system without high recurring costs. The presented system integrated a microcontroller, multiparametric sensors, a GPS module, and a hybrid power management solution, housed within a compact, buoyant PLA casing. It enabled real-time monitoring of water parameters, including temperature, dissolved oxygen, turbidity, and total dissolved solids, while providing geolocation data for precise tracking of water quality across diverse sites. The hybrid power system, combining rechargeable lithium polymer batteries and solar panels, ensured extended autonomous operation, making the device ideal for off-grid deployments. A web-based interface, utilizing open-source platforms such as Firebase, Plotly.js, and Leaflet.js, enabled real-time data visualization and remote access. This eliminated recurring server costs and enhanced accessibility for resource-limited settings. The AI and ML readiness of the system can further facilitated predictive modeling and automated water management, enabling timely responses to water quality fluctuations. The developed real-time water monitoring device successfully addresses critical shortcomings of traditional and proprietary systems. By offering an energy-efficient, cost-effective, and adaptable solution, it empowers users with accurate, real-time data for informed decision-making. This innovative approach represents a significant step toward improving water resource management and environmental sustainability, particularly in areas where affordable and reliable monitoring is urgently needed.

Chapter 6. Conclusion and future perspectives

6.1 Conclusion

The global water crisis remains one of the most pressing challenges of our time, demanding innovative and sustainable solutions that balance technological feasibility with environmental responsibility. As articulated in the introductory chapter, the contamination of water bodies by organic, inorganic, microbial, and emerging pollutants underscores the urgency for effective and sustainable solutions. Traditional methods, while foundational, are limited in their capacity to address the diverse and dynamic nature of contemporary water quality challenges. Against this backdrop, this thesis has pursued an integrative approach to water treatment by addressing critical aspects such as the remediation of pollutants and the monitoring of water quality, focusing on four interconnected domains: advanced oxidation processes, enzymatic degradation of plastic pollutants, energy-efficient household water purification systems, and innovative water quality monitoring techniques, culminating in the development of novel technological and biological solutions to meet these pressing needs.

One of the primary investigations of this thesis centered on the development of a human Hu-XO coupled Fenton reaction system for advanced bio-oxidation of industrial pollutants. This innovative approach demonstrated significant potential in degrading complex organic contaminants commonly found in industrial wastewater. The study optimized the Hu-XO gene and successfully expressed it heterologously in *Pichia pastoris*, a yeast system known for efficient protein expression. This allowed the in situ production of hydrogen peroxide, a critical reagent in Fenton reactions, eliminating the need for external H_2O_2 addition, a key limitation of traditional Fenton processes. Experimental results confirmed the efficacy of the Hu-XO coupled system in reducing BOD and COD in industrial wastewater by 91.8% and 86%, respectively. These reductions represent a substantial improvement over conventional treatment methods. The system also achieved over 99% (100 mg/L) decolorization of CR, a persistent azo dye in textile industry wastewater. Advanced spectroscopic and mass spectrometric analyses revealed the breakdown of CR into less toxic byproducts, highlighting the system's capability for effective and comprehensive pollutant degradation. Beyond chemical pollutant removal, the Hu-XO coupled system exhibited potent antimicrobial properties. Stress assays, electron microscopy, and live/dead viability tests demonstrated its effectiveness in significantly reducing microbial loads in treated wastewater. The dual functionality of this system-chemical pollutant degradation and microbial inactivation-addresses two critical aspects of wastewater treatment simultaneously. Toxicity assessments, including bioluminescence inhibition using *Aliivibrio fischeri* and phytotoxicity tests on seeds,

confirmed the reduced environmental toxicity of treated samples, further validating the environmental benefits of the system. This novel enzyme-assisted Fenton process overcomes traditional challenges, such as high reagent costs, stringent pH requirements, and incomplete degradation pathways. Operating under milder pH conditions and leveraging in situ hydrogen peroxide production, the Hu-XO system represents a sustainable and efficient alternative for wastewater treatment. Its ability to degrade diverse organic pollutants and inactivate microbial contaminants underscores its potential for large-scale industrial applications, paving the way for more sustainable water treatment practices.

Building on enzymatic approaches to environmental remediation, the second objective of this thesis explored the potential of engineered enzymes for degrading PET, a persistent plastic pollutant. Extensive use of PET in packaging and textiles, combined with its resistance to degradation, has exacerbated global plastic pollution. Conventional recycling methods, including mechanical and chemical processes, often fall short due to high costs, energy requirements, and limited scalability. Enzymatic degradation offers a promising alternative, leveraging the catalytic specificity and efficiency of natural enzymes. The study focused on engineering the Mors1 enzyme from the Antarctic bacterium *Moraxella* TA144 to enhance its thermal stability and catalytic efficiency. Strategic mutations were introduced in the enzyme's turn regions, resulting in a mutant variant named Mors1^{MUT}. This engineered enzyme exhibited remarkable improvements in both pH and thermal stability. For instance, Mors1^{MUT} retained 98% activity at pH 9 and demonstrated robustness across acidic and alkaline conditions. This broadened pH stability enhances its applicability in diverse environmental settings. Thermal stability, a critical factor for practical applications, was significantly improved in Mors1^{MUT}. The enzyme retained 61% activity at 40°C and 14% at 50°C, whereas the wild-type enzyme was completely inactivated at these temperatures. This advancement enables efficient PET degradation at lower temperatures, reducing the energy demands typically associated with enzymatic recycling processes. Experimental validation through PET hydrolysis tests revealed a 4.16-fold increase in catalytic efficiency for Mors1^{MUT} compared to the wild-type enzyme. Analytical techniques, including gravimetric weight loss measurements and ATR-FTIR spectroscopy, confirmed the degradation of PET into monomeric byproducts. Structural analyses using CD spectroscopy indicated minimal changes in the secondary structure of Mors1^{MUT}, suggesting that the introduced mutations enhanced stability without compromising functional integrity of the enzyme. Kinetic studies further highlighted the enzyme's improved performance, with a higher V_{max} and a lower K_M compared to the wild-type variant. These findings underscore the potential of Mors1^{MUT} for large-scale PET degradation. The practical

implications of this research extend beyond enzymatic performance. Visual and quantitative analyses using SEM and AFM revealed pronounced surface roughness and degradation features on PET films treated with Mors1^{MUT}. These observations provide tangible evidence of the enzyme's efficacy in breaking down PET at a molecular level. While the engineered enzyme represents a significant advancement in enzymatic plastic recycling, it is essential to contextualize its role within a broader waste management framework. Addressing the plastic pollution crisis requires a multifaceted strategy encompassing reduction in plastic consumption, enhancement of waste management infrastructure, and development of sustainable packaging alternatives. Nonetheless, the insights gained from this research lay the groundwork for more sustainable and scalable enzymatic recycling technologies.

The third component of this thesis addressed the pressing need for safe drinking water, particularly in regions where municipal water treatment is inadequate or unreliable. Rapid urbanization, industrialization, and agricultural expansion have compromised water quality, often overwhelming existing treatment infrastructure. To tackle this issue, an innovative household water purification system was developed, integrating piezoelectric ultrasonic mist technology, thermoelectric Peltier modules, and UV-C sterilization. The system was designed with sustainability in mind, utilizing biodegradable PLA materials to minimize environmental impact. Its integration of piezoelectric ultrasonic mist technology and thermoelectric Peltier modules represents a breakthrough in energy-efficient water purification. Unlike traditional distillation methods, which are energy-intensive, this system achieves effective water vaporization and condensation with significantly lower energy input. Performance evaluations revealed the system's exceptional capability in removing a wide range of contaminants, including dissolved salts, microbial pathogens, dyes, and VOCs. Under optimal conditions, the system achieved an 83% water recovery efficiency, surpassing the performance of typical RO systems. This high recovery rate is particularly valuable in water-scarce regions, where resource conservation is paramount. The system demonstrated robust performance in removing NaCl at concentrations of up to 490 mg/L, making it suitable for treating saline water sources. Its efficacy in addressing microbial contamination was evident in its ability to eliminate *E. coli* at concentrations as high as 1.5×10^8 CFU/mL, ensuring microbiologically safe drinking water. Additionally, the system effectively removed CR dye at concentrations of up to 50 mg/L, addressing challenges associated with industrial dye pollutants. A notable advancement of this system lies in its ability to remove volatile organic compounds, specifically toluene and o-xylene, at concentrations of 60 µL/L. VOC removal has been a persistent challenge for many water purification technologies, including traditional distillation and RO systems. The

incorporation of a VOC escape valve in the design addresses this gap, ensuring comprehensive contaminant removal. The final stage of purification involves UV-C sterilization, which provides an additional layer of microbial safety. This multi-barrier approach enhances the system's reliability, making it a robust solution for household water purification. Its energy efficiency, combined with high contaminant removal efficacy, positions it as a viable alternative to conventional purification methods, particularly in decentralized settings.

Building on the themes of environmental monitoring and resource management, the final chapter of the thesis focused on the development of an IoT-enabled real-time water monitoring system. Recognizing the limitations of traditional laboratory-based methods and the financial barriers of proprietary systems, this research adopted an open-source approach to create an affordable and accessible device. The system integrates advanced sensors for parameters such as dissolved oxygen, turbidity, and total dissolved solids, alongside GPS capabilities and a hybrid power system combining solar energy with rechargeable batteries. A web-based interface provides real-time data visualization and remote accessibility, leveraging platforms like Firebase and Plotly.js to ensure user-friendly operation and cost efficiency. By supporting machine learning readiness, the system offers the potential for predictive analytics, enabling proactive water resource management in diverse environments, including resource-constrained settings. The challenges posed by water pollution and scarcity demand continued innovation and collaboration. The advancements presented in this thesis demonstrate the potential of bio-inspired and energy-efficient technologies to address these challenges, offering pathways toward a more sustainable future.

6.2 Future perspectives

The advancements presented in this thesis spanning innovative enzymatic degradation systems, energy-efficient water purification technologies, and IoT-enabled real-time monitoring represents significant progress toward addressing the various aspects of water pollution and sensing. However, the challenges of scalability, sustainability, and integration with existing infrastructures remain pivotal areas for future exploration.

Optimizing the extracellular expression of enzymes, such as the Hu-XO and the Mors1^{MUT}, could drastically reduce production costs and make enzymatic water treatment technologies more commercially viable. By improving the efficiency of enzyme expression systems, researchers could achieve higher yields with lower resource inputs, a critical step toward scaling enzymatic solutions for widespread use. Similarly, immobilizing enzymes onto stable carriers offers the potential for reuse in continuous processes, significantly enhancing their

sustainability. Immobilized enzymes not only retain their activity over multiple cycles but also enable large-scale operations that are crucial for addressing pervasive pollutants like industrial dyes and plastics. Research into novel immobilization materials, such as biopolymers or engineered nanostructures, could further optimize these systems for durability and cost-effectiveness. Scaling up these technologies for broader applications will require addressing technical and economic challenges. The Hu-XO–Fenton system and the Mors1^{MUT} have demonstrated impressive laboratory-scale efficacy but translating these results into industrial or municipal applications necessitates the development of robust pilot projects. Adapting these systems for different industrial settings such as textile, pharmaceutical, and food processing wastewater could unlock their potential to address specific sectoral challenges.

Integration with existing water treatment infrastructure is another promising avenue. By combining enzymatic degradation and IoT-based monitoring, hybrid systems could offer a more comprehensive approach to water quality management. For instance, IoT-enabled devices can provide real-time data on pollutant concentrations, guiding the precise application of enzymatic treatments. Such integration would not only enhance efficiency but also reduce operational costs by ensuring targeted interventions. Furthermore, centralized treatment plants could incorporate enzyme-assisted systems as pre-treatment or polishing steps, improving overall water treatment efficacy. Interdisciplinary collaborations will be essential in driving these innovations forward. The convergence of biology, chemistry, and engineering can lead to breakthroughs that address complex water quality challenges. Moreover, these efforts should align with global sustainability goals, ensuring affordability and accessibility, particularly for resource-constrained regions. By fostering partnerships between academia, industry, and policymakers, future research can bridge the gap between innovation and implementation.

Appendix

A. Media composition

The compositions of all media used in this research are presented in Table A1.

Table A. 1 Composition of different media used in this study

Medium	Composition	Application
Low salt LB medium	Tryptone -10 g/L Yeast extract - 5 g/L NaCl– 5 g/L	Growth of *E. coli*
YPD	Yeast extract - 10 g/L Peptone – 20 g/L Dextrose –20 g/L	Growth of *P. pastoris*
BMGY	Yeast extract - 10 g/L Peptone – 20 g/L Yeast Nitrogen Base – 13.4 g/L Biotin – 0.0004 g/L Glycerol – 10 g/L Phosphate Buffer (pH 6) – 100 mL	Primary medium for expression for recombinant *P. pastoris*
BMMY	Yeast extract - 10 g/L Peptone – 20 g/L Yeast Nitrogen Base – 13.4 g/L Biotin – 0.0004 g/L Methanol – 5 g/L Phosphate Buffer (pH 6) – 100 mL	Induction of recombinant *P. pastoris* for protein expression
Zobell marine agar	Peptone- 5 g/L Yeast extract- 1 g/L Ferric citrate- 0.10 g/L Sodium chloride- 19.45 g/L Magnesium chloride- 8.80 g/L Sodium sulphate- 3.24 g/L Calcium chloride- 1.80 g/L Potassium chloride- 0.55 g/L Sodium bicarbonate- 0.16 g/L Potassium bromide- 0.08 g/L Strontium chloride- 0.034 g/L Boric acid- 0.022 g/L Sodium silicate- 0.004 g/L Sodium fluorate- 0.0024 g/L Ammonium nitrate- 0.0016 g/L Disodium phosphate- 0.008 g/L Agar- 15.00 g/L Final pH- (at 25°C) : 7.6 ± 0.2	Growth and maintenance of *A. fischeri*
Photobacterium Broth	Casein enzymic hydrolysate 5 g/L Yeast extract 2.5 g/L Sodium chloride 30 g/L Ammonium chloride 0.3 g/L Magnesium	Bio-luminescence experiments with *A. fischeri*

	sulphate 0.3 g/L Ferric chloride 0.010 g/L Calcium carbonate 1 g/L Monopotassium dihydrogen phosphate 3 g/L Sodium glycerophosphate 23.5 g/L Final pH (at 25°C) 7.0±0.2

B. Molecular biology protocols

The molecular biology protocols used in this followed the methods described in the 2001 edition of *Molecular Cloning* by Sambrook and Russell. The standard procedures, with or without modifications, are outlined below.

B.1 Amplification of DNA by PCR

All DNA fragments were amplified using Q5 or Phusion high-fidelity polymerases (NEB). PCR was conducted in a 50 µL reaction volume using an Applied Biosystems system (Massachusetts, USA), following the manufacturer's recommended conditions.

B.2 Agarose gel electrophoresis

For DNA fragment analysis, 0.8% (w/v) agarose gels were prepared in 1X TAE buffer, with EtBr added to a final concentration of 0.25 µg/mL. DNA samples were mixed with 6X loading dye to aid in loading and tracking migration. Electrophoresis was performed at 90 V, and fragment separation was visualized using a Gel Doc system (Bio-Rad, Munich, Germany). The compositions of solutions used for agarose gel electrophoresis are listed in Table A.2.

Table A. 2 Composition of the solutions used for agarose gel electrophoresis

50X TAE Buffer	Tris base	24.2g
	Glacial acetic acid	5.71 mL
	0.5M EDTA (pH 8)	10 mL
	Deionized water	Make up to 100ml
6X Gel Loading Dye	Glycerol	1.5 mL (100% Glycerol)
	EDTA	1.32 mL of 0.5M EDTA
	Tris	0.198 ml of 1M Tris (pH 8.0)
	SDS	0.102 mL OF 10% SDS
	Bromophenol Blue	0.009 g
	Deionized water	Make up to 10 mL

EtBr Solution (10 mL)	Ethidium bromide	10 mg
	Deionized water	Make up to 1 mL

B.3 Purification of PCR products and plasmid fragments

Following PCR or plasmid digestion, the desired DNA fragment was extracted from the gel and purified using the PCR cleanup and gel extraction kit (Macherey-Nagel, Düren, Germany) according to the manufacturer's guidelines.

B.4 Plasmid DNA isolation

Plasmid DNA of high quality, intended for the transformation of *E. coli* and *P. pastoris*, was extracted from *E. coli* DH5α harbouring the respective plasmid using the Mini Prep Kit (Macherey-Nagel, Düren, Germany) following the manufacturer's protocol. Deionized water was used for DNA elution from the columns.

B.5 *E. coli* transformation using $CaCl_2$ method

The transformation of *E. coli* DH5α was carried out using the heat shock method as described in *Molecular Cloning* by Sambrook and Russell. An overnight *E. coli* DH5α culture was used to inoculate 100 mL of low-salt LB medium and incubated at 37 °C until the optical density at 600 nm (OD_{600}) reached 0.4. The culture was then transferred into sterile 50 mL centrifuge tubes, placed on ice for 10 minutes, and centrifuged at 4000 × g for 10 minutes at 4 °C. The supernatant was carefully discarded, and the pellet was gently resuspended in 30 mL of ice-cold $MgCl_2$-$CaCl_2$ solution (80 mM $MgCl_2$ and 20 mM $CaCl_2$). After another round of centrifugation under the same conditions, the supernatant was removed, and the pellet was resuspended in 2 mL of ice-cold 0.1 M $CaCl_2$ per 50 mL of the initial culture. Glycerol was added to a final concentration of 15% (v/v) and mixed gently. Aliquots of 150 µL were transferred into sterile 1.5 mL Eppendorf tubes and stored at -80 °C for future use.

Frozen competent *E. coli* DH5α cells were retrieved from the -80 °C freezer and placed on ice for 15 minutes to thaw. Recombinant plasmid DNA was then added to the cells, followed by incubation on ice for 15 minutes with gentle mixing every 5 minutes. The mixture was subjected to a heat shock at 42 °C for 1 minute and then immediately returned to ice for another minute. To facilitate recovery, 1 mL of sterile LB medium was added, and the culture was incubated at 37 °C for 1 hour with shaking at 2000 × g. The cells were then centrifuged at 5000

rpm for 10 minutes at room temperature, and the resulting pellet was plated on LB agar supplemented with 25 µg/mL Zeocin for selection.

B.6 Protein expression analysis using SDS-PAGE

Protein samples were prepared by mixing 30 µL of the sample with 10 µL of 4X SDS loading buffer, followed by heating at 95°C for 5 minutes to ensure denaturation. Gel plates were assembled according to the manufacturer's guidelines, and a 12% resolving gel was prepared using the composition listed in Table A.3. The acrylamide solution was poured between the glass plates, leaving space for the stacking gel. Once polymerized, the stacking gel was prepared as per Table A3, poured over the resolving gel, and a comb was inserted.

After solidification, the gel was mounted into the electrophoresis apparatus, and 10X Tris-Glycine buffer was added to both reservoirs. Protein samples were further prepared by mixing 10 µL of the sample with 7 µL of loading dye, followed by heating at 95°C for 5 minutes. After electrophoresis, the gel was carefully removed and stained with Coomassie Brilliant Blue R-250. The staining solution was prepared by dissolving 0.3 g of Coomassie Brilliant Blue R-250 in 200 mL of a 5:4:1 mixture of water, methanol, and glacial acetic acid. The gel was incubated in the staining solution at room temperature for 4 hours, followed by destaining in the same solvent mixture for approximately 6 hours.

Table A. 3 Resolving and stacking gel composition

Component	Volume (mL) for Resolving gel	Volume (mL) for Stacking gel
H_2O	1.6	1.4
30% Acrylamide	2.0	0.34
1.5 M Tris (pH 8)	1.3	0.25
10% SDS	0.05	0.02
10% APS	0.05	0.02
TEMED	0.002	0.002
Total Volume	5	2

C. Sequences used in this study

C.1 Hu-XDH

ATGACTGCTGATAAGTTGGTTTTCTTTGTTAACGGTAGAAAGGTTGTTGAAAAGAATGCTGATCCTGAGACTACTTTGTTGG
CTTACTTGAGAAGAAAATTGGGTTTGTCTGGTACTAAGTTGGGTTGTGGTGAAGGTGGTTGTGGTGCTTGTACTGTTATGTT

GTCTAAGTACGATAGATTGCAAAACAAGATCGTTCATTTCTCTGCTAACGCTTGTTTGGCTCCAATTTGTTCTTTGCATCAC
GTTGCTGTTACTACTGTTGAAGGTATTGGTTCTACTAAAACTAGATTGCATCCTGTTCAAGAGAGAATTGCTAAGTCTCACG
GTTCTCAATGTGGTTTTTGTACTCCTGGTATTGTTATGTCTATGTACACTTTGTTGAGAAACCAACCAGAACCTACTATGGA
AGAGATTGAGAACGCTTTCCAGGGTAATTTGTGTAGATGTACTGGTTATAGACCTATTTTGCAAGGTTTCAGAACTTTTGCT
AGAGATGGTGGTTGTTGTGGTGGAGATGGTAACAACCCAAACTGTTGTATGAACCAAAAGAAAGATCACTCTGTTTCTCTTT
CTCCATCTTTGTTTAAGCCTGAAGAGTTCACTCCATTGGATCCTACTCAAGAACCTATTTTTCCACCTGAGTTGTTGAGATT
GAAAGATACTCCAAGAAAGCAATTGAGATTCGAAGGAGAGAGAGTTACTTGGATTCAAGCTTCTACTTTGAAGGAATTGTTG
GATTTGAAGGCTCAACATCCTGATGCTAAGTTGGTTGTTGGTAACACTGAAATCGGTATCGAGATGAAGTTTAAGAACATGT
TGTTCCCAATGATCGTTTGTCCAGCTTGGATTCCTGAATTGAACTCTGTTGAGCACGGTCCTGATGGTATTTCTTTTGGTGC
TGCTTGTCCATTGTCTATTGTTGAAAAGACTTTGGTTGATGCTGTTGCTAAATTGCCAGCTCAAAAGACTGAAGTTTTTAGA
GGTGTTTTGGAGCAATTGAGATGGTTCGCTGGTAAACAGGTTAAGTCTGTTGCTTCTGTTGGTGGTAACATTATTACTGCTT
CTCCAATTTCTGATTTGAATCCTGTTTTCATGGCTTCTGGTGCTAAGTTGACTTTGGTTTCTAGAGGTACTAGAAGAACTGT
TCAAATGGATCATACTTTCTTTCCTGGTTACAGAAAAACTTTGTTGTCTCCAGAAGAGATCTTGTTGTCTATCGAAATCCCT
TACTCTAGAGAAGGAGAGTATTTCTCTGCTTTTAAGCAAGCTTCTAGAAGAGAGGATGATATTGCTAAAGTTACTTCTGGTA
TGAGAGTTTTGTTTAAGCCAGGTACTACTGAAGTTCAAGAGTTGGCTTTGTGTTATGGTGGTATGGCTAACAGAACTATTTC
TGCTTTGAAGACTACTCAAAGACAATTGTCTAAATTGTGGAAGGAAGAGTTGTTGCAAGATGTTTGTGCTGGTTTGGCTGAA
GAGTTGCACTTGCCACCTGATGCTCCAGGTGGTATGGTTGATTTCAGATGTACTTTGACTTTGTCTTTCTTTTTCAAGTTCT
ACTTGACTGTTTTGCAAAAGTTGGGTCAAGAAAATTTGGAGGATAAGTGTGGTAAATTGGATCCTACTTTTGCTTCTGCTAC
TTTGTTGTTCCAAAAAGATCCACCTGCTGATGTTCAATTGTTTCAAGAAGTTCCAAAGGGTCAATCTGAAGAGGATATGGTT
GGTAGACCATTGCCTCATTTGGCTGCTGATATGCAAGCTTCTGGAGAGGCTGTTTACTGTGATGATATTCCTAGATACGAAA
ACGAGTTGTCTTTGAGATTGGTTACTTCTACTAGAGCTCACGCTAAAATTAAGTCTATCGATACTTCTGAAGCTAAGAAAGT
TCCTGGTTTCGTTTGTTTTATTTCTGCTGATGATGTTCCAGGTTCTAACATCACTGGTATCTGTAACGATGAGACTGTTTTC
GCTAAAGATAAGGTTACTTGTGTTGGTCATATTATTGGTGCTGTTGTTGCTGATACTCCAGAACACACTCAAAGAGCTGCTC
AAGGTGTTAAAATTACTTACGAAGAGTTGCCTGCTATCATCACTATCGAGGATGCTATTAAGAACAACTCTTTCTACGGTCC
AGAATTGAAGATCGAGAAGGGAGATTTGAAGAAGGGTTTCTCTGAAGCTGATAATGTTGTTTCTGGAGAGATCTACATTGGT
GGTCAAGAACATTTTTATTTGGAGACTCACTGTACTATTGCTGTTCCTAAGGGTGAAGCTGGTGAAATGGAGTTGTTCGTTT
CTACTCAAAACACTATGAAGACTCAATCTTTCGTTGCTAAGATGTTGGGTGTTCCAGCTAACAGAATCGTTGTTAGAGTTAA
GAGAATGGGTGGTGGTTTCGGTGGTAAAGAAACTAGATCTACTGTTGTTTCTACTGCTGTTGCTTTGGCTGCTTACAAAACT
GGTAGACCTGTTAGATGTATGTTGGATAGAGATGAAGATATGTTGATTACTGGTGGTAGACATCCATTTTTGGCTAGATACA
AGGTTGGTTTCATGAAGACTGGTACTGTTGTTGCTTTGGAAGTTGATCATTTCTCTAACGTTGGTAACACTCAAGATTTGTC
TCAATCTATCATGGAGAGAGCTTTGTTCCACATGGATAACTGTTACAAGATCCCAAACATCAGAGGTACTGGTAGATTGTGT
AAGACTAACTTGCCTTCTAATACTGCTTTCAGAGGTTTTGGTGGTCCACAAGGAATGTTGATTGCTGAATGTTGGATGTCTG
AGGTTGCTGTTACTTGTGGTATGCCTGCTGAAGAGGTTAGAAGAAAGAACTTGTACAAGGAAGGAGATTTGACTCATTTCAA
CCAAAAGTTGGAGGGTTTCACTTTGCCAAGATGTTGGGAAGAGTGTTTGGCTTCTTCTCAATATCACGCTAGAAAGTCTGAA
GTTGATAAGTTTAACAAGGAGAACTGTTGGAAGAAAAGAGGTTTGTGTATCATCCCTACTAAGTTCGGTATTTCTTTTACTG
TTCCATTCTTGAACCAAGCTGGTGCTTTGTTGCATGTTTACACTGATGGTTCTGTTTTGTTGACTCATGGTGGTACTGAAAT
GGGTCAAGGTTTGCACACTAAGATGGTTCAAGTTGCTTCTAGAGCTTTGAAGATCCCAACTTCTAAGATCTACATCTCTGAA
ACTTCTACTAACACTGTTCCAAATACTTCTCCTACTGCTGCTTCTGTTTCTGCTGATTTGAACGGTCAAGCTGTTTACGCTG
CTTGTCAAACTATCTTGAAGAGATTGGAACCATACAAGAAAAAGAATCCTTCTGGTTCTTGGGAGGATTGGGTTACTGCTGC
TTACATGGATACTGTTTCTTTGTCTGCTACTGGTTTTTACAGAACTCCTAACTTGGGTTATTCTTTCGAAACTAACTCTGGT

AATCCATTCCATTACTTTTCTTATGGTGTTGCTTGTTCTGAAGTTGAGATTGATTGTTTGACTGGAGATCACAAGAACTTGA
GAACTGATATTGTTATGGATGTTGGTTCTTCTTTGAATCCTGCTATTGATATTGGTCAAGTTGAAGGTGCTTTTGTTCAAGG
TTTGGGTTTGTTCACTTTGGAAGAGTTGCATTACTCTCCAGAGGGTTCTTTGCATACTAGAGGTCCATCTACTTATAAGATT
CCTGCTTTTGGTTCTATCCCAATCGAATTCAGAGTTTCTTTGTTGAGAGATTGTCCAAACAAGAAGGCTATCTACGCTTCTA
AAGCTGTTGGAGAGCCACCTTTGTTTTTGGCTGCTTCTATTTTCTTTGCTATTAAAGATGCTATTAGAGCTGCTAGAGCTCA
ACATACTGGTAACAACGTTAAGGAATTGTTTAGATTGGATTCTCCAGCTACTCCTGAGAAAATTAGAAACGCTTGTGTTGAT
AAGTTCACTACTTTGTGTGTTACTGGTGTTCCAGAAAATTGTAAGCCTTGGTCTGTTAGAGTCGTTGATCATCACCATCACC
ATCACTAA

C.2 Mors1^{WT}

ATGTTCATCATGATTAAGAAATCTGAATTGGCTAAGGCTATCATCGTTACTGGTGCTTTGGTTTTCTCTATTCCAACTTTGG
CTGAAGTTACTTTGTCTGAGACTACTGTTTCTTCTATTAAATCTGAGGCTACTGTTTCTTCTACTAAGAAAGCTTTGCCAGC
TACTCCTTCTGATTGTATTGCTGATTCTAAGATTACTGCTGTTGCTTTGTCTGATACTAGAGATAACGGTCCATTTTCTATC
AGAACTAAGAGAATCTCTAGACAATCTGCTAAAGGTTTCGGTGGTGGTACTATTCATTACCCTACTAACGCTTCTGGTTGTG
GTTTGTTGGGTGCTATTGCTGTTGTTCCAGGTTACGTTTCTTACGAAAATTCTATTAAGTGGTGGGGTCCTAGATTGGCTTC
TTGGGGTTTCGTTGTTATTACTATTAACACTAATTCTATCTACGATGATCCAGATTCTAGAGCTGCTCAATTGAACGCTGCT
TTGGATAATATGATTGCTGATGATACTGTTGGTTCTATGATTGATCCTAAAAGATTGGGTGCTATTGGTTGGTCTATGGGTG
GTGGTGGTGCTTTGAAGTTGGCTACTGAAAGATCTACTGTTAGAGCTATTATGCCATTGGCTCCTTACCATGATAAGTCTTA
TGGAGAGGTTAAAACTCCAACTTTGGTTATTGCTTGTGAAGATGATAGAATTGCTGAGACTAAGAAATACGCTAACGCTTTC
TACAAGAACGCTATCGGTCCTAAGATGAAGGTTGAAGTTAACAATGGTTCTCACTTTTGTCCATCTTACAGATTCAATGAGA
TCTTGTTGTCTAAGCCTGGTATTGCTTGGATGCAAAGATACATCAACAACGATACTAGATTCGATAAGTTCTTGTGTGCTAA
CGAGAACTACTCTAAGTCTCCAAGAATCTCTGCTTACGATTATAAGGATTGTCCTGTCGACCATCATCATCATCATCATTGA

C.3 Mors1^{MUT}

ATGTTCATCATGATTAAGAAATCTGAATTGGCTAAGGCTATCATCGTTACTGGTGCTTTGGTTTTCTCTATTCCAACTTTGG
CTGAAGTTACTTTGTCTGAGACTACTGTTTCTTCTATTAAATCTGAGGCTACTGTTTCTTCTACTAAGAAAGCTTTGCCAGC
TACTCCTTCTGATTGTATTGCTGATTCTAAGATTACTGCTGTTGCTTTGTCTGATACTAGAGATAACGGTCCATTTTCTATC
AGAACTAAGAGAATCTCTAGACAATCTGCTATTGGTTTCGGTGGTGGTACTATTCATTACCCTACTAACGCTTCTGGTTGTG
GTTTGTTGGGTGCTATTGCTGTTGTTCCAGGTTACGTTTCTTACGAAAATTCTATTAAGTGGTGGGGTCCTAGATTGGCTTC
TTGGGGTTTCGTTGTTATTACTATTAACACTAATTCTATCTACGATGATCCAGATTCTAGAGCTGCTCAATTGAACGCTGCT
TTGGATAATATGATTGCTGATGATACTGTTGGTTCTATGATTGATCCTAAAAGATTGGGTGCTATTGGTTGGTCTATGGGTG
GTGGTGGTGCTTTGAAGTTGGCTACTGAAAGATCTACTGTTAGAGCTATTATGCCATTGGCTCCTTACCATGATAAGTCTTA
TGGAATTGTTAAAACTCCAACTTTGGTTATTGCTTGTGAAGATGATTTCATTGCTGAGACTAAGAAATACGCTAACGCTTTC
TACAAGAACGCTATCGGTCCTAAGATGAAGGTTGAAGTTAACAATGGTTCTCACTTTTGTCCATCTTACAGATTCAATGAGA
TCTTGTTGTCTAAGCCTGGTATTGCTTGGATGCAAAGATACATCAACAACGATACTAGATTCGATAAGTTCTTGTGTGCTAA
CGAGAACTACTCTAAGTCTCCAAGAATCTCTGCTTACGATTATAAGGATTGTCCTGTCGACCATCATCATCATCATCATTGA

D. Programming code used in this research work

D.1 ESP32 Code

```
#include <Arduino.h>
```

```
#include <TinyGPSPlus.h>
#if defined(ESP32)
#include <WiFi.h>
#elif defined(ESP8266)
#include <ESP8266WiFi.h>
#endif
#include <Firebase_ESP_Client.h>
#include <Wire.h>
#include <Adafruit_Sensor.h>
#include <Adafruit_BME280.h>
#include "addons/TokenHelper.h"
#include "addons/RTDBHelper.h"
#define WIFI_SSID "Sam"
#define WIFI_PASSWORD "*******"
#define API_KEY "AIzaSyDz4ZcFUBou3megQ7P02b26_UsimHw2****"
#define USER_EMAIL "satyam19@iitg.ac.in"
#define USER_PASSWORD "*******"
#define DATABASE_URL "https://emtlab-sam-sensor-default-rtdb.asia-
southeast1.firebasedatabase.app/"
FirebaseData fbdo;
FirebaseAuth auth;
FirebaseConfig config;
String uid;
String databasePath;
String tempPath, humPath, presPath, doPath, turbidityPath, tdsPath, gpsLatPath,
gpsLngPath;
Adafruit_BME280 bme;
float temperature, humidity, pressure;
int doPin = 34, turbidityPin = 35, tdsPin = 32;
float doValue = 0, turbidityValue = 0, tdsValue = 0;
float doCalibrationOffset = 0, tdsCalibrationOffset = 0;
unsigned long sendDataPrevMillis = 0;
unsigned long timerDelay = 20;
// GPS
TinyGPSPlus gps;
HardwareSerial GPSSerial(2);

void initBME() {
if (!bme.begin(0x76)) {
Serial.println("Could not find a valid BME280 sensor, check wiring!");
while (1);
} else {
Serial.println("BME280 sensor initialized successfully.");
}
}
void initWiFi() {
WiFi.begin(WIFI_SSID, WIFI_PASSWORD);
Serial.print("Connecting to WiFi ..");
while (WiFi.status() != WL_CONNECTED) {
Serial.print('.');
delay(1000);
}
Serial.println(WiFi.localIP());
Serial.println("WiFi connected.");
}
void sendFloat(String path, float value) {
if (Firebase.RTDB.setFloat(&fbdo, path.c_str(), value)) {
Serial.print("Sending value: ");
Serial.print(value);
```

```
Serial.print(" to path: ");
Serial.println(path);
}
else {
Serial.print("Failed to send data to ");
Serial.print(path);
Serial.print(": ");
Serial.println(fbdo.errorReason());
}
}
// Custom function for mapping values with decimal precision
float mapFloat(float x, float in_min, float in_max, float out_min, float out_max)
{
return (x - in_min) * (out_max - out_min) / (in_max - in_min) + out_min;
}
void setup() {
Serial.begin(115200);
GPSSerial.begin(9600); // Initialize GPS Serial
initBME();
initWiFi();
config.api_key = API_KEY;
auth.user.email = USER_EMAIL;
auth.user.password = USER_PASSWORD;
config.database_url = DATABASE_URL;
Firebase.reconnectWiFi(true);
fbdo.setResponseSize(4096);
config.token_status_callback = tokenStatusCallback;
config.max_token_generation_retry = 5;
Firebase.begin(&config, &auth);

Serial.println("Getting User UID");
while ((auth.token.uid) == "") {
Serial.print('.');
delay(1000);
}
uid = auth.token.uid.c_str();
Serial.print("User UID: ");
Serial.println(uid);

databasePath = "/UsersData/" + uid;
tempPath = databasePath + "/temperature";
humPath = databasePath + "/humidity";
presPath = databasePath + "/pressure";
doPath = databasePath + "/do";
turbidityPath = databasePath + "/turbidity";
tdsPath = databasePath + "/tds";
gpsLatPath = databasePath + "/gps/latitude";
gpsLngPath = databasePath + "/gps/longitude";

Serial.println("Setup complete.");
}
void loop() {
if (Firebase.ready() && (millis() - sendDataPrevMillis > timerDelay ||
sendDataPrevMillis == 0)) {
sendDataPrevMillis = millis();

temperature = bme.readTemperature();
humidity = bme.readHumidity();
pressure = bme.readPressure() / 100.0F;
```

```
doValue = analogRead(doPin);
doValue = (doValue + 5300) / 1000.0; // Modified DO reading calculation
tdsValue = analogRead(tdsPin); // Raw TDS reading
turbidityValue = analogRead(turbidityPin); // Read turbidity value directly from
pin 35
float voltage = turbidityValue * (3.3 / 4095.0); // Convert to voltage based on
ESP32's 12-bit ADC
Serial.print("Turbidity Voltage: "); Serial.println(voltage);
Serial.print("Temperature: "); Serial.println(temperature);
Serial.print("Humidity: "); Serial.println(humidity);
Serial.print("Pressure: "); Serial.println(pressure);
Serial.print("DO Value: "); Serial.println(doValue);
Serial.print("Turbidity Value: "); Serial.println(voltage);
Serial.print("TDS Value: "); Serial.println(tdsValue);
sendFloat(tempPath, temperature);
sendFloat(humPath, humidity);
sendFloat(presPath, pressure);
sendFloat(doPath, doValue);
sendFloat(turbidityPath, voltage); // Send the turbidity voltage
sendFloat(tdsPath, tdsValue);
while (GPSSerial.available() > 0) {
if (gps.encode(GPSSerial.read())) {
if (gps.location.isValid()) {
float lat = gps.location.lat();
float lng = gps.location.lng();
Serial.print("Latitude: "); Serial.println(lat, 6);
Serial.print("Longitude: "); Serial.println(lng, 6);
sendFloat(gpsLatPath, lat);
sendFloat(gpsLngPath, lng);
} else {
Serial.println("GPS location not valid.");
}
}
}
delay(2000);
} else {
Serial.println("Firebase not ready.");
}
}
```

D.2 HTLM Code (without layout)

```
<!DOCTYPE html>
<html lang="en">
<head>
<meta charset="UTF-8">
<meta name="viewport" content="width=device-width, initial-scale=1.0">
<title>Real-time Water Monitoring System</title>
<!-- External Libraries -->
<link rel="stylesheet" href="https://unpkg.com/leaflet@1.7.1/dist/leaflet.css" />
<script src="https://unpkg.com/leaflet@1.7.1/dist/leaflet.js"></script>
<script src="https://www.gstatic.com/firebasejs/8.4.1/firebase-app.js"></script>
<script src="https://www.gstatic.com/firebasejs/8.4.1/firebase-
database.js"></script>
<script src="https://cdn.plot.ly/plotly-latest.min.js"></script>
<style>
.dashboard {
```

```
max-width: 1200px;
margin: 20px auto;
padding: 20px;
}
.sensor-grid {
display: grid;
grid-template-columns: repeat(auto-fit, minmax(250px, 1fr));
gap: 20px;
margin: 20px 0;
}
.sensor-card {
padding: 15px;
border-radius: 8px;
background: #f5f5f5;
}
#map {
height: 400px;
margin-top: 20px;
}
.chart-container {
height: 250px;
margin: 20px 0;
}
</style>

<script>
// Firebase Configuration
const firebaseConfig = {
apiKey: "AIzaSyDz4ZcFUBou3megQ7P02b26_UsimHw2knQ",
authDomain: "emtlab-sam-sensor.firebaseapp.com",
databaseURL: "https://emtlab-sam-sensor-default-rtdb.asia-
Southeast1.firebasedatabase.app",
            projectId: "emtlab-sam-sensor",
            storageBucket: "emtlab-sam-sensor.appspot.com",
            messagingSenderId: "1085693974125",
            appId: "1:1085693974125:web:7e6b487ddaea882d169164"
};
firebase.initializeApp(firebaseConfig);

// Firebase References
        const dbRef =
firebase.database().ref('UsersData/qXPTkurbJTf4JI4PV0Hvp7lbtfJ2');
        const sensors = {
            temp: dbRef.child('temperature'),
            hum: dbRef.child('humidity'),
            pres: dbRef.child('pressure'),
            tds: dbRef.child('tds'),
            turb: dbRef.child('turbidity'),
            do: dbRef.child('do'),
            lat: dbRef.child('gps/latitude'),
            lon: dbRef.child('gps/longitude')
};
</script>
</head>
<body>
<div class="dashboard">
<h1>Real-time Water Quality Monitoring Dashboard</h1>
<!-- Sensor Charts -->
<div class="chart-container" id="tdsChart"></div>
```

```
<div class="chart-container" id="turbidityChart"></div>
<!-- Sensor Values Grid -->
<div class="sensor-grid">
<div class="sensor-card">
<h3>Dissolved Oxygen <span id="do"></span></h3>
<p>mg/L</p>
</div>
<div class="sensor-card">
<h3>Temperature <span id="temperature"></span></h3>
<p>°C</p>
</div>
<div class="sensor-card">
<h3>Pressure <span id="pressure"></span></h3>
<p>hPa</p>
</div>
<div class="sensor-card">
<h3>Humidity <span id="humidity"></span></h3>
<p>%</p>
</div>
</div>
<!-- Location Map -->
<div id="map"></div>
</div>
<script>
// Chart Initialization
const initializeChart = (elementId, color) => ({
x: [], y: [],
type: 'scatter',
mode: 'lines',
line: {shape: 'spline', smoothing: 1.3, color}
});
const tdsTrace = initializeChart('tdsChart', '#2196F3');
const turbTrace = initializeChart('turbidityChart', '#4CAF50');
Plotly.newPlot('tdsChart', [tdsTrace], {
margin: {t: 0, b: 0, l: 0, r: 0},
yaxis: {showgrid: false, fixedrange: true}
});
// Map Initialization
const map = L.map('map').setView([0, 0], 13);
L.tileLayer('https://{s}.tile.openstreetmap.org/{z}/{x}/{y}.png').addTo(map);
const marker = L.marker([0, 0]).addTo(map);
// Real-time Updates
Object.entries(sensors).forEach(([key, ref]) => {
ref.on('value', snapshot => {
if (key === 'lat' || key === 'lon') {
const lat = sensors.lat._value || 0;
const lng = sensors.lon._value || 0;
marker.setLatLng([lat, lng]);
map.panTo([lat, lng]);
} else {
document.getElementById(key === 'pres' ?
'pressure' : key).textContent = snapshot.val();
}
});
});
</script>
</body>
</html>
```

Bibliography

1. Ahmed, S.F.; Kumar, P.S.; Kabir, M.; Zuhara, F.T.; Mehjabin, A.; Tasannum, N.; Hoang, A.T.; Kabir, Z.; Mofijur, M. Threats, Challenges and Sustainable Conservation Strategies for Freshwater Biodiversity. *Environ Res* **2022**, *214*, 113808, doi:10.1016/J.ENVRES.2022.113808.

2. Ahmad, N.B.; Jaafaru, M.S.; Isa, Z.; Abdulhamid, Y.; Kakudi, R.A.; Ugya, A.Y.; Meguellati, K. High Pollution Loads Engineer Oxygen Dynamics, Ecological Niches, and Pathogenicity Shifts in Freshwater Environments. *Journal of Hazardous Materials Advances* **2024**, *14*, 100425, doi:10.1016/J.HAZADV.2024.100425.

3. Issac, M.N.; Kandasubramanian, B. Effect of Microplastics in Water and Aquatic Systems. *Environmental Science and Pollution Research 2021 28:16* **2021**, *28*, 19544–19562, doi:10.1007/S11356-021-13184-2.

4. Ferreira, D.C.; Graziele, I.; Marques, R.C.; Gonçalves, J. Investment in Drinking Water and Sanitation Infrastructure and Its Impact on Waterborne Diseases Dissemination: The Brazilian Case. *Science of The Total Environment* **2021**, *779*, 146279, doi:10.1016/J.SCITOTENV.2021.146279.

5. Bhuiyan, M.M.U.; Rahman, M.; Naher, S.; Shahed, Z.H.; Ali, M.M.; Islam, A.R.M.T. Oxygen Declination in the Coastal Ocean over the Twenty-First Century: Driving Forces, Trends, and Impacts. *Case Studies in Chemical and Environmental Engineering* **2024**, *9*, 100621, doi:10.1016/J.CSCEE.2024.100621.

6. Kim, H.; Franco, A.C.; Sumaila, U.R. A Selected Review of Impacts of Ocean Deoxygenation on Fish and Fisheries. *Fishes 2023, Vol. 8, Page 316* **2023**, *8*, 316, doi:10.3390/FISHES8060316.

7. Satyam, S.; Patra, S. Innovations and Challenges in Adsorption-Based Wastewater Remediation: A Comprehensive Review. *Heliyon* **2024**, *10*, doi:10.1016/J.HELIYON.2024.E29573.

8. Ahmad, A.; Azam, T. Water Purification Technologies. *Bottled and Packaged Water* **2019**, 83–120, doi:10.1016/B978-0-12-815272-0.00004-0.

9. Satyam; Gangar, T.; Hazarika, R.; Patra, S. Emerging Role of Internet of Things (IoT) for Wastewater Management : Sensing, Treatment and Process Optimization. *Emerging Technologies in Wastewater Treatment* **2023**, 85–98, doi:10.1201/9781003164982-6.

10. Satyam; Mukherjee, P. Implications of Progressive Data Transfer Technologies for IoTBased Wastewater Management in Smart Cities. *Applications of 5G and Beyond in Smart Cities* **2023**, 129–142, doi:10.1201/9781003227861-8/IMPLICATIONS-PROGRESSIVE-DATA-TRANSFER-TECHNOLOGIES-IOT-BASED-WASTEWATER-MANAGEMENT-SMART-CITIES-SATYAM-PAYAL-MUKHERJEE.

11. Madhav, S.; Ahamad, A.; Singh, A.K.; Kushawaha, J.; Chauhan, J.S.; Sharma, S.; Singh, P. Water Pollutants: Sources and Impact on the Environment and Human Health. **2020**, 43–62, doi:10.1007/978-981-15-0671-0_4.

12. Borah, P.; Kumar, M.; Devi, P. Types of Inorganic Pollutants: Metals/Metalloids, Acids, and Organic Forms. *Inorganic Pollutants in Water* **2020**, 17–31, doi:10.1016/B978-0-12-818965-8.00002-0.

13. Han, J.; Xin, Z.; Han, F.; Xu, B.; Wang, L.; Zhang, C.; Zheng, Y. Source Contribution Analysis of Nutrient Pollution in a P-Rich Watershed: Implications for Integrated Water Quality Management. *Environmental Pollution* **2021**, *279*, 116885, doi:10.1016/J.ENVPOL.2021.116885.

14. Shayo, G.M.; Elimbinzi, E.; Shao, G.N.; Fabian, C. Severity of Waterborne Diseases in Developing Countries and the Effectiveness of Ceramic Filters for Improving Water Quality. *Bulletin of the National Research Centre 2023 47:1* **2023**, *47*, 1–14, doi:10.1186/S42269-023-01088-9.

15. Nair, N.V.; Nayak, P.K. Exploring Water Quality as a Determinant of Small-Scale Fisheries Vulnerability. *Sustainability 2023, Vol. 15, Page 13238* **2023**, *15*, 13238, doi:10.3390/SU151713238.

16. Guimarães, L.S.F.; de Carvalho-Junior, L.; Façanha, G.L.; Resende, N. da S.; Neves, L.M.; Cardoso, S.J. Meta-Analysis of the Thermal Pollution Caused by Coastal Nuclear Power Plants and Its Effects on Marine Biodiversity. *Mar Pollut Bull* **2023**, *195*, 115452, doi:10.1016/J.MARPOLBUL.2023.115452.

17. Liu, X.; Sathishkumar, K.; Zhang, H.; Saxena, K.K.; Zhang, F.; Naraginti, S.; Anbarasu K; Ramya Rajendiran; Rajasekar, A.; Guo, X. Frontiers in Environmental Cleanup: Recent Advances in Remediation of Emerging Pollutants from Soil and Water. *Journal of Hazardous Materials Advances* **2024**, *16*, 100461, doi:10.1016/J.HAZADV.2024.100461.

18. Girones, L.; Oliva, A.L.; Negrin, V.L.; Marcovecchio, J.E.; Arias, A.H. Persistent Organic Pollutants (POPs) in Coastal Wetlands: A Review of Their Occurrences, Toxic Effects, and Biogeochemical Cycling. *Mar Pollut Bull* **2021**, *172*, 112864, doi:10.1016/J.MARPOLBUL.2021.112864.

19. Karki, B.K.; Philip, L.; Karki, K.; Ghimire, A. Insight into Urban River Water Quality Using Ecological Risk Assessment Based on Risk Quotient. *Water Conservation Science and Engineering* **2024**, *9*, 1–17, doi:10.1007/S41101-024-00289-1/FIGURES/6.

20. Rad, S.M.; Ray, A.K.; Barghi, S. Water Pollution and Agriculture Pesticide. *Clean Technologies 2022, Vol. 4, Pages 1088-1102* **2022**, *4*, 1088–1102, doi:10.3390/CLEANTECHNOL4040066.

21. Ahmed, J.; Thakur, A.; Goyal, A. Industrial Wastewater and Its Toxic Effects. *Biological Treatment of Industrial Wastewater* **2021**, 1–14, doi:10.1039/9781839165399-00001.

22. Oladoye, P.O.; Bamigboye, M.O.; Ogunbiyi, O.D.; Akano, M.T. Toxicity and Decontamination Strategies of Congo Red Dye. *Groundw Sustain Dev* **2022**, *19*, 100844, doi:10.1016/J.GSD.2022.100844.

23. Yang, Y.; Wang, J.; Wang, Y.; He, Z. Biomass Decay Rate and Influencing Factors of Four Submerged Aquatic Vegetation in Everglades Wetland. *Int J Phytoremediation* **2020**, *22*, 963–971, doi:10.1080/15226514.2020.1774500.

24. Lin, L.; Yang, H.; Xu, X. Effects of Water Pollution on Human Health and Disease Heterogeneity: A Review. *Front Environ Sci* **2022**, *10*, 880246, doi:10.3389/FENVS.2022.880246/BIBTEX.

25. Hashemi, S.H.; Kaykhaii, M. Azo Dyes: Sources, Occurrence, Toxicity, Sampling, Analysis, and Their Removal Methods. *Emerging Freshwater Pollutants: Analysis, Fate and Regulations* **2022**, 267–287, doi:10.1016/B978-0-12-822850-0.00013-2.

26. Zhang, S.; Gitungo, S.; Dyksen, J.E.; Raczko, R.F.; Axe, L. Indicator Compounds Representative of Contaminants of Emerging Concern (CECs) Found in the Water Cycle in the United States. *International Journal of Environmental Research and Public Health 2021, Vol. 18, Page 1288* **2021**, *18*, 1288, doi:10.3390/IJERPH18031288.

27. Raya, S.; Tandukar, S.; Kattel, H.P.; Sharma, S.; Sangsanont, J.; Sirikanchana, K.; Ngo, H.T.T.; Inson, J.G.M.; Enriquez, M.L.D.; Alam, Z.F.; et al. Prevalence of Hepatitis A and E Viruses in Wastewater in Asian Countries. *Science of The Total Environment* **2024**, *951*, 175473, doi:10.1016/J.SCITOTENV.2024.175473.

28. Siwila, J.; Mwaba, F.; Chidumayo, N.; Mubanga, C. Food and Waterborne Protozoan Parasites: The African Perspective. *Food Waterborne Parasitol* **2020**, *20*, e00088, doi:10.1016/J.FAWPAR.2020.E00088.

29. Mendez, F.I.; Piedrahita-Gó mez, L.E.; Fernando Toro, A.; Salazar-Benitez, J.; Zapata, H.; Peña, M.I. The Invisibility of Health Effects Associated with Water Pollution within Disease Burden Estimates: Analysis from a Colombian Andean Watershed. *PLOS Water* **2024**, *3*, e0000125, doi:10.1371/JOURNAL.PWAT.0000125.

30. Meki, C.D.; Ncube, E.J.; Voyi, K. Community-Level Interventions for Mitigating the Risk of Waterborne Diarrheal Diseases: A Systematic Review. *Syst Rev* **2022**, *11*, 1–12, doi:10.1186/S13643-022-01947-Y/FIGURES/1.

31. Dutta, S.; Gupta, B.; Srivastava, S.K.; Gupta, A.K. Recent Advances on the Removal of Dyes from Wastewater Using Various Adsorbents: A Critical Review. *Mater Adv* **2021**, *2*, 4497–4531, doi:10.1039/D1MA00354B.

32. Kumar, D.; Gupta, S.K. Sustainable Approach for the Treatment of Dye-Containing Wastewater – a Critical Review. *Reviews in Chemical Engineering* **2024**, *40*, 723–763, doi:10.1515/REVCE-2023-0030/ASSET/GRAPHIC/J_REVCE-2023-0030_FIG_004.JPG.

33. Al-Tohamy, R.; Ali, S.S.; Li, F.; Okasha, K.M.; Mahmoud, Y.A.G.; Elsamahy, T.; Jiao, H.; Fu, Y.; Sun, J. A Critical Review on the Treatment of Dye-Containing Wastewater: Ecotoxicological and Health Concerns of Textile Dyes and Possible Remediation

Approaches for Environmental Safety. *Ecotoxicol Environ Saf* **2022**, *231*, 113160, doi:10.1016/J.ECOENV.2021.113160.

34. Walker, T.R. (Micro)Plastics and the UN Sustainable Development Goals. *Curr Opin Green Sustain Chem* **2021**, *30*, 100497, doi:10.1016/J.COGSC.2021.100497.

35. Kurniawan, S.B.; Abdullah, S.R.S.; Imron, M.F.; Ismail, N. 'Izzati Current State of Marine Plastic Pollution and Its Technology for More Eminent Evidence: A Review. *J Clean Prod* **2021**, *278*, 123537, doi:10.1016/J.JCLEPRO.2020.123537.

36. Akindele, E.O.; Alimba, C.G. Plastic Pollution Threat in Africa: Current Status and Implications for Aquatic Ecosystem Health. *Environmental Science and Pollution Research 2021 28:7* **2021**, *28*, 7636–7651, doi:10.1007/S11356-020-11736-6.

37. Rai, P.K.; Lee, J.; Brown, R.J.C.; Kim, K.H. Environmental Fate, Ecotoxicity Biomarkers, and Potential Health Effects of Micro- and Nano-Scale Plastic Contamination. *J Hazard Mater* **2021**, *403*, 123910, doi:10.1016/J.JHAZMAT.2020.123910.

38. Ahmed, S.F.; Mofijur, M.; Nuzhat, S.; Chowdhury, A.T.; Rafa, N.; Uddin, M.A.; Inayat, A.; Mahlia, T.M.I.; Ong, H.C.; Chia, W.Y.; et al. Recent Developments in Physical, Biological, Chemical, and Hybrid Treatment Techniques for Removing Emerging Contaminants from Wastewater. *J Hazard Mater* **2021**, *416*, 125912, doi:10.1016/J.JHAZMAT.2021.125912.

39. Kumari, P.; Kumar, A. ADVANCED OXIDATION PROCESS: A Remediation Technique for Organic and Non-Biodegradable Pollutant. *Results in Surfaces and Interfaces* **2023**, *11*, 100122, doi:10.1016/J.RSURFI.2023.100122.

40. Ribeiro, J.P.; Nunes, M.I. Recent Trends and Developments in Fenton Processes for Industrial Wastewater Treatment – A Critical Review. *Environ Res* **2021**, *197*, 110957, doi:10.1016/J.ENVRES.2021.110957.

41. Machado, F.; Teixeira, A.C.S.C.; Ruotolo, L.A.M. Critical Review of Fenton and Photo-Fenton Wastewater Treatment Processes over the Last Two Decades. *International Journal of Environmental Science and Technology 2023 20:12* **2023**, *20*, 13995–14032, doi:10.1007/S13762-023-05015-3.

42. Wang, Z.; Liu, M.; Xiao, F.; Postole, G.; Zhao, H.; Zhao, G. Recent Advances and Trends of Heterogeneous Electro-Fenton Process for Wastewater Treatment-Review. *Chinese Chemical Letters* **2022**, *33*, 653–662, doi:10.1016/J.CCLET.2021.07.044.

43. Abujazar, M.S.S.; Karaağaç, S.U.; Abu Amr, S.S.; Alazaiza, M.Y.D.; Bashir, M.J. Recent Advancement in the Application of Hybrid Coagulants in Coagulation-Flocculation of Wastewater: A Review. *J Clean Prod* **2022**, *345*, 131133, doi:10.1016/J.JCLEPRO.2022.131133.

44. Ansari, I.; Sundararajan, M.; Maiti, D.; Kumar, A.; Rout, J.R. Role of Bioremediation in Wastewater Treatment. *Biotechnological Advances for Microbiology, Molecular Biology, and Nanotechnology* **2022**, 39–64, doi:10.1201/9781003161158-4.

45. Li, X.; Wu, S.; Dong, Y.; Fan, H.; Bai, Z.; Zhuang, X. Engineering Microbial Consortia towards Bioremediation. *Water 2021, Vol. 13, Page 2928* **2021**, *13*, 2928, doi:10.3390/W13202928.

46. Narayanan, M.; Ali, S.S.; El-Sheekh, M. A Comprehensive Review on the Potential of Microbial Enzymes in Multipollutant Bioremediation: Mechanisms, Challenges, and Future Prospects. *J Environ Manage* **2023**, *334*, 117532, doi:10.1016/J.JENVMAN.2023.117532.

47. Osuoha, J.O.; Nwaichi, E.O. Enzymatic Technologies as Green and Sustainable Techniques for Remediation of Oil-Contaminated Environment: State of the Art. *International Journal of Environmental Science and Technology* **2021**, *18*, 1299–1322, doi:10.1007/S13762-020-02876-W/FIGURES/10.

48. Feng, S.; Hao Ngo, H.; Guo, W.; Woong Chang, S.; Duc Nguyen, D.; Cheng, D.; Varjani, S.; Lei, Z.; Liu, Y. Roles and Applications of Enzymes for Resistant Pollutants Removal in Wastewater Treatment. *Bioresour Technol* **2021**, *335*, 125278, doi:10.1016/J.BIORTECH.2021.125278.

49. Romeh, A.A.A. Remedial Potential of Plant Growth Promoting Rhizobacteria (PGPR) for Pesticide Residues: Recent Trends and Future Challenges. *Pesticides Bioremediation* **2022**, 381–397, doi:10.1007/978-3-030-97000-0_14.

50. Sharma, P.; Gaur, P.; Dwivedi, S.; Kumari, K.; Srivastava, J.K.; Dhakar, K.; Gaur, V.K.; Varjani, S.; Chang, J.S.; Ngo, H.H.; et al. Harnessing Microbial Potentials by Advancing Bioremediation of PAHs through Molecular Insights and Genetics. *Int Biodeterior Biodegradation* **2024**, *194*, 105861, doi:10.1016/J.IBIOD.2024.105861.

51. Mousavi, S.M.; Hashemi, S.A.; Iman Moezzi, S.M.; Ravan, N.; Gholami, A.; Lai, C.W.; Chiang, W.H.; Omidifar, N.; Yousefi, K.; Behbudi, G. Recent Advances in Enzymes for the Bioremediation of Pollutants. *Biochem Res Int* **2021**, *2021*, 5599204, doi:10.1155/2021/5599204.

52. Albayati, S.H.; Nezhad, N.G.; Taki, A.G.; Rahman, R.N.Z.R.A. Efficient and Easible Biocatalysts: Strategies for Enzyme Improvement. A Review. *Int J Biol Macromol* **2024**, *276*, 133978, doi:10.1016/J.IJBIOMAC.2024.133978.

53. Pandit, A.B.; Kumar, J.K. Drinking Water Treatment for Developing Countries: Physical, Chemical and Biological Pollutants. *Drinking Water Treatment for Developing Countries* **2019**, doi:10.1039/9781788012935.

54. Almehmadi, F.A.; Najib, A.; Ali, E.; Al-Ansary, H.; Orfi, J. Sustainable Approach of Generating Water and Energy: Techno-Economic Analysis of a Hybrid Solar Photoactive Thermal System Coupled with Direct Contact Membrane Distillation for Water Purification and Electricity Generation. *Applied Sciences 2022, Vol. 12, Page 9137* **2022**, *12*, 9137, doi:10.3390/APP12189137.

55. Yang, H.; Xu, S.; Chitwood, D.E.; Wang, Y. Ceramic Water Filter for Point-of-Use Water Treatment in Developing Countries: Principles, Challenges and Opportunities. *Front Environ Sci Eng* **2020**, *14*, 1–10, doi:10.1007/S11783-020-1254-9/METRICS.

56. Tan, K.L.; Foo, K.Y. The Viable Role of Activated Carbon for the Effective Remediation of Refinery and Petrochemical Wastewaters. *Petroleum Industry Wastewater: Advanced and Sustainable Treatment Methods* **2022**, 185–203, doi:10.1016/B978-0-323-85884-7.00016-3.

57. Wu, J.; Cao, M.; Tong, D.; Finkelstein, Z.; Hoek, E.M.V. A Critical Review of Point-of-Use Drinking Water Treatment in the United States. *npj Clean Water 2021 4:1* **2021**, *4*, 1–25, doi:10.1038/s41545-021-00128-z.

58. Minh Tran, H.D.; Boivin, S.; Kodamatani, H.; Ikehata, K.; Fujioka, T. Potential of UV-B and UV-C Irradiation in Disinfecting Microorganisms and Removing N-Nitrosodimethylamine and 1,4-Dioxane for Potable Water Reuse: A Review. *Chemosphere* **2022**, *286*, 131682, doi:10.1016/J.CHEMOSPHERE.2021.131682.

59. Kammakakam, I.; Lai, Z. Next-Generation Ultrafiltration Membranes: A Review of Material Design, Properties, Recent Progress, and Challenges. *Chemosphere* **2023**, *316*, 137669, doi:10.1016/J.CHEMOSPHERE.2022.137669.

60. Kucera, J. Introduction to Reverse Osmosis: History, Challenges, and Future Directions. *Reverse Osmosis* **2023**, 1–32.

61. Chidiac, S.; El Najjar, P.; Ouaini, N.; El Rayess, Y.; El Azzi, D. A Comprehensive Review of Water Quality Indices (WQIs): History, Models, Attempts and Perspectives. *Reviews in Environmental Science and Bio/Technology 2023 22:2* **2023**, *22*, 349–395, doi:10.1007/S11157-023-09650-7.

62. Zulkifli, S.N.; Rahim, H.A.; Lau, W.J. Detection of Contaminants in Water Supply: A Review on State-of-the-Art Monitoring Technologies and Their Applications. *Sens Actuators B Chem* **2018**, *255*, 2657–2689, doi:10.1016/J.SNB.2017.09.078.

63. Vigiak, O.; Grizzetti, B.; Udias-Moinelo, A.; Zanni, M.; Dorati, C.; Bouraoui, F.; Pistocchi, A. Predicting Biochemical Oxygen Demand in European Freshwater Bodies. *Sci Total Environ* **2019**, *666*, 1089, doi:10.1016/J.SCITOTENV.2019.02.252.

64. Gayuh, P.; Putro, L.; Hadiyanto, H.; Program, A.G.; Diponegoro, U. Water Quality Parameters of Tofu Wastewater: A Review. *IOP Conf Ser Mater Sci Eng* **2021**, *1156*, 012018, doi:10.1088/1757-899X/1156/1/012018.

65. Ali, B.; Mishra, A.; Author, C. Effects of Dissolved Oxygen Concentration on Freshwater Fish: A Review. *Int J Fish Aquat Stud* **2022**, *10*, 113–127, doi:10.22271/FISH.2022.V10.I4B.2693.

66. Wang, B.B. Research on Drinking Water Purification Technologies for Household Use by Reducing Total Dissolved Solids (TDS). *PLoS One* **2021**, *16*, e0257865, doi:10.1371/JOURNAL.PONE.0257865.

67. Matos, T.; Martins, M.S.; Henriques, R.; Goncalves, L.M. A Review of Methods and Instruments to Monitor Turbidity and Suspended Sediment Concentration. *Journal of Water Process Engineering* **2024**, *64*, 105624, doi:10.1016/J.JWPE.2024.105624.

68. Bonacina, L.; Fasano, F.; Mezzanotte, V.; Fornaroli, R. Effects of Water Temperature on Freshwater Macroinvertebrates: A Systematic Review. *Biological Reviews* **2023**, *98*, 191–221, doi:10.1111/BRV.12903.

69. Mathys, A.; Knorr, D. The Properties of Water in the Pressure-Temperature Landscape. *Food Biophys* **2009**, *4*, 77–82, doi:10.1007/S11483-009-9103-1/FIGURES/6.

70. Gangar, T.; Satyam, K.; Patra, S. Monitoring/Sensing Techniques to Address Pollutant Heterogeneity Assessment in Wastewater. *Microbial Ecology of Wastewater Treatment Plants* **2021**, 279–314, doi:10.1016/B978-0-12-822503-5.00014-X.

71. Zulkifli, C.Z.; Garfan, S.; Talal, M.; Alamoodi, A.H.; Alamleh, A.; Ahmaro, I.Y.Y.; Sulaiman, S.; Ibrahim, A.B.; Zaidan, B.B.; Ismail, A.R.; et al. IoT-Based Water Monitoring Systems: A Systematic Review. *Water 2022, Vol. 14, Page 3621* **2022**, *14*, 3621, doi:10.3390/W14223621.

72. Martin, S. Teaching and Learning Advances on Sensors for IoT. *Teaching and Learning Advances on Sensors for IoT* **2021**, 122, doi:10.3390/BOOKS978-3-0365-0523-7.

73. Calderwood, A.J.; Pauloo, R.A.; Yoder, A.M.; Fogg, G.E. Low-Cost, Open Source Wireless Sensor Network for Real-Time, Scalable Groundwater Monitoring. *Water 2020, Vol. 12, Page 1066* **2020**, *12*, 1066, doi:10.3390/W12041066.

74. de Camargo, E.T.; Spanhol, F.A.; Slongo, J.S.; da Silva, M.V.R.; Pazinato, J.; de Lima Lobo, A.V.; Coutinho, F.R.; Pfrimer, F.W.D.; Lindino, C.A.; Oyamada, M.S.; et al. Low-Cost Water Quality Sensors for IoT: A Systematic Review. *Sensors 2023, Vol. 23, Page 4424* **2023**, *23*, 4424, doi:10.3390/S23094424.

75. Ahmed, M.; Mavukkandy, M.O.; Giwa, A.; Elektorowicz, M.; Katsou, E.; Khelifi, O.; Naddeo, V.; Hasan, S.W. Recent Developments in Hazardous Pollutants Removal from Wastewater and Water Reuse within a Circular Economy. *npj Clean Water 2022 5:1* **2022**, *5*, 1–25, doi:10.1038/s41545-022-00154-5.

76. Yusuf, A.; Al Jitan, S.; Garlisi, C.; Palmisano, G. A Review of Recent and Emerging Antimicrobial Nanomaterials in Wastewater Treatment Applications. *Chemosphere* **2021**, *278*, 130440, doi:10.1016/J.CHEMOSPHERE.2021.130440.

77. Chen, V.J.; Minto, R.E.; Manicke, N.; Smith, G.D. Structural Elucidation of Two Congo Red Derivatives on Dyed Historical Objects Indicative of Formaldehyde Exposure and the Potential for Chemical Fading. *Dyes and Pigments* **2022**, *201*, 110173, doi:10.1016/J.DYEPIG.2022.110173.

78. Siddiqui, S.I.; Allehyani, E.S.; Al-Harbi, S.A.; Hasan, Z.; Abomuti, M.A.; Rajor, H.K.; Oh, S. Investigation of Congo Red Toxicity towards Different Living Organisms: A Review. *Processes 2023, Vol. 11, Page 807* **2023**, *11*, 807, doi:10.3390/PR11030807.

79. Liu, Y.; Zhao, Y.; Wang, J. Fenton/Fenton-like Processes with in-Situ Production of Hydrogen Peroxide/Hydroxyl Radical for Degradation of Emerging Contaminants: Advances and Prospects. *J Hazard Mater* **2021**, *404*, 124191, doi:10.1016/J.JHAZMAT.2020.124191.

80. Polito, L.; Bortolotti, M.; Battelli, M.G.; Bolognesi, A. Xanthine Oxidoreductase: A Leading Actor in Cardiovascular Disease Drama. *Redox Biol* **2021**, *48*, 102195, doi:10.1016/J.REDOX.2021.102195.

81. De Brabander, P.; Uitterhaegen, E.; Delmulle, T.; De Winter, K.; Soetaert, W. Challenges and Progress towards Industrial Recombinant Protein Production in Yeasts: A Review. *Biotechnol Adv* **2023**, *64*, 108121, doi:10.1016/J.BIOTECHADV.2023.108121.

82. Umezawa, K.; Akaike, T.; Fujii, S.; Suga, M.; Setoguchi, K.; Ozawa, A.; Maeda, H. Induction of Nitric Oxide Synthesis and Xanthine Oxidase and Their Roles in the Antimicrobial Mechanism against Salmonella Typhimurium Infection in Mice. *Infect Immun* **1997**, *65*, 2932–2940, doi:10.1128/IAI.65.7.2932-2940.1997.

83. Stevens, C.R.; Millar, T.M.; Clinch, J.G.; Kanczler, J.M.; Bodamyali, T.; Blake, D.R. Antibacterial Properties of Xanthine Oxidase in Human Milk. *Lancet* **2000**, *356*, 829–830, doi:10.1016/S0140-6736(00)02660-X.

84. Martin, H.M.; Hancock, J.T.; Salisbury, V.; Harrison, R. Role of Xanthine Oxidoreductase as an Antimicrobial Agent. *Infect Immun* **2004**, *72*, 4933–4939, doi:10.1128/IAI.72.9.4933-4939.2004/ASSET/ED843EB3-0409-4017-B60F-9EBA10E71814/ASSETS/GRAPHIC/ZII0090441820005.JPEG.

85. Ozturk, G.; German, J.B.; de Moura Bell, J.M.L.N. Effects of Industrial Heat Treatments on the Kinetics of Inactivation of Antimicrobial Bovine Milk Xanthine Oxidase. *npj Science of Food 2019 3:1* **2019**, *3*, 1–7, doi:10.1038/s41538-019-0046-8.

86. Ozturk, G.; Shah, I.M.; Mills, D.A.; German, J.B.; de Moura Bell, J.M.L.N. The Antimicrobial Activity of Bovine Milk Xanthine Oxidase. *Int Dairy J* **2020**, *102*, 104581, doi:10.1016/J.IDAIRYJ.2019.104581.

87. Ramos, G.K.; Goldfarb, D.S. Update on Uric Acid and the Kidney. *Curr Rheumatol Rep* **2022**, *24*, 132–138, doi:10.1007/S11926-022-01069-3/TABLES/1.

88. Liu, W.; Wang, Y.; Ai, Z.; Zhang, L. Hydrothermal Synthesis of FeS2 as a High-Efficiency Fenton Reagent to Degrade Alachlor via Superoxide-Mediated Fe(II)/Fe(III) Cycle. *ACS Appl Mater Interfaces* **2015**, *7*, 28534–28544, doi:10.1021/ACSAMI.5B09919/ASSET/IMAGES/LARGE/AM-2015-09919X_0006.JPEG.

89. Ziembowicz, S.; Kida, M. Limitations and Future Directions of Application of the Fenton-like Process in Micropollutants Degradation in Water and Wastewater Treatment: A Critical Review. *Chemosphere* **2022**, *296*, 134041, doi:10.1016/J.CHEMOSPHERE.2022.134041.

90. Invitrogen life technologies User Manual EasySelect ™ Pichia Expression Kit For Expression of Recombinant Proteins Using PPICZ and PPICZα in Pichia Pastoris (accessed on 18 August 2024).

91. Offei, B.; Braun-Galleani, S.; Venkatesh, A.; Casey, W.T.; O'Connor, K.E.; Byrne, K.P.; Wolfe, K.H. Identification of Genetic Variants of the Industrial Yeast Komagataella Phaffii (Pichia Pastoris) That Contribute to Increased Yields of Secreted

Heterologous Proteins. *PLoS Biol* **2022**, *20*, e3001877, doi:10.1371/JOURNAL.PBIO.3001877.

92. Nishino, T.; Okamoto, K.; Kawaguchi, Y.; Hori, H.; Matsumura, T.; Eger, B.T.; Pai, E.F.; Nishino, T. Mechanism of the Conversion of Xanthine Dehydrogenase to Xanthine Oxidase: Identification of the Two Cysteine Disulfide Bonds and Crystal Structure of a Non-Convertible Rat Liver Xanthine Dehydrogenase Mutant. *Journal of Biological Chemistry* **2005**, *280*, 24888–24894, doi:10.1074/JBC.M501830200/ATTACHMENT/3ECE90A0-443C-444F-8F5F-FF5FAEE79726/MMC1.PDF.

93. Netzahual-Lopantzi, A.; García-Nieto, E.; Juárez-Santacruz, L.; Torres-Dorsal, A.; Gutiérrez-Fuentes, R.; García-Vidal, U.O.; Jiménez-Pérez, J.L.; Sánchez-Ramírez, J.F. Monitoring Congo Red Discoloration Using Thermal Properties in Photocatalytic Processes: A New Approach. *Chemical Engineering and Processing - Process Intensification* **2023**, *192*, 109506, doi:10.1016/J.CEP.2023.109506.

94. Ramu, V.; Wijaya, L.S.; Beztsinna, N.; Van de Griend, C.; van de Water, B.; Bonnet, S.; Le Dévédec, S.E. Cell Viability Imaging in Tumor Spheroids via DNA Binding of a Ruthenium(Ii) Light-Switch Complex. *Chemical Communications* **2024**, *60*, 6308–6311, doi:10.1039/D4CC01425A.

95. ISO ISO 11348-3:2007 - Water Quality — Determination of the Inhibitory Effect of Water Samples on the Light Emission of Vibrio Fischeri (Luminescent Bacteria Test) — Part 3: Method Using Freeze-Dried Bacteria Available online: https://www.iso.org/standard/40518.html (accessed on 6 July 2024).

96. Wallraff, J.P.; Ungeheuer, F.; Dombrowski, A.; Oehlmann, J.; Vogel, A.L. Occurrence and in Vitro Toxicity of Organic Compounds in Urban Background PM2.5. *Science of The Total Environment* **2022**, *817*, 152779, doi:10.1016/J.SCITOTENV.2021.152779.

97. Kienle, C.; Werner, I.; Fischer, S.; Lüthi, C.; Schifferli, A.; Besselink, H.; Langer, M.; McArdell, C.S.; Vermeirssen, E.L.M. Evaluation of a Full-Scale Wastewater Treatment Plant with Ozonation and Different Post-Treatments Using a Broad Range of in Vitro and in Vivo Bioassays. *Water Res* **2022**, *212*, 118084, doi:10.1016/J.WATRES.2022.118084.

98. Ren, Q.W.; Wang, Y.; Qian, J.; Zhang, X.X.; Cheng, Y.Y.; Yu, D.; Lu, L.; He, X.; Mei, H.; Wu, C. Biosynthesis of Ag2Se Nanoparticles as a Broad-Spectrum Antimicrobial Agent with Excellent Biocompatibility. *J Hazard Mater* **2024**, *465*, 133201, doi:10.1016/J.JHAZMAT.2023.133201.

99. Lilge, L.; Ersig, N.; Hubel, P.; Aschern, M.; Pillai, E.; Klausmann, P.; Pfannstiel, J.; Henkel, M.; Morabbi Heravi, K.; Hausmann, R. Surfactin Shows Relatively Low Antimicrobial Activity against Bacillus Subtilis and Other Bacterial Model Organisms in the Absence of Synergistic Metabolites. *Microorganisms* **2022**, *10*, 779, doi:10.3390/MICROORGANISMS10040779/S1.

100. Hejna, M.; Kapuścińska, D.; Aksmann, A. A Sensitive and Reliable Method for the Quantitative Determination of Hydrogen Peroxide Produced by Microalgae Cells. *J Phycol* **2024**, *60*, 1356–1370, doi:10.1111/JPY.13524.

101. Su, Y.; Zhu, M.; Zhang, H.; Chen, H.; Wang, J.; Zhao, C.; Liu, Q.; Gu, Y. Application of Bacterial Agent YH for Remediation of Pyrene-Heavy Metal Co-Pollution System: Efficiency, Mechanism, and Microbial Response. *J Environ Manage* **2024**, *351*, 119841, doi:10.1016/J.JENVMAN.2023.119841.

102. Chen, Y.; Sun, J.; Luo, M.; Cao, Y.; Chen, Q.; He, S. Quantifying the Viability of Lactic Acid Bacteria Using Ratiometric Fluorescence Assays. *Microchemical Journal* **2024**, *206*, 111485, doi:10.1016/J.MICROC.2024.111485.

103. Aguilar-Torrejón, J.A.; Balderas-Hernández, P.; Roa-Morales, G.; Barrera-Díaz, C.E.; Rodríguez-Torres, I.; Torres-Blancas, T. Relationship, Importance, and Development of Analytical Techniques: COD, BOD, and, TOC in Water—An Overview through Time. *SN Appl Sci* **2023**, *5*, 1–13, doi:10.1007/S42452-023-05318-7/TABLES/4.

104. Singh, P.K.; Kumar, V.; Pratap, S.G.; Singh, P.K.; Kumar, M.; Negi, S.; Raj, A. Characterization of Inorganic and Organic Pollutants Load in Tannery Wastewater: Biochemical and Haematological Induced Changes in Swiss Mice. *Journal of Hazardous Materials Advances* **2023**, *12*, 100387, doi:10.1016/J.HAZADV.2023.100387.

105. Rice, E.W.; Bridgewater, L.; Association, A.P.H. *Standard Methods for the Examination of Water and Wastewater*; American public health association Washington, DC, 2012; Vol. 10;.

106. Ge, S.; Tian, W.; Lou, Z.; Wang, X.; Zhuang, L.L.; Zhang, J. Long-Term Toxicity Assessment of Antibiotics against Vibrio Fischeri: Test Method Optimization and Mixture Toxicity Prediction. *J Hazard Mater* **2024**, *469*, 133933, doi:10.1016/J.JHAZMAT.2024.133933.

107. Wang, G.; Yang, Y.; Kong, Y.; Ma, R.; Yuan, J.; Li, G. Key Factors Affecting Seed Germination in Phytotoxicity Tests during Sheep Manure Composting with Carbon Additives. *J Hazard Mater* **2022**, *421*, 126809, doi:10.1016/J.JHAZMAT.2021.126809.

108. Zaahkouk, S.A.M.; Darwish, D.A.; Masoud, H.M.M.; Abdel-Monsef, M.M.; Helmy, M.S.; Esa, S.S.; Ghazy, A.-H.M.; Ibrahim, M.A. Purification and Characterization of Xanthine Oxidase from Liver of the Sheep (Ovis Aries). *Journal of Antioxidant Activity* **2019**, *1*, 8–18, doi:10.14302/ISSN.2471-2140.JAA-19-2699.

109. Kusano, T.; Nishino, T.; Okamoto, K.; Hille, R.; Nishino, T. The Mechanism and Significance of the Conversion of Xanthine Dehydrogenase to Xanthine Oxidase in Mammalian Secretory Gland Cells. *Redox Biol* **2023**, *59*, 102573, doi:10.1016/J.REDOX.2022.102573.

110. Sellami, K.; Couvert, A.; Nasrallah, N.; Maachi, R.; Abouseoud, M.; Amrane, A. Peroxidase Enzymes as Green Catalysts for Bioremediation and Biotechnological Applications: A Review. *Science of The Total Environment* **2022**, *806*, 150500, doi:10.1016/J.SCITOTENV.2021.150500.

111. Pereira, L.M.S.; Milan, T.M.; Tapia-Blácido, D.R. Using Response Surface Methodology (RSM) to Optimize 2G Bioethanol Production: A Review. *Biomass Bioenergy* **2021**, *151*, 106166, doi:10.1016/J.BIOMBIOE.2021.106166.

112. Pimentel Prates, M.; de Oliveira Loures Marcionílio, S.M.; Borges Machado, K.; Medeiros de Araújo, D.; Martínez-Huitle, C.A.; Leão Arantes, A.L.; Ferreira da Silva Gadêlha, J.E. Fenton: A Systematic Review of Its Application in Wastewater Treatment. *Processes* **2023**, *11*, 2466, doi:10.3390/PR11082466/S1.

113. Tang, J.; Hou, B.; Liu, J.; Deng, R.; Wang, C.; Li, Z.; Jiao, Y. Enhancing the Treatment Efficiency of Three-Dimensional Electro-Fenton System for Organic Wastewater: An Analysis from the Comprehensive Perspective of H2O2 Generation. *J Environ Chem Eng* **2024**, *12*, 112666, doi:10.1016/J.JECE.2024.112666.

114. Susaimanickam, A.; Manickam, P.; Joseph, A.A. A Comprehensive Review on RSM-Coupled Optimization Techniques and Its Applications. *Archives of Computational Methods in Engineering 2023 30:8* **2023**, *30*, 4831–4853, doi:10.1007/S11831-023-09963-4.

115. Alexov, E. Numerical Calculations of the PH of Maximal Protein Stability. *Eur J Biochem* **2004**, *271*, 173–185, doi:10.1046/J.1432-1033.2003.03917.X.

116. Iark, D.; Buzzo, A.J. dos R.; Garcia, J.A.A.; Côrrea, V.G.; Helm, C.V.; Corrêa, R.C.G.; Peralta, R.A.; Peralta Muniz Moreira, R. de F.; Bracht, A.; Peralta, R.M. Enzymatic Degradation and Detoxification of Azo Dye Congo Red by a New Laccase from Oudemansiella Canarii. *Bioresour Technol* **2019**, *289*, 121655, doi:10.1016/J.BIORTECH.2019.121655.

117. Rueda-Márquez, J.J.; Levchuk, I.; Manzano, M.; Sillanpää, M. Toxicity Reduction of Industrial and Municipal Wastewater by Advanced Oxidation Processes (Photo-Fenton, UVC/H2O2, Electro-Fenton and Galvanic Fenton): A Review. *Catalysts 2020, Vol. 10, Page 612* **2020**, *10*, 612, doi:10.3390/CATAL10060612.

118. Sarkar, S.; Echeverría-Vega, A.; Banerjee, A.; Bandopadhyay, R. Decolourisation and Biodegradation of Textile Di-Azo Dye Congo Red by Chryseobacterium Geocarpopshaerae DD3. *Sustainability (Switzerland)* **2021**, *13*, 10850, doi:10.3390/SU131910850/S1.

119. Kishor, R.; Purchase, D.; Saratale, G.D.; Ferreira, L.F.R.; Bilal, M.; Iqbal, H.M.N.; Bharagava, R.N. Environment Friendly Degradation and Detoxification of Congo Red Dye and Textile Industry Wastewater by a Newly Isolated Bacillus Cohnni (RKS9). *Environ Technol Innov* **2021**, *22*, 101425, doi:10.1016/J.ETI.2021.101425.

120. Liu, Q.; Wu, Y.K.; Li, J.; Liu, E.; Tian, F.; Zhao, H.; Chen, R. Construction of Ag-Decorated ZnO with Oxygen Vacancies for Enhanced Antibacterial Activity via Increased H2O2 Production. *J Inorg Biochem* **2022**, *231*, 111778, doi:10.1016/J.JINORGBIO.2022.111778.

121. Aribisala, J.O.; Sabiu, S. Redox Impact on Bacterial Macromolecule: A Promising Avenue for Discovery and Development of Novel Antibacterials. *Biomolecules 2022, Vol. 12, Page 1545* **2022**, *12*, 1545, doi:10.3390/BIOM12111545.

122. Qin, J.; Su, J.; Li, H.; Zhang, L.; Jiang, K. Fenton Chemistry Activation in Metal-Organic Frameworks for Synergistic Bacteria Eradication. *Chemical Engineering Journal* **2024**, *497*, 154413, doi:10.1016/J.CEJ.2024.154413.

123. Giannakis, S.; Gupta, A.; Pulgarin, C.; Imlay, J. Identifying the Mediators of Intracellular E. Coli Inactivation under UVA Light: The (Photo) Fenton Process and Singlet Oxygen. *Water Res* **2022**, *221*, 118740, doi:10.1016/J.WATRES.2022.118740.

124. Li, S.; Liu, Z.; Süring, C.; Chen, L.; Müller, S.; Zeng, P. The Impact of the Antibiotic Fosfomycin on Wastewater Communities Measured by Flow Cytometry. *Front Microbiol* **2022**, *12*, 737831, doi:10.3389/FMICB.2021.737831/BIBTEX.

125. Shi, W.; Sun, W.; Liu, Y.; Zhang, K.; Sun, H.; Lin, X.; Hong, Y.; Guo, F. A Self-Sufficient Photo-Fenton System with Coupling in-Situ Production H2O2 of Ultrathin Porous g-C3N4 Nanosheets and Amorphous FeOOH Quantum Dots. *J Hazard Mater* **2022**, *436*, 129141, doi:10.1016/J.JHAZMAT.2022.129141.

126. Lin, Z.; Cheng, S.; Sun, Y.; Li, H.; Jin, B. Realizing BOD Detection of Real Wastewater by Considering the Bioelectrochemical Degradability of Organic Pollutants in a Bioelectrochemical System. *Chemical Engineering Journal* **2022**, *444*, 136520, doi:10.1016/J.CEJ.2022.136520.

127. Mahtab, M.S.; Farooqi, I.H.; Khursheed, A. Optimization of Fenton Process for Concurrent COD Removal and Lower Sludge Production: Process Intensification and Impact of Reagents Dosing Mode. *J Environ Manage* **2022**, *315*, 115207, doi:10.1016/J.JENVMAN.2022.115207.

128. Paula Floriano Santos, A.; Gozzi, F.; Evaristo de Carvalho, A.; Roberta Ferreira de Oliveira, K.; Rodrigues Lima Caires, A.; Pereira Cavalcante, R.; Fabbro Cunha, R.; Antônio da Silva, D.; Roberto Vieira Guelfi, D.; de Melo da Silva, L.; et al. Leachate Degradation Using Solar Photo-Fenton like Process: Influence of Coagulation-Flocculation as a Pre-Treatment Step. *Sep Purif Technol* **2022**, *289*, 120712, doi:10.1016/J.SEPPUR.2022.120712.

129. Chowdhary, P.; Singh, A.; Chandra, R.; Kumar, P.S.; Raj, A.; Bharagava, R.N. Detection and Identification of Hazardous Organic Pollutants from Distillery Wastewater by GC-MS Analysis and Its Phytotoxicity and Genotoxicity Evaluation by Using Allium Cepa and Cicer Arietinum L. *Chemosphere* **2022**, *297*, 134123, doi:10.1016/J.CHEMOSPHERE.2022.134123.

130. Meng, J.; Liu, S.; Gao, L.; Hong, K.; Liu, S.; Wu, X. Economical Production of Pichia Pastoris Single Cell Protein from Methanol at Industrial Pilot Scale. *Microb Cell Fact* **2023**, *22*, 1–16, doi:10.1186/S12934-023-02198-9/TABLES/3.

131. Eskandari, A.; Nezhad, N.G.; Thean, ·; Leow, C.; Basyaruddin, M.; Rahman, A.; Siti, ·; Oslan, N.; Siti, *; Leow, T.C. Current Achievements, Strategies, Obstacles, and Overcoming the Challenges of the Protein Engineering in Pichia Pastoris Expression System. *World Journal of Microbiology and Biotechnology 2023 40:1* **2023**, *40*, 1–28, doi:10.1007/S11274-023-03851-6.

132. Maghraby, Y.R.; El-Shabasy, R.M.; Ibrahim, A.H.; Azzazy, H.M.E.S. Enzyme Immobilization Technologies and Industrial Applications. *ACS Omega* **2023**, *8*, 5184–5196, doi:10.1021/ACSOMEGA.2C07560/ASSET/IMAGES/LARGE/AO2C07560_0003.JPEG.

133. Horton, A.A. Plastic Pollution: When Do We Know Enough? *J Hazard Mater* **2022**, *422*, 126885, doi:10.1016/J.JHAZMAT.2021.126885.

134. Bharadwaaj, S.K.; Jaudan, M.; Kushwaha, P.; Saxena, A.; Saha, B. Exploring Cutting-Edge Approaches in Plastic Recycling for a Greener Future. *Results in Engineering* **2024**, *23*, 102704, doi:10.1016/J.RINENG.2024.102704.

135. Mamun, A. Al; Prasetya, T.A.E.; Dewi, I.R.; Ahmad, M. Microplastics in Human Food Chains: Food Becoming a Threat to Health Safety. *Science of The Total Environment* **2023**, *858*, 159834, doi:10.1016/J.SCITOTENV.2022.159834.

136. Lamtai, A.; Elkoun, S.; Robert, M.; Mighri, F.; Diez, C. Mechanical Recycling of Thermoplastics: A Review of Key Issues. *Waste 2023, Vol. 1, Pages 860-883* **2023**, *1*, 860–883, doi:10.3390/WASTE1040050.

137. Shojaei, B.; Abtahi, M.; Najafi, M. Chemical Recycling of PET: A Stepping-Stone toward Sustainability. *Polym Adv Technol* **2020**, *31*, 2912–2938, doi:10.1002/PAT.5023.

138. Hong, H.; Ki, D.; Seo, H.; Park, J.; Jang, J.; Kim, K.J. Discovery and Rational Engineering of PET Hydrolase with Both Mesophilic and Thermophilic PET Hydrolase Properties. *Nature Communications 2023 14:1* **2023**, *14*, 1–13, doi:10.1038/s41467-023-40233-w.

139. Ding, Z.; Xu, G.; Miao, R.; Wu, N.; Zhang, W.; Yao, B.; Guan, F.; Huang, H.; Tian, J. Rational Redesign of Thermophilic PET Hydrolase LCCICCG to Enhance Hydrolysis of High Crystallinity Polyethylene Terephthalates. *J Hazard Mater* **2023**, *453*, 131386, doi:10.1016/J.JHAZMAT.2023.131386.

140. Meyer Cifuentes, I.E.; Wu, P.; Zhao, Y.; Liu, W.; Neumann-Schaal, M.; Pfaff, L.; Barys, J.; Li, Z.; Gao, J.; Han, X.; et al. Molecular and Biochemical Differences of the Tandem and Cold-Adapted PET Hydrolases Ple628 and Ple629, Isolated From a Marine Microbial Consortium. *Front Bioeng Biotechnol* **2022**, *10*, 930140, doi:10.3389/FBIOE.2022.930140/BIBTEX.

141. Liu, C.; Shi, C.; Zhu, S.; Wei, R.; Yin, C.C. Structural and Functional Characterization of Polyethylene Terephthalate Hydrolase from Ideonella Sakaiensis. *Biochem Biophys Res Commun* **2019**, *508*, 289–294, doi:10.1016/J.BBRC.2018.11.148.

142. Son, H.F.; Cho, I.J.; Joo, S.; Seo, H.; Sagong, H.Y.; Choi, S.Y.; Lee, S.Y.; Kim, K.J. Rational Protein Engineering of Thermo-Stable PETase from Ideonella Sakaiensis for Highly Efficient PET Degradation. *ACS Catal* **2019**, *9*, 3519–3526, doi:10.1021/ACSCATAL.9B00568/SUPPL_FILE/CS9B00568_SI_005.CIF.

143. Sun, J.; Cui, Y.; Wu, B. GRAPE, a Greedy Accumulated Strategy for Computational Protein Engineering. *Methods Enzymol* **2021**, *648*, 207–230, doi:10.1016/BS.MIE.2020.12.026.

144. Shroff, R.; Cole, A.W.; Diaz, D.J.; Morrow, B.R.; Donnell, I.; Annapareddy, A.; Gollihar, J.; Ellington, A.D.; Thyer, R. Discovery of Novel Gain-of-Function Mutations Guided by Structure-Based Deep Learning. *ACS Synth Biol* **2020**, *9*, 2927–2935, doi:10.1021/ACSSYNBIO.0C00345/ASSET/IMAGES/LARGE/SB0C00345_0003.JPEG.

145. Lu, H.; Diaz, D.J.; Czarnecki, N.J.; Zhu, C.; Kim, W.; Shroff, R.; Acosta, D.J.; Alexander, B.R.; Cole, H.O.; Zhang, Y.; et al. Machine Learning-Aided Engineering of Hydrolases for PET Depolymerization. *Nature 2022 604:7907* **2022**, *604*, 662–667, doi:10.1038/s41586-022-04599-z.

146. Biswas, K.M.; DeVido, D.R.; Dorsey, J.G. Evaluation of Methods for Measuring Amino Acid Hydrophobicities and Interactions. *J Chromatogr A* **2003**, *1000*, 637–655, doi:10.1016/S0021-9673(03)00182-1.

147. Zhou, Y.; Pan, Q.; Pires, D.E.V.; Rodrigues, C.H.M.; Ascher, D.B. DDMut: Predicting Effects of Mutations on Protein Stability Using Deep Learning. *Nucleic Acids Res* **2023**, *51*, W122–W128, doi:10.1093/NAR/GKAD472.

148. Vila, J.A. Proteins' Evolution upon Point Mutations. *ACS Omega* **2022**, *7*, 14371–14376, doi:10.1021/ACSOMEGA.2C01407/ASSET/IMAGES/MEDIUM/AO2C01407_M003.GIF.

149. Micsonai, A.; Wien, F.; Kernya, L.; Lee, Y.H.; Goto, Y.; Réfrégiers, M.; Kardos, J. Accurate Secondary Structure Prediction and Fold Recognition for Circular Dichroism Spectroscopy. *Proc Natl Acad Sci U S A* **2015**, *112*, E3095–E3103, doi:10.1073/PNAS.1500851112/SUPPL_FILE/PNAS.201500851SI.PDF.

150. Blázquez-Sánchez, P.; Engelberger, F.; Cifuentes-Anticevic, J.; Sonnendecker, C.; Griñén, A.; Reyes, J.; Díez, B.; Guixé, V.; Richter, P.K.; Zimmermann, W.; et al. Antarctic Polyester Hydrolases Degrade Aliphatic and Aromatic Polyesters at Moderate Temperatures. *Appl Environ Microbiol* **2022**, *88*, doi:10.1128/AEM.01842-21/SUPPL_FILE/AEM.01842-21-S0001.PDF.

151. Furtado, A.A.; Blazquez-Sanchez, P.; Grinen, A.; Vargas, J.A.; Leonardo, D.A.; Sculaccio, S.A.; Pereira, H.M.; Diez, B.; Garratt, R.C.; Ramirez-Sarmiento, C.A. Crystal Structure of Antarctic PET-Degrading Enzyme Available online: https://www.wwpdb.org/pdb?id=pdb_00008spk (accessed on 23 December 2024).

152. Khairul Anuar, N.F.S.; Abdul Wahab, R.; Huyop, F.; Normi, Y.M.; Oyewusi, H.A.; Susanti, E. In Silico Mutagenesis on Active Site Residues of Acinetobacter Haemolyticus Lipase KV1 for Improved Binding to Polyethylene Terephthalate (PET). *J Biomol Struct Dyn* **2024**, doi:10.1080/07391102.2024.2431655.

153. Tiong, E.; Koo, Y.S.; Bi, J.; Koduru, L.; Koh, W.; Lim, Y.H.; Wong, F.T. Expression and Engineering of PET-Degrading Enzymes from Microbispora, Nonomuraea, and Micromonospora. *Appl Environ Microbiol* **2023**, *89*, doi:10.1128/AEM.00632-23/SUPPL_FILE/AEM.00632-23-S0001.PDF.

154. Guo, R.T.; Li, X.; Yang, Y.; Huang, J.W.; Shen, P.; Liew, R.K.; Chen, C.C. Natural and Engineered Enzymes for Polyester Degradation: A Review. *Environmental Chemistry Letters 2024 22:3* **2024**, *22*, 1275–1296, doi:10.1007/S10311-024-01714-6.

155. Jaiswal, N.; Jaiswal, P. Thermostable α-Amylases and Laccases: Paving the Way for Sustainable Industrial Applications. *Processes 2024, Vol. 12, Page 1341* **2024**, *12*, 1341, doi:10.3390/PR12071341.

156. Kauts, S.; Mishra, Y.; Yousuf, S.; Bhardwaj, R.; Singh, S.K.; Alshabrmi, F.M.; Abdurahman, M.; Vamanu, E.; Singh, M.P. Toxicological Profile of Polyethylene Terephthalate (PET) Microplastic in Ingested Drosophila Melanogaster (Oregon R+) and Its Adverse Effect on Behavior and Development. *Toxics 2023, Vol. 11, Page 782* **2023**, *11*, 782, doi:10.3390/TOXICS11090782.

157. Liu, Y.; Wang, P.; Gojenko, B.; Yu, J.; Wei, L.; Luo, D.; Xiao, T. A Review of Water Pollution Arising from Agriculture and Mining Activities in Central Asia: Facts, Causes and Effects. *Environmental Pollution* **2021**, *291*, 118209, doi:10.1016/J.ENVPOL.2021.118209.

158. Swain, C.K. Environmental Pollution Indices: A Review on Concentration of Heavy Metals in Air, Water, and Soil near Industrialization and Urbanisation. *Discover Environment 2024 2:1* **2024**, *2*, 1–14, doi:10.1007/S44274-024-00030-8.

159. Li, N.; Liu, Y.-W.; Li, X.; Fan, X.-Y.; Wang, N.; Zhao, L. Comprehensive Control of Water Quality Deterioration in Building Water Supply Systems: A Review on Configuration, Purification and Regulation. *Water 2024, Vol. 16, Page 3132* **2024**, *16*, 3132, doi:10.3390/W16213132.

160. Jan, F.; Min-Allah, N.; Düştegör, D. IoT Based Smart Water Quality Monitoring: Recent Techniques, Trends and Challenges for Domestic Applications. *Water 2021, Vol. 13, Page 1729* **2021**, *13*, 1729, doi:10.3390/W13131729.

161. Lee, Y. An Evaluation of Microbial and Chemical Contamination Sources Related to the Deterioration of Tap Water Quality in the Household Water Supply System. *International Journal of Environmental Research and Public Health 2013, Vol. 10, Pages 4143-4160* **2013**, *10*, 4143–4160, doi:10.3390/IJERPH10094143.

162. Family, L.; Zheng, G.; Cabezas, M.; Cloud, J.; Hsu, S.; Rubin, E.; Smith, L. V.; Kuo, T. Reasons Why Low-Income People in Urban Areas Do Not Drink Tap Water. *The Journal of the American Dental Association* **2019**, *150*, 503–513, doi:10.1016/J.ADAJ.2018.12.005.

163. March, H.; Garcia, X.; Domene, E.; Sauri, D. Tap Water, Bottled Water or In-Home Water Treatment Systems: Insights on Household Perceptions and Choices. *Water 2020, Vol. 12, Page 1310* **2020**, *12*, 1310, doi:10.3390/W12051310.

164. Chen, R.; Zhang, T.; Kim, J.; Peng, H.; Ye, M.; Huang, C.H. Interfacial Solar Distillation for Freshwater Production: Fate of Volatile and Semivolatile Organic Contaminants. *Environ Sci Technol* **2021**, *55*, 6248–6256, doi:10.1021/ACS.EST.0C07191/ASSET/IMAGES/LARGE/ES0C07191_0007.JPEG.

165. Shehata, N.; Egirani, D.; Olabi, A.G.; Inayat, A.; Abdelkareem, M.A.; Chae, K.J.; Sayed, E.T. Membrane-Based Water and Wastewater Treatment Technologies: Issues, Current Trends, Challenges, and Role in Achieving Sustainable Development Goals, and Circular Economy. *Chemosphere* **2023**, *320*, 137993, doi:10.1016/J.CHEMOSPHERE.2023.137993.

166. Ruiz, J.; Martínez, P.; Martín, Í.; Lucas, M. Numerical Characterization of an Ultrasonic Mist Generator as an Evaporative Cooler. *Energies 2020, Vol. 13, Page 2971* **2020**, *13*, 2971, doi:10.3390/EN13112971.

167. Robertson, J.; McGoverin, C.; Vanholsbeeck, F.; Swift, S. Optimisation of the Protocol for the LiVE/DEAD®BacLightTM Bacterial Viability Kit for Rapid Determination of Bacterial Load. *Front Microbiol* **2019**, *10*, 448819, doi:10.3389/FMICB.2019.00801/BIBTEX.

168. Rosenberg, M.; Azevedo, N.F.; Ivask, A. Propidium Iodide Staining Underestimates Viability of Adherent Bacterial Cells. *Scientific Reports 2019 9:1* **2019**, *9*, 1–12, doi:10.1038/s41598-019-42906-3.

169. Ozerova, A.M.; Potylitsyna, A.R.; Bauman, Y.I.; Tayban, E.S.; Lipatnikova, I.L.; Nartova, A. V.; Vedyagin, A.A.; Mishakov, I. V.; Shubin, Y. V.; Netskina, O. V. Synthesis of Chlorine- and Nitrogen-Containing Carbon Nanofibers for Water Purification from Chloroaromatic Compounds. *Materials* **2022**, *15*, 8414, doi:10.3390/MA15238414/S1.

170. Cao, Y.; Zhang, F.; Sha, A.; Liu, Z.; Hao, Y.; Hao, Y. Energy Conversion Models and Characteristics under Various Inner Connections of a Novel Packaged Piezoelectric Transducer for Pavements. *Energy Convers Manag* **2021**, *245*, 114563, doi:10.1016/J.ENCONMAN.2021.114563.

171. Shi, L.; Abed, A.M.; Fayed, M.; Abdulghani, Z.R.; Anqi, A.E.; Khadimallah, M.A.; Moria, H.; Wae-Hayee, M. Economic Cost Analysis of Air-Cooling Process Using Different Numbers of Peltier Modules; Experimental Case Study. *Case Studies in Thermal Engineering* **2023**, *41*, 102627, doi:10.1016/J.CSITE.2022.102627.

172. Wezgowiec, J.; Wieczynska, A.; Wieckiewicz, M.; Czarny, A.; Malysa, A.; Seweryn, P.; Zietek, M.; Paradowska-Stolarz, A. Evaluation of Antimicrobial Efficacy of UVC Radiation, Gaseous Ozone, and Liquid Chemicals Used for Disinfection of Silicone Dental Impression Materials. *Materials 2022, Vol. 15, Page 2553* **2022**, *15*, 2553, doi:10.3390/MA15072553.

173. Varma, R.K.; Chatterjee, J. An Improved Technique for Reducing Water Wastage from Micro-RO-Membrane-Based Water Purification Systems: An Experimental Study. *Water Pract Technol* **2023**, *18*, 1172–1183, doi:10.2166/WPT.2023.065.

174. Ahmed, U.; Mumtaz, R.; Anwar, H.; Mumtaz, S.; Qamar, A.M. Water Quality Monitoring: From Conventional to Emerging Technologies. *Water Supply* **2020**, *20*, 28–45, doi:10.2166/WS.2019.144.

175. Calderwood, A.J.; Pauloo, R.A.; Yoder, A.M.; Fogg, G.E. Low-Cost, Open Source Wireless Sensor Network for Real-Time, Scalable Groundwater Monitoring. *Water 2020, Vol. 12, Page 1066* **2020**, *12*, 1066, doi:10.3390/W12041066.

176. Zhou, Z.Z.; Choudhary, V. Impact of Competition from Open Source Software on Proprietary Software. *Prod Oper Manag* **2022**, *31*, 731–742, doi:10.1111/POMS.13575/ASSET/IMAGES/LARGE/10.1111_POMS.13575-FIG0003.JPEG.

177. Mao, F.; Khamis, K.; Krause, S.; Clark, J.; Hannah, D.M. Low-Cost Environmental Sensor Networks: Recent Advances and Future Directions. *Front Earth Sci (Lausanne)* **2019**, *7*, 461015, doi:10.3389/FEART.2019.00221/BIBTEX.

178. August, T.; Chen, W.; Zhu, K. Competition Among Proprietary and Open-Source Software Firms: The Role of Licensing in Strategic Contribution. *https://doi.org/10.1287/mnsc.2020.3674* **2020**, *67*, 3041–3066, doi:10.1287/MNSC.2020.3674.

179. Alvisi, S.; Franchini, M.; Marsili, V.; Mazzoni, F.; Lloys, M.; Lluis Guixà, J.; Dragoste, C.; Cots, J.; Escobet, T.; Grau, S. Development of an Integrated System for Efficient Water Resource Management Using ESP32, MicroPython and the IoT. *Engineering Proceedings 2024, Vol. 69, Page 170* **2024**, *69*, 170, doi:10.3390/ENGPROC2024069170.

180. Ohyver, M.; Moniaga, J. V.; Sungkawa, I.; Subagyo, B.E.; Chandra, I.A. The Comparison Firebase Realtime Database and MySQL Database Performance Using Wilcoxon Signed-Rank Test. *Procedia Comput Sci* **2019**, *157*, 396–405, doi:10.1016/J.PROCS.2019.08.231.

181. Tiwari, V.; Singh, K.P.; Bharti, S.K. A Comparative Study on Hosting of Client Server Architecture Based Application on Various Cloud Hosting Platform. *NeuroQuantology* **2023**, *21*, 1417.

List of Patent, Publications, Conferences & Workshops Attended

Patents

1. **Satyam**, S., & Patra, S. (2024). Method of producing recombinant Human xanthine oxidase using *Pichia pastoris* for bioremediation of azo dyes (Application no. 202431047152; Published).
2. **Satyam**, S., & Patra, S. (2025). IoT enabled real-time water monitoring system with hybrid power management and remote data accessibility (Application no. 202531000806; Published).
3. **Satyam**, S., & Patra, S. (2025). Energy efficient water distillation unit using Piezoelectric and Peltier technologies with sterile UV-C integrated water collector (Application no. 202531002175; Published).

Research paper

1. **Satyam**, S., & Patra, S. (2024). The potential of Human xanthine oxidase-coupled Fenton reaction for advanced bio-oxidation of pollutants in sustainable wastewater treatment. **International Journal of Biological Macromolecules. DOI:** https://doi.org/10.1016/j.ijbiomac.2025.144323
2. **Satyam**, S., & Patra, S. (2024). Optimization of a novel enzyme-coupled Fenton reaction for effective degradation and detoxification of the azo dye Congo red. **Heliyon** (Submitted: 20-12-2024, ID: HELIYON-D-24-69220, 2nd Minor revision submitted)
3. **Satyam**, S., & Patra, S. (2024). Engineered Mors1 enzyme from Antarctic bacteria Moraxella TA144 for enhanced thermal stability and activity for polyethylene terephthalate degradation. **International Biodeterioration & Biodegradation** (Submitted: 22-04-2025 IBB-D-25-00354)
4. IoT-driven water quality monitoring system with hybrid power management and remote access capabilities (**Manuscript under preparation**).
5. Sustainable water purification via piezoelectric and Peltier-assisted distillation with UV-C sterile collection chamber (**Manuscript under preparation**).

Review

1. **Satyam**, S., & Patra, S. (2024). Innovations and challenges in adsorption-based wastewater remediation: a comprehensive review. Heliyon. DOI: https://doi.org/10.1016/j.heliyon.2024.e29573
2. **Satyam**, S., & Patra, S. (2025).The evolving landscape of advanced oxidation processes in wastewater treatment: challenges and recent innovations. Processes. DOI: https://doi.org/10.3390/pr13040987

Book Chapters

1. **Satyam, S**. and Patra, S. (2022). Biofunctionalized nanomaterials for sensing and bioremediation of pollutants. Biotechnology for Zero Waste: Emerging Waste Management Techniques, (pp. 343-360). https://doi.org/10.1002/9783527832064.ch22
2. **Satyam, S**. Gangar, T. Patel, S. Patra, S. (2021) Electro-and Photo-Fenton-Based Techniques in Wastewater Treatment for Advanced Oxidation of Recalcitrant

Pollutants. In Advanced Oxidation Processes for Wastewater Treatment (pp. 17-26). CRC Press. https://doi.org/10.1201/9781003165958-2

3. **Satyam, S.,** Gangar, T., Hazarika, R., Patra, S. (2023) Emerging Role of Internet of Things (IoT) for Wastewater Management: Sensing, Treatment and Process Optimization. In Emerging Technologies in Wastewater Treatment (pp. 85-98). CRC Press. https://doi.org/10.1201/9781003164982-6

4. **Satyam, S.***, Das, B.*, & Patra, S. (2023). Some recent innovations related to enzyme immobilization. In Biocatalyst immobilization (pp. 149-163). Academic Press. (*equal contribution) https://doi.org/10.1016/B978-0-323-91317-1.00014-1

5. Gangar, T., **Satyam, S.**, & Patra, S. (2021). Monitoring/sensing techniques to address pollutant heterogeneity assessment in wastewater. In Microbial Ecology of Wastewater Treatment Plants (pp. 279-314). Elsevier. https://doi.org/10.1016/B978-0-12-822503-5.00014-X

6. Gangar, T., **Satyam, S.**, Hazarika, R., & Patra, S. (2022). Molecular Techniques to Study Microbial Ecology and Dynamics for Wastewater Treatment. In Wastewater Treatment (pp. 25-34). CRC Press. https://doi.org/10.1201/9781003165057-3

7. Gangar, T., **Satyam, S.**, Sushovan, D., & Sanjukta, P. (2023). Nanobiotechnology in Wastewater Treatment. In Emerging Technologies in Wastewater Treatment (pp. 67-83). CRC Press. https://doi.org/10.1201/9781003164982-5

Conference

1. **Satyam, S**., Patra S. (2021) Potential bioremediation techniques for an effective and sustainable breakdown of medical gear waste footprints surge during COVID-19 pandemic. International Conference on Biotechnology for Sustainable Agriculture, Environment and Health (BSAEH-2021). 2021-8-4 Jaipur, India. (Poster presentation).

2. **Satyam, S.**, Patra S. (2021) Rapid painstaking in-silico characterization and structure prediction of metagenomic ORFs using AlphaFold2 and LZerD. International Conference on Biotechnology for Resource efficiency, Energy, Environment, Chemical and Health (BREECH-2022). 2022-12-01 Dehradun, India. (Poster presentation).

3. **Satyam, S.**, Patra S. (2024) Development of a low-cost ESP32-based real-time water monitoring system with hybrid power management and remote data accessibility. Research & Industrial Conclave (RIC 2023). 2023-05-18 IIT Guwahati, India. (Poster presentation).

4. **Satyam, S.**, Patra S. (2024) Developing a methylotrophic yeast based high level extracellular expression system for bioremediation of polyethylene terephthalate. Bioprocessing India 2024 (BPI-2024). 2024-12-16 IIT Madras, India (Poster presentation).

Publications from collaborative research

1. Aakula, M., Kedare, M. M., **Satyam, S.**, Patra, S., & Singha, S. (2024) Unravelling Microbial Dynamics in Hydrocarbon Contaminated Sites: A Comparative Metagenomic Perspective. **Ecological Genetics and Genomics**. DOI: https://doi.org/10.1016/j.egg.2025.100363

2. Kedare, M. M., Aakula, M., **Satyam, S.**, Bhat, S., Singh, K. K., Patra, S. (2024) Metagenomics insight of compost microbiome for exploration of industrially relevant

enzymes. Environmental Microbiology (Submitted: 21-10- 2024, ID: EMI-2024-1245, Under peer review)

Workshop

1. Nano-Bioengineering; Organized by the Department of Biotechnology, Indian Institute of Technology (IIT) Roorkee and Centre for Biomedical Research (CBR), University of Victoria (UVic) Canada.

Awards & Achievements

1. Best Product Design' Award at Vishwakarma Awards 2023. Organized by IIT Delhi & Makerbhawan foundation (Product development grant ₹1,40,000 & Travel grant | Link 1, 2, 3).